PhD Thesis

NEW DEVELOPMENTS ON PREPARATION OF COOLED AND BUNCHED RADIOACTIVE ION BEAMS AT ISOL–FACILITIES: THE ISCOOL PROJECT AND THE ROTATING WALL COOLING

Ivan Podadera Aliseda

UPC
Universitat Politècnica de Catalunya
Departament de Física i
Enginyeria Nuclear

CERN
European Organization
for Nuclear Research
Accelerators and Beams department

Director: Dr. Ari Jokinen
Co-directors: Dr. Francisco Calviño Tavares
Dr. Mats Lindroos

Genève
April 2006

I'm not kidding.
I'm telling you what I've found.
Knowledge can be conveyed,
but not wisdom.
Siddharta, Herman Hesse.

A mis padres...

Abstract

The future of physics research with radioactive isotopes is linked to the development of more accurate and specific experiments which will work with more exotic and energetic nuclei.

Requirements from experiments are getting more and more stringent and represent a big challenge for the preparation of ion beams, since each one demands different optical specifications to optimize its setup and improve its results.

This thesis focuses on the new developments achieved in preparation of RIB's (Radioactive Ion Beams) at ISOL facilities. Optical beam improvements based on cooling and bunching are the main points of the work. The design of a new general purpose second generation RFQCB (Radio Frequency ion Quadrupole Cooler and Buncher) for ISOLDE, the oldest ISOL facility, will be completely described. Nowadays, RFQCB's are one of the most important devices in the beam preparation stage thanks to the capacity to cool and bunch low-intensity ion beams quickly, easily and with great efficiency. The thesis will detail the improvements afforded by the design of the new RFQCB and provide a helpful guide for all who need to design new similar devices in the future.

This thesis also focuses on the problem of cooling and bunching high-intensity ion beams. This is very important for future ISOL facilities like EURISOL or SPIRAL-2. The last part of this thesis is devoted to comparing different cooling methods for Penning traps. The results obtained with rotating wall cooling at REXTRAP, the REX-ISOLDE Penning trap, will be presented.

List of variables

A	mass number [u]
a_u	first Mathieu parameter [-]
α	acceptance [π mm·mrad]
B	magnetic field [T]
c	damping constant [kg $\cdot$ s$^-$1]
C	capacitance [F] or conductance [m^3/s]
d_0	inner diameter of a quadrupole [m]
e	elementary charge [$1.6 \cdot 10^{-19}$ C]
E	energy [J] or electric field [V/m]
E_a	axial electric field [V/m]
ε	emittance [π mm·mrad] or [m^2/s]
ε_0	vacuum permittivity [$8.854 \cdot 10^{-12}$ F/m]
ε_r	relative permittivity [-]
f	frequency [Hz]
F	force [N] or particle fraction function [-]
F_d	damping force [N]
F_e	electric force [N]
k	Boltzmann's constant [$1.38 \cdot 10^{-23}$ J/K]
K	mobility constant [m^2·V^{-1}·s^{-1}]
K_0	standard mobility constant [m^2·V^{-1}·s^{-1}]
$\dot{m}$	mass flow [kg/s]
N	gas density [m^{-3}]
N_0	standard gas density [m^{-3}]
N_A	number of Avogradro [$6.022 \cdot 10^{-23}$ mol^{-1}]
P	pressure [Pa]
P_0	standard pressure [Pa]
Q	ion charge [C] or throughput [Pa·m^3/s]
q_u	second Mathieu parameter [-]
R	resolution of a separator
$\Re$	radius of curvature [m]
r_0	inner radius of a quadrupole [m]
t	time [s]
t_{acc}	accumulation time [s]
t_{cool}	cooling time [s]
t_{coll}	collection or accumulation time [s]
T	temperature [K]
T_0	standard temperature [293.15 K]
$T_{1/2}$	half-decay time [s]
τ	breeding time [s] or normalized time [s]
u	x or y coordinates
U_{RF}	amplitude radio frequency field [V]
U_{DC}	static field voltage amplitude [V]
v_d	drift velocity [m/s]
V	volume [m^3]
w	radial velocity [rad/s]
x, y	transversal displacement [m]
$\dot{x}, \dot{y}$	transversal velocity [m/s]
$\ddot{x}, \ddot{y}$	transversal acceleration [m/s^2]
z	longitudinal displacement [m]
$\dot{z}$	longitudinal velocity [m/s]
$\ddot{z}$	longitudinal acceleration [m/s^2]
ξ	normalized time [-]
Z	atomic number

Abbreviations and acronyms

BO	Beam Observation box
BTS	Beam Transfer Separator
CERN	Conseil Européenne pour la Recherche Nucléaire
CF	ConFlat flange standard
CW	Continuous Wave
EBIS	Electron Beam Ion Source
ECRIS	Electron Cyclotron Resonant Ion Source
ELENA	Engineering tooL for Emittance aNAlysis
EURISOL	EURopean Isotope Separation On-Line Radioactive Ion Beam Facility
FC	Faraday Cup
FWHM	Full-Width Half-Maximum
GUI	Graphical User Interface
HV	High Voltage or High Vacuum
IGISOL	Ion Guide Isotope Separator On-Line
ISCOOL	ISolde COOLer
ISOL	Isotope Separator On-Line
ISOLDE	Ion Separation On-Line facility
ISOLTRAP	ISOLde TRAP experiment
IUPAC	International Union of Pure and Applied Chemitry
JYFLTRAP	Jyväskylä Yliopisto Fysiikan Laitos TRAP
LHC	Large Hadron Collider
LINAC	LINear ACcelerator
MCP	Multi Channel Plate
MRP	Mass Resolving Power
PLC	Programmable Logic Controller
PS	Proton Synchrotron
PSB	Proton Synchrotron Booster
REXEBIS	REX-isolde EBIS
REX-ISOLDE	Radioactive EXperiment at ISOLDE
REXTRAP	REX-isolde penning TRAP
RF	Radio Frequency
RFQ	Radio Frequency Quadrupole
RFQCB	Radio Frequency Quadrupole ion Cooler and Buncher
RIA	Rare Isotope Accelerator
RIB	Radioactive Ion Beam
rms	Root Mean Square
RNB	Radiactive Nuclear ion Beam
TOF	Time of Flight
UHV	Ultra High Vacuum

Contents

Introduction

ISotope On-Line (ISOL) facilities are devoted to providing Radioactive Ion Beams (RIB) for their use in experiments of a wide variety of topics: nuclear physics, astrophysics, solid state physics, mass spectrometry, laser spectroscopy, atomic physics or medical investigations.

The huge quantity of applications makes ISOL facilities into one of the most interesting tools for these exciting research fields. Several facilities around the world are using this technique: the pioneering ISOLDE (CERN, Switzerland), SPIRAL (France), LNL (Belgium), CIAE (China), ISAC (Canada) or IGISOL (Finland) among others. New facilities are planned to be constructed e.g. EURISOL in Europe or RIA in USA. In RIA the two principal techniques to produce and deliver RIB (ISOL and In-flight) are combined. Both ISOL and In-flight techniques can be used in a complementary way.

The normal layout of ISOL facilities presents: a target where a high-energy particle beam is impinging and producing a variety of isotopes, downstream a mass separator where a particular isotope is chosen, and a beam preparation stage before the final transport of the beam to the different experiments. Independently from the technique used to provide RIB, preparation of the beam is always needed to match the optics of the RIB with the requirements from the experiments. The most extended techniques applied at the beam preparation stage are: the cooling -reduction of the beam transversal and longitudinal emittance-, the bunching -to convert a CW beam into a pulsed beam and to reduce the time structure of the beam to a few of microseconds- and the charge breeding -to increase the charge state of the ions-. This thesis focuses on developing a practical description of the beam preparation at ISOL facilities through cooling and bunching and trying to give some guidelines about the possible schemes for these facilities.

Within the framework of this thesis two main contributions have been achieved. Firstly, the design and construction of a new general purpose RadioFrequency Cooler and Buncher (RFQCB) for all experiments at ISOLDE, the so-called ISolde COOLer (ISCOOL). This device will be able to convert the quasi-continuous beam of ISOLDE High Resolution Separator (HRS) in a pulsed and cooled beam which can fit with the different specifications of ISOLDE experiments, e.g. REX-ISOLDE, MISTRAL or NICOLE. Secondly measurements have been carried out at the Penning trap of REX-ISOLDE (REXTRAP) to verify the feasibility of using rotating wall cooling instead of sideband cooling as method for normal use with high intensity beams.

This thesis consists in 11 chapters. A description of ISOL facilities and post-accelerators is given in Chapter 1, with ISOLDE and REX-ISOLDE as main examples in the framework of CERN laboratory. Chapter 2 introduces the ion beam motion and related concepts, as the beam emittance, crucial to understand the topics discussed along this thesis work. Chapter 3 focuses on the beam preparation stage at ISOL facilities. The main challenges of the beam preparation which motivated this thesis work are explained. The main devices and instrumentation associated with this stage are also presented. Ion traps and more particularly RFQCB and Penning traps are introduced in Chapter 4. The fundamental theory, based on the ion motion theory, is developed.

A presentation of the ISCOOL project, the motivation and requirements, is given in Chapter 5. The aim of the following chapters is to develop each of the most important systems of ISCOOL in particular. Chapter 6 gives an overview about the optical system. The dimensions of ISCOOL are established. A new scheme for the optics of RFQCB's, with separate axial electrodes, is presented.

Chapter 7 discusses the vacuum system. A model for simple calculation of the pressures inside the chambers is developed. The model is applied to the calculation of the pressures with the turbopumps selected. The integration of the system in the ISOLDE vacuum system is presented.

Chapter 8 presents the mechanical system. The guidelines to electrical breakdowns and misalignments are given. Chapter 9 presents the electronics and the control systems. For the electronics, the scheme of the electrical components and a comparison between a standard broadband amplifier and a new self-tuned oscillator is discussed. Calculations of the capacitances inside the RFQCB chamber based on electrostatic simulations are outlined. For the control system, the main achievement is the integration of industrial and robust Programmable Logic Controllers for the control of the main components of ISCOOL.

The assembly of the system based on the design presented in previous chapters is given in Chapter 10. The chapter also introduces possible upgrades and improvements that could be carried out in the system in the future to optimize the performance.

The last part of the thesis, Chapter 11, is devoted to discussing the results obtained after measurements with high intensity ion beams at REXTRAP for the verification of new cooling methods. The technique, from plasma physics, is for first time studied for manipulation of RIB's.

Chapter 1

ISOL- facilities

The investigation with rare nuclei has attracted many physicist during last decades. The RIB facilities and in particular the ISOL method were invented in Copenhagen over 50 years ago and afterwards migrated to CERN for using the old Syncho-Cyclotron as proton driver (see [RA89]). In the beginning, the work focused on producing a few radioactive elements for analysis in single experiments. The interest quickly grew world-wide and Radioactive Ion Beam (RIB) facilities were built to analyze the properties of exotic nuclei. In this chapter the present situation of these facilities is described. Special emphasis will be given to ISOLDE (the first ISOL facility in the world), and REX-ISOLDE (a compact linear post-accelerator coupled to ISOLDE), where the work presented in this thesis was carried out.

1.1 RIB facilities

RIB facilities are devoted to the production of ion beams formed by radioactive isotopes for different kind of experiments. The application of RIB comprises several research fields, the main ones are:

- Nuclear structure.
- Astrophysics.
- Mass spectroscopy.
- Laser spectroscopy.
- Solid state physics.
- Medicine and other applications.

At RIB facilities, radioactive isotopes from many elements of the periodic table (see Fig. 1.1 and 1.2) are produced and studied, and new elements have been discovered. Recently, the element Z=110, discovered at GSI in 1994, has been named Darmstadtium by the IUPAC. Other elements with high Z have been also at GSI (Z=111,112) and Dubna (Z=114,116). The main objective of the existing and planned facilities is the study of the properties of more unstable and exotic nuclei. A significant number of rare nuclides has been and is being studied, filling an important part of the nuclei chart (see Fig. 1.2).

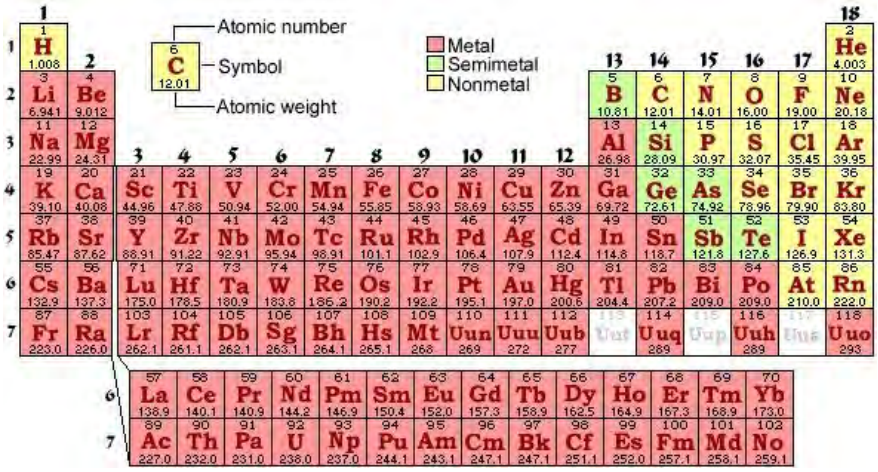

Figure 1.1: Basic periodic table of the elements

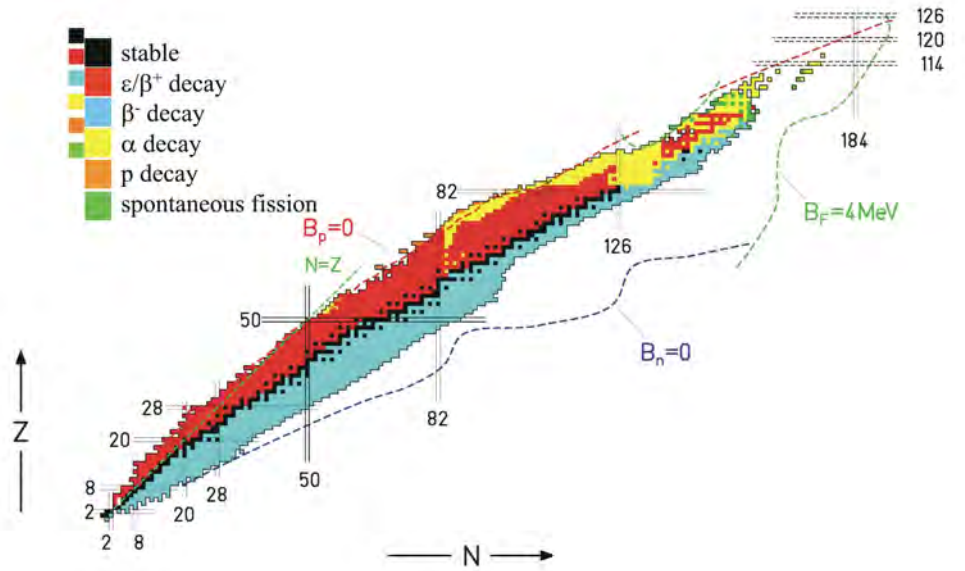

Figure 1.2: The nuclei chart

	ISOL	In-flight
Advantages	High-intensities for long-lived isotopes High beam quality Low energy	Limitation at $T_{1/2}$ <10 μs All elements High sensitivity
Disadvantages	Limitation at $T_{1/2} < 10$ ms Low or null production of refractory elements	Low intensities Low beam quality High energy

Table 1.1: Comparison of ISOL and In-flight techniques

In the case of nuclei very far from stability, it is necessary to increase the energy (for their production) and intensity of the beam in order to carry out high-precision measurements. With this aim, several are today under study, for example EURISOL and FAIR in Europe, or RIA in USA.

1.1.1 Comparison of ISOL and In-flight methods

The two major methods to produce RIB's are the ISOL method [Rav92] and the In-flight method [HGR95]. This thesis will be focused only to the first one, but a brief introduction of each concept will follow.

The **ISOL method** is based on the ionization, acceleration up to low-energies and mass separation of products from radioactive reactions produced in thick targets (fragmentation, spallation and fission) from the collision of a high-energy proton beam. The **In-flight method** is based on the fragmentation and separation in-flight of a high-energy primary-heavy ion beam by a thin target.

In Table 1.1, a comparison of the advantages and disadvantages offered by the two methods is given. As can be seen, both methods provide complementary features. ISOL was the first method developed and provides high-quality low energy beams suited for nuclear decay spectroscopy experiments, solid state physics, hyperfine studies, isotope shifts or high precision mass measurements. The In-flight technique was pioneered at Berkeley [SVGDW$^+$79], GSI [MFH$^+$79] and later at GANIL [MA91]. Thanks to this technique, the border lines of the nuclear stability could be mapped, and closed shell nuclei studied.

1.1.2 Facilities around the world

The first generation of RIB facilities includes: In-flight facilites like NSCL (MSU, USA) in North America; RIKEN (Japan) and HIRFL (Lanzhou, China) in Asia; or GANIL (France), GSI (Germany) and DRIBS (Dubna, Russia) in Europe; and ISOL- facilities like Oak Ridge, ISAC-TRIUMF (Canada) in North America; ARENAS3 (Belgium), IGISOL (Finland), ISOLDE (Switzerland), SPIRAL (France), EXCYT (Italy) in Europe. The exact location of these facilities can be consulted in Fig. 1.3.

Nowadays, second generation RIB facilities are being planned:

- **EURISOL**, in Europe [The03]. A second generation ISOL facility which is in the design study phase. One of the design study tasks is dedicated to the beam preparation in the new facility. The main deliverables of the task are the design of a high resolution separator, a high current Radio Frequency ion Cooler and Buncher (RFQCB) and the design and constructon of a high frequency Electron Cyclotron Resonance (ECR). The commissioning of the new

RFQCB for ISOLDE (ISCOOL, see Chapter 5) will contribute to the design study as a step forward for handling more intense and divergent beams in a permanent installation.

- **FAIR**, in Europe [Hen04]. An In-flight facility that will be located at the GSI accelerator complex. RIB's with energies up to 1.0-1.5 GeV/u will be reached. Research with more exotic nuclei will be available. ISOL-type beams will be obtained by stopping radioactive isotopes after the Super-FRS [GWW+03] in a dedicated gas cell and afterwards extracting them as a low energy beam.

- **RIA**, in North America. This facility will provide a combination of ISOL and In-flight techniques. The driver linac will deliver ion from protons to uranium with a beam power of 400 kW or more, and a beam energy of 900 MeV for protons or 400 MeV per nucleon for primary heavy ions. The production method can be optimized for a given nuclide.

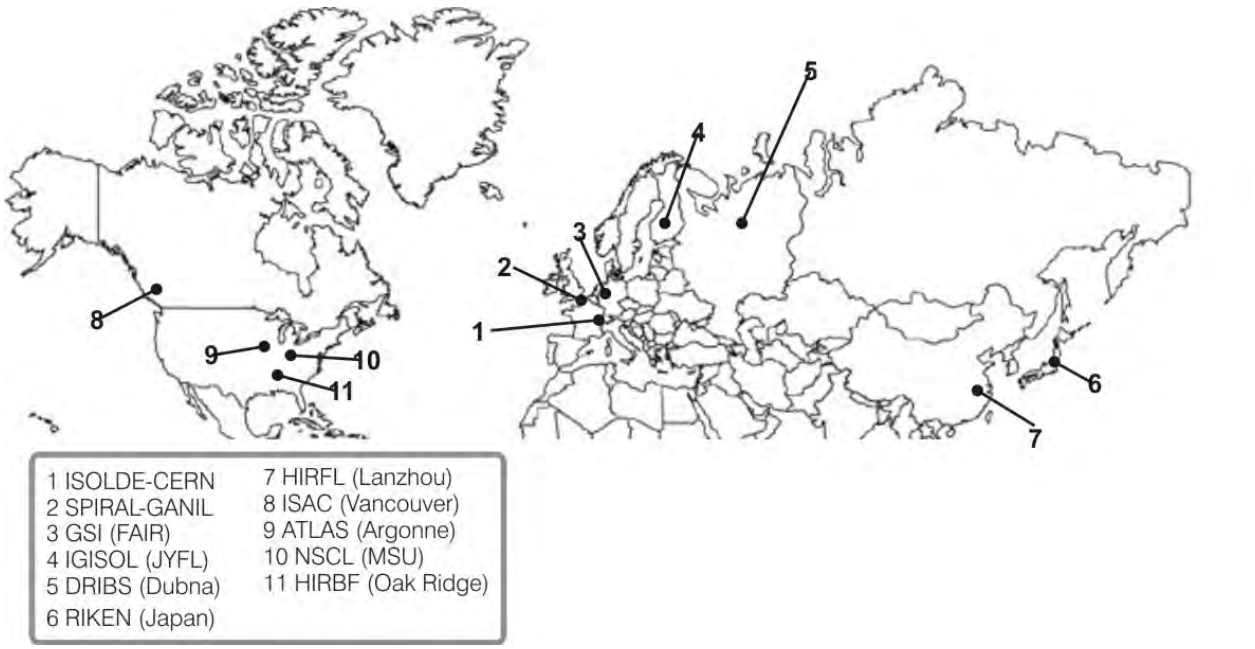

Figure 1.3: RIB facilities around the world

Other projects, like SPES at Legnaro National Laboratory in Italy, MAFF in Munich, and E-ARENA are also planned or under study. An overview of the existing and planned facilities can be found elsewhere [Lin04, Mue00].

1.2 Components of ISOL facilities

The first ISOL beams were created in 1951 at Niels Bohr Institute in Denmark with the production of a beam of krypton isotopes. As shown in Fig. 1.4, the production of RIB's with the ISOL method follows a basic scheme in the majority of the installations. The nuclei of interest are produced in nuclear reactions, released from the target, ionized and thereafter separated from less exotic nuclei. Each of the components of the ISOL layout will be presented in the following. Other ISOL layouts have been developed successfully. The most representative example is the IGISOL method (see Sec. 1.3.3), based on the ion guide principle.

Facility	P [kW]	E_D	E_f [MeV/u]	Beams available	Physics research
REX-ISOLDE	3	1.1-1.4 GeV	0.8-3 (LINAC)	^{9,11}Li,^{11,12}Be,^{17}F, ^{68,69,70}Cu,^{74,76,78}Zn,^{70}Se, ^{86,92}Kr,^{108}In,^{108,110}Sn, ^{122,124,126}Cd,^{138,140}Xe, ^{148}Pd,^{153}Sm,^{156}Eu	Condensed matter, astrophysics, Coulomb excitation
SPIRAL-GANIL (France)	6	100 MeV/u	2-25 (cyclotron)	^{7}Be,^{17,18}F,^{69}As, ^{67}Ga,$^{75-79}$Cu,$^{80-87}$Ge, ^{84}Se,^{92}Sr,^{118,120,122,124}Ag, ^{129}Sb,$^{130-136}$Sn,^{132,134,136}Te	Coulomb excitation, transfer
LLN (Belgium)	6	30 MeV	10 (cyclotron)	^{6}He,^{7}Be,^{10,11}C,^{13}N, ^{15}O,^{18}F,^{18,19}Ne,^{35}Ar	Astrophysics
HRIBF-ORNL (USA)	1	100 MeV	2-10 (tandem)	^{7}Be,^{17,18}F,^{69}As, ^{67}Ga,$^{75-79}$Cu,$^{80-87}$Ge, ^{84}Se,^{92}Sr,^{118,120,122,124}Ag, ^{129}Sb,$^{130-136}$Sn,^{132,134,136}Te	Astrophysics, Coulomb excitation transfer
ISAC1-TRIUMF (Canada)	50	500 MeV protons	1.5 (LINAC)	^{8,11}Li,^{20,21,26,32}Na, $^{36-41}$K,^{75}Ga, ^{74,79,91,80}Rb	Astrophysics

Table 1.2: Comparative of the present ISOL facilities around the world with post-accelerated beams, P is the beam power, E_D the driver energy and E_f the post-accelerated energy (from [The03, But05]).

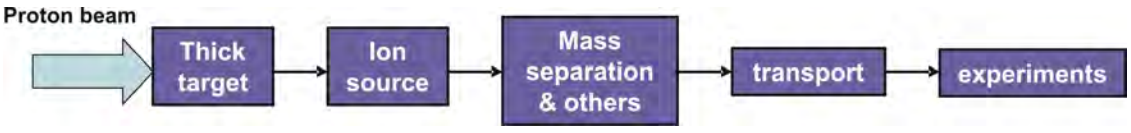

Figure 1.4: Scheme of the procedure to produce and transport RIB's at ISOL facilities

1.2.1 Targets

At ISOL facilities, the high-energy primary-proton beam produces radioactive products after impinging in a thick target. The target development involves multiple fields of research, like radiochemistry, metallurgy, high temperature chemistry or surface physics. Targets could consist of molten metals kept at temperatures from 700°C and up to about 1400°C. Such targets are characterized by a relatively long release time of the produced isotopes. A typical time constant of the release is about 30 s. Faster release times, in the order of 1 s or less, can be obtained, if the target material in the form of refractory metal powder, metals or carbides is used at temperatures above 2000°C. When bunched beams impinge on the target container, the shock-waves produced in the target container decrease the release time. This effect has been studied by Wilfinger [Wil05] for ISOLDE targets. Time constants down to some tenths of a second can be reached for the fastest targets.

1.2.2 Ion sources

The ion source together with the target constitutes the most important element of an ISOL facility. The development of ion sources is a combination of chemistry, mass-transport and material physics. The function of an ion source is to ionize the radioactive nuclei coming from the target material and to release them with the maximum efficiency and as fast as possible. In addition, an ion beam preferably should contain isotopes of only one chemical element. The different types of ion sources which are used at typical ISOL facilities are explained in the following.

Surface ion sources

The so-called surface ion source is the simplest ionization method. The set-up (see Fig. 1.5) consists of a line (a metal tube of e.g. tantalum or tungsten) which has a higher work function than the atom that should be ionized. In surface ionization, atoms of elements with low ionization potential (I) are converted to singly charged ions after they get into contact with a metal surface of high work function (f). Once the atoms produced in the target are in the line (see Fig. 1.5), they capture the electrons released by the metal and they get ionized. In principle, for alkali elements such as K, Rb and Cs (I = 4.3, 4.2 and 3.9 eV respectively) in contact with Re surfaces (f = 5.1 eV), ionization efficiencies of 100% are possible. The line can be heated up to 2400°C. The maximum temperature depends on the construction material. After the line, an extraction electrode accelerates the ions up to the desired energy trying to maximize the efficiency. The surface technique has been demonstrated to be an efficient method used in combination with most of the different target materials.

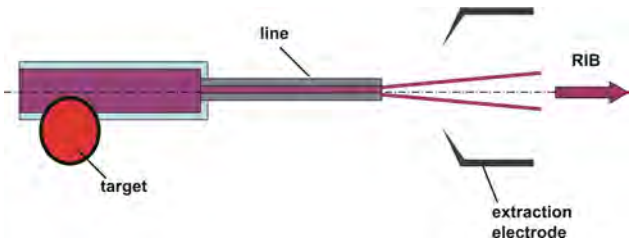

Figure 1.5: Scheme of production of ions from a target by the surface method (*surface ion source*).

Plasma ion sources

Plasma ion sources are used when the surface ionization method is not practicable due to the high ionization potential of the element of interest. In this method, a heated cathode (up to 2000°C) acts as an electron emitter. The cavity is filled with a plasma made typically of a mixture of noble gases (Ar and Xe). The electrons from the cathode are guided to the anode by applying a drift voltage of 150 V to the anode. In their way to the anode the electrons knock out the atoms from the plasma: the atoms are ionized. An additional magnetic field can be used to increase the interaction between the electrons and the plasma. The plasma method has been used in combination with most of target materials. The maximum efficiency is around a few ten percent for ^{132}Xe (see [CCE$^+$02] and [Kos02]).

Laser ion sources

Even though the two methods explained before, surface and plasma ionization, are very general and applied to produce most of the RIB's, there are some isotopes that cannot be ionized efficiently with neither of these techniques. In practically all cases the beam obtained with these methods contains undesirable impurities that decrease the selectivity purity of the source. The laser ion source has been developed to obtain a purified beam since it works only on the element for which the laser wavelength is tuned for. Thus, the isobaric contamination is reduced (caused by surface ionization inside the tube where laser ionization takes place and which needs moderate heating). The global effect is the release of beams with enhanced optical properties with respect to plasma ion sources. The laser system consists of copper vapor lasers, tuneable dye lasers and non linear crystals for frequency doubling or tripling, offering the possibility for most efficient two or three step ionization. More information about this technique can be found in [MFK$^+$93, LCF$^+$98, vD00].

1.2.3 Mass separators

The beam produced at the target-ion source normally does not fit the requirements for the experiments in terms of purity or optical quality. Magnetic mass separators are implemented in the beam line to get the required purity. These devices use a magnetic field perpendicular to the beam axis to bend the ion trajectories. Since the curvature radius is different for different masses (see Sec. 2.1.2 for further information) a specific isotope can be selected out. The quality of a mass separator is determined by the resolution (R_Δ, see Sec. 2.1.2).

1.3 Examples of ISOL facilities

1.3.1 ISOLDE

The ISOLDE facility [Kug00] is located at the CERN particle accelerator complex as one of the experiments of the largest physics laboratory in the world, see Fig. 1.6. The CERN accelerator complex consists in a chain of accelerators where the energy of particle beams is progressively increased. Beams are created in one of the ion sources and accelerated first at linear accelerators (LINAC 1, 2 or 3). After the LINACs, the beam is transported to the first synchrotron, the PSB (Proton Synchrotron Booster). Due to the space-charge effects, the LINAC beam is divided in four separated bunches. The PSB is made of four parallel accelerator rings where each bunch from the LINAC is accelerated individually. After acceleration, the four bunches join together at the exit

of the PSB. At the PSB, the energy of proton beams is increased up to energies of 1.4 GeV. With this energy, the beam can either be sent to some experiments, like ISOLDE or AD (antimatter experiment), or to the next accelerator, the PS (Protron Synchrotron). At the PS, the beam energy is increased up to 30 GeV. Once again, the beam can either be transported to some experiments or to the next synchrotron, the SPS (Super Proton Synchrotron). The SPS still pushes further up the energy of the particles and some experiments can also be performed at this step.

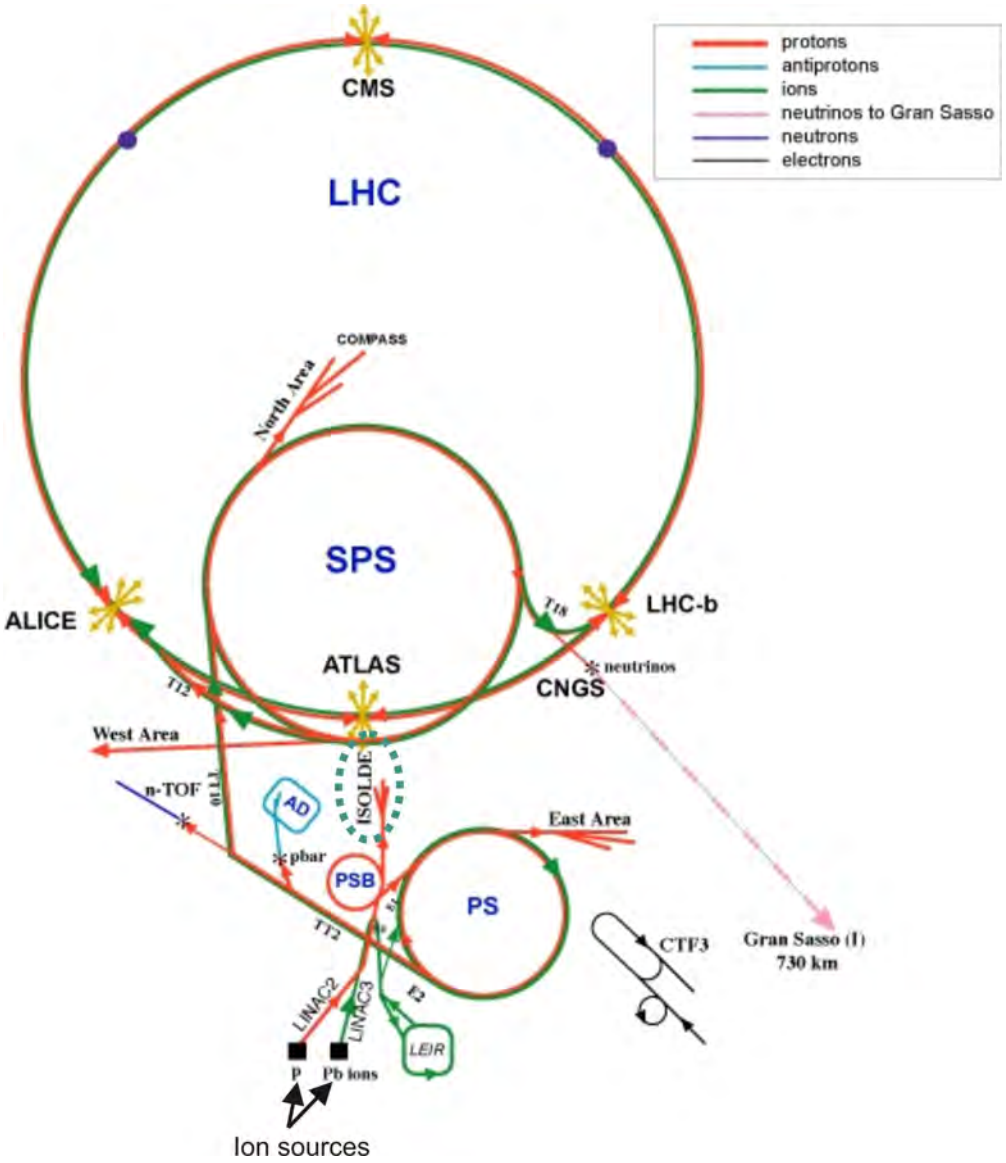

Figure 1.6: Layout of CERN accelerators complex.

From 2007, it is planned that the new accelerator, the LHC (Large Hadron Collider) will be fully operating. The beam will be injected in the LHC by the SPS. The LHC will be the most powerful particle accelerator in the world. At the LHC, two proton beams will be simultaneously accelerated up to an energy of 14 TeV in the center of mass. Within this energy, it is foreseen that the LHC will provide some outstanding experimental results to prove some of the theoretical physics developed in the past years, e.g. the existence of Higgs boson will be tested in experiments like ATLAS or CMS.

As mentioned above, ISOLDE (see Fig. 1.7) uses the PSB as a driver with a beam energy of 1 or 1.4 GeV. The proton pulses impinge each 1.4 s on one the two ISOLDE targets with an average intensity of about 2 μA, producing radioactive nuclides. The beam is accelerated at the front-ends and purified by one of the two mass separators, the GPS (General Purpose Separator) or the HRS (High Resolution Separator). So far, ISOLDE is providing 950 isotopes of 70 elements between $^{6}_{2}$He and $^{228}_{89}$Ac. Up to 40 target/ions source units can be used during one year of operation.

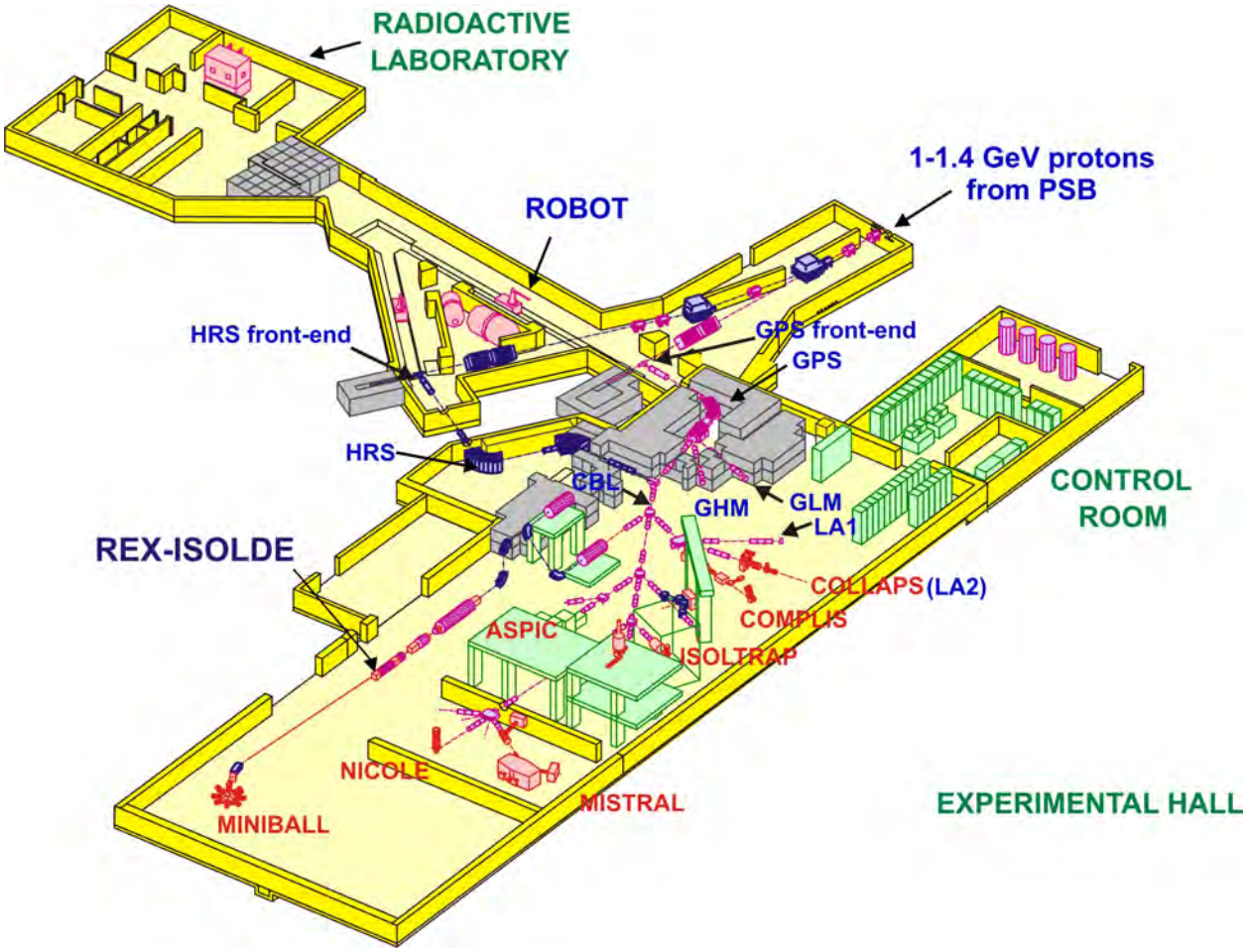

Figure 1.7: Layout of the ISOLDE-CERN facility with the extended hall and future REX-ISOLDE extension.

After the RIB is mass separated, it is delivered to the experiments located in the ISOLDE hall. In Figure 1.7 the main experiments are indicated. For beams with an isotopic mass difference minor than 15%, different experiments can be carried out in parallel if their set-up is located at one of the beam lines emerging from the Central BeamLine (CBL). GLM and GHM can be used for temporary on-line experiments. The GLM (for low masses 2-15% less than the center of mass) and the GHM (for high mass, 2-15% more) can operate simultaneously. LA1 and LA2 are dedicated to decay spectroscopy experiments for nuclear physics or astrophysics. Special beamlines are used for experiments with complicated set-ups. This is the case of COLLAPS (which produces polarized ion beams by laser polarization for both atomic and nuclear solid state physics), COMPLIS (atomic physics experiments), NICOLE (nuclear orientation experiments at temperature below 1 K

for weak interaction studies, nuclear physics or solid-state physics), ISOLTRAP (mass spectrometry experiment using a double Penning trap system in combination with an ion cooler), MISTRAL (mass spectrometry experiment based in a cyclotron technique). In addition one of the beam lines is capable to host experiments that require ultra-high vacuum like ASPIC (Apparatus for Surface Physics and Interfaces at CERN).

Physics at ISOLDE follows several paths due to the large variety of available isotopic species. This feature allows the systematic study of atomic and nuclear properties and exotic decays far from the line of stability. Results coming from these studies have implications in different fields: astrophysics, weak-interaction physics, solid-state physics, biomedicine or properties of the nucleus (mass spectrometry, collinear laser spectroscopy). A graph comparing the numbers of experiments at ISOLDE in different research fields and their required beam time is described in [FIN04].

An extension of the ISOLDE hall (see Fig. 1.8) has been constructed in the year 2004 to set up new experiments, to liberate space of the present experiments and to upgrade existing ones. An example is the post-accelerator REX-ISOLDE and the MINIBALL detector (see following section).

Figure 1.8: The new building constructed as extension of the ISOLDE hall: external view (*left view*) and internal view of the extension (*right view*).

1.3.2 Post-acceleration of RIB's: REX-ISOLDE

At ISOLDE, the REX-ISOLDE machine [ACSW05, HDc94, HKS$^+$00, KSE$^+$03, VDCJ$^+$98] (see Fig. 1.9) makes possible to post-accelerate the RIB to energies around 2.2-3.1 MeV/u. This is nowadays an unique feature world-wide. The main applications of REX-ISOLDE RIB's are:

- Acceleration of radioactive isotopes to energies close to the Coulomb barrier.
- γ-spectroscopy of neutron rich light isotopes.
- Investigation of halo nuclei.
- Study of astrophysically relevant reactions.

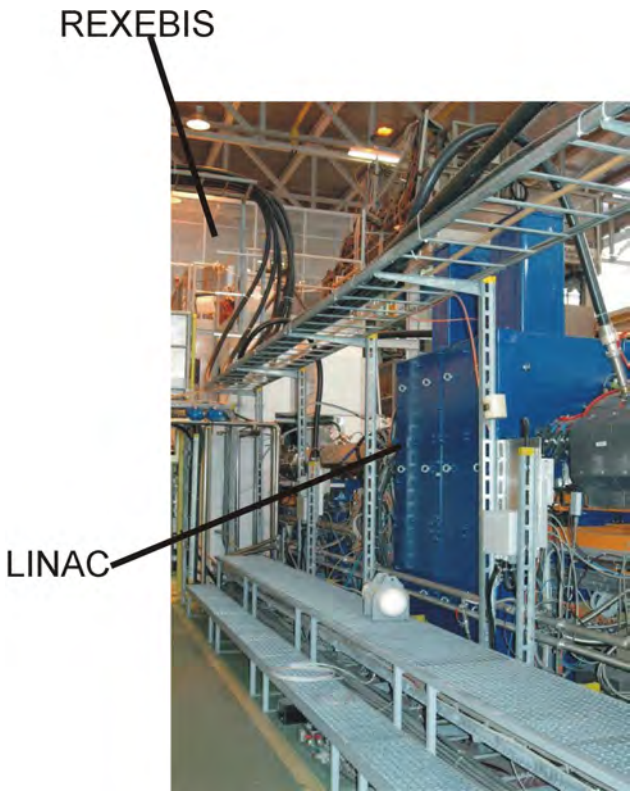

Figure 1.9: Picture of the present REX setup at the ISOLDE hall. At the top it is possible to see the high voltage cage of REXEBIS.

The layout of the machine is shown in Fig. 1.10. The main element is a LINAC which accelerates the ions from an initial energy of 60 keV to 2.2-3.1 MeV/u. Before acceleration, the RIB is charge bred using an EBIS. For an ion of the same mass, increase of the ion charge state implies a higher acceleration in the same electric field. Thus, the length of the LINAC so as to reach a certain energy can be diminished after charge breeding. The acceptance of REXEBIS obliges the normal ISOLDE optical beam properties to be improved. The operation is made in this case using a Penning trap (see Chapter 2), the so-called REXTRAP.

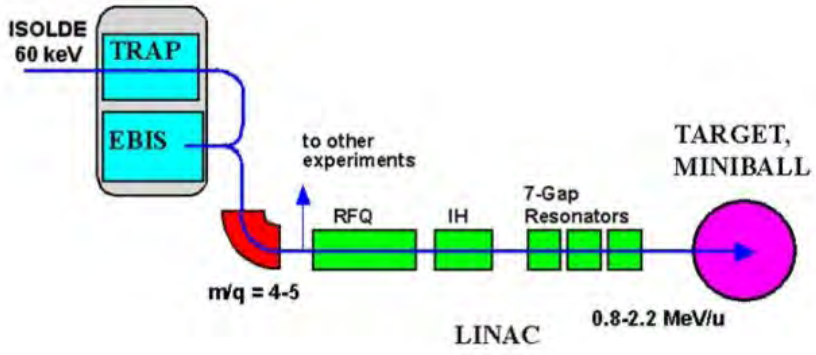

Figure 1.10: Layout of the REX-ISOLDE facility.

In the near future an upgrade of REX-ISOLDE will increase the beam energy of the post-accelerated beams from 3.1 MeV/u to 5.5 MeV/u. In a longer perspective, the energy of REX-ISOLDE is planned to be upgraded to 10 MeV/u in collaboration with the State Research Center of Russian Federation Institute for High Energy Physics (IHEP) of Moscow.

1.3.3 The ion guide technique: IGISOL at Jyväskylä

IGISOL is based on the so-called ion guide method [Den97]. This technique relies on stopping energetic primary recoil ions in a gas cell at relatively high pressure. While entering the gas, ions will end up to 1^+ charge in ion-atom interactions. Just after the singly charged ions are transported by the gas flow through a differentially pumped skimmer section for acceleration and mass purification in a typical ion mass separator. The advantages of this method in front of the typical target/ion source method are the rapidity (production of very short-life isotopes, less than ms), and high independency on the chemistry of the ionic species. For IGISOL, the quality of the beam delivered depends only on the parameters of the ion guide, mainly the skimmer voltage and the gas pressure inside the gas cell. In addition the optical quality is normally inversely proportional to the yield of the radioactive ions [Äystö01].

Due to the poor optics quality of the beam, IGISOL was one of the pioneers on commissioning an RFQCB for the improvement of the accuracy of the mass spectrometry experiment JYFLTRAP. The experience obtained in the design and operation of this device have been very useful during the work developed in this dissertation (see Chapter 5).

Chapter 2

The ion motion at RIB facilities

This chapter will introduce a basic theory of the main topics related to the ion motion of low-energy beams at ISOL facilities. A detailed description can be found elsewhere [Wol87]. In the following a further discussion of each topic is given to present the notation. Concepts that will be used along this work as focusing, steering or beam emittance are explained.

2.1 Optical devices

One of the most important topics at RIB facilities is the transport of the ion beam from the front-ends, where the ion beam is created, to the experiments. In this step, ion optical devices modify the beam to assure either transport, purification or improvement of the properties by using electric and magnetic fields.

In an electromagnetic field, a particle with an elementary charge e moving with velocity **v** is subjected to the Lorentz force **F**:

$$\mathbf{F} = e(\mathbf{E} + \mathbf{v} \times \mathbf{B}). \tag{2.1}$$

Magnetic fields cannot contribute to change the particle's energy ΔE as can be seen from the integration between two points r_1 and r_2 of the Eq. 2.1:

$$\triangle E = \int_{r_1}^{r_2} \mathbf{F} d\mathbf{r} = e \int_{r_1}^{r_2} (\mathbf{E} + \mathbf{v} \times \mathbf{B}) \cdot d\mathbf{r}. \tag{2.2}$$

It is clear that always $(\mathbf{v} \times \mathbf{B}) \cdot d\mathbf{r} = 0$. However the magnetic field can be used to guide and the focuse the ion beams.

2.1.1 Electrostatic elements

The construction of the devices based on electric fields is in general less complex. Furthermore, the operation and the maintenance of the magnetic devices is more tedious and complicated. For high energy beams, as in the synchrotrons, electrostatic elements are not convenient since the required fields are too high. At relativistic energies, electric and magnetic fields have the same effect on the particle trajectory if $E = cB$ (E electric field strength, c speed of light and B magnetic field strength). A magnetic field of 1 T is thus equivalent to an electric field of $3{\cdot}10^8$ V/m. Therefore, for high-energy beams, magnetic dipoles are the sole technical option available to bend the beams. At low ion beam energies, the use of electric rather than magnetic fields to act on the particles is more widespread for beam transport.

Dipoles

It is very usual that the beam lines are not straight but they have either to follow some curvature in some point or to divide in different sections. In synchrotrons, magnetic dipoles are used to guide the beam along the circular trajectory of the accelerator. For example, at the future LHC accelerator superconducting magnets have been developed to create the required 8 T (perpendicular to the longitudinal axis) to guide the beam along a circular trajectory of 27 km. However, at low energies, an electric field pointing towards the curvature radii is normally used to bend the ion beam. Figure 2.1 shows this principle. $\mathbf{E}$ is an static electric field coplanar with the bending plane, Q is the charge of the ion, m the mass and $\Re$ the curvature radii. The two arcs represent the shapes of the cathode and anode electrodes which form the proper electric field.

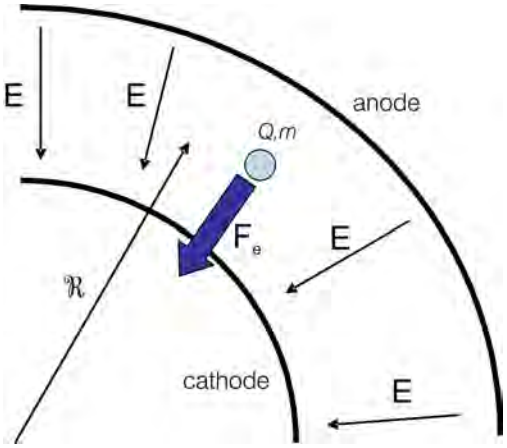

Figure 2.1: Principle of bending the trajectory of an ion in an electrostatic dipole.

Quadrupole multiplets

The beam consists, as explained in Sec. 2.2, of particles with some transverse motion (either diverging or converging). The transverse position x and dispersion x' of the ions along a straight beam line section, without optical elements, can be formulated as:

$$\begin{bmatrix} x_2 \\ x_2' \end{bmatrix} = \begin{bmatrix} 1 & l \\ 0 & 1 \end{bmatrix} \begin{bmatrix} x_1 \\ x_1' \end{bmatrix}. \tag{2.3}$$

Ions are lost when $x_2 = d_{pipe}/2$, with d_{pipe} the diameter of the pipe of the beam line. Searching for a lens, it would be very useful to look for a system in which the x and y components of the magnetic flux density or electrostatic field increase linearly with the distance from the straight optic axis. One such system is the quadrupole lens. This field focuses the ion beam in one of the transverse planes whilst defocusing in the other one. A quadrupolar electric field $\mathbf{E}$ is created using two pairs of electrodes of different polarities, as for example it is shown in Fig. 2.2. In this case the strength of the electric field will increase proportionally to the distance from the z-axis of the quadrupole. The electric field can be expressed as:

$$\mathbf{E} = E_0 \left(\lambda \mathbf{x} + \eta \mathbf{y} + \gamma \mathbf{z}\right), \tag{2.4}$$

where E_0, λ, η and γ are constants. This field corresponds to hyperbolas in the transverse $x - y$ plane. In practice, electrodes with hyperbolical shape are difficult to manufacture. For that reason a good way to create a hyperbolical field is the use of a set of four circular electrodes whose radius follows the approximation [LWY71]:

$$\frac{R}{r_0} = 1.14511. \tag{2.5}$$

The expression gives the best relation between the radius of the electrode R and the half-distance between opposite electrodes r_0 (see Fig. 2.2).

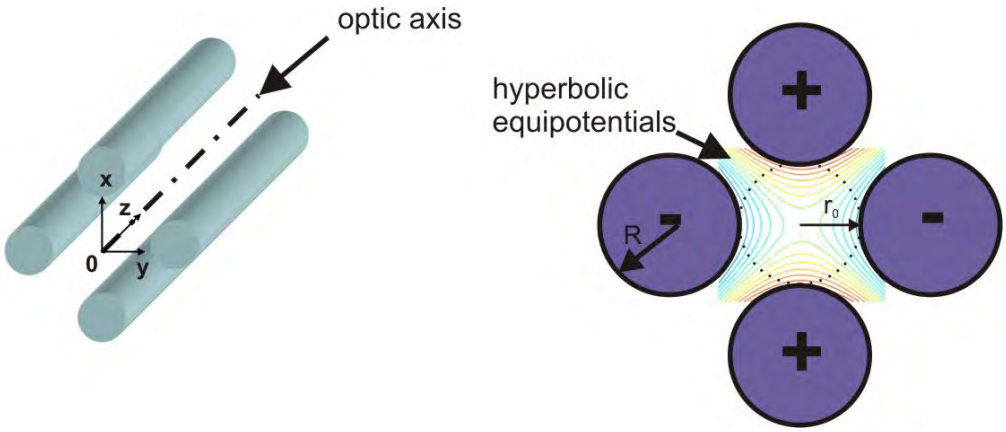

Figure 2.2: Threedimensional sketch of the quadrupole rods (*left*) and transverse sketch the equipotential lines of the hyperbolical electric field which is created along the quadrupole (*right*). The half distance between opposite rods r_0 and the radius of the rods R are shown to scale.

At low energies, static electric fields are the most suitable tool to focus and transport the beam along the vacuum chambers of the beam lines without losses. One way to manipulate the beam, focusing or defocusing as required, is the use of quadrupole multiplets. They consist of j quadrupoles and $j + 1$ drift distances. The position of a beam particle in the $x - x'$ phase space after the quadrupole multiplet would read:

$$\begin{bmatrix} x_2 \\ x_2' \end{bmatrix} = \begin{bmatrix} (x|x) & (x|a) \\ (a|x) & (a|a) \end{bmatrix} \begin{bmatrix} x_1 \\ x_1' \end{bmatrix}, \tag{2.6}$$

where (x_1, x_1') are the coordinates in the phase space at the starting point, (x_2, x_2') the coordinates after the multiplet and the matrix transfer for a multiplet with i quadrupoles is:

$$\begin{bmatrix} (x|x) & (x|a) \\ (a|x) & (a|a) \end{bmatrix} = \begin{bmatrix} 1 & l_2 \\ 0 & 1 \end{bmatrix} \prod_{i=1}^{n} \begin{bmatrix} c_{xi} & s_{xi} \\ -k_{xi}^2 s_{xi} & c_{xi} \end{bmatrix} \begin{bmatrix} 1 & d_i \\ 0 & 1 \end{bmatrix}, \tag{2.7}$$

where k_{xi} is the proportionality constant in the x coordinate, d_i the distance between the quadrupole i and $i + 1$ and l_2 the distance from the end of the last length to the point of measurement. The constants c_{xi} and s_{xi} can be found directly from k_{xi} as can be seen in [Wol87].

There is freedom to choose the number of quadrupoles, but the most typical is the quadrupole triplet ($i = 3$). The reason is that it is still not too complex and the overall beam stays rounder than in doublets. The quadrupole triplets are normally design to focus the beam in a certain point

after the quadrupole (*focusing quadrupole triplets*). However, sometimes it is useful to have the opposite effect than the focusing quadrupole, that means to defocus the beam, to make it more divergent. The main purpose is to try to transport the beam as parallel as possible. Using combinations of focusing and defocusing elements can improve the beam transport. The principle of the defocusing quadrupoles is the same as the focusing quadrupoles but applying different voltages to the rods to create a net defocusing effect.

Higher multipoles
Electric fields with more than four poles are normally used to correct the distortions on the beam motion created by non-ideal dipole or quadrupole electric fields. For example, **hexapoles** correct aberrations of field errors x^2 and **octupoles** of x^3. Higher aberrations are negligible and therefore devices with more than eigth poles are not used.

Einzel lenses

The device consists of three charged lenses in which the first and the last are held at the same voltage. The result is a strong focusing of the ions without changing their kinetic energy. The Einzel lenses have normally a cylindrical geometry and the ion beam travels along the axis.

Steering plates

Steering plates are elements which correct inevitable misalignments of the beam with respect to the mechanical axis of the beam line. The principle is the creation of an electrostatic field in the direction in which the misalignment has to be corrected. For example, a correction of a misalignment in a vertical plane will need a vertical electrostatic field. The principle to create the field is the same as in the dipoles mentioned before, but in this case the plates are just planar conducting surfaces which are parallel to eah other. This system of beam correction works well but has the disadvantage that it can distort the beam profile if the fields applied are too big. Normally the steering plates are used in couples (one for the vertical and one for the horizontal direction), or even better in two couples (two vertical and two horizontal plates), so one can control more precisely the beam alignment.

2.1.2 Magnetic mass separators

The magnetic mass separators are the crucial device at ISOL facilities. They are based on the bending of the ion trajectory in a magnetic field perpendicular to the direction of the ion motion. From Eq. 2.1, if no electric field is applied but only a perpendicular magnetic field, the strength of the force F perpendicular to the velocity of the ion is:

$$F = evB. \tag{2.8}$$

As the trajectory of the ion bends due to the perpendicular magnetic field, the acceleration is expressed as:

$$a = a_n = \frac{v^2}{\Re}, \tag{2.9}$$

where $\Re$ is the radius of curvature of the ion. Grouping Eq. 2.8 and Eq. 2.9, the radius of curvature $\Re$ can be expressed as:

$$\Re = \frac{eB}{mv} \tag{2.10}$$

For different masses, the radius of the trajectory differs. Therefore for a certain mass to be selected, the magnetic field has to be chosen so the ions fit into the extraction slit of the magnet. Only these ions will be extracted. The quality in the design of the magnetic field (like absence of distortions and field uniformity), the mechanical geometry of the separator and the quality of the injected beam will finally determine the quality of the separation. To express this feature, the so-called *rigidity resolving power* R_Δ is used (see [Wol87]) and is defined as:

$$R_\Delta = \frac{D_\Delta}{(x|x)2x_{10}}, \tag{2.11}$$

where D is the *rigidity dispersion* defined as:

$$D_\Delta = (x|\Delta). \tag{2.12}$$

The distance $(x|\Delta)$ is the separation in the image plane of the separator between the area of particles with $\Delta = 1$, where:

$$\Delta = \frac{p_1 - p_0}{p_0} \tag{2.13}$$

where p_1 and p_0 are the momentum of a certain particle and the reference particle respectively. The distance in the image plane between two beams of momentum p_1 and p_0 will be then ΔD or in other terms $\Delta(x|\Delta)$. Figure 2.3 shows an schematic view of a $180°$ mass separation of a beam with area $2x_{10}y_{10}$ at the injection. Therefore the value $2x_{10}(x|x)$ represents the size of the particle distribution with momentum p_1 in the image plane. For non-relativistic energies, which is the case for ISOL facilities, the rigidity resolving power (R_Δ) and the mass resolving power (R_m) are equivalent.

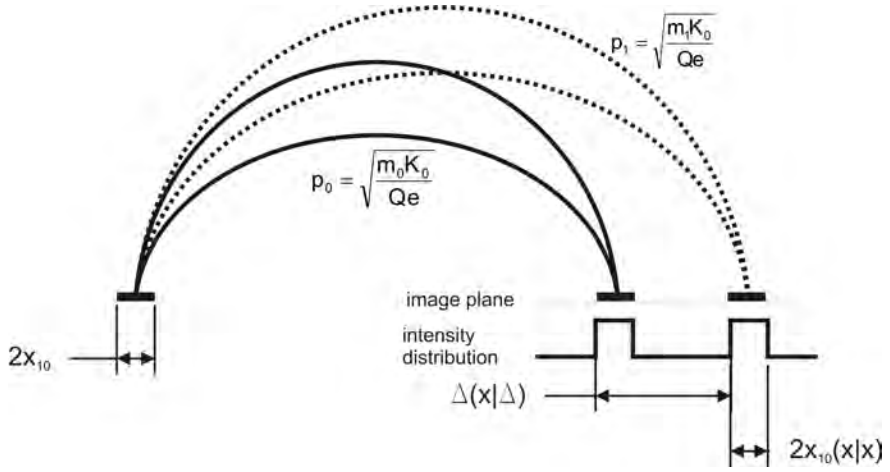

Figure 2.3: Sketch of the focusing and dispersion of a homogeneous $180°$ sector magnet (from [Wol87]). The kinetical energy is represented by K_0. A complete explanation of the different values is given through the text.

High values of R_Δ means a good separation, e.g. the HRS at ISOLDE has a designed value for the resolution of $\sim$30 000 ($\sim$5000 at the moment). At the GPS, also at ISOLDE, used for experiments with less optical constraints, the resolution is only about 2400. The diminution in the operating value from the design value is normally due to distortions in the magnetic field that track the ions to the wrong direction.

2.2 The concept of beam emittance

The emittance can be defined as the evaluation of the quality of the beam. The importance of this concept comes from the Liouville's theorem [Law83]. It states that all the points inside a phase space volume, V, at a time t will be transformed in another set of points at a time $t + \Delta t$, with the same volume V, if only conservative forces are applied. The phase space volume is represented by $(\mathbf{r}, \mathbf{r}')$, where $\mathbf{r}$ is the position vector and $\mathbf{r}'$ the vector of divergences. Three independent phase spaces can be identified. The area occupied by the beam is constant in each phase space, although the shape can change. The are occupied by the beam in these planes is named as the *emittance* of the beam. An ideal beam would be the one where all the ions have the same energy, parallel and close to the longitudinal axis. In addition, if the beam is bunched, all the ions would occupy the same position on the longitudinal axis (point-like beam).

A good overview about the concept of emittance can be found in references [Lap70, Kim97, Nie03, Wen01]. The aim of this thesis work is to distinguish and clarify the different existing theoretical approaches and the notations that has been chosen.

2.2.1 Transverse and longitudinal emittance

The concept of emittance can be developed separately for each direction. Hereafter, *z* is defined as the longitudinal axis of the beam (or direction of transmission), and *x* and *y* the transverse axes. It is possible to define two different transverse emittance and one longitudinal emittance.

Transverse emittance

The concept of transverse emittance refers to the dispersion of the beam in the transverse axes (x or y). In one of the transverse coordinates, the dispersion of an ion x' can be calculated as the angle formed by its transverse v_x and longitudinal velocity v_L. The area occupied by the beam in the *phase space* -$(x - x')$ plane- or in the *action diagram* -(x, v_x) plane- gives the emittance value. The emittance would have then units of [mm·mrad]. A beam can be classified, according to the orientation of its transverse phase space ellipse in (see Fig. 2.4):

- *Divergent*. Particles are moving away from the longitudinal axis as the beam is advancing.
- *Convergent*. Particles are moving towards the longitudinal axis as the beam is advancing.
- *Focus*. The beam is narrow as the particles are completely focalized in the reference point. After the beam will be completely divergent.
- *Parallel*. The beam is transported along the longitudinal axis with the particles moving completely parallel to the longitudinal axis.

Longitudinal emittance

The longitudinal emittance is defined as the area of the beam in a (E, t) plane, where E is the longitudinal energy and t the time of flight. Therefore, the longitudinal emittance is only considered for bunched beams. The main parameters used to define the longitudinal emittance are the time structure and the energy spread. The longitudinal emittance ϵ_{long} is then expressed as,

$$\epsilon_{long} = \Delta E_{FWHM} \cdot \Delta t_{FWHM}. \tag{2.14}$$

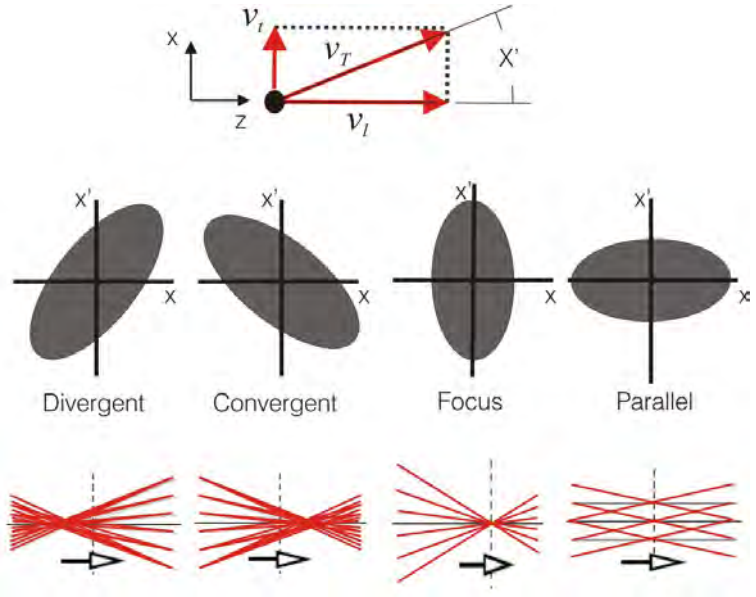

Figure 2.4: Different types of transverse beam emittance situations. The coordinate x' represents the divergence angle expressed in mrad and x the transverse beam size in mm, z is the longitudinal coordinate and v_T, v_t and v_l the total, transversal and longitudinal velocities, respectively.

where ΔE is the energy spread of the bunched beam and Δt the bunch width. Although the international system (SI) units of this magnitude would be in [J·s], for the purpose of low-energy beams results a small value. For this reason, the longitudinal emittance is normally expressed as [eV·μs], which is 10^{25} times smaller than the SI unit and fits better for the RIB's.

2.2.2 Normalized and non-normalized transverse emittance

As mentioned before, the transverse emittance can be usually represented in the phase space (x, x') or in the action diagram (x, v_x). Each case represents a different definition:

- **Non-normalized transverse emittance**. The beam is represented in the so-called *phase space*. The non-normalized emittance is the area of the beam in the phase space. The horizontal axis x represents the distance of the particles from the longitudinal axis z. Normally the unit used is a multiple of the SI unit, the millimeter, due to the small dimensions of the RIB's. In the vertical axis of a phase space the unit used is normally the milliradian, and identifies the dispersion of the beam since represents the angle that forms the particles of the beam with the longitudinal axis.

- **Normalized transverse emittance**. If the longitudinal energy of the beam is included, the emittance is plotted in the so-called *action space* or *action diagram* $(x-p_x)$ -p_x the transverse momentum- or $(x - v_x)$. The horizontal axis represents the same that in the phase space (distance of the particles from the longitudinal axis), but the vertical axis represents the transversal velocity of the particle. In this way, units of emittance will be now [mm^2/s] instead of [mm/rad], with the transversal velocity of the particles defined in [mm/s].

The benefits of using the *normalized emittance* are coming from the Liouville's theorem. The theorem asserts that the area enclosed by a beam in the action diagram is constant if non-conservative forces are not applied. The area in the phase space is constant if the longitudinal energy of the beam is constant. If the beam modifies its longitudinal energy, the area changes: the *non-normalized emittance* changes as:

$$\epsilon_2 = \epsilon_1 \sqrt{\frac{E_1}{E_2}}, \tag{2.15}$$

where ϵ_1,ϵ_2 are the initial and final non-normalized emittances and E_1, E_2 longitudinal energies, respectively . The non-normalized transverse emittance is the usual definition when working at the same energy with different kind of beams and is the value that will be mostly used in this work. However, for a good use of this value, the longitudinal beam energy to which the emittance refers to must always be given.

2.2.3 Geometrical emittance vs rms-emittance

Once the beam data is obtained with some instrumentation device (see Sec. 3.5), there are two main approaches for the calculation of the emittance value. Both of them are defined and explained in the following.

Geometrical emittance

The geometrical emittance is referred to the emittance value -either in action volume or in phase space- obtained from the calculation of the area containing a certain percentage of the beam. To calculate the percentage of the beam two main criterias are followed. They are based on:

- The total current. In this case, the percentage is obtained from the total current captured by an emittance scanner (see Sec. 3.5.4).
- The signal levels. The data captured by the emittance scanner is in some cases divided in some levels. The number of levels assigned depend on the resolution of the scanner and the beam intensity. To each of these signal levels a percentage of the beam can be assigned. To obtain an exact emittance value for the required percentage, it is normally necessary to interpolate the value from two signal levels.

The accuracy of the result obtained is constrained by the resolution of the device used for the measurements.

rms-emittance

The rms-emittance is calculated using the statistical deviation for each coordinate (x, x', y, y', E, t) of the phase space or action volume (see [Lap70]). The rms-emittance is defined as:

$$\epsilon_{rms} = \sqrt{\langle \mathbf{x}^2 \rangle \cdot \langle \mathbf{x}'^2 \rangle - \langle \mathbf{x} \cdot \mathbf{x}' \rangle^2}, \tag{2.16}$$

where:

$$\langle \mathbf{x}^2 \rangle = \frac{\sum_i \rho_i x_i^2}{\sum_i \rho_i}, \quad \langle \mathbf{x}'^2 \rangle = \frac{\sum_i \rho_i x_i'^2}{\sum_i \rho_i}, \quad \langle \mathbf{x} \cdot \mathbf{x}' \rangle = \frac{\sum_i \rho_i x_i x_i'}{\sum_i \rho_i}. \tag{2.17}$$

The position and dispersion vectors are represented by $\mathbf{x}$ and $\mathbf{x}'$ and ρ is the distribution of particles. In other terms:

$$\epsilon_{k-rms} = \frac{\pi(k\sigma_x)(k\sigma_{x'})}{\beta}, \tag{2.18}$$

where σ_x, $\sigma_{x'}$ represent the standard deviation of the beam in x and x' axes, k a proportionality constant referred to the proportion of the beam chosen, and β is a constant related with the cartesian coordinate representation of the ellipse equation (see [RS94]). The standard deviations are approximated as $\sigma_x \approx \sigma_{x'}$ in normal conditions. The rms-emittance (ϵ_{rms}) is identified normally as the ϵ_{1-rms} ($k = 1$). The ϵ_{2-rms} is called the **Lapostolle emittance** ϵ_{Lap}:

$$\epsilon_{Lap} = 4\epsilon_{rms}. \tag{2.19}$$

Correlation between rms and geometrical emittance

One can establish a relation between the value obtained for a certain percentage of the geometrical emittance and the statistical emittance for a beam. For simplification, the beam is supposed to have a gaussian distribution of particles in the spatial and momentum coordinates. For example, in one of the transverse coordinates, the distribution of particles $n(u)$ can be represented following the relation:

$$n(u) = \frac{1}{\sqrt{2\pi}\sigma_u} e^{-\frac{u^2}{2\sigma_u^2}}, \tag{2.20}$$

$$n(p_u) = \frac{1}{\sqrt{2\pi}\sigma_{p_u}} e^{-\frac{p_u^2}{2\sigma_{p_u}^2}}, \tag{2.21}$$

where u stands for x and y, p_u for the momentum in x and y directions, σ_u for the standard deviation of x and y, and $\sigma_{p_u}^2$ for the standard deviation of the momentum.The two dimensional probability distribution of a gaussian action volume is then:

$$n(u, p_u) = \frac{1}{2\pi\sigma_u^2} e^{-\frac{u^2+p_u^2}{2\sigma_u^2}}. \tag{2.22}$$

The area of the action volume can normally be represented as an ellipse. For simplification, here it is presented as a circumference ($\sigma_u = \sigma_{p_u}$) to simplify the calculations. Thus:

$$u^2 + p_u^2 = a^2. \tag{2.23}$$

Using Eq. 2.23 in Eq. 2.22, the two dimensional probabality reads:

$$n(u, p_u) = \frac{1}{2\pi\sigma_u^2} e^{-\frac{a^2}{2\sigma_u^2}}. \tag{2.24}$$

The fraction of particles dF within a given element of the action volume with area $dudp_u$ is:

$$dF(u, p_u) = n(u, p_u) dudp_u. \tag{2.25}$$

Changing to polar coordinates (r, θ), $u = r \cdot \cos\theta, p_u = r \cdot \sin\theta$, Eq. 2.25 can be written as:

$$dF(r, \theta) = n(r, \theta) r dr d\theta, \tag{2.26}$$

where:

$$n(r, \theta) = \frac{1}{2\pi\sigma_u^2} e^{-\frac{r^2}{2\sigma_u^2}}. \tag{2.27}$$

Integrating Eq. 2.26 to find the fraction of particles in a certain volume of radius a (assuming circular area), the expression will be:

$$F(r,\theta) = \int_0^{2\pi}\int_0^a n(r,\theta) r dr d\theta = \frac{1}{\sigma_u^2}\int_0^a r e^{-\frac{r^2}{2\sigma_u^2}}. \tag{2.28}$$

Applying the variable change $\zeta = \frac{r}{\sqrt{2}\sigma_u^2}$, the expression reads:

$$F(\zeta) = 2\int_0^{\frac{a}{\sqrt{2}\sigma_u}} \zeta e^{-\zeta^2} d\zeta. \tag{2.29}$$

After the integration and coming back to cartesian coordinates, the fraction of particles contained in a phase space area of radius a is:

$$F(u,p_u) = 1 - e^{-\frac{a^2}{2\sigma_u^2}}. \tag{2.30}$$

It can be more useful to work directly with emittance values (defined as the area contained by the beam in the phase space, in this case circular). Multiplying every term of the last fraction by π yields:

$$F(u,p_u) = 1 - e^{-\frac{\pi a^2}{2\pi\sigma_u^2}}, \tag{2.31}$$

where the term πa^2 represents the geometrical emittance of the beam, and the term $\pi\sigma^2$ the *k-rms-emittance* when $k = 1$.
Eq. 2.31 could be expressed as a relation between the geometrical and statistical emittance:

$$F(x,p_x) = 1 - e^{-\frac{k^2\epsilon_{geom}}{2\epsilon_{k-rms}}}. \tag{2.32}$$

For a certain k yielding a certain F, $\epsilon_{geom} = \epsilon_{k-rms}$ if $\epsilon_{geom} = \epsilon_{geom}^{100F}$, that means, if the fraction enclosed by the geometrical emittance is the same than by the statistical one. Therefore:

$$F(x,p_x) = 1 - e^{-\frac{k^2}{2}}. \tag{2.33}$$

Figure 2.5 shows the relation in a visual mode. For a fraction of the action volume of the 86.5%, that means a geometrical emittance of 86.5% ($\sim \epsilon^{90\%}$), the geometrical emittance equals the Lapostolle emittance:

$$\epsilon_{geom} = 4\epsilon_{rms} = \epsilon_{Lap}. \tag{2.34}$$

2.2.4 Acceptance

In the design phase of an optics device it is important to define which kind of beam one can accept, namely the acceptance of the device. The acceptance can be defined as the maximum value of emittance that a certain device can manage under some specific conditions. The acceptance is a value related to the device itself and other apparatus like the injection optics system and other components placed upstream of the device.

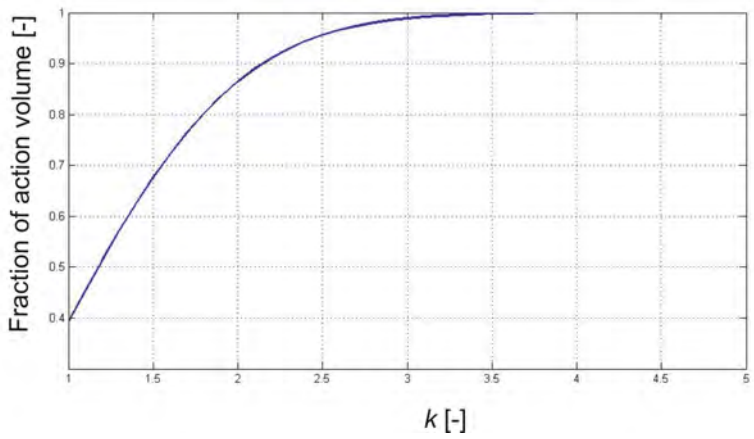

Figure 2.5: Fraction of particles enclosed depending on the relation between geometrical and statistical emittance or the k-factor

2.3 Brilliance

Another property to measure the density and thus the optical quality of the beam in a certain region of the beam line is the so-called **brilliance** B. It is defined as:

$$\mathbf{B}_N^{E_L} = \frac{N}{\epsilon_x \epsilon_y}, \tag{2.35}$$

where N is the number of particles and ϵ_x,ϵ_y are the non-normalized emittances for a certain longitudinal beam energy E_L in the transverse coordinates x and y, respectively. The units are then [part $\cdot\pi^{-2}\cdot$ mm^{-2} $\cdot$ mrad^{-2}]. The alternative definition with the intensity I is:

$$\mathbf{B}_I^{E_L} = \frac{I}{\epsilon_x \epsilon_y}, \tag{2.36}$$

with the units [A $\cdot\pi^{-2}\cdot$ mm^{-2} $\cdot$ mrad^{-2}].

2.4 Measurement of cooling efficiency

In order to measure the performance of a device which intends to improve the optical quality of the beam, two parameters are important:

- The emittance value of the extracted beam: optical quality (see Sec. 2.2).
- The efficiency: transmission quality (see Eq. 4.75).

Emittance and efficiency are related with the brilliance (see Eq. 2.35). The brilliance is a good measurement but it does not take into account the efficiency of the cooling method used in case of the ion coolers. Therefore another quantity would be more appropiate for this use.

The injection brilliance for the number of ions is defined as:

$$\mathbf{B}_{inj,N}^{E_{inj}} = \frac{N_{inj}}{\epsilon_{inj,x} \epsilon_{inj,y}}, \tag{2.37}$$

and the extraction brilliance as:

$$\mathbf{B}_{ext,N}^{E_{ext}} = \frac{N_{ext}}{\epsilon_{ext,x}\epsilon_{ext,y}}, \tag{2.38}$$

where N_{inj} is the number of ions injected into the trap and N_{ext} the number of ions extracted. Dividing Eq. 2.38 by 2.37 yields:

$$\frac{\mathbf{B}_{ext,N}}{\mathbf{B}_{inj,N}} = \frac{\frac{N_{ext}}{\epsilon_{ext,x}\epsilon_{ext,y}}}{\frac{N_{inj}}{\epsilon_{inj,x}\epsilon_{inj,y}}} = \frac{\frac{N_{ext}}{N_{inj}}}{\frac{\epsilon_{ext,x}\epsilon_{ext,y}}{\epsilon_{inj,x}\epsilon_{inj,y}}}, \tag{2.39}$$

where N_{ext}/N_{inj} is the typical efficiency or transmission η of any device. The ratio $(\epsilon_{ext,x}\epsilon_{ext,y})/(\epsilon_{inj,x}\epsilon_{inj,y})$ is defined as the emittance efficiency η_ϵ. If the injected and extracted energy are the same ($E_{inj} = E_{ext}$) one can define the brilliance or cooling efficiency as:

$$\eta_B = \frac{\eta}{\eta_\epsilon} \tag{2.40}$$

In this case, high number of ions extracted, low extraction emittance, high efficiency or small ratio of the emittance efficiency, will bring into high brilliance efficiencies.

Chapter 3

The beam preparation at ISOL facilities

This chapter is devoted to clarifying and to delimiting the signification of the beam preparation at RIB and ISOL facilities. The devices used for this purpose will be presented. In addition, the specific instruments required for the analysis of the quality of the low-energy RIB's are presented, for a global understanding of the components used during this work.

3.1 The beam preparation concept

At ISOL facilities, beam preparation can be defined as the process consisting in modifying the optics properties of the RIB in order to:

- Fulfil the requirements to perform the experiments.
- Accomplish post-acceleration.

This process starts after the ion source and comprises the following steps:

- **Mass separation or purification**. A separator is used in order to select precisely the isotope of interest.
- **Cooling**. Beam cooling of the RIB improves the transmission along the beam lines.
- **Bunching**. Many experiments require a short time structure of the ion beam to increase the signal to noise ratio. This is the case for instance of collinear laser spectroscopy or devices like EBIS.
- **Charge breeding**. For a compact and efficient postaccelerator, there is the need of increasing the charge state of singly-charged ions (high Q/Ab ratio).

The different tasks can be done in different steps using separated devices, or some of them can be often combined in a single device as it will be demonstrated. This work will focus on the cooling and bunching tasks, which are by their own a major field of research and development.

Figure 3.1: Typical scheme of an ISOL facility for mass separated RIB's.

3.2 Layouts

In most of the facilities, the beam preparation section comprises a magnetic mass separator and optical elements to transport the purified ion beam to the experiments (see Fig. 3.1).

Because of the quest for more energetic beams (energies close to the Coulomb barrier), as mentioned before, a new scheme appeared recently which uses the post-acceleration (or re-acceleration) of the low-energy ISOL beams (see Fig. 3.2). To assure a proper post-acceleration, the beam preparation stage has to be more developed including a cooling and bunching section (e.g. as done at REX-ISOLDE, see Sec. 1.3.2) and a charge breeding section.

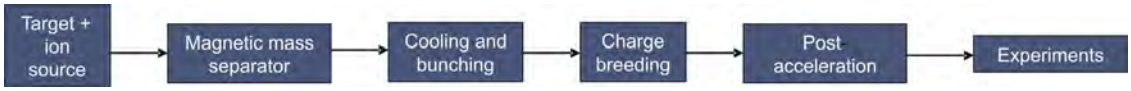

Figure 3.2: Scheme of an ISOL facility with a post-accelerated RIB.

In future facilities, like EURISOL, the proposed scheme for the beam preparation places the cooling and bunching devices before the magnetic mass separators (see Fig. 3.3). In that way the purity of the beam from the mass separators is enhanced thanks to the improved ion optical properties of the incoming beam. For example, cooling the ion beam before the HRS at ISOLDE could increase its resolution by a factor of 10 (depending on the quality of the incoming beam). Since the present cooling devices have a constraint in intensity of the beam that they can manage successfully, a pre-separator is required downstream of the cooling section (between the front-end and the mass separator). Hence the presence of a pre-separator acts both as a first filter of the activity of the beam and reducing the intensity to adapt it to the requirements of the cooling device. Actually, this scheme could also include the post-acceleration concept which will benefit from a better emittance.

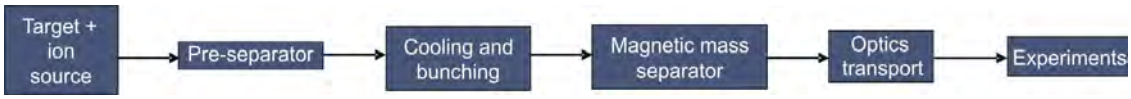

Figure 3.3: Scheme of an ISOL facility cooling the RIB before the mass separation.

3.3 Radioactive ion beam properties

This section is devoted to justifying the necessity to add some devices for beam preparation (manipulation) at ISOL facilities to the beam line between the mass spectrometers and the experiments. The properties of the ion beams are outlined as well as how there are affected by the mass spectrometers. A comparison between the properties requested by different kind of experiments is detailed.

3.3.1 Beam properties after the ion source

In an ISOL facility, the optical properties of the ion beam depends mainly on the ionization method used. The surface or plasma ion source and the ion guide technique create an RIB with very poor optical properties. They have strong needs of beam selection and preparation. The laser ion source delivers very pure and good optical beams with low cooling requirements, but for some experiments still bunching would be necessary.

The use of magnetic dipoles to filter the undesirable species, by selecting one of the masses, causes in addition some disturbances to the RIB. The worse the optical properties of the beam are before the separation, the bigger the disturbances will be. Therefore, surface, plasma or ion guides sources are not well separated due to a very poor resolution arising from the poor optical properties of the incoming beam.

3.3.2 Beam properties required by experiments

The ideal beam to perfectly match with the experiments would be a point in the three-dimensional space. However, in reality the beam has a certain size in the phase space. The best way to represent these conditions is by the use of the concepts of transverse emittance (transverse size and divergence). In the case of bunched beams, it is also important the longitudinal emittance (time width and energy spread). In addition for some of the experiments it is very important to maintain the intensity released by the ion source to improve the statistics. A diminution of the beam size and temperature will enhance the global transmission and the efficiency of the experiments.

For some of the experiments it is important to have a precise knowledge of the time structure of the ion beam (e.g. collinear laser spectroscopy). In this case, a perfect control of the bunch timing and the reduction of the ion-bunch density will improve drastically the efficiency of the experiment.

Last but not least, the increasing requests by the experimentalists of more beam time and beam lines, make the schedule of the facilities really tight. Therefore the improvement of the optical properties would reduce the required shifts for certain experiments. That gives the chance to either improve the statistics of the experiments or to fit more experiments in the schedule. Anyway, it is obvious that the improvement of the beam optics will push the physicists to conceive new experiments which will benefit from the improved beam.

3.4 Principle and devices for the beam preparation task

3.4.1 Cooling and bunching

The reduction of the beam size which increases the ion density is called beam cooling, since it is based on a global diminution of the thermal motion of the ions of the beam. The concept of beam cooling comes then from the fact that the temperature of the ions is decreased. The ions are cooler than before and therefore they occupy a smaller region of the phase space. One of the main aims of the beam preparation task is to obtain the smallest possible beam, in both transversal and longitudinal dimensions. Beam cooling counteracts the degradation of the beam quality due to: interaction of ions with other ions, with rest-gas, the presence of non-ideal or fringe fields in the optical elements or instabilities. Furthermore, beam cooling automatically increases the transport efficiency along the beam lines. A small size avoids losses due to small acceptances of some

devices (dipoles, quadrupoles,...) or undesirable interactions with other devices inside the vacuum beam lines (diagnostic devices, cables,...).

In accelerator physics, there are a variety of procedures applied to cool ion beams: stochastic cooling, electron cooling, radiation cooling generally applied in storage rings. Resistive cooling, laser cooling and buffer-gas cooling are mostly used in ion trapping applications). Reviews of cooling applications for ion traps can be found elsewhere [IBBW95, ÄystöJ03].

For RIB's, the cooling method should be: universal, to cool the entire range of elements, and fast since the lifetime of these exotic isotopes are very short life. In this frame, the buffer-gas technique is the best option because it depends only on the mass of the ions and the cooling times are quite reasonable, a few miliseconds are normally sufficient.

The buffer-gas cooling technique is based on the reduction of the motion amplitude of the ions of the beam due to the collisions with the buffer-gas atoms or molecules. Two main types of ion trap coolers have been developed: 1) *Penning traps* which combine a magnetic and an electrostatic field to trap the ions and a Radio Frequency electric field to cool the beam; and 2) *Paul traps* which use only an RF field in combination with the buffer gas. Penning traps are mostly used for purification and mass measurements, thanks to their great accuracy for mass selection. Paul traps are the most used device around the world for cooling and bunching RIB's because of their less complex construction and operation, basically due to the absence of magnetic field. In 1989 the Royal Swedish Academy of Sciences awarded the Nobel Prize in Physics for the very important contributions for the development of atomic precision spectroscopy to Hans Dehmelt and Wolfang Paul, who developed the Penning and the Paul traps, respectively. The first demonstration of damping of the ion motion using a buffer gas was given by Hugget and Menasian in 1965 for Hg^+ ions in a Paul trap into which was introduced a small amount of helium [Deh67]. In Penning traps, buffer gas cooling was demonstrated by Savard et al. [SBB$^+$91].

During the 90s the theory of the ion motion for these devices together with cooling and bunching was developed for beam preparation purposes [RBM88, LBM92, Kim97]. In the 90s (1998) an European network, under the Fifth Framework of the European Commission (EU FP5) contract called EXOTRAPS, started a collaboration to develop the cooling and bunching technique in order to trap exotic nuclei. The main goal was to commission and test the principle in new designs of Paul or Penning traps. Due to the importance for this thesis work, both are widely discussed in Chapter 4.

3.4.2 Charge breeding

Nowadays, some experiments benefit more from beams with ions with charge states higher. The process when an ion beam increases its charge state is called charge breeding process. In REX-ISOLDE, for example, charge breeding is used to decrease the length of the post-accelerator. A higher charge state means a higher acceleration for an ion of the same mass in the same electric field. Hence, the main application of the charge breeding is as preparation device for the facilities devoted to accelerating the beams to increase the energy of the ions above the Coulomb barrier. In the near future, post-accelerated beams will serve new purposes as injection for the so-called beta beams (GeV range). The RIB will be injected in a decay ring where the ions will decay and the accompanying neutrinos will be directed to a detector for study [Lin04]. A good overview and comparison of charge breeding devices is given in [Wen01, Wen04]. A brief description is given in the following.

Stripper foils

Foils of Al, Al_2O_3 or gas (mainly noble gases) are used to create highly charged ions. The only requirement is that the ions must be pre-accelerated up to 150 keV/u when using foils or 5 to 25 keV/u in the case of gas [Wen04]. The ions are slowed down by the dense cloud of slow electrons created. For example, the planned RIA facility will use the multiple stripping technique in combination with multi-charge state. With stripper foils, the ions are not selected after the charge breeding and, therefore, a broad band of charges (δQ/Q$\sim$10%) will be accelerated. That implies the beam emittance will increase much more than in the case of the single-charge state acceleration.

EBIS

The use of an electron beam to increase the charge state of an ion beam is one of the basic concepts in the charge breeding field. The best example of the success of this application is the REXEBIS which charge breeds the RIB coming for the Penning trap REXTRAP for the REX-ISOLDE post-accelerator [Wen01] (see Fig. 3.4). The EBIS combines a strong magnetic field with an electric field to trap the ion beam, and an electron beam which interacts with the ion beam and increases the charge state of the ions.

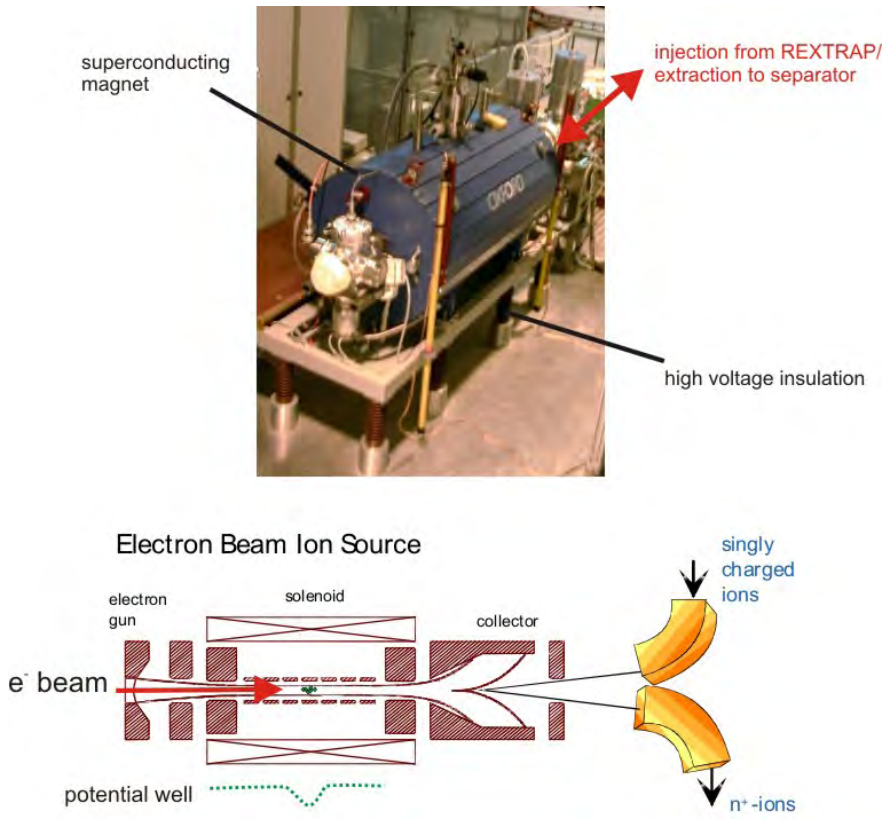

Figure 3.4: (*Top view*) Picture of REXEBIS. The injection of the radioactive beam from REXTRAP shares the beam line with the extraction to the mass separator. (*Bottom view*) EBIS set-up.

ECRIS

The Electron Cyclotron Resonance Ion Source (ECRIS), or Trap (ECRIT), charge breeds singly charged ions which are slowly injected into a plasma with hot electrons. The free electrons are heated by an RF power of several 100 W. They are confined inside a magnetic structure with a so-called *minimum magnetic field configuration* of ∼0.5 T. More detailed information about the ECRIS as charge breeder can be found in the references [Gel00, Sor00, Jeo03].

3.5 Instrumentation for the measurement of the RIB properties

The quality of the beam and the operation of the devices installed in the beam line require the use of diagnostics instrumentation to verify and monitor the properties of the beam. In the accelerator field, the diagnostics system constitutes a key task that needs the development of specific devices. These devices can be divided into various groups depending on the property to be checked. A very extensive overview of the existing instrumentation can be found in [For03]. At RIB facilities, the diagnostics devices are more specific due to the low energy of those beams and differ quite a lot from those ones used in high energy accelerator physics. In the following, the main devices are presented divided according to the properties they measure.

3.5.1 Faraday cups

Faraday Cups (FC) are devices devoted to measuring the electrical current of an ion beam. Normally the FC's work for low beam energies, e.g. at ISOLDE (see Fig. 3.5) and are destructive beam stoppers, like e.g. the beam transformers for high energy beams. The principle consists of an insulated metal cup. The ion beam impinges a metal cup which is connected to a sensitive current pre-amplifier (a low impedance input and a conversion to a voltage). The signal read-out is generated by the ion beam and proportional to its intensity.

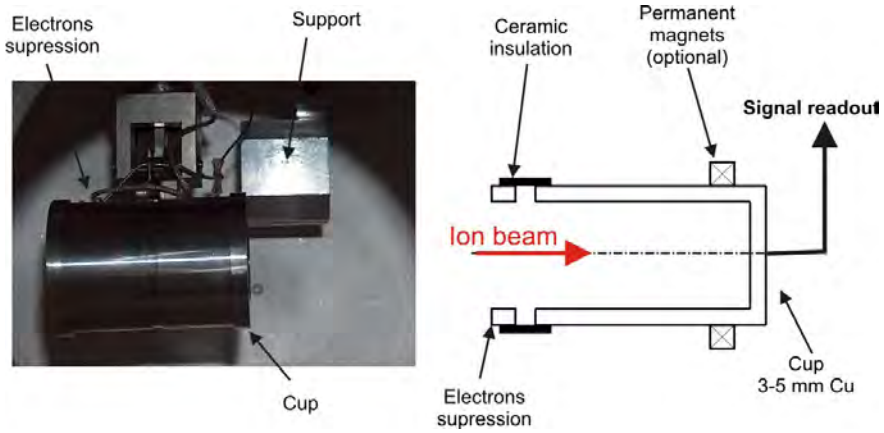

Figure 3.5: Picture of an standard ISOLDE faraday cup (*left*) and scheme of the main components of a Faraday cup (*right*). Copper wall where the beam impinges and secondary electrons suppressors are detailed.

Faraday Cups are very sensitive devices and beam currents as low as 10 pA, even for a DC-beam, are possible to be detected with a low noise current-to-voltage amplifier and careful mechanical design. In the field of RIB's, the measurement of really low currents is very important since the available quantity of exotic ions is very small and losses have big consequences on the experiments.

One of the drawbacks of the FCs is the liberation of secondary electrons with an average energy of 10 eV. The flux of these electrons is proportional to $\cos\theta$, where θ is the angle of the electron trajectory with respect to the surface. To avoid wrong read-outs of the beam current, an electron suppression system is normally added, except for very long cups where the contribution of lost electrons is small. The system consists of a HV suppression close to the entrance of the cup which creates a potential well above the mean energy of the secondary electrons so that they are pushed back to the cup surface.

3.5.2 Microchannel Plate detector

The MicroChannel Plate detector (MCP's) is used for the measurement of very low-intensity beams and time of flight measurements. It consists of an array of glass capillaries 10-12 μm diameter. The capillaries are biased at a high voltage. The ions impinging on the walls of the capillaries produce secondary electron emission. The electrons produced are accelerated by the voltage applied to the capillaries and hit again the walls. Finally, an avalanche effect is produced and the initial signal is amplified. Usual gain values of 10^4 are obtained for one MCP. Several MCP's can be placed in series if more amplification is required.

3.5.3 Beam scanners

Beam scanners (BO) are used to measure the beam profile in the transverse plane ($x-y$). ISOLDE standard beam scanners consist of a two needle system placed at 90° with respect to each other. They move along a guide to scan the x and y directions at the same time. For this reason, the guide that is supporting the needles is entering at 45° of the ground, otherwise the axes scanned would not correspond to the horizontal and vertical axes of the ground.

3.5.4 Measurement of the transverse emittance

Emittance meters (scanners) are instruments devoted to the analysis of the emittance (see Sec. 2.2 for the theoretical explanation). They give a picture of the transverse phase space of a beam. Different types of devices are used for this purpose, such as the slit-grid method, the pepper-pot device, and the quadrupole variation or the 'three grid' method [For03]. An emittance meter used during the development of this thesis work based on the three grid method is pictured in Fig. 3.6 and described in [Bac00, Huc02]. The meter scans the values V_1 and V_2 to read intensities for different positions and dispersions of the ions of the beam. The resolution and time consumption depends on the steps chosen for the scan.

A new emittance meter is being developed at ISOLDE. It is based on the two slits principle presented in [ASH83]. The new device will stand out from the existing ones for a very small and compact size, that will make possible place it along the ISOLDE beam lines, in the same way as the diagnostic boxes including the faraday cups and the beam-position scanners. ISCOOL will benefit from this device since it could be installed before and after the injection and acceleration (see details of the layout of the project in Chapter 5). This will give very valuable figures for the

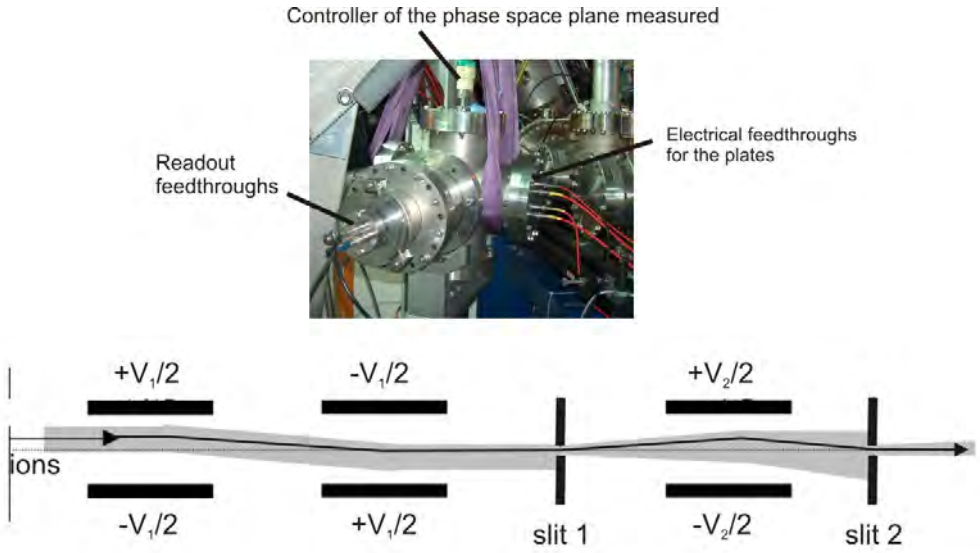

Figure 3.6: Picture of the vacuum chamber containing the meter of the transverse beam emittance (*top*) and scheme of the ion motion along the meter (*bottom*, see [Bac00, Huc02]). The potentials applied to the grids V_1 and V_2 are shown.

transverse emittance on-line. In that way it will be possible to monitor the performance of the device with each RIB from the HRS front-end and afterwards mass-separated.

Unlike FC's or beam scanners, with instantaneous response, the problem of this kind of the devices is the time consumption for a measurement. For a single measurement of a phase space, the time required increases for low intensity beams, since the collection time has to be higher, or with measurements with high resolution, small steps in the space or angle coordinates.

3.5.5 Measurement of longitudinal emittance

At low energy devices as the RFQCB's, the calculation of the longitudinal emittance for the extracted bunched beam can be done by an independent measure of the bunch width (time spread, Δt) and the energy spread (ΔE). The beam profile could be measured by the combination of a Multi Channel Plate and a CCD camera, as in REXTRAP at REX-ISOLDE. The readout of this device would provide the bunch width of the beam. To measure the energy spread in an RFQCB, the simplest method is to vary smoothly the voltage applied to trap the beam, from the total trapping to the total transmission. In that way, only the ions with more energy than the trap potential can escape and be detected by the diagnostic device. The energy spread of the beam is the FWHM of the derivative of the signal [Nie02, Rod03].

3.6 Beam quality requirements of ISOLDE experiments

3.6.1 REX-ISOLDE

The injection into the LINAC of REX-ISOLDE for acceleration of the RIB from 60 keV to 2.2 or 3.1 MeV/u makes some specific requirements of the quality of the beam that must be provided by

ISOLDE:

- Cooling.
- Bunching. REXEBIS needs a bunched beam for a good operation. The Penning trap REX-TRAP fulfils these requirements.
- Charge breeding. The limited length of the REX-ISOLDE LINAC obliges the charge state of the singly-charged ions from the ISOLDE beam to be increased.

A further upgrade of REX-ISOLDE is expected soon with a longer LINAC using the space of the extension of the ISOLDE hall. The new upgrade will provide an energy of 4.2 MeV/u and a complete integration of the experiment into the ISOLDE control system.

The charge breeding before the LINAC is carried out inside an EBIS (see Sec. 3.4.2), the REXEBIS. For a good efficiency, the ion beam coming into REXEBIS should fulfill certain requirements (see [Wen04]):

- The time width of the ion bunch should be below 50 μs.
- The maximum energy spread should not exceed 50 eV.
- The acceptance of 95% of the beam at 60 keV (see Sec. 2.2.4) must be 10 π·mm·mrad maximum, usually smaller than the emittance from a radioactive ion source.

These requirements oblige to use certain devices for beam preparation before the REXEBIS. The decision was the use of the Penning trap REXTRAP for cooling and bunching the RIB from ISOLDE, which is quasi-continuous (CW) and with usually worse transverse emittance than required from REXEBIS. This layout works fine and has been already used in REX-ISOLDE for a high number of experiments providing successful results. A highlight is the use the combination of REXTRAP and REXEBIS for the separation of the molecule of SeCO (from the ISOLDE beam) to yield Se-70, to inject it into the LINAC, and to finally analyze it into the MINIBALL detector.

Although the combination of REXTRAP and REXEBIS has shown fruitful results, it is a very complex system, very delicate to operate, to set up and to maintain. In addition, the Penning trap seems to have some limitations for the cooling of high intensity beams (see Chapter 11). Therefore some alternative solutions have been proposed and some of them tested during this dissertation:

- The use of an ECRIS as direct injector for the REX-LINAC.
- The use of an RFQCB as injector for REXEBIS. The RFQCB is supposed to deliver the beam with better conditions compared to REXTRAP (see Chapters 5 and 11).
- The development of new cooling methods for high intensity beams in Penning traps (see Chapter 11).

3.6.2 Collinear laser spectroscopy with bunched beams

Presently, one of the experiments that has known how to benefit the best from the improved beam using cooling and bunching devices is probably the collinear laser spectroscopy.

Collinear laser spectroscopy experiments have been widely used for over twenty years in on-line facilities for the measurements of optical isotope shifts and hyperfine structures. Most of the basic ground state properties of radioactive nuclei (e.g. spins, moments, or radii) can be deduced from these measurements [Bil01, NCB$^+$02].

The limitation of these measurements come only from the background counting levels in the signal. It has been demonstrated (see [Bil01]) that the use of a bunched beam (less than 10 μs of time width and less than 10 eV) energy spread reduces the effective background levels at least four orders of magnitude. That means laser spectroscopy can be performed on very exotic nuclei.

In ISOLDE, the installation of the new ISCOOL (see Chapter 5), to produce cooled and bunched beams, will make possible the applicability of collinear laser spectroscopy to light elements as Mn (A=49-65), Ni (56-69), Cu (57-78), Zn (60-74) and Ga (lower bound of A=63). Heavier isotopes could be also studied with the only limitation of the life-time. ISCOOL will mean an improvement of the sensitivity, the minimum number of particles necessary to carry out the experiments will decrease from the present 10^6 ion/s to 10^3 ion/s.

3.6.3 Other experiments

Not only the new laser experiment and REX will benefit from an improvement of the optical properties of the ISOLDE beam. The efficiency of the beam transport through all the beam lines of the ISOLDE hall will be highly increased. That will benefit specially the experiments located further downstream from the mass separators, e.g. NICOLE. In addition, a better beam optics will enhance the performance of the mass spectrometry experiments like ISOLTRAP or MISTRAL. Although they already have a RFQCB for use in their setups, a much better injection efficiency into these coolers is expected, improving globally the efficiency of the experiment.

3.7 New requirements in beam preparation

In future facilities, like EURISOL, the intensity and the energy of the ion beam will be much higher. The preparation of these kind of beams will require some developments like:

- RFQCB with bigger capacity . The success of the second generation RFQCB which combine the manipulation of bigger beam emittances, cryogenic capabilities or RF-funnel ideas, will determine the use in the future EURISOL facility.
- New layout for mass separators .
- Charge breeding techniques.
- Pre-separators.

All these ideas have to be tested to assure the success of the future facilities. The ISCOOL RFQCB (see Chapter 5) designed in the frame of this work, represents the first test of an RFQCB used on-line continuously in a complex facility as ISOLDE to deliver high quality beam to a huge number of experiments. Still at ISOLDE, the development of a new layout for the ISOLDE HRS [GCF$^+$03] will serve to test this idea for EURISOL. In the future, the location of ISCOOL could be changed, and be placed together with a pre-separator between the HRS front-end and the new HRS magnet. It is expected that such a combination would provide the best results in terms of purity, intensity and optical properties.

Chapter 4

The ion traps as ion coolers and bunchers

After the introduction of the main concepts used in this thesis, it is time to focalize on the Paul [PS53, PR55] and Penning traps [KBK$^+$95]. These devices, used to prepare (manipulate) the low-energy RIB's, form the main body of this thesis work. Their theory is summarized in this chapter, giving an special emphasis to the applications improving the quality of the beam.

4.1 Paul traps and RFQCB's

Paul traps were developed by W. Paul in the 50s [PS53]. In this kind of devices, the ions are trapped using RF electric fields. The Paul trap evolved later from the hyperbolical electrodes, as shown in Fig. 4.1, to the linear Radio Frequency Quadrupoles (RFQ's or called as well ion guides). Although the use of ion guides instead of ideal Paul traps brings imperfections, the easy construction and operation makes the ion guides the best solution.

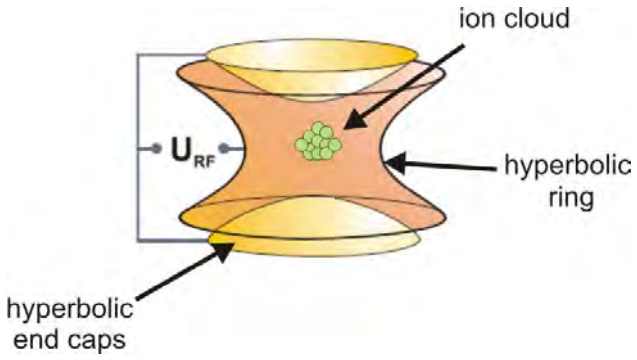

Figure 4.1: Classical hyperbolic configuration of a Paul trap. A medium RF frequency is applied between the ring electrode and the end caps to confine the ion cloud in the center of the trap.

After the EXOTRAPS collaboration, the first Radio Frequency Quadrupole ion Coolers and Bunchers (RFQCB's) were designed and commissioned. RFQCB's are ion guides (RFQ's) which combine a Radio Frequency electric field to confine the ions around the longitudinal axis, a buffer gas to cool the ions, and an electrostatic axial field, to trap the ions in the three-dimensional space and release the beam as bunches. The experiments ISOLTRAP in ISOLDE and IGISOL in Jyväskylä were the first to succeed in proving the utility of these devices [NCB$^+$02, FHKB$^+$01]. After these fruitful experiences, new RFQ coolers have appeared around the world: in ANL for

the CPT experiment [MBB+01], in GSI for SHIPTRAP [Rod03], in LPC [BDD+04, RMD+05], in MSU for LEBIT [BSD+04, SBL+03] and in ISOLDE again for the MISTRAL experiment [Lun04, Bac04]. The characteristics of all these devices are listed in Tab. 4.1. Figure 4.2 shows pictures comparing the structure of some of these RFQCB's.

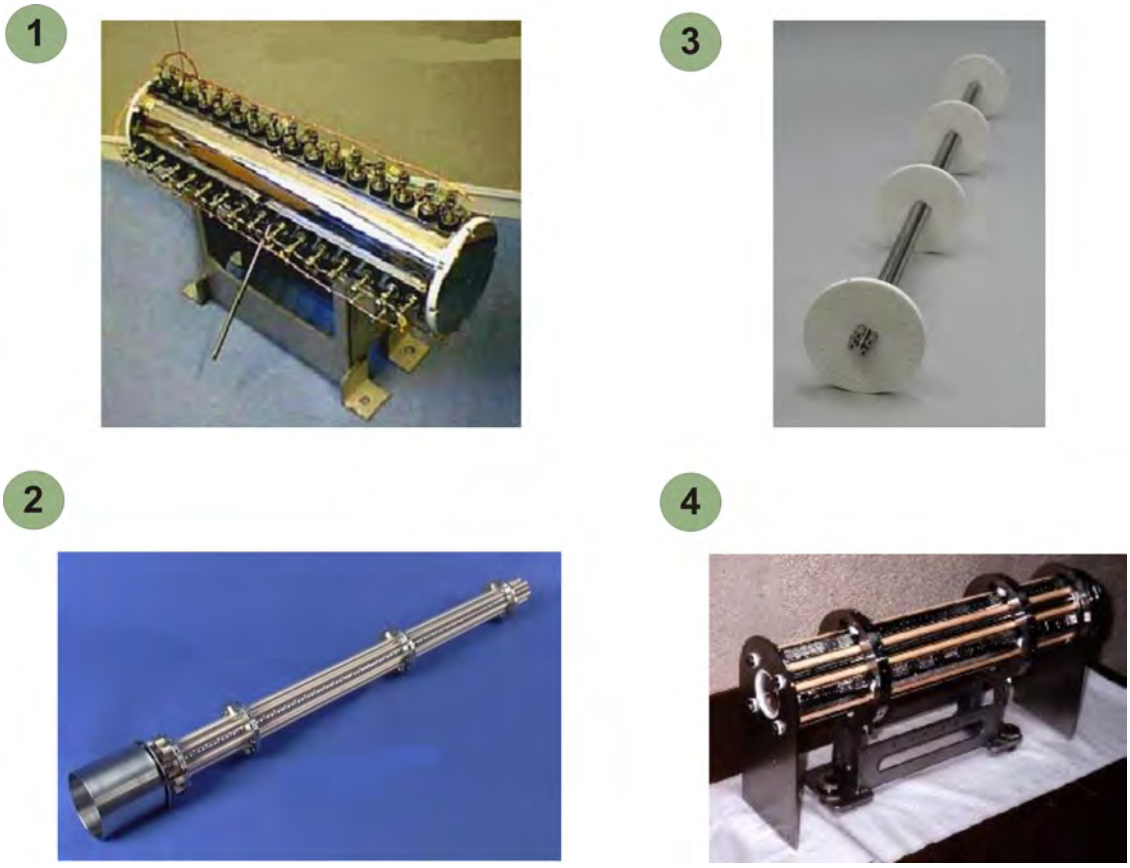

Figure 4.2: Picture of different first generation RFQCB designed: 1) the RFQCB at IGISOL Jyväskylä, 2) the RFQCB for ISOLTRAP at ISOLDE, 3) the buncher at SHIPTRAP-GSI and 4) the RFQCB at LPC-Caen.

As an evolution of the same concept, the RF ring electrode cooler of LMU has efficiently transmitted high intensity beams, applying only RF electric field to a stack of ring electrodes of different diameters, electrically isolated among them (see [HJH+04]).

For a correct comprehension of the operation of the RFQCB's, it is essential to explain the theoretical processes involved. The main points are:

- The optics of an ion beam in presence of a quadrupolar RF electric field.
- The collisions between buffer gas atoms or molecules and ions.
- The presence of the buffer gas of an axial electric field.
- The combination of all the effects above.

In the following the theory of each item presented before will be described, to end up with a complete representation of the physics process acting the ion beam inside the device.

Facility	E_{ext} [keV]	ϵ_{ext} [π mm·mrad]	Buffer gas	η [%]	Δt [μs]	ΔE [eV]
JYFLTRAP[1)]	40	3	He	60-70	10	0.7
ISOLTRAP[2)]	2.5	10	He	20-40	10 eV·μs	
NSCL[3)]	2	1.55	He	-	2.4	4
SHIPTRAP[4)]	0.07	20 @ 2.5 keV	He	≥ 58	0.25-2	2.4
LPC[5)]	10-20	10 (@12 keV)	He,H_2	5-10	0.15	3
MISTRAL[6)]	60	2	He	60	No buncher	
KVI	No re-accelerated	-		80	0.2	-

Table 4.1: Comparative of some of the present ion guides working as coolers and/or bunchers in different ISOL-facilities around the world: E_{ext} -extraction energy-, ϵ_{ext} -emittance at the extraction-, η -efficiency-, ΔE -energy spread of the bunches- and Δt -time width of the bunches-. 1) from [NCB$^+$02], 2) from [FHKB$^+$01], 3) from [BSD$^+$04], 4) from [Rod03], 5) from [BDD$^+$04, RMD$^+$05], 6) from [Lun04]. The extraction beam parameters are at the extracted energy except at LPC.

4.1.1 Radio Frequency Quadrupole electric field

Use of RFQ electric fields is a widespread tool in accelerator physics where they are used as optical devices to focus and confine the beam, see [Wol87]. This section will be centered in developing the theory of the specific RFQ's which are devoted to the beam manipulation. Inside an RFQ, the RF electric field is perpendicular (x and y directions) to the longitudinal motion of the beam (axis z), see Fig. 2.2).

The three-dimensional quadrupole electric field $\mathbf{E}$ is governed by Eq. 2.4. In the RFQ, the quadrupole field is zero in the longitudinal direction z. As the electric field has to fulfill $\nabla \cdot \mathbf{E} = 0$ (no space charge in the system, $\rho_t = 0$), and is zero in the axial direction ($\gamma = 0$), the following relation between the electric field can then be represented as:

$$\mathbf{E} = E_0(\lambda \mathbf{x} - \lambda \mathbf{y}). \tag{4.1}$$

From last expression, the electric potential can be obtained by integrating $\mathbf{E} = -\nabla\Phi$. The expression obtained is:

$$\Phi = \frac{1}{2} E_0 \lambda (x^2 - y^2). \tag{4.2}$$

The equipotential lines are hyperbolas as can be seen in Fig. 2.2. In this case the potential is generated by four rods. Opposite rods have the same potential and the potential of both pair of electrodes is phase-shifted $180°$. Taking r_0 as half of the distance between two opposite rods, the transverse electric potential Φ inside the quadrupole can be expressed as:

$$\Phi = \frac{\Phi_0}{r_0^2}(x^2 - y^2), \tag{4.3}$$

where Φ_0 is the potential of one of the rods.

On the other hand, for an ion moving in a potential field, the equations of motion are governed by:

$$m\ddot{\mathbf{r}} = -e\nabla\Phi, \tag{4.4}$$

where m is the mass of the ion and **r** the position vector. Taking Eq. 4.3 and Eq. 4.4, the equations of motion of the ions in such a field will be:

$$\ddot{x} + \frac{2e}{mr_0^2}\Phi_0 x = 0, \tag{4.5}$$

$$\ddot{y} - \frac{2e}{mr_0^2}\Phi_0 y = 0, \tag{4.6}$$

$$\ddot{z} = 0. \tag{4.7}$$

The motion of an ion in a quadrupolar electric field is independent in each spatial coordinate. If an RF electric field is considered to be applied to the rods, with a magnitude $\Phi_0 = U_{RF}\cos\omega_{RF}t$, the equations found are:

$$\ddot{x} + \frac{2eU_{RF}\cos\omega_{RF}t}{mr_0^2}x = 0 \tag{4.8}$$

$$\ddot{y} - \frac{2eU_{RF}\cos\omega_{RF}t}{mr_0^2}y = 0 \tag{4.9}$$

The normalized time τ and the **dimensionless quantities** q_x and q_y:

$$\tau = \frac{\omega_{RF}t}{2}, \tag{4.10}$$

$$q = q_u = q_x = -q_y = \frac{4eU_{RF}}{m\omega_{RF}^2 r_0^2}, \tag{4.11}$$

are to be substituted in Eq. 4.8 and 4.9 to give:

$$\frac{d^2u}{d\tau^2} - (2q_u\cos 2\tau)u = 0 \tag{4.12}$$

where u represents either x or y [Daw95]. Equation 4.12 represents a particular case of the Mathieu equation [Ars64]. The general expression of the equation applied to a spatial coordinate u is:

$$\frac{d^2u}{d\tau^2} + (a_u - 2q_u\cos 2\tau)u = 0 \tag{4.13}$$

where a_u is a constant. It can be defined as,

$$a_u = a_x = -a_y = \frac{8eU_f}{m\omega_{RF}^2 r_0^2} \tag{4.14}$$

where U_f is the amplitude of a DC quadrupole field. For the purpose of this work, $a_u = 0$ ($U_f = 0$).

The **solutions of the Mathieu equations** are studied in [McL51, Cam55, Ars64] and correspond to the following general solution [Daw95]:

$$u(\tau) = \alpha' e^{\mu\tau}\sum_{n=-\infty}^{\infty} C_{2n}e^{2ni\tau} + \alpha'' e^{-\mu\tau}\sum_{n=-\infty}^{\infty} C_{2n}e^{-2ni\tau} \tag{4.15}$$

where α' and α'' are constants depending on the initial conditions: $u(0)$, $\dot{u}(0)$ and $\tau(0)$. Constants C_{2n} and μ depend on the so called mathieu parameters a and q.

For stable solutions ($\mu = i\beta$) the expression becomes [WSL59, Deh67, MD68, Daw95]:

$$u(\tau) = \alpha' \sum_{n=-\infty}^{\infty} C_{2n} e^{(2n+\beta)i\tau} + \alpha'' \sum_{n=-\infty}^{\infty} C_{2n} e^{-(2n+\beta)i\tau} \tag{4.16}$$

Using $e^{i\omega} = \cos\omega + i\sin\omega$, Eq. 4.16 results in:

$$u(\tau) = A \sum_{n=-\infty}^{\infty} C_{2n} \cos\left[(2n+\beta)\tau\right] + B \sum_{n=-\infty}^{\infty} C_{2n} \sin\left[(2n+\beta)\tau\right] \tag{4.17}$$

where $A = \alpha' + \alpha''$ and $B = i(\alpha' - \alpha'')$. The stable solution is a superposition of the frequencies:

$$\omega_n = (2n+\beta)\frac{\omega_{RF}}{2}, \tag{4.18}$$

for $n = 0, 1, 2, ...$ The lowest angular frequency ω_0 ($n = 0$) is the **macromotion or natural angular frequency**. The constant β is for stable solutions only related with the a and q parameters by the expression [MH89, Cam55, McL47]:

$$\beta^2 = a + \frac{q^2}{(\beta+2)^2 - a - \frac{q^2}{(\beta+4)^2 - a - \frac{q^2}{(\beta+6)^2 - a - \ldots}}} + \frac{q^2}{(\beta-2)^2 - a - \frac{q^2}{(\beta-4)^2 - a - \frac{q^2}{(\beta-6)^2 - a - \ldots}}} \tag{4.19}$$

The process of calculation of β is thus iterative. However, for low values of a and q, the expression can be simplified as [Car72]:

$$\beta = \sqrt{a - \frac{(a-1)q^2}{2(a-1)^2 - q^2} - \frac{(5a-7)q^4}{32(a-1)^3(a-4)} - \frac{(9a^2+58a+29)q^6}{64(a-1)^5(a-4)(a-9)}} \tag{4.20}$$

If $|q| \ll 1$ and $|a| \simeq 0$, β is described by:

$$\beta = \sqrt{a + \frac{q^2}{2}} \tag{4.21}$$

There are always two different solutions for $u(t)$, the even $u_1(t)$ and the odd $u_2(t)$ solution. Therefore the general solution can be expressed as the lineal combination of both solutions with A and B constants,

$$u(t) = Au_1(t) + Bu_2(t) \tag{4.22}$$

The constants A and B depend on the initial conditions of the ions, and the following expressions are obtained [MH89, LTB75]:

$$A = \frac{u(\tau_0)\dot{u}_2(\tau_0) - \dot{\tau}_0 u_2(\tau_0)}{W} \tag{4.23}$$

$$B = \frac{-u(\tau_0)\dot{u}_1(\tau_0) + \dot{\tau}_0 u_1(\tau_0)}{W} \tag{4.24}$$

where $u(\tau_0)$ and $\dot{u}(\tau_0)$ are the initial displacement and velocity, respectively and where

$$u_1(\tau_0) = \sum_{n=-\infty}^{\infty} C_{2n} \cos\left((2n+\beta)(\tau - \tau_0)\right) \tag{4.25}$$

$$u_2(\tau_0) = \sum_{n=-\infty}^{\infty} C_{2n} \sin\left((2n+\beta)(\tau-\tau_0)\right) \tag{4.26}$$

$$\dot{u}_1(\tau_0) = \sum_{n=-\infty}^{\infty} C_{2n}(2n+\beta) \sin\left((2n+\beta)(\tau-\tau_0)\right) \tag{4.27}$$

$$\dot{u}_2(\tau_0) = \sum_{n=-\infty}^{\infty} C_{2n}(2n+\beta) \cos\left((2n+\beta)(\tau-\tau_0)\right) \tag{4.28}$$

$$W = u_1(\tau_0)\dot{u}_2(\tau_0) - u_2(\tau_0)\dot{u}_1(\tau_0) \tag{4.29}$$

In the solution of the equation several stability regions appear depending on the value of q_u and a_u (see Fig. 4.1.2). But for RFQCB's, the interesting region is when $a_u = 0$, since no DC field for mass filtering is supplied, that implies $0 \leq q_u \leq 0.91$ to reach the stability in the ion motion.

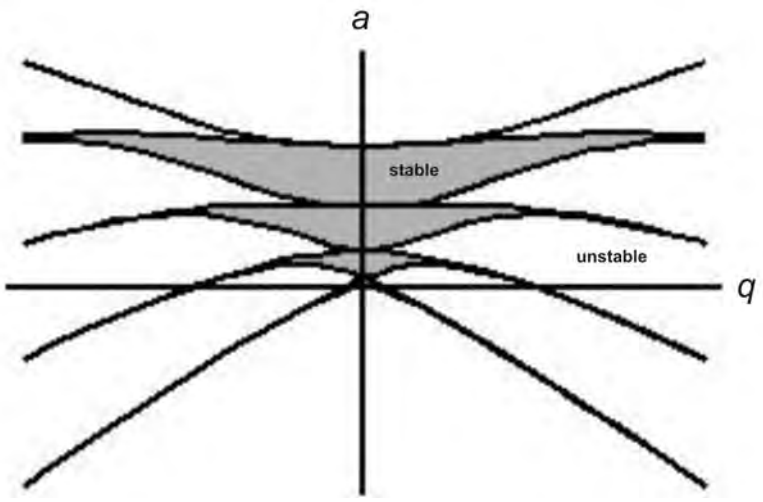

Figure 4.3: Stability plot for one of the transverse coordinates depending on the value of parameters a and q. The stable areas appears shaded.

For one coordinate, the nature of the stability of the solution only depends on the value of μ and not on the other parameters. The constant μ may get different values:

- Real.
- Imaginary. If $\mu = i\beta$ and β is not an integer, the solutions are periodic and stable.
- Complex.

In the experimental case, the stable region is placed in the region created in the $a_u - q_u$ diagram by the isolines $\beta_x = 1$ and $\beta_y = 1$ of the even and the odd solutions.

In this region, if $|q| << 1$ and $|a| \simeq 0$, the solutions can be approximated by [Rod03]:

$$u(t) \approx u_0 \cos(\omega_0 t)(1 + \frac{q}{2}\cos(\omega_{RF} t)) \tag{4.30}$$

where ω_0 is the macromotion angular frequency. Therefore it is a particular solution of Eq. 4.18, for $n = 0$:

$$\omega_0 = \frac{1}{2}\omega_{RF}\beta \tag{4.31}$$

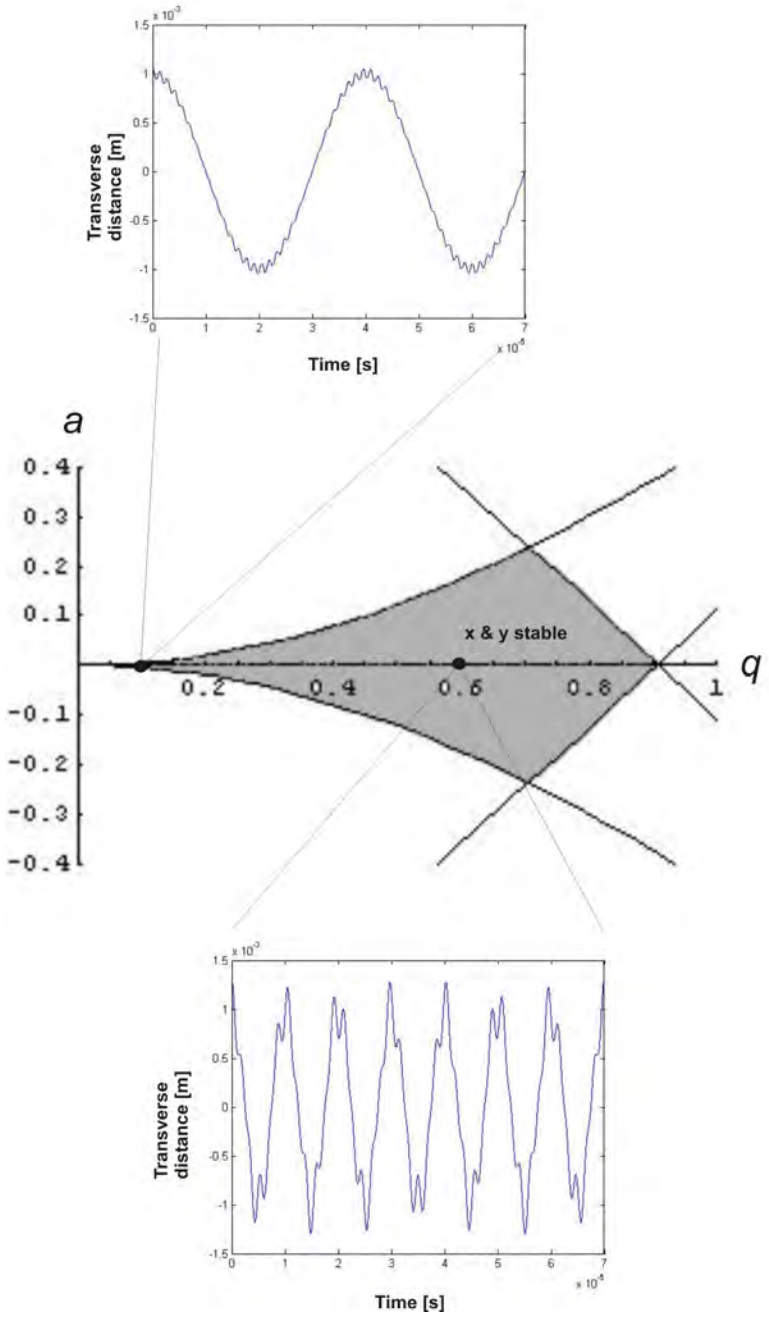

Figure 4.4: Combination of stability plot for both transverse coordinates x and y (*center*). The shaded area shows the region of parameters a and q used experimentally where both transverse coordinates x and y are stable. In addition, two ion motions for different stable $a - q$ pair of values are presented: ($a = 0$, $q = 0.1$) (*top*) and ($a = 0$, $q = 0.6$) (*bottom*).

and β is defined by:

$$\beta = \sqrt{a + \frac{q^2}{2}} \tag{4.32}$$

As a simplified model, the ion motion inside the RFQ electric field can be assumed as a superposition of a high frequency motion derived directly from the RF electric field (**micromotion**), and a low frequency motion, the **macromotion**. In RFQCB's, the micromotion is usually much smaller than the macromotion in normal experimental conditions (for $q < 0.4$). For $a = 0$ the equation of motion for an ion reads:

$$\ddot{u} + \frac{2eU_{RF}\cos\omega_{RF}t}{mr_0^2}u = 0 \tag{4.33}$$

The amplitude of the motion u is the sum of the amplitude of the micromotion (u_{mic}) and that of the macromotion (u_{mac}):

$$u = u_{mic} + u_{mac}, \tag{4.34}$$

In this particular case: $u_{mic} << u_{mac}$ and $\ddot{u}_{mic} >> \ddot{u}_{mac}$, and Eq. 4.33 transforms into:

$$\ddot{u}_{mic} = -\frac{2eU_{RF}\cos wt}{mr_0^2}u_{mac} = 0, \tag{4.35}$$

which yields:

$$u_{mic} = -\frac{1}{2}qu_{mac}\cos(\omega_{RF}t) \tag{4.36}$$

The amplitude of the motion is then:

$$u(t) = u_{mac}\left(1 - \frac{1}{2}q\cos(\omega_{RF}t)\right) \tag{4.37}$$

Substituting then in Eq. 4.33, one can find the relation between the frequency of the macromotion f_0 and the micromotion f_{RF}:

$$f_0 = \frac{q}{2\sqrt{2}}f_{RF} \tag{4.38}$$

Another theoretical approach to the ion motion inside the RFQCB is to calculate the value of the **pseudopotential** applied D to the ion. It can be obtained using the relations $eE = m\ddot{u}$ or $e\frac{dV}{du_0} = m\ddot{u}_0$:

$$D = \frac{qU_{RF}}{4r_0^2}(x^2 + y^2) = \frac{qU_{RF}}{4r_0^2}r^2, \tag{4.39}$$

where r is the radial component from the axis of the device. Figure 4.5 represents an example of a pseudopotential created in an RFQ.

The maximum allowable transverse energy of the confined ions is thus determined by the maximum value of the pseudopotential well D_{max}:

$$D_{max} = \frac{qU_{RF}}{4}. \tag{4.40}$$

It can also be expressed in terms of the RF electric field applied (U_{RF} and ω_{RF}) and the ion properties (e and m) using Eq. 4.11:

$$D_{max} = \frac{eU_{RF}^2}{m\omega_{RF}^2 r_0^4}. \tag{4.41}$$

For a fixed RF (ω_{RF} and U_{RF}), the confining capacity is decreasing for higher masses of the ions.

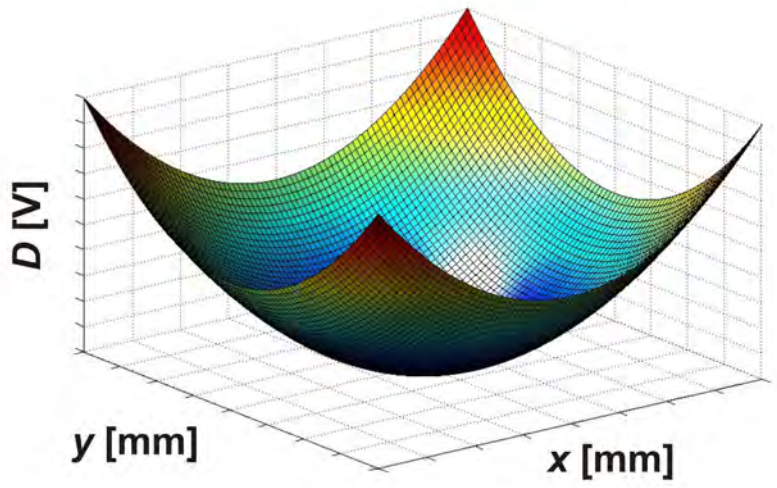

Figure 4.5: Example of the pseudopotential well D created in an RFQCB by the RF electric field for the transverse motion of the ions in the $x - y$ plane.

4.1.2 Buffer gas

The inlet of a buffer gas to fill the quadrupole modifies the motion of the ions inside the device. To characterize the interaction of the ions and the gas atoms/molecules, there are two main approaches:

- **Macroscopic**. The net effect of the gas on the ion motion is considered to be similar to that in a linear damping device:
$$\mathbf{F}_d = -c\mathbf{v}_d, \tag{4.42}$$
where $\mathbf{F}_d$ is the damping force applied to the ion, c the damping constant and $\mathbf{v}_d$ the drift velocity of the ion in the gas.

- **Microscopic**. The effect of each collision between the ion and the molecules of the gas is considered. The type of collision and the probability of such collisions have to be taken into account. The typical solution to manage this kind of approach is the use of a Monte Carlo code to simulate the evolution of the ion in the buffer gas [Pet02b].

In the frame of this thesis, only the macroscopic approach will be developed in the theory, although the microscopic approach has been chosen for the simulations of ISCOOL (see Chapter 5 and [Pet02b]). The macroscopic approach can be considered good enough to explain and discuss the physical reasons for adding a gas into the chamber.

As previously stated, the gas behaves as a damping (pneumatic) device. The new expression for the equation of the ion motion is:

$$m\ddot{\mathbf{r}} = -e\nabla\Phi - \mathbf{F}_d, \tag{4.43}$$

or in other terms:

$$\ddot{\mathbf{r}} + \frac{c}{m}\mathbf{v}_d + \frac{e}{m}\nabla\Phi = 0. \tag{4.44}$$

Using Eq. 4.2, Eq. 4.44 can be rewritten for the different coordinates as follows:

$$\ddot{u} + \frac{c}{m}\dot{u} + \frac{2e}{mr_0^2}\Phi_0 u = 0, \tag{4.45}$$

$$\ddot{z} + \frac{c}{m}\dot{y} = 0, \tag{4.46}$$

where $u = x, y$. The expression $\frac{c}{m}$ can be substituted as in [Kim97] for a constant b defined as $b = \frac{e}{mK}$, where K is the mobility of the ions in a certain gas. The mobility is related with the motion of an ion in a gas due to a weak electric field (around 0.1 V/cm in the RFQCB's) by the expression $v_d = KE$. The mobilities on standard conditions K_0 (T=273 K and P=101.325 kPa) are listed in [EAM88]. To apply the constants to the experimental conditions of the buffer gas, the following expression can be used:

$$K_2 = \frac{P_1}{P_2}\frac{T_2}{T_1}K_1, \tag{4.47}$$

where K_1 and K_2 are the constants in the initial and final conditions respectively, T_1 and P_1 the initial conditions, and T_2 and P_2 the final conditions. Figure 4.6 shows the fit mobility for cesium ions in helium gas at 0.1 mbar and 293 K, calculated from the data in [EAM88].

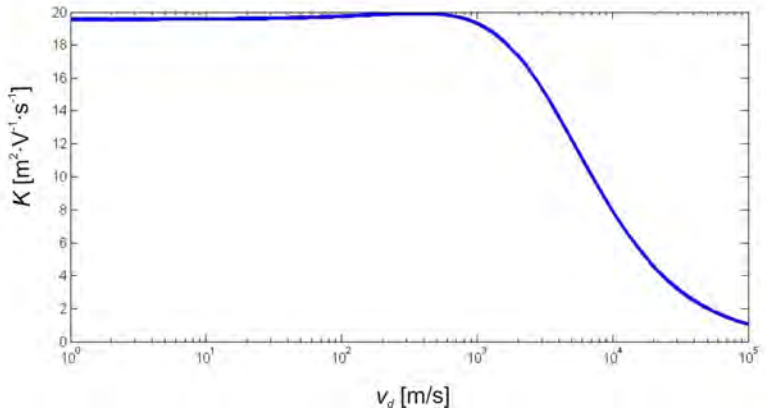

Figure 4.6: Plot of the fitted mobility for cesium ions in helium gas at a pressure of 0.1 mbar and a temperature of 293 K. The mobility is calculated from the data of K_0 from [EAM88].

Eqs. 4.48,4.49,and 4.50 are transformed into,

$$\ddot{x} + b\dot{x} + \frac{2e}{mr_0^2}\Phi_0 x = 0, \tag{4.48}$$

$$\ddot{y} + b\dot{y} - \frac{2e}{mr_0^2}\Phi_0 x = 0, \tag{4.49}$$

$$\ddot{z} + b\dot{y} = 0. \tag{4.50}$$

Taking into account the mathieu parameters a and q, and the dimensionless parameter $\tau = \frac{\omega_{RF}t}{2}$, the equations transform into:

$$\ddot{x} + b\dot{x} + (a_x - 2q_x\cos 2\tau)x = 0, \tag{4.51}$$

$$\ddot{y} + b\dot{y} - (a_y - 2q_x\cos 2\tau)y = 0, \tag{4.52}$$

$$\ddot{z} + b\dot{y} = 0. \tag{4.53}$$

Using $a_u = a_x = -a_y$ and $q_u = q_x = -q_y$, Eqs. 4.51 and 4.52 converts to a single expression, which is a Mathieu equation including a damping term:

$$\frac{d^2u}{d\tau^2} + 2\alpha\frac{du}{d\tau} + (a_u - 2q_u\cos 2\tau)u = 0, \tag{4.54}$$

where $\alpha = b/2$. Making the substitution (see [Kim97]), $u(\tau) = u_1(\tau)e^{-\alpha\tau}$ the equation becomes:

$$\frac{d^2u_1}{d\tau^2} + (\overline{a_u} - 2q_u\cos 2\tau)u_1 = 0, \tag{4.55}$$

where $\overline{a_u} = a_u - (b/2)^2$. In the case of the RFQCB where $a_u = 0$, the expression will become:

$$\frac{d^2u_1}{d\tau^2} + (-b^2 - 2q_u\cos 2\tau)u_1 = 0. \tag{4.56}$$

As shown in Fig. 4.4, the amplitude of the macromotion is normally much larger than the one from micromotion (direct excitation by the RF electric field). Hence, if the micromotion is neglected, the motion of an ion might be aproximated to a damped free single oscillation, although it has to be noticed that the real oscillation is caused by the RF electric field which is erased from the equation. In a damped single-harmonic system, the equation of the motion reads:

$$m\frac{d^2u}{dt^2} + c\frac{du}{dt} + ku = 0, \tag{4.57}$$

where c is the damping constant, k the spring constant and m the mass (of the ion in this case). In a normal simple harmonic movement (SHM), the equation can be transformed into:

$$\frac{d^2u}{dt^2} + 2\xi\omega_0\frac{du}{dt} + \omega_0^2u = 0, \tag{4.58}$$

with the solution:

$$u(t) = u_0e^{-\xi\omega_0 t}\cos(\omega t + \phi), \tag{4.59}$$

where $\omega_0 = \sqrt{\frac{k}{m}}$ is the natural angular frequency of oscillation of the system (if there were no damping), and $\xi = \frac{c}{2\sqrt{km}}$ is the damping ratio. The real angular frequency of the oscillations ω is related with the natural angular frequency ω_0 of the system: $\omega = \omega_0\sqrt{1-\xi^2}$. In the absence of a damping term $\xi = 0$, and then $\omega = \omega_0$. The natural angular frequency and the damping ratio can be expressed with general parameters (see [Kim97]):

$$\omega_0 \cong \frac{q}{2\sqrt{2}}\omega_{RF}, \tag{4.60}$$

$$\xi = \frac{\sqrt{2}e}{qKm\omega_{RF}}, \tag{4.61}$$

or:

$$\xi = \frac{1}{2\sqrt{2}}\frac{\omega_{RF}r_0^2}{KU_{RF}}, \tag{4.62}$$

where K is the mobility of the ion in the gas. The critical damping condition $\xi^2 = 1$ yields [Kim97]:

$$K = \sqrt{2}\frac{e}{qm\omega_{RF}} \tag{4.63}$$

An important figure when talking about cooling is the **temperature** of the beam. Several expressions have been given to evaluate the ion temperature in traps [LBM92, Fon01, Pet02b]. The cooling mechanisms which influences the final temperature of the cooled ion beam inside the RFQCB's are [Fon01]:

- **Collisional cooling**. When the mass of the buffer gas atoms or molecules (m_{gas}) is smaller than the mass of the ions of the beam (m_{ion}), the collisions among them reduce the kinetic energy of the ions. Therefore, since the ions lose energy, the beam is reducing the size and the velocity. In conclusion, acting as a non-conservative force that resuces the volume in the phase space, the emittance.

- **Evaporative cooling**. Despite this effect causes a reduction of the temperature of the beam, it is in fact an undesirable effect, since it has to do with the loss of hotter ions. The effect is called cooling due to the fact that the most energetic ions are lost because the confinement provided by the RF field (the pseudopotential well) is not sufficient.

- **RF heating**. One effect that is normally not considered in a first theoretical approach is that the cooled beam does not reach the same temperature as the buffer gas. The buffer gas has a kinetic energy distribution around the room temperature but the energy of the cooled ions is always bigger. That comes from the fact that the micromotion (coherent) associated with the RF is independent of the collisions between the ions and the the buffer gas (uncoherent). Among the collisions, some of the coherent motion is transferred to the uncoherent motion therefore increasing the real kinetic energy of the ions [Kim97, LBM92]. The larger the RF heating the greater the temperature and therefore the emittance of the ion beam. That means the q parameter has to be kept as low as possible (inside the stable regions): RF amplitude small (U_{RF}), or inner radius (r_0) or frequency (f_{RF}) large.

4.1.3 Axial electric field

An axial electric field along the longitudinal direction z is superimposed to the RF field to guide the ions along the RFQCB to the exit. The axial field minimizes the cooling, accumulation and transition time inside the RFQCB. The field can be considered constant in the longitudinal axis, but some other components in x and y directions are present. Hence, the axial electric field $\mathbf{E}_a$ can be expressed as:

$$\mathbf{E}_a = \begin{bmatrix} E_x \\ E_y \\ E_{z0} + k_z z \end{bmatrix}. \tag{4.64}$$

The minimum of the potential curve ϕ_{DC} created to accumulate the ions before released them as a bunch might be approximated by a parabola [Her01]:

$$\phi_{DC}(r = 0, z) = (U_{DC}/z_0^2) \cdot z^2, \tag{4.65}$$

and expressed in general as:

$$\phi(r, z) = \frac{U_{DC}}{z_0^2} \left(z^2 - \frac{r^2}{2} \right), \tag{4.66}$$

where U_{DC} is a the axial potential and z_0 is a constant characteristic of the axial curve which is created. It is clear that the axial field provides a defocusing component in the radial direction [DB00]. The value pseudopotential well is decreased by the term $U_{DC}r^2/2z_0^2$. Therefore, the maximum value for the constant U_{DC}/z_0^2:

$$U_{DC}/z_{0\,max}^2 = \frac{qU_{RF}}{2}\left(\frac{1}{r_0}\right)^2, \tag{4.67}$$

or substituting Eq. 4.11:

$$U_{DC}/z_0^2 = \frac{2e}{m}\left(\frac{U_{RF}}{\omega_{RF}r_0^2}\right)^2. \tag{4.68}$$

Eq. 4.68 implies that higher axial electric fields could be applied if either high amplitude of the RF field or low RF frequency are applied. However, that would mean a worse cooling due to the RF heating (see Sec. 4.1.2). Therefore, a compromise has to be found to optimize the cooling inside the RFQCB. In addition, the stability parameter a_u can be modified as [Nie02]:

$$a_u = \tilde{a} = \frac{4eU_{eff}}{mr_0^2\omega_{RF}^2}, \tag{4.69}$$

where U_{eff} is a voltage proportional to the applied DC voltages U_{DC}. The exact proportionality depends on the specific trap geometry [DB00].

4.1.4 Space charge

RFQCB's have a limit in the maximum intensity of the ion beam that can be manipulated. This constraint has been studied before in [Daw95, Gho95]. The limit is caused by the Coulomb interaction between the ions in the ion cloud. According to [Pet02b, Rod03], the final expression for the maximum number of ions inside the trap n_{max} is expressed by:

$$n_{max} = \frac{\epsilon_0}{e}\cdot\frac{qU_{RF}}{r_0^2}, \tag{4.70}$$

where ϵ_0 is the permittivity constant in in the vacuum. Hence, it is clear from the expression that the number of ions is a function of the physical properties of the ions and the operation parameters of the RFQCB.

U_{RF} could be substituted in Eq. 4.70 Eq. 4.11 and the maximum density is expressed as:

$$n_{max} = \frac{\epsilon_0\pi^2 f_{RF}^2 q^2 m}{e^2}. \tag{4.71}$$

Most of the times, it is better to show the space charge limit as the maximum number of ions the trap can accumulate or, even better, as the maximum intensity the trap can accept. The first approximation, as function of the maximum number of ions N_{max}, is expressed as:

$$N_{max} = n_{max}\cdot\pi r_s^2\cdot L, \tag{4.72}$$

where L is the length of the RFQCB chamber, and r_s the radius of an imaginary cylinder along the RFQCB where the beam is confined. The intensity of the ion beam I can be calculated from the number of ions per unit of length N_{max}/L:

$$N_{max}/L = n_{max}\cdot\pi r_s^2. \tag{4.73}$$

From here, the maximum intensity I_{max} is:

$$I_{max} = N_{max}/L \cdot v_{ion}, \tag{4.74}$$

where v_{ion} is the speed velocity of the ion inside the trap after cooling. The velocity can be calculated from the initial energy of the ions into the RFQCB and the final temperature of the ions, see e.g. in [LBM92, Pet02b].

4.1.5 Efficiency

The transmission efficiency is one of the most important parameters to describe the performance of an RFQCB. It is worth to define some magnitude which allows the beam losses in the device to be understood. Three main definitions are given here for the total efficiency of an RFQCB:

- $\eta_{cool} = \frac{N_{cool-out}}{N_{inj-in}}$. Ratio of the ions coming out from the RFQCB and the ions coming in when only cooling without bunching is applied.
- $\eta_{bunch} = \frac{N_{bunch-out}}{N_{inj-in}}$. Ratio of the ions coming out from the RFQCB and the ions coming in when both cooling and bunching are applied.
- $\eta_{RFQCB} = \frac{N_{out}}{N_{in}}$. Ratio of the total number of ions coming out after extraction and the total number of ions before deceleration phase.

The last efficiency figure can be separated in:

$$\eta_{RFQCB} = \frac{N_{out}}{N_{in}} = \frac{N_{out}}{N_{bunch-out}} \cdot \frac{N_{bunch-out}}{N_{inj-in}} \cdot \frac{N_{inj-in}}{N_{in}} \tag{4.75}$$

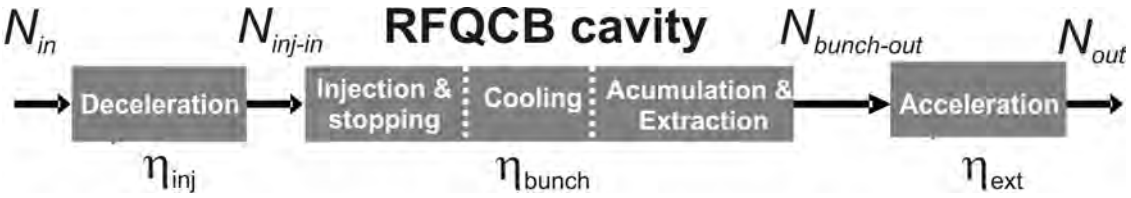

Figure 4.7: Scheme of the main parts of an RFQCB together with the definition of the number of ions and efficiencies in each part (see text for more information).

The three parts can be defined as the efficiency for the deceleration phase $\eta_{inj} = \frac{N_{inj-in}}{N_{in}}$, the efficiency of the RFQCB itself (in this case in the bunching operation mode) η_{bunch}, and the efficiency of the acceleration phase $\eta_{ext} = \frac{N_{out}}{N_{bunch-out}}$. Figure 4.7 shows the main parts in which an RFQCB can be split regarding efficiency.

The separation of the efficiencies allows the distinction of the different losses processes along each part of the transmission chain. In the injection part, the efficiency (η_{inj}) is limited by the ion losses due to a bad focusing of the ion into the RFQCB, either due to a tuning of the voltage on the injection electrodes or the use of holes too small in diameter. The efficiency in the extraction part (η_{ext}) is affected in a similar way as η_{inj}. In addition an excessive gas pressure in the first region of acceleration, just after the exit of the RFQCB, could cause the blown-up of the beam and more ion losses.

The efficiency inside the RFQCB itself (η_{bunch}) is affected, mainly during the bunching operation mode, by the following loss mechanisms:

- **Ion-ion collisions**.
- **Ion-neutral atom collisions**. Three main processes are involved (see [Daw95, Rod03]): the inelastic scattering, the elastic scattering and the charge exchange.
- **Radioactive decay**. It is only applied to the radioactive nuclei.

From [Daw95], the loss rate of trapped ions inside the RFQCB chamber, $N(t)$, is:

$$\frac{dN}{dt} = -\frac{\alpha_1}{V}N^2 - \alpha_2 PN, \tag{4.76}$$

where α_1 and α_2 are constants, P the buffer gas pressure and V the confinement volume of the RFQCB caviy. The first term represents the losses due to the ion-ion collisions and the second one the ion-neutral atom collisions. The general solution of Eq. 4.76 is:

$$N(t) = \frac{\frac{\alpha_2}{\alpha_1}PV}{\left(\frac{\alpha_2 P+\alpha_1 N_0/V}{N_0\alpha_1/V}\right)e^{\alpha_2 Pt} - 1}, \tag{4.77}$$

where N_0 is the initial number of ions. As mentioned above, for low intensities of the ion beam, the interaction due to ion-ion collisions is negligible per unit number in comparison with the losses due to the ion-neutral atom collisions. For low intensities, $\alpha_1 = 0$ then Eq. 4.77 might be converted to a more simple expression [Nie02, Rod03]:

$$N(t) = N_0 e^{-\alpha_2 Pt}. \tag{4.78}$$

The constant parameter α_2 depends on the reactions between the ion and the buffer gas atoms or impurities molecules. It also includes the losses due to molecular formation by chemical reactions.

In [Nie02], the efficiency factor for the transmission of native ions is described as:

$$\eta_{mol} = \frac{t_{mol}}{t_{acc}}\left(1 - e^{-t_{acc}/t_{mol}}\right), \tag{4.79}$$

where t_{dec} represents the time constant for the exponential decay in an ion-molecule association reaction described as [KBH$^+$01]:

$$\frac{dN(t)}{dt} = -R[M]N(t) \tag{4.80}$$

where R is the reaction rate constant and $[M]$ the concentration of the impurity molecule.

Moreover, the ISOL beams are radioactive and a term for the radioactive decay must be added. The ion losses inside the trap are well known for a certain ion with decay constant λ ($t_{rad} = 1/\lambda$) and a beam injected intensity of I_{inj} is [Nie02]. The ions left inside the cooler for an instant t are:

$$N(t) = I_{inj} t_{rad}\left(1 - e^{-\lambda t}\right). \tag{4.81}$$

The efficiency term related with the radioactive decay η_{decay} taking into account that the ions stay in the trap during a maximum that corresponds to the accumulation time t_{acc} expressed as [Nie02]:

$$\eta_{decay} = \frac{t_{rad}}{t_{acc}}\left(1 - e^{-t_{acc}/t_{rad}}\right) \tag{4.82}$$

The efficiency for radiactive decay and for molecular formation can be put together to obtain a total efficiency due to non-optics phenomenons η_{loss}:

$$\eta_{loss} = \eta_{mol} \cdot \eta_{decay} = \left(\frac{t_{dec}t_{rad}}{t_{acc}^2}\right)\left(1 - e^{-t_{acc}/t_{rad}}\right)\left(1 - e^{-t_{acc}/t_{dec}}\right) \tag{4.83}$$

	a	q	Φ_0
RFQ	$\frac{8eU_f}{m\omega_{RF}^2 r_0^2}$	$\frac{4eU_{RF}}{m\omega_{RF}^2 r_0^2}$	$\frac{qU_{RF}}{4r_0^2}r^2$
With buffer gas	$\frac{8eU_f}{m\omega_{RF}^2 r_0^2} - \left(\frac{b}{2}\right)^2$	$\frac{4eU_{RF}}{m\omega_{RF}^2 r_0^2}$	$\frac{qU_{RF}}{4r_0^2}r^2$
With axial electric field	$\frac{4eU_{eff}}{m\omega_{RF}^2 r_0^2}$	$\frac{4eU_{RF}}{m\omega_{RF}^2 r_0^2}$	$\frac{U_{DC}}{z_0^2}z^2 + (\frac{qU_{RF}}{4r_0^2} - \frac{U_{DC}}{2z_0^2})r^2$

Table 4.2: Evolution of the Mathieu parameters a and q for different situations: 1) **RFQ**, only applying RFQ electric field, 2) **With buffer gas**, adding the buffer gas inside the cavity and 3) **With axial electric field**, adding an axial electric field. The potential for the different situations is also shown. The parameters are explained along the text.

4.1.6 Summary and conclusions

Mathieu parameters a and q and the transverse pseudopotential Φ_0 are given in Tab. 4.2 as a function of geometrical and electrical parameters for three cases: 1) only taking into account the RF quadrupole electric field, 2) adds the effect of the buffer gas and 3) adds the defocusing effect of the axial field.

4.2 Penning traps

The idea of the Penning traps was invented by F. M. Penning [Pen36] and developed later on by Dehmelt [Deh67]. They combine a magnetic field and an electrostatic field to trap the ions. Like in Paul traps, Penning traps evolved from classical hyperbolic configurations (see Fig. 4.8) to cylindric ones (see Chapter 11). So far, the main application of these instruments has been the mass spectrometry, thanks to the existing relation between the mass of the ion measure, the magnetic field applied and the frequency of the motion inside the trap (see Sec. 4.2). Currently, many experiments devoted to mass measurements make use of Penning traps, e.g at the ISOLTRAP experiment at ISOLDE, at the IGISOL experiment at Jyväskylä or at the CPT experiment at ANL.

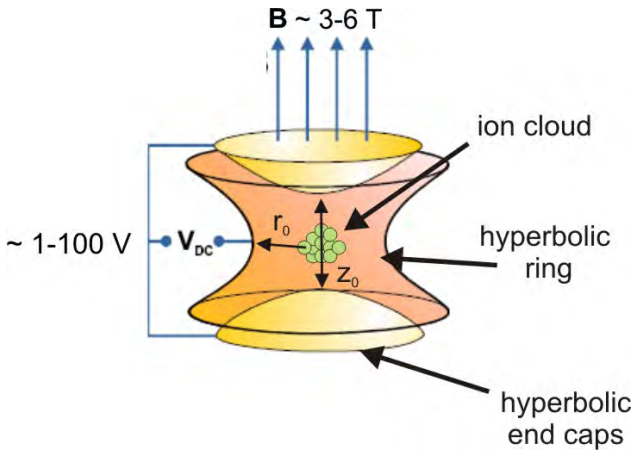

Figure 4.8: Classical hyperbolic configuration of a Penning trap. A constant difference potential is applied between the ring electrode and the end caps together with a constant magnetic field to confine the ion cloud in the center of the trap.

At RIB facilities, Penning traps are also suitable for the beam preparation stage and as beam purification devices to prepare the beams for mass spectrometry devices. In this case, the Penning trap REXTRAP at REX-ISOLDE represents an unique device around the world. There is no other Penning trap involved in the beam preparation stage for cooling and bunching the RIB of an ISOL facility. As explained in Sec. 3.6.1 REXTRAP has as mission the preparation of the ISOLDE quasi-continuous beam for the operation of the charge breeder REXEBIS (see following section). REXTRAP is therefore a pioneer device which has shown that such a complex system as the Penning traps can be suitable and reliable for the beam preparation stage. However, Penning traps have a limitation in intensity due to the space charge. New methods which intend to diminish this effect and push up the limit of the intensity handled by the Penning traps, are investigated later within the framework of this thesis. Ion traps were developed because of the necessity to confine small quantities of ions in a small space for their study or as ion mass filters in chemical applications.

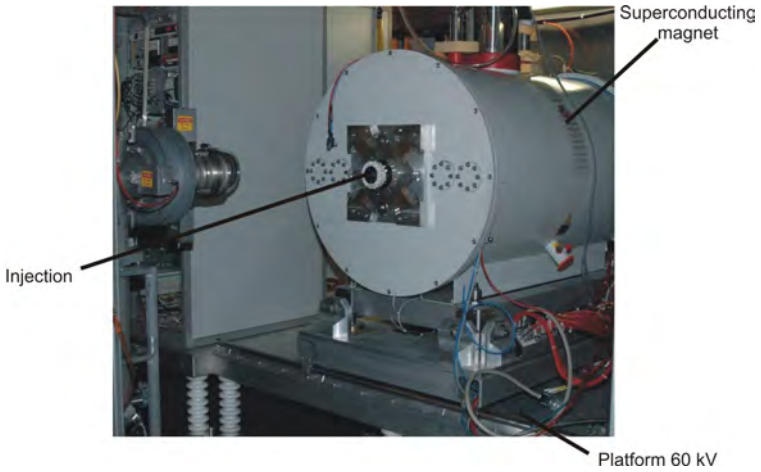

Figure 4.9: Picture of REXTRAP during one maintenance operation in the shutdown.

In Penning traps, the combination of the static magnetic field, the electrostatic field and the RF field makes the trajectories of an ion inside a Penning trap be governed by the following motions (see Fig. 4.10):

- The magnetron motion ω_-.
- The reduced cyclotron motion ω_+.
- The axial motion ω_z.

A potential U_0 applied to the electrodes creates a constant electrostatic field:

$$\Phi_T(x, y, z) = \frac{U_0}{4d^2}(2z^2 - x^2 - y^2), \tag{4.84}$$

where x,y and z are the coordinates from the center of the trap, and d is a characteristic parameter of the trap given by:

$$d = \sqrt{\frac{1}{2}\left(z_0 + \frac{r_0^2}{2}\right)}, \tag{4.85}$$

which is function of the radius of the central electrode of the trap r_0 and the distance between the cap electrodes $2z_0$. The ions are confined in the center of the trap. The expression of the equations of the ion motion are:

$$\begin{cases} \ddot{x} - \frac{1}{2}\omega_z^2 x - \omega_c \dot{y} = 0 \\ \ddot{y} - \frac{1}{2}\omega_z^2 y - \omega_c \dot{x} = 0 \\ \ddot{x} + \omega_z^2 = 0 \end{cases} \tag{4.86}$$

Where ω_c the total cyclotron angular frequency. The axial angular frequency is given by:

$$\omega_z = \sqrt{\frac{QU_0}{md^2}} \tag{4.87}$$

The following relations apply between different angular frequencies:

$$\begin{cases} \omega_c = \omega_+ + \omega_- \\ \omega_+ \cdot \omega_- = \frac{1}{2}\omega_z^2 \\ \omega_c^2 = \omega_z^2 + \omega_+^2 + \omega_-^2 \end{cases} \tag{4.88}$$

The true cyclotron motion ω_c depends only on the mass of the ion, m, and the strength of the magnetic field B:

$$\omega_c = \frac{QB}{m} \tag{4.89}$$

with Q the charge of the ion. The other motions are expressed as:

$$\omega_- \approx \frac{U_0}{2d^2 B} \tag{4.90}$$

$$\omega_+ \approx \frac{QB}{m} - \frac{U_0}{2d^2 B} \tag{4.91}$$

As the cyclotron angular frequency, the magnetron does not depend on the mass of the ions.

4.2.1 Overview of cooling methods for Penning traps

Cooling of the ion motion is important to enhance the efficiency or improve the optical properties of the beam for all precision experiments. So far various techniques have been developed to cool the ion motion inside a Penning trap (see [KBK$^+$95]):

- Resistive cooling: energy dissipation in a resistance inside a cooled circuit. The current is that induced by the ions in the trap electrodes.
- Laser cooling: interaction with an intense laser beam of appropiate wavelength.
- Electron cooling: interaction with an electron beam (for antiprotons and high-charged ions).
- "Sympathetic" cooling: interaction with cooled charged particles.
- Sideband cooling: interaction with a buffer gas.

Of all these methods, the last one, buffer gas cooling, is the best suited for the application to low energy RIB's. If a buffer gas is included, the damping effect is similar to that produced in RFQCB's. The equations of the motion read:

$$\begin{cases} \ddot{x} + \frac{c}{m}\dot{x} - \frac{1}{2}\omega_z^2 x - \omega_c \dot{y} = 0 \\ \ddot{y} + \frac{c}{m}\dot{y} - \frac{1}{2}\omega_z^2 y - \omega_c \dot{x} = 0 \\ \ddot{x} + \frac{c}{m}\dot{z} + \omega_z^2 = 0 \end{cases} \tag{4.92}$$

Where c is the damping constant due to the gas. It is clear that the axial motion is decoupled from the other motions:

$$z(t) = A' \exp \frac{-ct}{2m} \cos\left(\omega_2' t + \phi_z'\right), \tag{4.93}$$

with:

$$\omega_z' = \sqrt{\omega_z^2 - \frac{1}{4}\frac{c^2}{2m}}. \tag{4.94}$$

In the same way, the amplitude of the reduced cyclotron motion decreases exponentially as:

$$A^+(t) = A_0^+ \cdot \exp -\alpha^+ t, \tag{4.95}$$

with:

$$\alpha^+ = \frac{c}{m}\frac{\omega_+}{\omega_+ - \omega_-}. \tag{4.96}$$

At the same time, the magnetron motion increases exponentially as:

$$A^-(t) = A_0^+ \cdot \exp +\alpha^+ t, \tag{4.97}$$

with:

$$\alpha^- = \frac{c}{m}\frac{\omega_-}{\omega_+ - \omega_-}. \tag{4.98}$$

Since $\omega_- \ll \omega_+$, the reduced cyclotron motion is damped much faster than the magnetron is lowered. The magnetron motion is then unstable and the different cooling techniques will be devoted to stabilize both motions.

Sideband cooling

The cooling of the ion motion in a Penning trap is slightly more complicated than in the RFQCB's, as the magnetron motion is unstable, and any dissipative process (as the buffer gas interaction with the beam) leads to an increase in the amplitude of this motion until the ion is lost. One method to achieve cooling is to couple the magnetron motion ω_- to either the axial motion ω_z or to the reduced-cyclotron motion ω_+ (see Eq. 4.88).

In reality, the coupling is carried out by applying an azimuthal electric quadrupole field oscillating with a frequency which is equal to the real cyclotron motion. The field is created by a four-fold segmented electrode. An alternating field with a frequency f_{RF} (or ω_{RF} in terms of angular frequency) and a voltage amplitude of U_q is applied to the segments, and is phase-shifted 180° for consecutive segments. Therefore the voltage applied to the consecutive segments is always opposite in value. The additional potential created by applying the potential $\phi_{Q,sid}(t) = U_q \cos(\omega_{RF} t + \phi_{RF})$ to the electrodes has the form (see [Rei02]):

$$\phi_{Q,sid}(t) = \frac{aU_q}{r_e^2}(x^2 - y^2)\cos(\omega_{RF} t + \phi_{RF}), \tag{4.99}$$

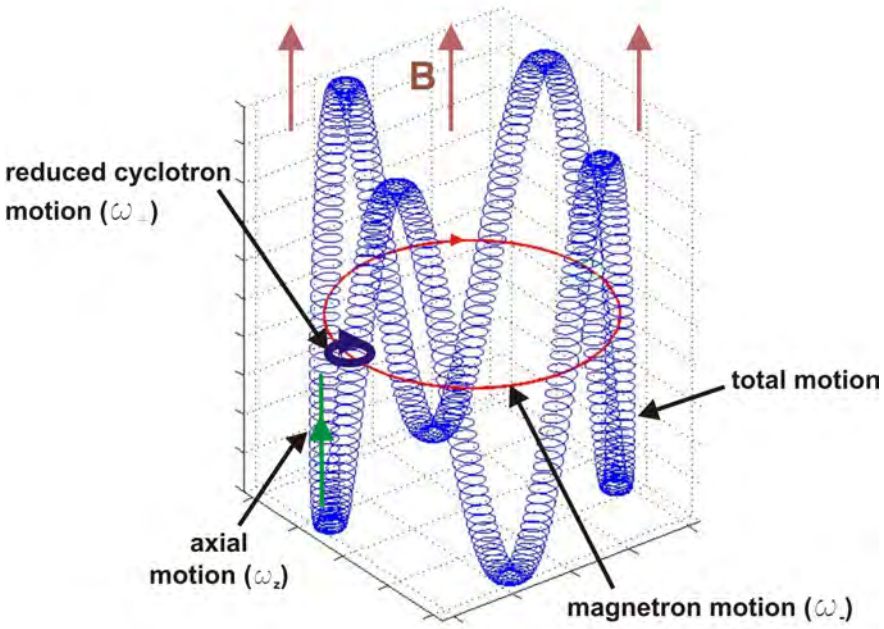

Figure 4.10: Ion motion inside a Penning trap: the reduced cyclotron motion (ω_-), the magnetron motion (ω_+) and the total motion are shown.

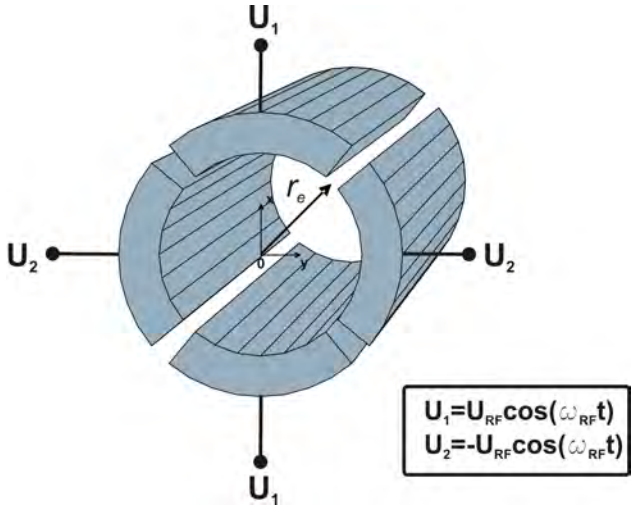

Figure 4.11: Scheme of the segmented cylindrical electrode used for the creation of the RF field for the sideband cooling technique and the voltages applied to each segment.

where r_e is the radius of the cylindrical electrode and a is an experimental correction factor to consider the deviation of an ideal quadrupole potential due to the geometry of the electrodes (see 4.11).

The potential has to be added to the other potential created inside the trap to solve the equation of motion of the ions inside. The solution shows (see [KBK$^+$95]) that there exists a periodic transfer of energy between the two motions which are coupled by the new potential. In this case the maximum coupling is found when the frequency of the new potential f_{RF} is equal to the true cyclotron frequency f_c. The strength of the coupling makes a periodic conversion of both motions (magnetron and reduced-cyclotron) but their amplitudes are constantly decreasing. Figure 4.12 compares the motion with a buffer gas without sideband (conversion between motions) and with the sideband field coupled to the cyclotron motion.

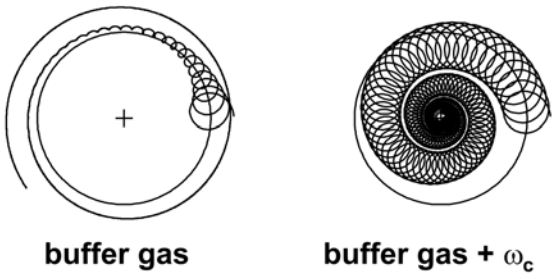

Figure 4.12: Comparison of the motion of an ion inside a Penning trap with buffer gas: without additional field applied (*left*) and with sideband field coupled to the cyclotron motion ω_c (*right*)..

Equation 4.89 shows that the true cyclotron motion depends on the mass of the ion due to the interaction with the buffer gas atoms. For cooling the ions, the frequency of the new potential has to be coupled with the cyclotron motion, that means that only one of the isotopes in the beam will be cooled. The other possible masses will be lost in the Penning trap walls, or partially removed if their mass is near to the mass of the selected ion. Therefore the Penning trap in combination with the sideband cooling acts not only as a cooling and bunching device but also as a purification system.

Rotating wall cooling

This technique, coming from the plasma physics, is based on the application of RF electric fields to a segmented cylindric electrode. The RF fields are phase-shifted in the symmetrical electrodes around the cylinder making the effect so-called "rotating wall", see Fig. 4.13. The new force counteracts the repulsion space charge effect by adding the Lorentz force, keeping the beam together. Hence better efficiencies are expected for higher intensities of the beam. In equilibrium, the Lorentz force ($\mathbf{F}_L$) equals the sum of the Coulomb ($\mathbf{F}_C$) and centrifugal force ($\mathbf{F}_{centr}$):

$$\mathbf{F}_L = \mathbf{F}_C + \mathbf{F}_{centr}. \tag{4.100}$$

Substituting every term for its expression yields:

$$Q\omega r B = \frac{ne^2 r}{2\epsilon_0} + m\omega^2 r, \tag{4.101}$$

where n is the ion density and ω the rotation angular frequency. First term in Eq. 4.101 can be expressed in terms of the plasma angular frequency ω_p that reads:

$$\omega_p = \sqrt{\frac{Q^2 n}{\epsilon_0 m}}, \tag{4.102}$$

and stands for the collective oscillations of the electrons and the ions due to the space charge differences. Equation 4.89 can be written in terms of ω_p and ω_c as:

$$\omega\omega_c = \omega^2 + \frac{\omega_p^2}{2}. \tag{4.103}$$

The solutions for ω are:

$$\omega_\pm = \frac{1}{2}\left(\omega_c \pm \sqrt{\omega_c^2 - 2\omega_p^2}\right). \tag{4.104}$$

The rotating fields are created by applying sinusoidal voltages appropriately phased-shifted to the different segments of an electrode (see Fig. 4.14). One can derive the radial (E_r) and angular (E_θ) dependance of the fields as:

$$E_r(r,\theta) = E_0 \left(\frac{r}{r_0}\right)^{p-1} \cos\left(p(\theta - \omega t)\right), \tag{4.105}$$

$$E_r(r,\theta) = -E_0 \left(\frac{r}{r_0}\right)^{p-1} \sin\left(p(\theta - \omega t)\right). \tag{4.106}$$

For the dipole rotating field ($p = 1$), a four-fold segmented electrode can be used. The angular frequency of the field excites the plasma at the axial angular frequency of the ions ω_z (resonance). In particular, the dipolar rotating field originates the following potential:

$$\phi_{D,rot}(t) = \frac{aU_d}{r_0}\left[(x\cos(\omega_{RF}t + \phi_{RF}) + y\sin(\omega_{RF}t + \phi_{RF})\right], \tag{4.107}$$

An eight-fold electrode is adequate for a quadrupolar rotating field ($p = 2$). In this case, the excitation frequency corresponds to the axial angular frequency of the ions ω_z or to the cyclotron angular frequency ω_c. For the quadrupolar rotating field the potential created is:

$$\phi_{Q,rot}(t) = \frac{aU_q}{r_0^2}\left[((x^2 - y^2)\cos(2\omega_{RF}t) + 2xy\sin(\omega_{RF}t)\right]. \tag{4.108}$$

According to [Rei02] a quadrupolar rotating field would suit better because of the linear dependance on the radius r, in the same way as the force due to the tangetial friction by the buffer gas:

$$\mathbf{F} = -c\omega r\hat{\mathbf{r}}, \tag{4.109}$$

where c is a damping constant. A good overview of this technique is given in [HAH$^+$97, Rei02], where the concepts of plasma, shape of the beam due to the space charges and the effects of a rotating quadrupole field on the equilibrium state are widely explained. The technique was used before in electron plasmas [AHD98], positron plasmas [RCG00] and for compressing ion clouds of Mg^+ [HAD00].

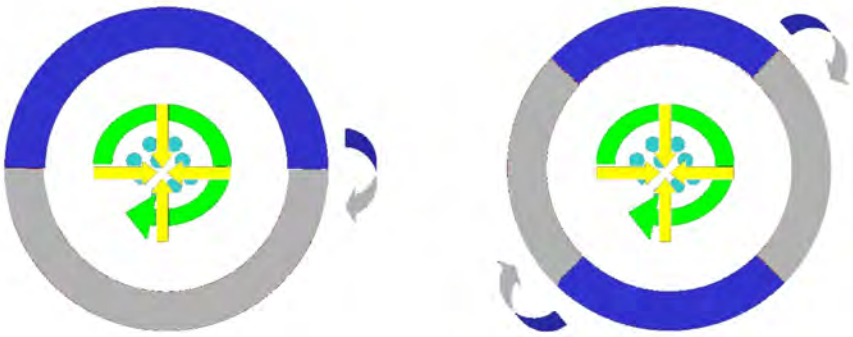

Figure 4.13: Schemes of the rotating wall cooling: for a dipolar field, two electrodes $\pi/2$ phase-shifted in RF voltage (*left view*), and for a quadrupolar field, four electrodes $\pi/4$ phase-shifted in RF voltage (*right view*). The straight arrows show the direction of the Lorentz force which compresses the ion cloud.

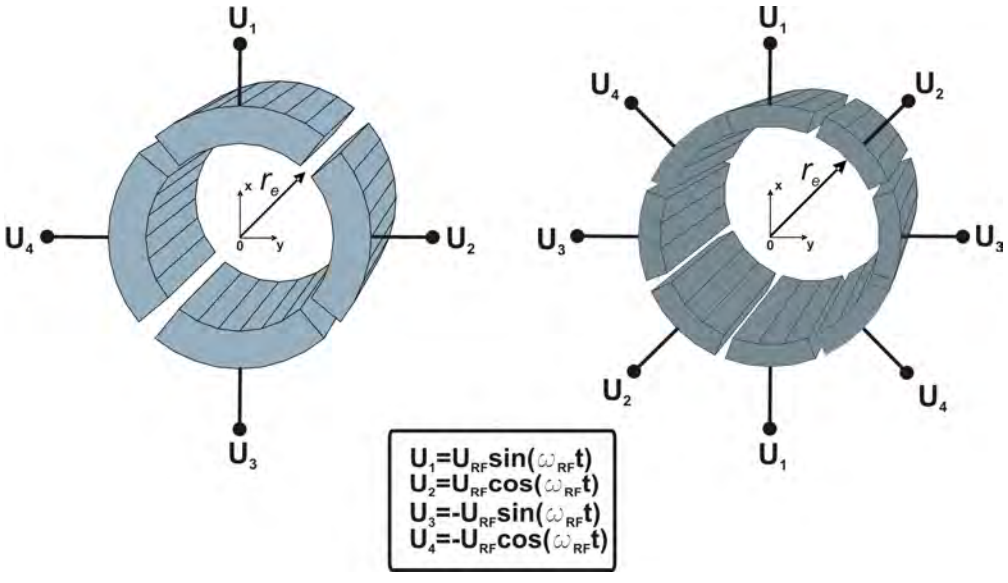

Figure 4.14: Scheme of the segmented cylindrical electrode used for the creation of the RF field for the rotating cooling technique and the voltages which are applied to each segment: the four-segmented electrode is used for the dipolar technique (*left view*) and the eight-segmented electrode for the quadrupolar technique (*right view*). The same four RF signals are applied in both cases.

Chapter 5

New RFQCB for ISOLDE: the ISCOOL project

In the beginning of this decade, Paul traps, which were usually only applied to trap and to study particles, were tested for the improvement of the optical properties of the RIB facilities. The working groups which participated in this study developed new geometries and features, adapted to the requirements of this application. The progress in the theoretical and practical studies achieved successful results with the adoption of the new tool, the Radio Frequency ion Cooler and Buncher (RFQCB), a direct evolution of the Paul traps, but fully oriented to the manipulation of the beam. From the first achievements, the field has grown and more technical advanced and modern RFQCB's have been commissioned in experiments around the world. Different mechanical geometries have been tested and the beam capacity and transmission have been improved. However, so far, although the applications of the RFQCB's are very diverse, there is no RFQCB installed on-line in the main line of an ISOL facility. For the on-line installation, the challenges are: the huge number of experiments and applications to deliver the beam, the reliability of the system or the transmission and the intensity optimization for the high number of RIB's available in the facility. The ISCOOL (ISolde COOLer) project was launched in order to study, design, test and commission the implantation of a new general purpose RFQCB for ISOLDE to serve all the ISOLDE experiments. ISCOOL aims to increase the excellence at the ISOLDE facility and keep it as a leading RIB facility around the world. In the following a global description of the project is given.

5.1 Why an RFQCB for ISOLDE?

The primary motivation for installing a beam cooler at ISOLDE came from REX-ISOLDE. The transmission and injection into REXTRAP wanted to be optimized which would maximize the efficiency of the critical low-energy part of REX. The main motivations were:

- A reduced transverse emittance,
- a reduced energy spread,
- and beam bunching capability.

Unfortunately, the layout of the ISOLDE hall did not allow the installation (without major modifications) of a cooler for the benefit of both the HRS and GPS beams. Due to the importance of

Mass range	10÷300 u
Transverse emittance (90% at 60 keV)	$< 20\ \pi$ ·mm·mrad
Intensity	$< 10^{10}$ ions/s
Mean energy	60 keV
Energy spread	5 eV
Type of beam-timing	CW (quasi-continuous beam)

Table 5.1: Main preliminary specifications for ISCOOL and the incoming beam fom HRS.

the HRS for REX-ISOLDE, all the locations were proposed in the HRS beam lines. Three main locations were initially proposed:

- Before the first magnet of the HRS.
- Between the first and second magnet of the HRS.
- After the focal point of the HRS.

The first two proposals would require major engineering work at ISOLDE. In addition, due to the high current of the beam before the separation at the HRS, a pre-separator magnet would be necessary for the first option (see Chapter 3).

As two RFQCB's have been running successfully at the ISOLDE hall for single experiments [FHKB$^+$01, Bac04], a general purpose RFQCB was the device chosen: the ISCOOL (ISOLDE COOLer). The project is an important contribution to the new HIE-ISOLDE project (High Intensity and Energy-ISOLDE, see [NL05]). The project will represent an upgrade of ISOLDE in terms of intensity, energy and quality of the RIB's offered to the users. Furthermore, it will attract new users, as for example experimentalists doing collinear laser spectroscopy of RIB's similar to the experiments done at IGISOL (see [Bil01]). It represents also a milestone for the EURISOL design study [The03], which is being carried out nowadays.

5.2 Specifications

Once the final placement of ISCOOL in the ISOLDE beam lines was decided, the requirements of a cooler in such position could be established according to the specifications of the RIB's on that point, and the requirements of the experiments connected to that beam lines. A detailed report about the technical and physics requirements and specifications of the ISCOOL project can be found elsewhere [JLMP03, Pod04b].

The preliminary specifications of the project were given for the beam optics at the focusing point downstream of the HRS. The beam optics varies depending on: the target and the ion source installed in the HRS front-end, the extraction energy, or the isotope selected at the HRS separator [GCF$^+$03]. General figures of the transverse emittances at 60 keV are 7-14 π mm mrad but higher values are possible [WLL03]. ISCOOL has to take into account all these situations. The worst case in terms of optics of the RIB fixed the requirement for the ISCOOL specifications at the injection side. In Table 5.1, the range of the main parameters that were the base for the preliminary design of ISCOOL are listed.

5.3 Layout of the new beam line

The place where ISCOOL will be installed at ISOLDE was determined by space constraints at the facility. The most feasible location to install ISCOOL was the beam line section just after the HRS separator (see Fig. 5.1). The space available (length of the beam line, height of the ceiling and walls surrounding the beam line) makes the project of the installation of ISCOOL really challenging.

To check out the feasibility of the installation of ISCOOL in this beam line section, firstly the length of the main components of the new beam line was verified. This investigation has taken into account the following lengths: the main vacuum chamber placing ISCOOL, the high voltage insulators at both sides of the chamber, the cross pieces for the turbomolecular pumps, the injection and extraction quadrupole triplets, bellows to assure all the components can be set up and dismantled and absorb misalignments. Figure 5.6 compares the layout of the existing beam line with the simulated layout of the new beam line. The main parts are marked in the figure.

Figure 5.2 shows an scheme of the main components of the designed beam line which substitute the old beam section. In the existing beam line section there are two standard ISOLDE diagnostic boxes, one around the focal point after the HRS and one just before the merging switchyard. For the purposes of this project, these devices could serve quite well for the on-line operation of ISCOOL. If other diagnostic devices are required to measure properties that are not beam intensity or profile, the flanges of two cross pieces (6 each one) might be used.

ISCOOL could not be so interesting for use with light ion beams, e.g. helium or lithium RIB's. The reason is that the cooling ability of the RFQCB's is determined by the mass of the buffer gas atoms or molecules which has to be smaller than the ions to be cooled. The heavier the ions of the beam, the more efficient the cooling (see Sec. 4.1). This situation has been foreseen in the design of the new beam line. The design allows ISCOOL to be removed and to replace it for a straight beam line pipe. In this situation, see Fig. 5.3, the line is only pumped down with the turbomolecular pump at the injection side of ISCOOL. The transport of the beam from the HRS to the switchyard is assured by the two quadrupole triplets.

With these parameters, a three-dimensional design of the components composing the beam line was done (see Fig. 5.4). A high voltage cage will be installed to enclose all the area and restrict the access during the operation. The wall has to protect people from outside against high voltage. Nevertheless it has to permit as well an easy access to the area for maintenance or removal operations, like breakdown of electronic components of the high voltage area, gas bottle change, move of the trolley or disconnection of the vacuum system from the recovery lines. Figure 5.5 pictures a half section of all the beam line and enumerates the main components.

5.4 Transport optics

The best solution for the transport of the beam line through the new beam line was to use two quadrupole triplets, one before ISCOOL, the *injection quadrupole triplet*, and another after ISCOOL, the *extraction quadrupole triplet*. They are in charge of:

- The transport of the RIB from the HRS to the merging switchyard without any losses in case ISCOOL is removed from the new beam line and substituted by an empty drift tube.

- Injecting efficiently the beam from HRS into the RFQCB (injection quadrupole triplet) and guiding the cooled and/or bunched ions to the merging switchyard of the two ISOLDE mass separators (extraction quadrupole triplet).

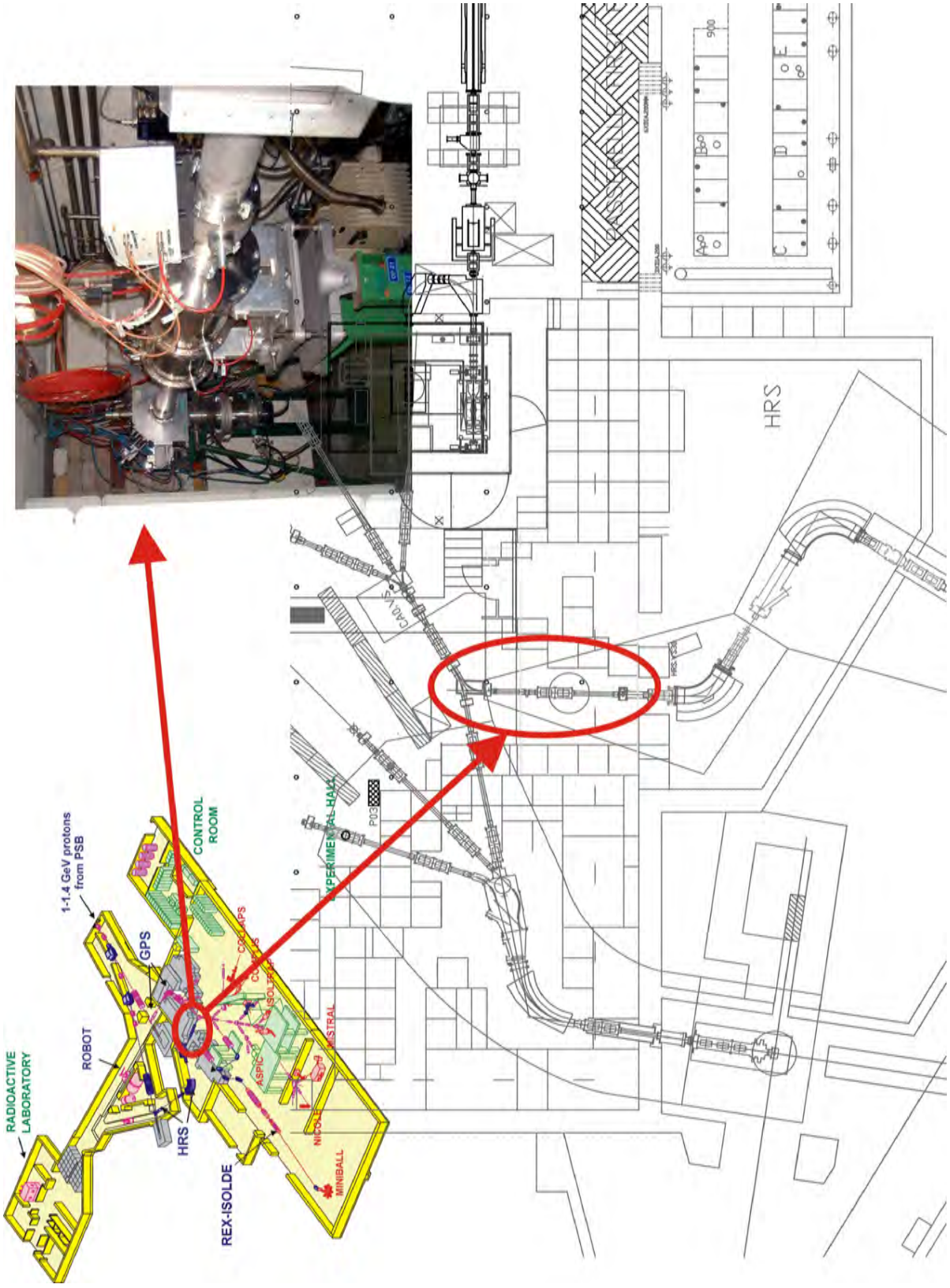

Figure 5.1: Scheme of the existing beam line section from end of the HRS to the merging switchyard: at a global view of the ISOLDE facility (*top left*), a picture (*top right*) and at a layout of the HRS separator (*bottom*). This section will be removed to install the new ISCOOL in this position.

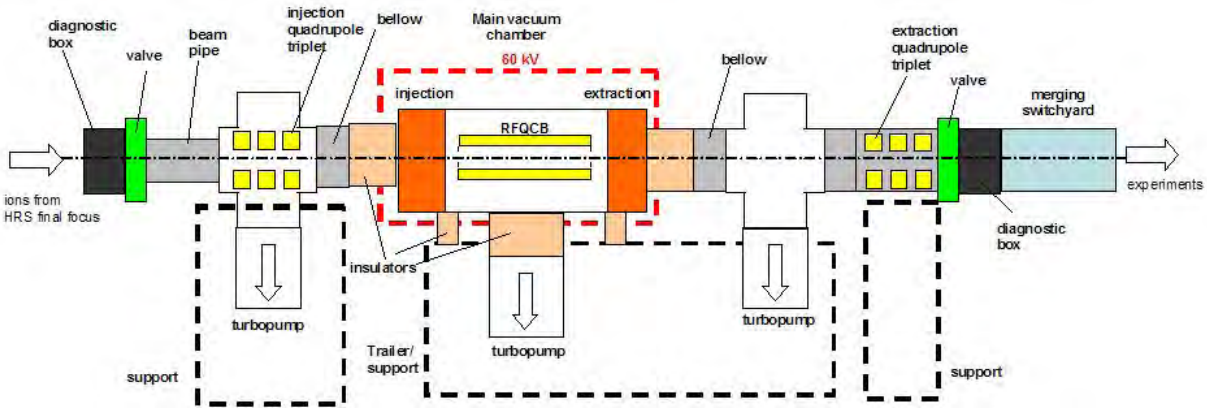

Figure 5.2: Scheme of the main components of the new beam line (not to scale).

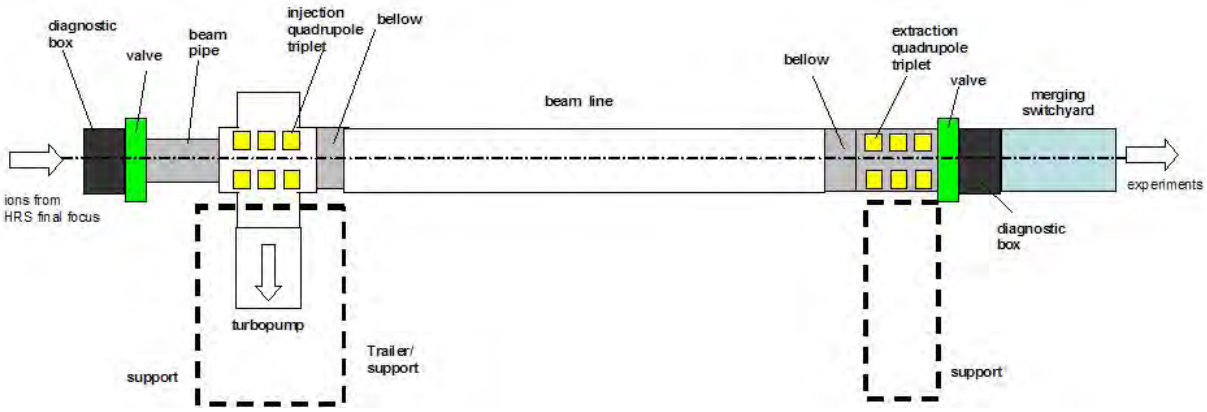

Figure 5.3: Scheme of the main components of the new beam line without ISCOOL (not to scale).

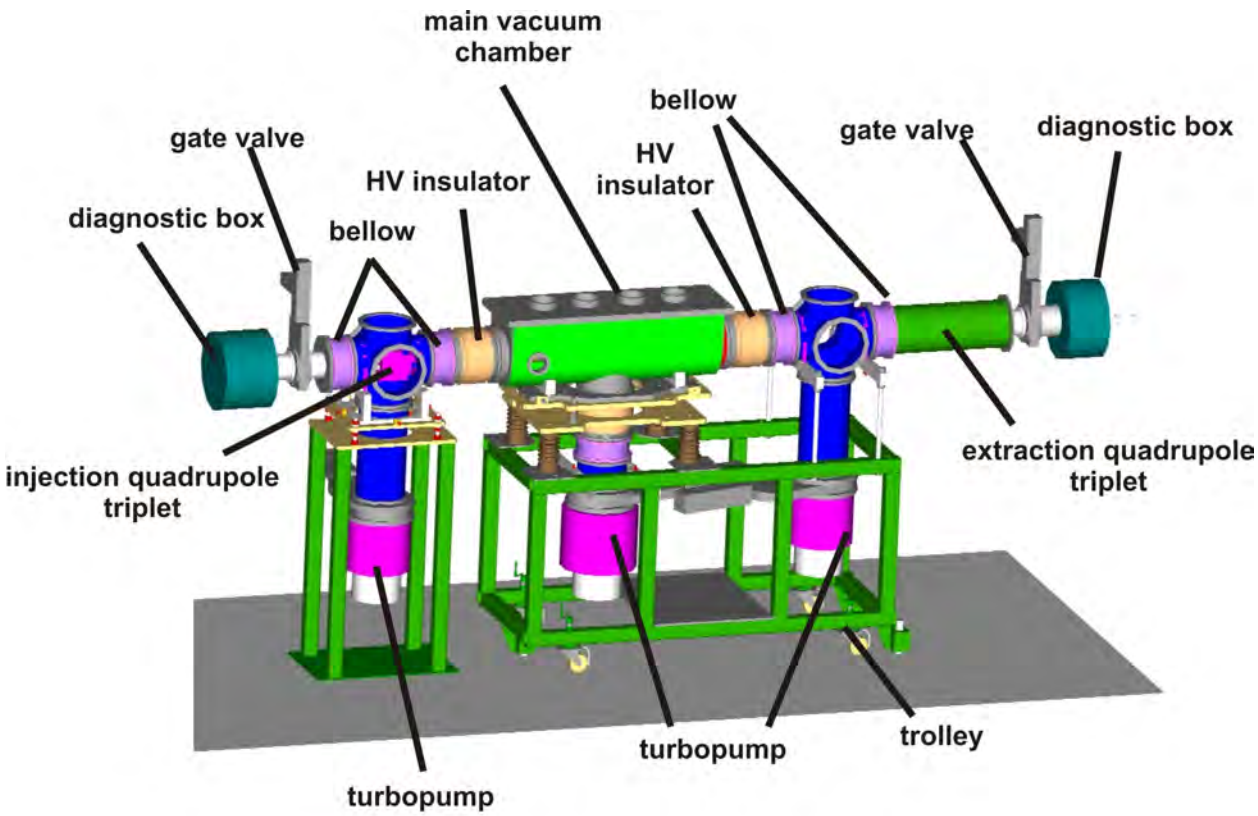

Figure 5.4: 3D design of the new ISCOOL beam line. The main components are identified.

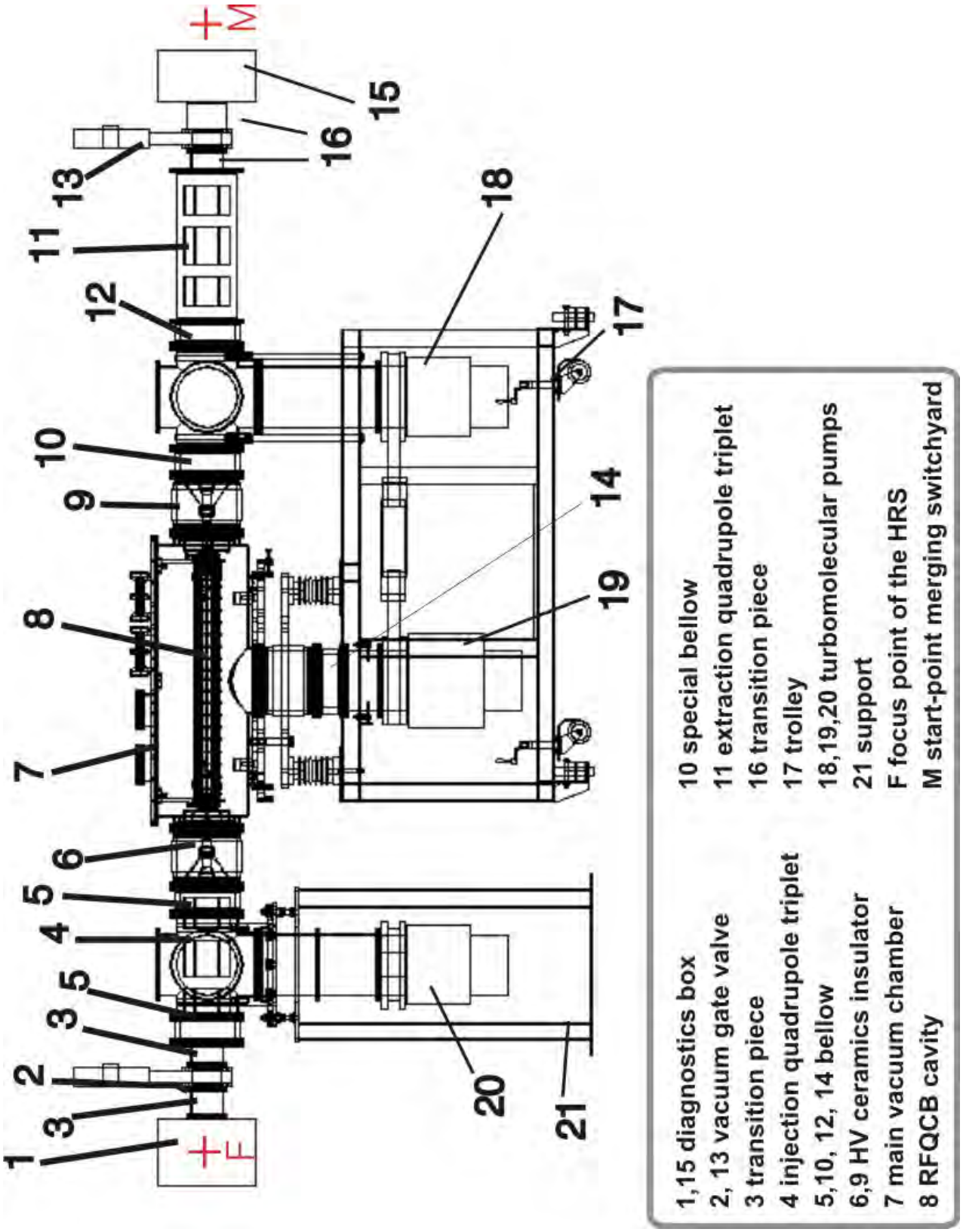

Figure 5.5: Section of the beam line (to scale). All the optical components and the main parts of the new beam line are shown.

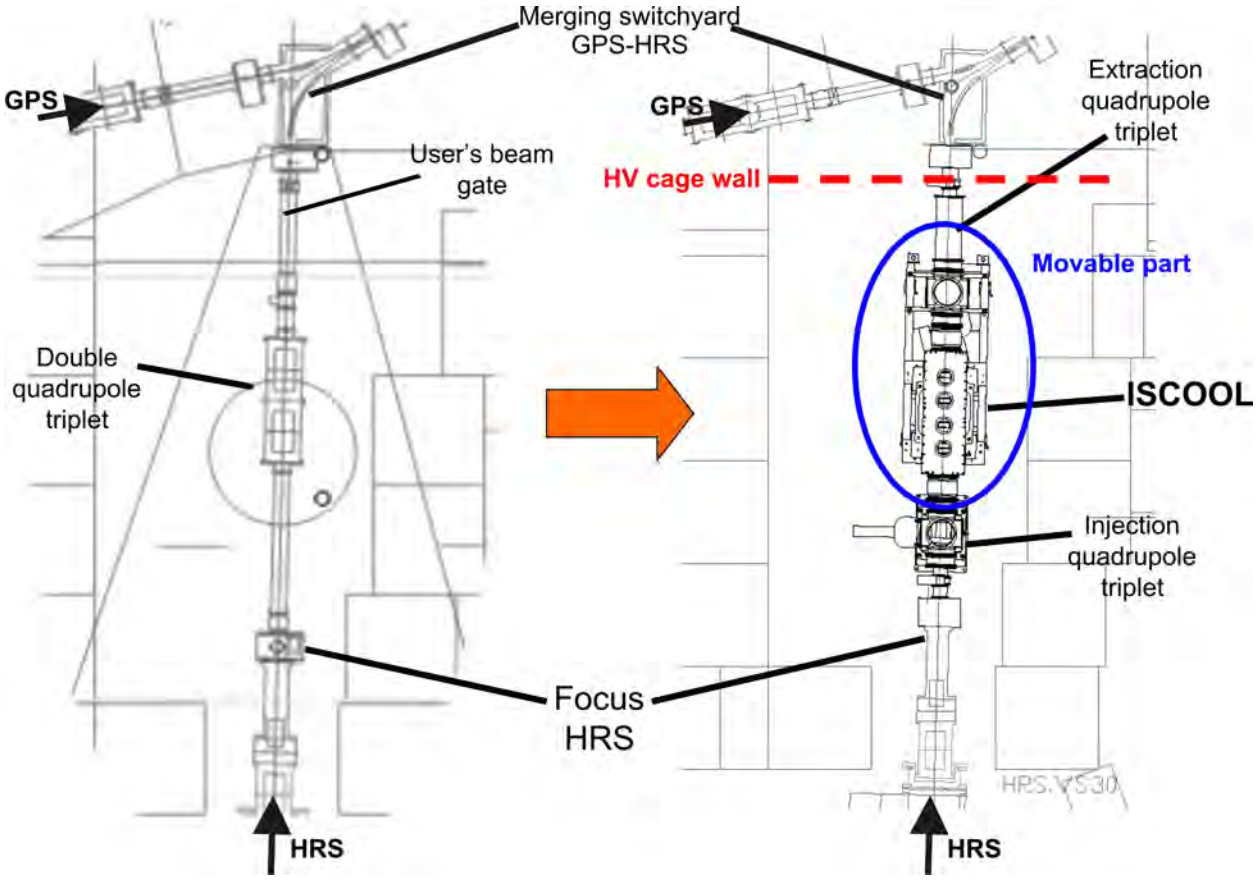

Figure 5.6: Comparative between the existing beam line and the new ISCOOL beam line.

Measurement points	Distances [mm]
Focus point of the HRS- Beginning injection quadrupole triplet	440
End injection quadrupole triplet- Beginning RFQCB chamber	318
End ISCOOL injection optics- Beginning extraction quadrupole triplet	∼600
End extraction quadrupole triplet- Beginning merging switchyard	∼650

Table 5.2: Optical distances between the main elements of the new beam line.

Length of the first quadrupole	100 mm
Distance first-second quadrupole	40 mm
Length of second quadrupole	120 mm
Distance second-third quadrupole	40 mm
Length of third quadrupole	100 mm
Total length	400 mm
Inner radius	35 mm
Voltages applied	<5 kV

Table 5.3: Specifications of the injection and extraction quadrupole triplets of the new beam line.

When the RFQCB is installed, the injection quadrupole serves to focus the aberrate beam coming from the HRS into the RFQCB, and the extraction quadrupole corrects the beam exiting the trap in case it is a bit divergent and focuses into the merging switchyard for further transport to to the experiments.

If the RFQCB is not installed, the ion beam does not need focusing into the RFQCB but in the extraction quadrupole. For this reason, the acceptance of the second quadrupole has to be very similar to the injection quadrupole.

Changes in the focusing of the quadrupoles are done by varying the voltages applied to the triplet (see Sec. 2.1.1). Table 5.2 shows the beam distances and Tab. 5.3 the specifications of the designed quadrupoles after calculations for the quadrupoles [Fri] and for the injection into ISCOOL [Ero02].

5.5 Design of ISCOOL: the general purpose ISOLDE RFQCB

The design of an RFQCB is a complex process including several physics and technical topics. The design process of such a device follows an scheme as in Fig. 5.7 divided into three main phases:

- Physics requirements. In a first phase an study of the implementation of the RFQCB has to be done. The physics of the device and the specifications of the RIB of the facility will give the technical specifications of the device. The main parameters will be the maximum injected emittance and the longitudinal energy of the RIB.

- Optics-vacuum compromise. The value of the transverse emittance of the incoming beam determines the *acceptance*. The design of the optics will influence the vacuum system, in particular the differential pumping. A compromise has to be found between the necessity of increasing as much as possible the acceptance of the device and having the lower pressure outside the RFQCB chamber.

- Technology constraints. Once the optics has been fixed, the design of all the other systems can start: mechanics, vacuum, electronics and control. All these systems, but most particularly the mechanical one, might modify the optics design, so a feedback between the mechanical system and the optics and vacuum systems has to be found.

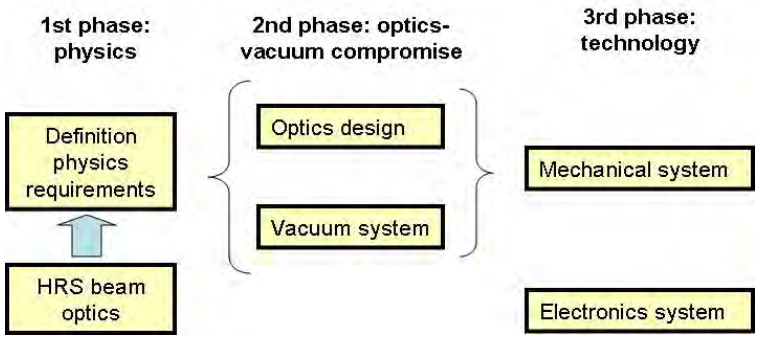

Figure 5.7: Scheme of the procedure for the design of an RFQCB

Chapter 6

Optics system of ISCOOL

The design of a good optics system is one of the most important topics in the general design of an RFQCB. The fact that ISCOOL is working at a nominal high voltage of 60 keV is a challenge due to the beam losses and the possible blow-up of the beam during the acceleration. Therefore the design of the deceleration from this HV and injection into the RFQCB, and the extraction and re-acceleration to the nominal HV need to be carefully simulated. These parts have to assure an efficient transmission of different types of RIB's, to avoid losses during all the stages. First, a conceptual study was carried out following the theory and the experience of other devices. Later the optical design of all the parts was optimized using SIMION [Dah00], a ray-tracing code for three-dimensional simulation of the ion motion. The data obtained in the simulations were analyzed using a GUI (Graphical User Interface) developed in MATLAB. The design of the optics is constrained by the requirements of the mechanical manufacturing and assembly. Due to this limitation, the shapes of the real electrodes were simplified for comparison with the previous results.

In the following all the optics design will be reported and discussed.

6.1 Optical structure

As all the RFQCB devices, ISCOOL can be divided concerning the optical structure, as seen in Sec. 4.1, in the following parts:

- **Injection (deceleration) part**. It contains the electrodes to decelerate the ions from the ISOLDE ion beam energy (≤ 60 keV) down to the injection energy into the RFQCB (around ~ 100 eV). The beam is injected in the cavity through the injection plate (as explained in next section).

- **Accumulation and bunching part**. This part consists of the electrodes of the RFQCB chamber. It encloses the buffer gas and the RF electrodes. It can be divided into two parts: the first half of the RFQCB chamber is devoted to confining efficiently the injected beam and to cooling it progressively with the buffer gas. In the last part, pulsed axial electrodes create a potential well in the longitudinal direction to confine the beam and create the bunches, which are then released from the RFQCB chamber through the extraction plate.

- **Extraction (acceleration) part**. It contains the electrodes that makes the ion beam to accelerate from the thermal energy of the ions cooled and trap inside the RFQCB chamber up to

the ISOLDE ion beam nominal energy that the ions had before the injection into ISCOOL (≤ 60 keV).

6.2 Deceleration and injection

The principle of deceleration and injection of an ISOLDE RIB into ISCOOL is based on a ground electrode in which the ground potential is defined, and two electrodes with potentials intended to progressively stop and focus the beam into the RFQCB chamber. In the case of ISCOOL the injection is quite delicate since the beam coming from the HRS, at a typical energy of 60 keV, has to be injected without losses into the RFQCB. To maximize the efficiency in all the situations (different kinds of beams at various high voltages), a combination of a quadrupole triplet and three deceleration electrodes is used. The quadrupole triplet allows the focus of the beam to be placed in a region around the injection hole of the RFQCB.

Afterwards, the convergent beam can be efficiently focused into the RFQCB chamber thanks to the ground electrode and the two potential electrodes placed just before the RFQCB injection plate. The first sketch of the injection system can be seen in Fig. 8.20 (as detailed in [Ero02]). Reference voltages used in the simulations are given in Tab. 6.1.

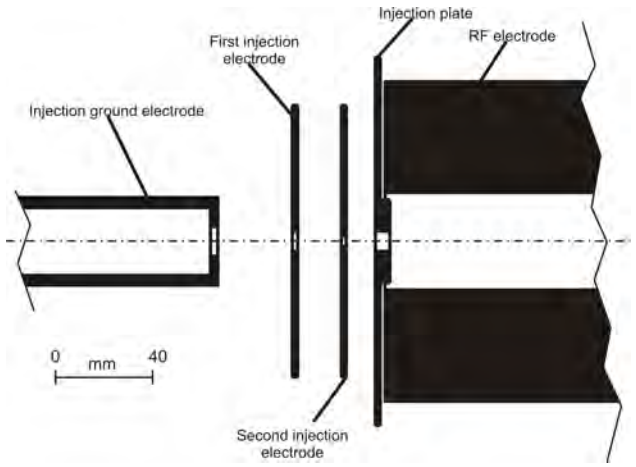

Figure 6.1: Sketch of the first injection optics design

The optical properties of the incoming RIB can vary depending on different parameters as the target, the element chosen in the mass separator or the longitudinal beam energy of operation. One of the worst cases of RIB's coming to ISCOOL can be seen in Fig. 6.2. The figure shows a phase space plot of a beam just after the HRS separator. Clearly one can see the huge size of the beam (around 10 mm of transverse size), due mainly to the presence of isobaric contamination of N_2^+ ions (right peak) in the CO^+ ion beam (left peak).

The simulations concluded that the most suitable voltages for a good injection efficiency were those listed in Tab. 6.1. The voltage of the injection plate is set by the injection energy of the ions into the RFQCB. For the calculations the injection energy is supposed to be about 100 eV. The voltage of the injection plate V_{ip} is then set according to the expression,

$$V_{ip} = V_{HV} - V_{ion} \tag{6.1}$$

where V_{HV} is the high voltage value and V_{ion} the injection energy of the singly-charged ions into ISCOOL in the potential form.

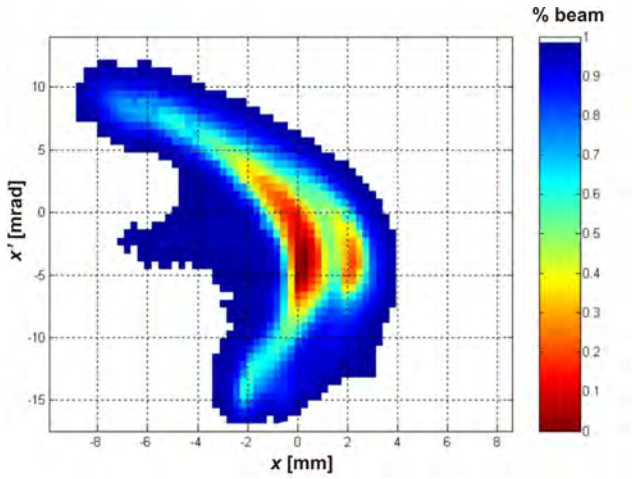

Figure 6.2: Plot of the transverse phase space at 60 keV of a beam from the HRS (from [Fri]). The beam contains two different isobars: CO (left peak) and N_2 (right peak).

Electrode	Voltage [V]
1st extraction electrode	54000
2nd extraction electrode	55000
Injection plate	59800-59900

Table 6.1: Optimized voltages for the injection electrodes based on the data from [Ero02].

6.3 Cooling and bunching

Inside the RFQCB chamber, the RIB is first cooled along the axis and thereafter trapped and bunched. The first process, the cooling, has been explained in Sec. 4.1. According to the features of the HRS beam, with a maximum energy of 60 keV, the necessary cooling length of the structure was simulated in the first phase of the project [Pet02b]. The first step was to choose the minimum distance between the RF electrodes r_0. It is a bit larger than in previous devices (Tab. 4.1) to have a better acceptance and manage the large emittances of the HRS beams. The final value was fixed to $r_0 = 20$ mm. The simulations were done using SIMION. An algorithm was implemented for the buffer gas simulation based in a Monte Carlo code [Pet02b]. Thanks to the results obtained with this code, the length of the RFQCB chamber was worked out (see Fig. 6.3). It is clear that the cooling distance is bigger for heavy ions than for light ions. For buffer gas pressures above 0.05 mbar and an injection energy of the ions below 200 eV the maximum cooling distance required is around 0.5 m. For smaller injection energies or higher pressures the cooling distance would decrease. According to these calculations, the final length chosen for the cooling region was 600 mm. That allows an optimization of the RFQCB parameters (buffer gas pressure and voltage of the injection plate). The last 200 mm of the RFQCB chamber are left for bunching the beam. Hence the **total length** of the chamber is around 800 mm.

As mentioned in Sec. 4.1, once all the ions of the beam are thermalized with the buffer gas, the ions are cooled down near to the temperature of the latter. The beam looks symmetrical in both phase spaces. Figure 6.4 shows a simulation of the normalized transverse emittance of a thermalized beam. In the right figure, an small axial field which guides the beam is added. Section 4.1 described how the axial field acts as a defocusing mechanism and it can be confirmed in the

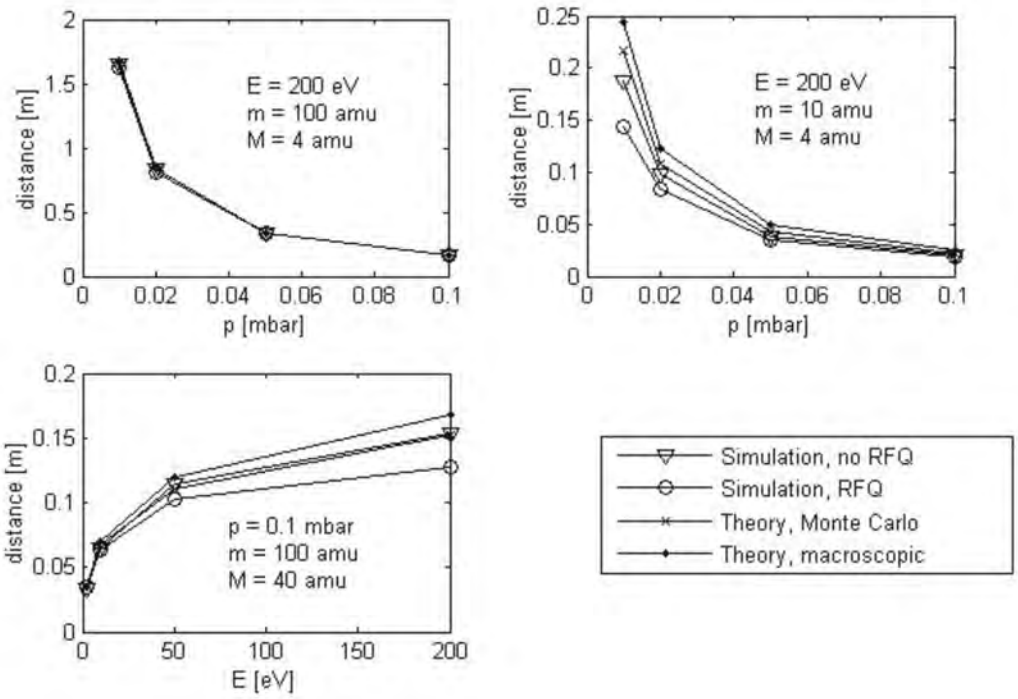

Figure 6.3: Cooling distance of the ions as a function of the helium buffer gas pressure: at injection energy of 200 eV and heavy ions 100 u (*top left*) or light ions (*top right*), and as a function of the injection energy for heavy ions (*bottom left*) [Pet02b].

bigger emittance value, as shown in the figure. Therefore the value of the emittance is bigger if higher components of the axial field are created. The other point is that the guiding axial field helps to decrease the cooling time. During the operation of ISCOOL, the axial field set will influence the efficiency, rapidity and quality of the system, as discussed later on.

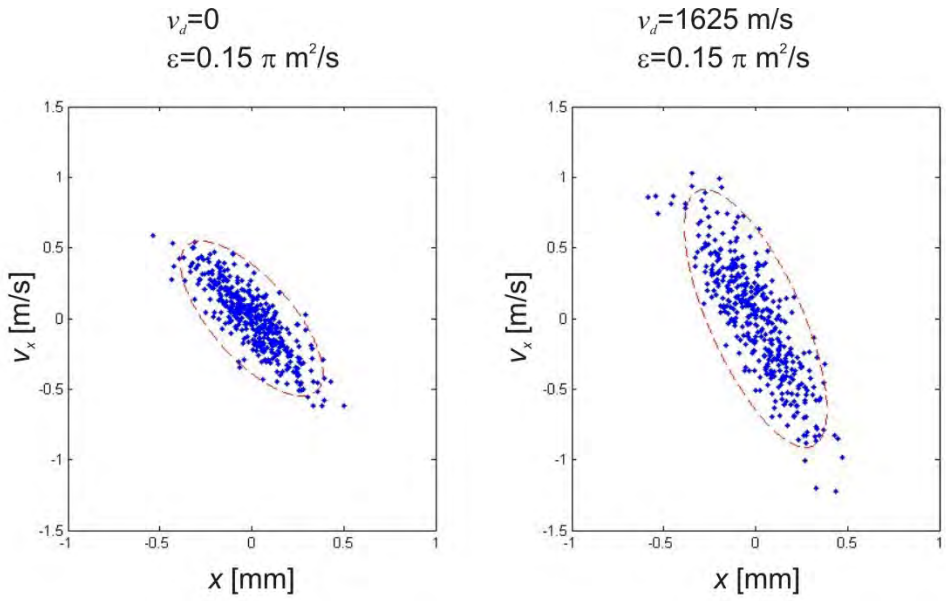

Figure 6.4: Action diagrams for an ion beam in thermal equilibrium with the buffer gas. *Right plot* corresponds to the same beam of the *left plot* but with a longitudinal (drift) velocity component v_d given by an axial electric field [Pet02b]. The normalised beam emittance is calculated for both examples.

6.3.1 The RF field

While cooling and bunching, to assure that the ions are not lost inside ISCOOL and their motion is stable, it is necessary to use the correct values for the frequency and amplitude of the radio frequency electric field of the quadrupole rods (f_{RF},U_{RF}). The idea is to calculate the q value (Eq. 4.11) and to check out if it is within the stability region (from 0 to 0.91). A value around 0.5 is normally fixed in these devices to assure the stability in both transverse motions (see operation values of existing RFQCB's in [Her01],[NCB$^+$02], [Rod03] or [Lun04]. Table 6.2 shows the calculated f_{RF} and U_{RF} to obtain $q = 0.5$.

It is clear from Tab. 6.2 that the amplitude values of the RF electric field are inside the safe region, and they will not cause electrical breakdowns. The operation frequency is similar to that from other devices.

6.3.2 Pseudopotential well

The pseudopotential well (see Sec. 4.1) in ISCOOL is defined by the parameters of the RF electric field applied (see Eq. 4.39). Table 6.2 details the different values obtained for different ion masses. For the calculations the q value was fixed to 0.5. Figure 6.5 shows that, for the design parameters in Table 6.2, the transverse confinement for heavy ions inside ISCOOL is slightly larger than for light ions. Better confinements could be obtained by increasing the voltage amplitude of the RF

m [u]	f_{RF} [MHz]	U_{RF} (0-peak) [V]	q	D [eV]
10	0.80	130	0.50	16.13
20	0.60	147.5	0.50	18.46
50	0.42	180	0.50	22.44
100	0.30	185	0.50	23.23
120	0.28	192.5	0.50	24.07
140	0.26	192.5	0.50	23.92
160	0.24	190	0.50	23.93
180	0.22	180	0.50	22.72
200	0.21	180	0.50	22.44
220	0.21	200	0.50	25.19
240	0.20	195	0.50	24.20
250	0.20	200	0.49	24.44

Table 6.2: Calculated values of the frequency f_{RF} and amplitude zero-to-peak U_{RF} of the RF electric field applied for a $q = 0.5$ for different ions of mass m. The transverse pseudopotential D for each ion is also calculated.

electric field. That would mean that the RF frequency should be increased as the square ratio of the voltage to maintain the q value constant.

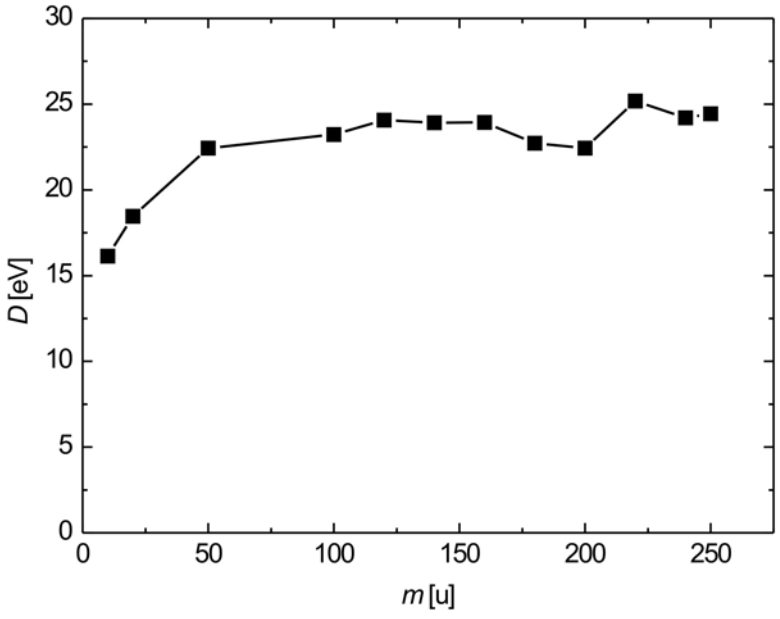

Figure 6.5: Plot of the transverse pseudopotential well D (without axial field applied) in ISCOOL as function of the mass of the ions confined m.

Through the injection plate, the maximum transverse energy E_t of an RIB with a transverse non-normalized emittance $\epsilon_{geom} \leq 40\pi$ mm·mrad, at a total potential energy E_L around 60 keV (13.6 mm$^2/\mu$s normalized emittance) and a diameter of the hole in the injection plate of the

RFQCB chamber d_{inj} of 8 mm is given by the following expression:

$$E_t \cong \left(\frac{2 \cdot 10^{-3} \epsilon_{geom}}{\pi d_{inj}}\right)^2 E_L, \tag{6.2}$$

where ϵ_{geom} is the value of the emittance before deceleration and expressed in mm·mrad and d_{inj} in mm. which is derived from the relation between the area of the non-normalized emittance at the injection plate ϵ_2:

$$\epsilon_2 = \pi \cdot x_{max} x'_{max}. \tag{6.3}$$

At the entrance of the injection hole to ISCOOL, x_{max} will represent the maximum size of the decelerated beam, which is constrained by the size of the hole $x_{max} = d_{inj}/2$, and x'_{max} (in mrad) reads:

$$x'_{max} \cong \sin x'_{max} = 1000 \cdot \frac{v_t}{v_2} \tag{6.4}$$

where v_t is the transverse velocity of the ion at the injection plate and v_2 represents the total velocity for the (decelerated) injected ions. Therefore x'_{max} is in terms of energy:

$$x'_{max} \cong 1000 \cdot \sqrt{\frac{E_t}{E_2}}, \tag{6.5}$$

where E_2 is the total kinetical energy of the ions at the injection plate. As $\epsilon_2 = \epsilon_{geom}\sqrt{\frac{E_L}{E_2}}$, it yields Eq. 6.2. For the data given before, Eq. 6.2 gives a maximum transverse energy of the ions around 6 eV, where applying the rule of thumbs (see [Moo88]) according to which:

$$D \approx 10 E_t \tag{6.6}$$

represents a value which is 3 times smaller than the potential well for ISCOOL for 1^+ ions and it is independent of the mass of the RIB. In addition the value used as input emittance for the incoming ISOLDE RIB from HRS is a top limit. For typical ion sources, the values are around $10 - 15\pi$mm·mrad at 60 keV [GCF$^+$03, WLL03]. Hence the pseudopotential would allow the diameter of the injection hole to be slightly decreased. In Fig. 6.6 is displayed the study of the minimum hole which would be possible for different optics quality of the incoming RIB from the HRS. It is clear that the limit will be placed around an injection hole diameter of 5 mm for the worst case, and 3 mm for a beam with good optics quality. Anyway the diameter depends also on the transmission efficiency at the injection part. A small diameter in the injection plate would cut a great percentage of the beam due to the small diameter of the second injection electrode does not allow all the incoming beam to be focused properly (see Sec. 6.2).

6.3.3 Axial electric field

The axial electric field along the axis of the RFQCB is supplied by the so-called *axial electrodes*. A more detailed description of these electrodes can be found in [Pod04a] and in Sec. 8.1.1. Firstly, the axial electrodes where designed as depth-variable, stacked four wedges around the quadrupole rods similar to the design proposed in [LKL$^+$00]. Each electrode is made of four *wedges* which enter into the RFQCB chamber in the empty regions left by the quadrupole electrodes. Applying different potentials to each of these electrodes, the axial electric field demanded is created. According to [LKL$^+$00], the potential created in the axis of the quadrupole U_a varies along the longitudinal axis z, following the relationship:

$$U_a(z) = \alpha(z) U_f + \beta(z) U_{DC} \tag{6.7}$$

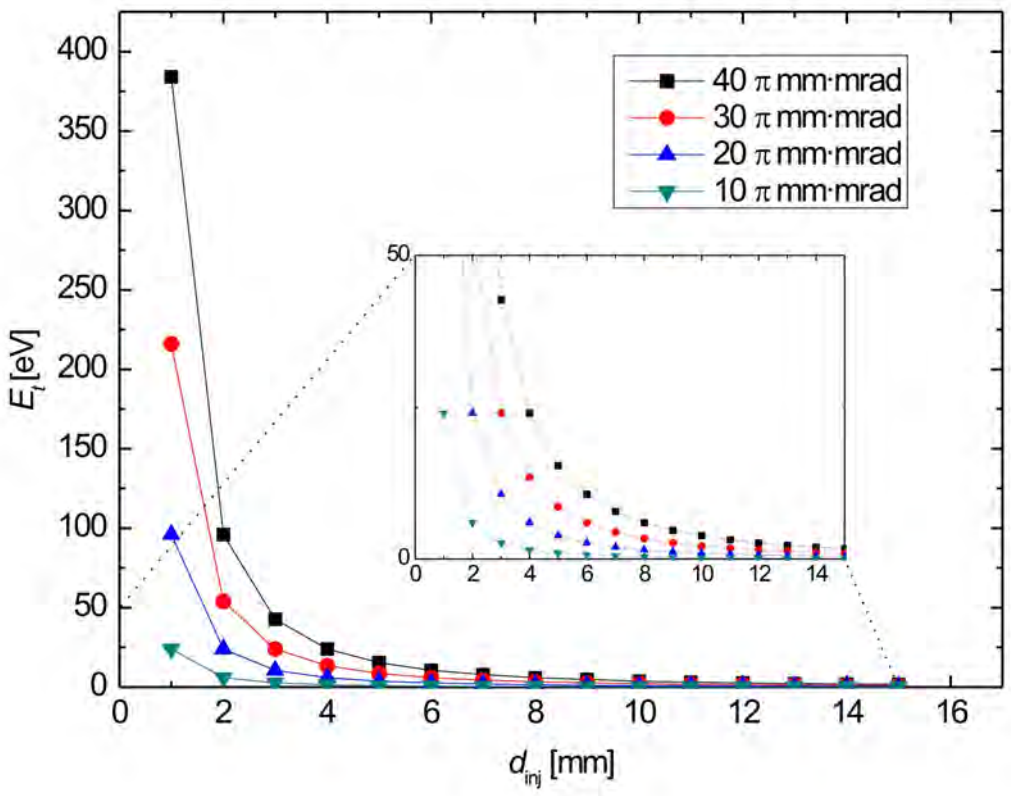

Figure 6.6: Plot of the transverse energy E_t of the injected ions in ISCOOL for different incoming beam emittances as a function of the diameter of the hole of the injection plate d_{inj}. E_t is calculated following Eq. 6.2. The right figure zoomed the important region for the study.

where U_f is the bias voltage applied to the quadrupole rods (see Sec. 4.1), and the parameters α and β depend on the geometry of both the quadrupole rods and the axial electrodes. U_{DC} is the voltage supplied by the power converters to the axial electrodes. At ISCOOL, $U_f = 0$ so only the second term is taken into account. The most important parameter is then the function $\beta(z)$ which depends basically on the length of the four wedges of the axial electrodes and the length of the electrode. The potential to be supplied to a certain axial electrode i can be defined as $U_L(i)$. The wedges have to be long enough to minimize the value of all the supplied potentials $i = 1, .., n$ (for n axial electrodes), which is required to create an axial field U_a along the axis. It is important that this field does not disturb the RF electric field created by the quadrupole rods.

The configuration of these electrodes could be mechanically simplified if only depth-variable segmented cylindrical electrodes (without wedges) were placed around the quadrupole rods. But U_L (the real potential supplied to each electrode) would increase dramatically with that geometry. The simulations tried to evaluate the value of the voltages U_L to generate an axial electric field of 0.1 V/cm ($\Delta U_a = 0.8$ V along the structure). The values cannot be too high in order to avoid:

- **Electrical breakdowns between the electrodes**. The distance between the electrodes is only of 1 mm. In vacuum, as a general design rule, a separation of 1 mm/kV is applied. In this case the potentials were in order of tens of kV but as the working pressure (around 0.1 mbar) cannot be considered as high vacuum but medium vacuum, care has to be taken with this parameter to avoid electrical breakdowns inside the RFQCB chamber. More information about the breakdown process in low pressure helium gas can be found elsewhere [JMM53, HR74, PHR00, Gia02] where an experimental RFQ was constructed for analyzing the use of high electric fields in these devices. Further discussion about this topic is given later in Chapter 8.

- **Power supplies requirements too high**. Obviously, the cost of the power supplies increases with the voltage to be supplied to the electrodes. In addition, the precision and stability of the power supplies is more difficult to obtain if the range of the amplitude of the voltages applied is overestimated. Therefore, minimizing U_L is an important factor in structures as big as ISCOOL, which will be the largest RFQCB set-up up to date. The discussion about the electronic components is followed-up in Sec. 9.1.

In the standard configuration of ISCOOL, there are 25 axial electrodes along the quadrupole structure. The number of axial electrodes can be changed but the total length of the RFQCB chamber is preserved. The normal configuration of these electrodes is to have small depth electrodes near the injection and extraction sides. The reason is to have more freedom in the control of the gradient of the electric field in these parts. Whereas in the center region the axial electric field is approximately constant, at injection it needs a better control to maximize the entering of the ions. A better control is also needed in the extraction to release the bunched or the continuous beam after trapping.

With SIMION different values of the axial electric field inside ISCOOL were simulated. In Figure 6.7 is plotted the value of the electric field exerted over an ion, the reference value in this case is around 1 V/cm. The plot only represents the last 20 cm of the RFQCB chamber at the extraction part of ISCOOL. The strange shape of the curve in the last part is due to the effect of the potential well allocated in this region that causes the ions to go back and forth until the potential is decreased and the ions permitted to be extracted from the RFQCB. The value of the axial field increases for the extraction but not too much to avoid blowing up the normalized emittance during the re-acceleration of the beam.

Figure 6.8 shows the sketch of the electrodes used for study the axial field with SIMION. The 25 axial electrodes (SIMION is limited to 30) are placed with the real lengths. The simulation is

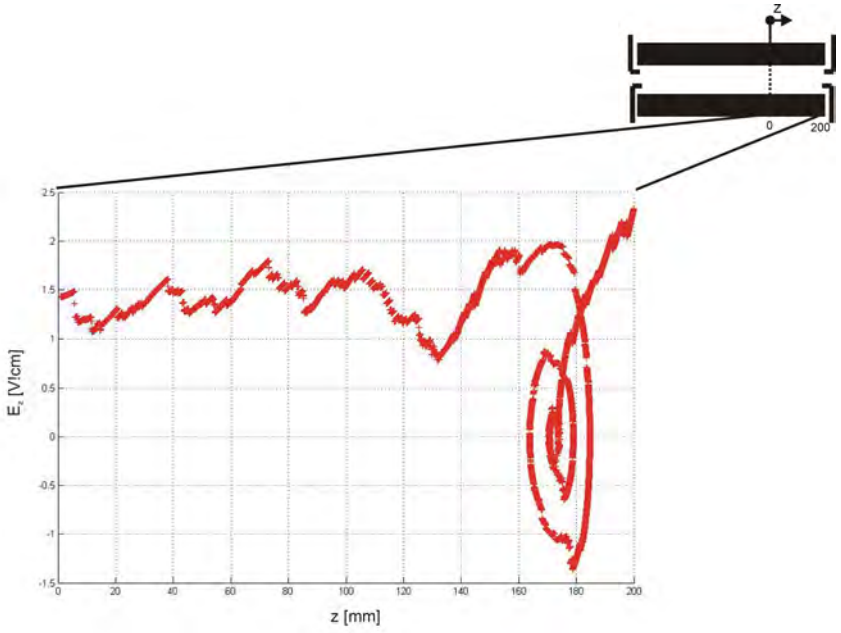

Figure 6.7: Plot of the value of the axial electric field for the flight of an ion along the axis of the RFQCB (only last 20 cm of the flight along ISCOOL are shown).

simplified by removing the RF electrodes and the injection and extraction plates. The figure shows the axial field in the optic axis for a difference potential of 5 V between each electrode. A constant value of 0.1 V/cm is obtained in the center region (see Fig. 6.9). If the value is decreased to 1 V between electrodes, the field strength is about 0.01 V/mm, which fits with the axial field values used in similar devices [NCB$^+$02]. In the injection and extraction regions the values are higher due to the smaller dimensions of the electrodes and the presence of fringe fields.

6.4 Extraction and re-acceleration

The optics system, which extracts and accelerates the beam back to the same energy as that of the injected beam, is based on a similar layout as the deceleration and injection system.

The layout can be seen in Fig. 6.10. The beam is extracted from the RFQCB through the extraction plate and is guided with a small acceleration to the first acceleration electrode. Once the beam passes through this electrode, it is strongly accelerated using a cone-shape electrode. Its mixed shape, conical in the beginning and cylindrical afterwards, provides a better control of the focusing of the beam. Finally, a ground electrode provides the final acceleration of the beam up to the ISOLDE beam energy. The final extraction energy of the beam E_{fe} will be given by:

$$E_{fe} = QV_{HV} \tag{6.8}$$

where Q is the charge state of the ions of the beam (normally 1^+) and V_{HV} the high voltage at the ISCOOL platform.

The most critical point in the acceleration of the beam is the area between the extraction plate and the first extraction electrode. Besides extracting the beam from the RFQCB chamber and giving the first acceleration, this electrode has a very small hole in order to create a differential pumping between the regions before and after the electrode. The problem comes up in case the

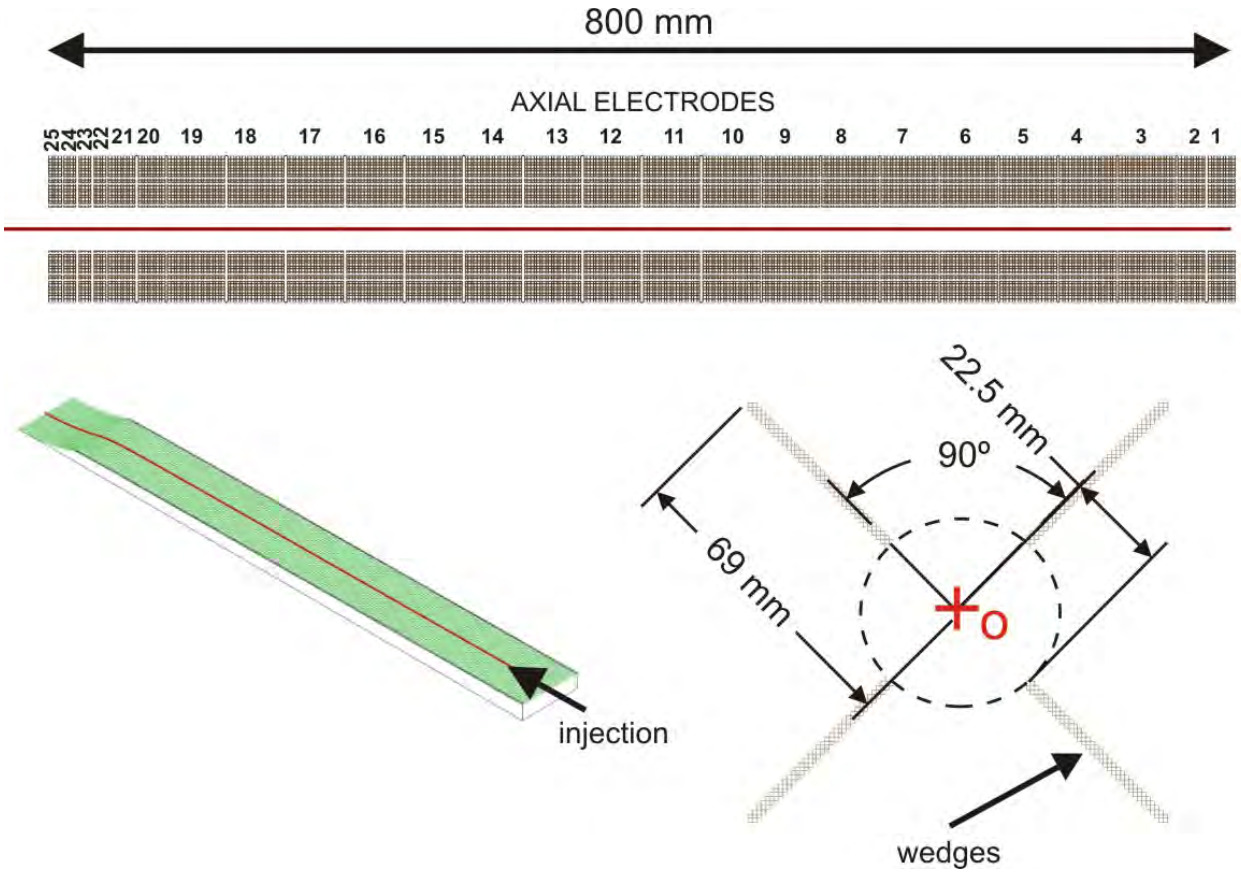

Figure 6.8: Sketch of the axial electrodes used in the SIMION simulations (without RF electrodes and injection and extraction plates). The figure below shows the 3D potential for a positive ion for a difference potential of 5 V applied to consecutive electrodes (from 59900 V applied to the electrode 1).

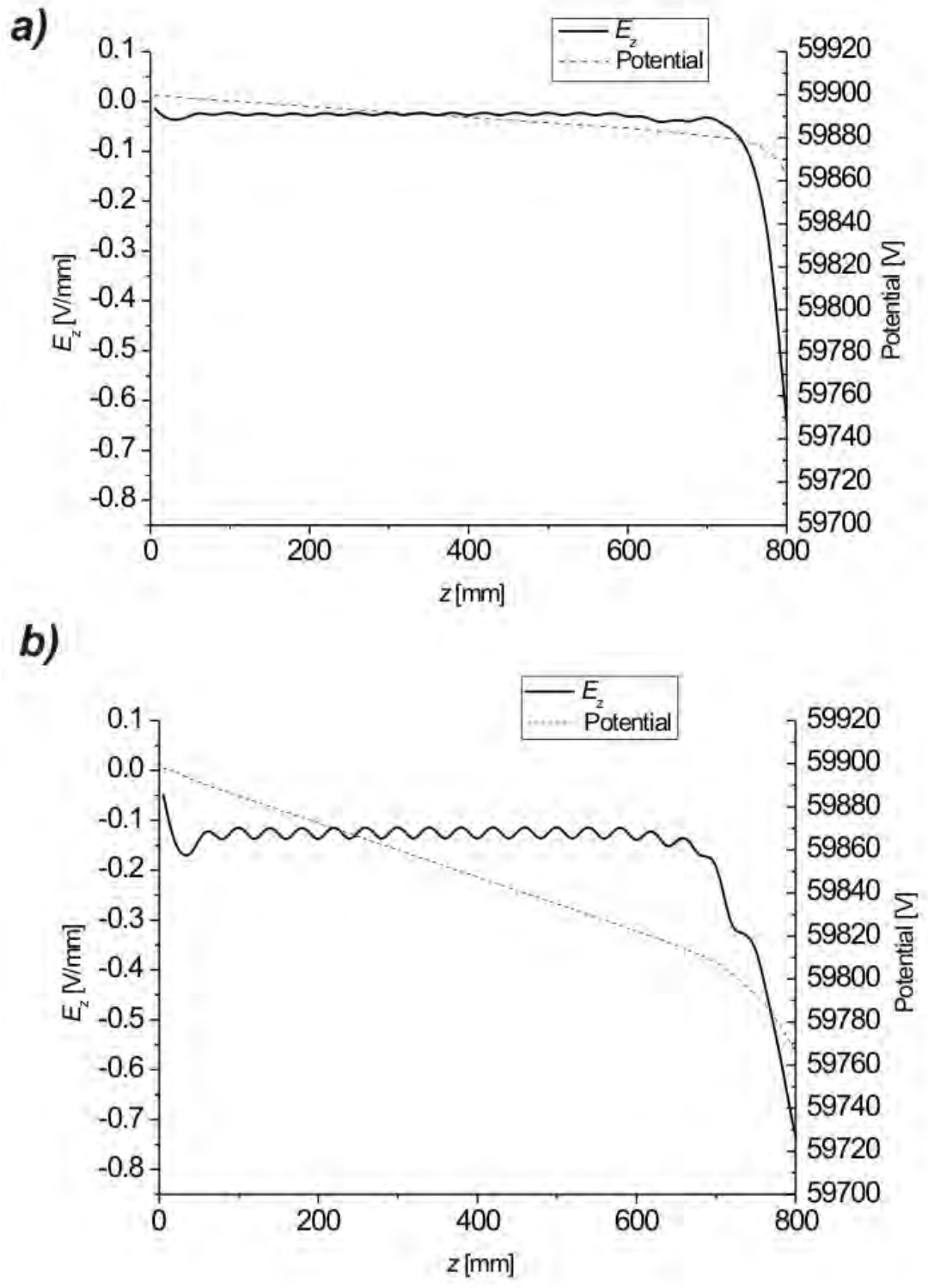

Figure 6.9: Plot of the simulated axial electric field and potential along the axis created by the axial electrodes used in the SIMION simulations (without RF electrodes and injection and extraction plates) according to Fig. 6.8. *a)* 1 V between consecutive electrodes, *b)* 5 V between consecutive electrodes.

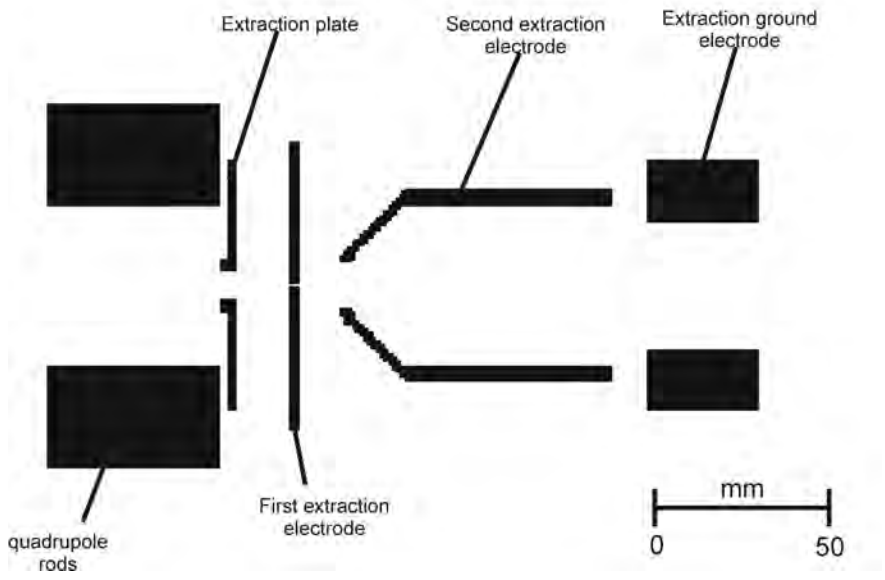

Figure 6.10: Layout of the optics extraction system of ISCOOL.

pressure in this region is too high for the acceleration field. The good optical properties achieved by cooling the beam inside the quadrupole could be partially lost due to undesirable collisions of the accelerated ions with the buffer gas atoms. In addition, the accelerated ions could ionize the gas atoms or molecules, creating beam impurities. However, this could be avoided by trying to pump this region more efficiently: decreasing the pressure, or minimizing the acceleration field applied.

Some simulations were performed in order to optimize the extraction of the beam from the RFQCB. First simulations were done with SIMION in [Pet02b] using a new Monte Carlo code to generate a microscopic gas-ion interaction depending on the gas pressure. Further simulations were concentrated in an optimization of the voltages, distances and diameters of the different extraction electrodes and last electrodes of the RFQCB. Figure 6.11 shows a simulation of cesium ions using the Monte Carlo code cited before and the specifications listed in the figure. The equipotential lines created by the electrodes are represented, and the track of 100 ions are represented in a longitudinal plane (symmetry of the motion). With the potential applied in this simulation, a 100 % efficiency is obtained and the extracted ion beam is small and parallel (small transverse emittance value).

The simulations were later repeated using more realistic electrode shapes (according to the mechanical design). The data obtained were analyzed using a self-made software interface created in MATLAB. An example of results obtained can be observed in Fig. 6.12. If it is compared with Fig. 6.2, it is easy to understand that an improvement in the quality of the optics of the ion beam has been produced. On the other hand, in the transverse action volume, the distribution of the ions looks gaussian in both coordinates (space and velocity).

Looking carefully Fig. 6.12, one can rapidly observe that in the point were the data has been taken the beam is diverging. That means more work should be carried out with the voltages of the extraction electrodes to better focus the beam. The problem comes from the extremely slow computation of the simulations with SIMION. A realistic simulation would require smaller grid size with an expense of reduce computation speed and huge memory capacity, making the calculation and an optimization of the design unfeasible (see for further details [Dah00]) . In addition even with small grids (that means in SIMION to double the ratio grid size/geometry),

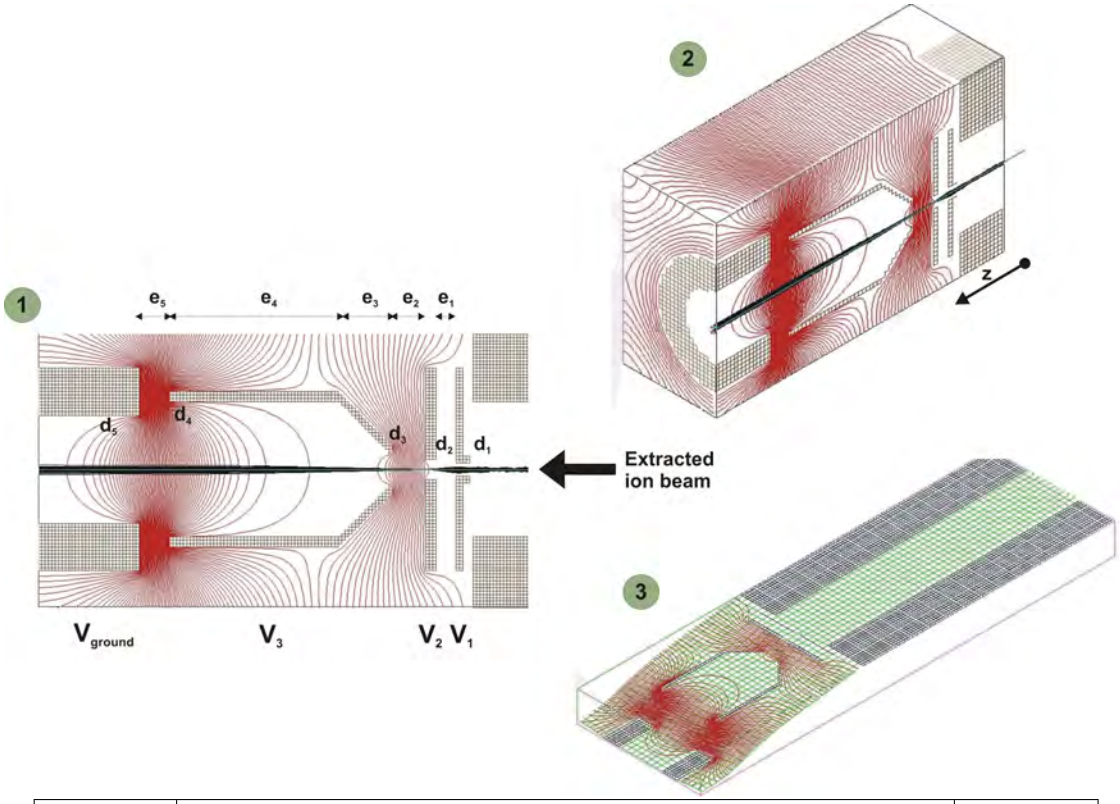

d_1	Diameter extraction plate [mm]	4
d_2	Diameter 1st extraction electrode [mm]	6
d_3	Diameter entry 2nd extraction electrode [mm]	10
d_4	Diameter out 2nd extraction electrode [mm]	40
d_5	Diameter extraction ground electrode [mm]	30
e_1	Distance injection plate-1st extraction electrode [mm]	5
e_2	Distance 1st-2nd extraction electrode [mm]	10
e_3	Length of the cone 2nd extraction electrode [mm]	15
e_4	Length of the cylindric part 2nd extraction electrode [mm]	50
e_5	Distance 2nd-ground extraction electrode [mm]	10
V_1	Voltage injection plate [kV]	60
V_2	Voltage first extraction electrode [kV]	59.935
V_3	Voltage second extraction electrode [kV]	45
V_{ground}	Voltage ground extraction electrode [kV]	0
n	Number ions simulated	100
M	Mass ions simulated [u]	133 (Cs)
m	Mass buffer gas ions [u]	4 (He)
t_{acc}	Accumulation time ions in the trap [ms]	300
t_{bunch}	Space between consecutive bunches [ms]	200
f_{RF}	Frequency of RF electric quadrupolar field [MHz]	1
q	q-Mathieu stability parameter	0.5
P_{RFQCB}	Pressure inside the RFQCB chamber [mbar]	0.1

Figure 6.11: Simulation of the extraction part of ISCOOL for a cesium ion beam: 1) Longitudinal cut, 2) 3D half cut, 3) 3D representation of the electric potential in the moment of the extraction (accumulation potential well not represented). The equipotential lines are represented in all the figures.

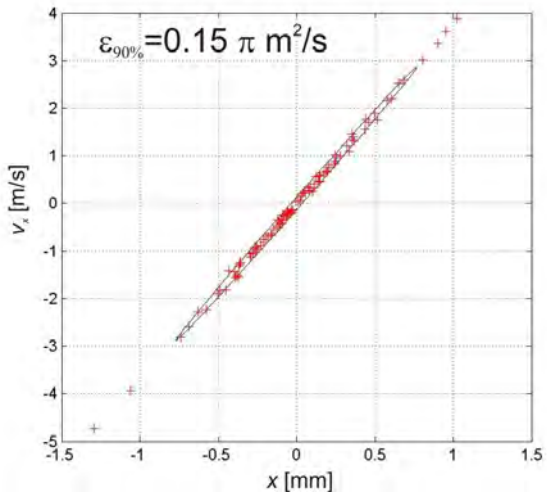

Figure 6.12: Simulation of the beam action diagram at the entrance of the extraction ground electrode. The ellipse encloses the 90% of the ions.

the errors in the energy of the ions are not comparatively small. In particular, when the energy spread of the bunch is analyzed, the results are quite bigger than expected. Experimental results obtained at the JYFL cooler [Nie02] and ISOLTRAP cooler [FHKB$^+$01] placed the value of the energy spread of the re-accelerated beam in the region of 1 eV, although that depends on the type of extraction used. The larger energy spread values obtained in the simulations are most probably caused by the high electric fields at the extraction region. The high electric fields (up to 10^4 V/cm in the region between the first and the second conical extraction electrode) causing high velocities of the ions in combination with the "large" grid size could be one of the reasons of the energy errors. The ions in these simulations are accelerated from quasi-static values (thermal energy of the gas) up to a mean longitudinal energy of 60 keV. If the aim is to search for an energy spread around 1 eV, it means that a precision of 1/60000 is required in terms of energy, or even bigger precision since the data is acquired in terms of longitudinal velocity (square root of the energy). Recording the kinetical energy error with SIMION one observes that it is increasing along the extraction up to a level around 20 eV (result obtained with a grid of 0.5 mm size). Figure 6.13 shows the kinetical error along the extraction of ISCOOL for one of the simulations. That will mean that for an expected energy spread of 1 eV, the error is tremendous.

More investigation about this problem is required for future applications. A probably more reliable result could be obtained with an adaptable mesh. Simulation programs using Finite Element Methods (FME) for meshing a model like ANSYS, Microwave, HFSS or Opera, allow the mesh generated to the geometry of the system to be adapted. Refining the mesh is possible in regions where the gradient of the physical property analyzed (deformation, electric field, temperature,...) is stronger and the mesh can be simplified in regions where it is small. Hence more reliability of the results is obtained and less computer requirements are needed since less calculation points are involved. Recently a new simulation code called GEMIOS has shown good capabilities to solve the multiphysics problem involving the gas-ion interaction, the gas flow and the electromagnetic

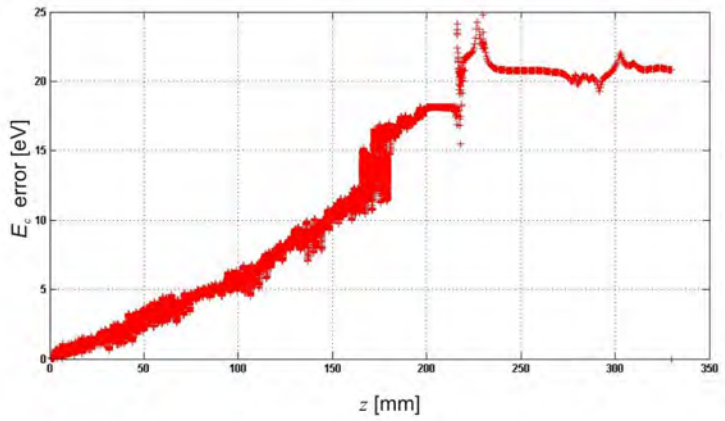

Figure 6.13: Simulation of kinetic energy E_c error of the ions along the extraction phase. The z axis represents the axis of the quadrupole. z =200 mm corresponds to the end point of the extraction plate.

	Normal extraction	**Kick extraction**
Time spread [μs]	High	Low
Energy spread [eV]	Low	High

Table 6.3: Comparison of extraction methods

fields, using ANSYS as the common platform. The use of a FEM code like ANSYS improves the quality of the mesh and the solutions and graphical plots obtained. For further information about this new code see in [Hie04, Hie05].

6.4.1 Extraction of the bunches

As explained before, the bunching of the RIB is achieved by applying an electric potential well in the longitudinal direction. The optical properties of the bunch released from the RFQCB depend on the potentials that are applied to the electrodes during the accumulation and extraction process. Figure 6.14 refers to two types of extraction of the bunched beam from ISCOOL. One is a normal extraction (*left side*): the ions are first accumulated and afterwards the potential of the electrode closest to the extraction is down to release the beam. The other case is the so-called "kick" extraction (*right side*), besides putting down the potential in the region closest to the extraction, the potential of the electrodes just before where the ions were accumulated is pushed up. In that way, the bunch of ions which were trapped in the potential well are more strongly accelerated and pushed out of the trap. The comparison of the two methods is done in Tab. 6.3. The method chosen will mainly depend on the final application for which the beam will be used . Therefore it will be the user who decides the kind of beam required for the experiment and consequently the operation parameters to apply to ISCOOL. For example, in collinear laser spectroscopy experiments, a short time spread is mandatory though a low value of the energy spread is suitable.

As explained in the previous section, SIMION was used to simulate the extraction of the ions from the trap. Even though the results are not completely realistic, an idea of the results obtained is given in Fig. 6.15. The transverse envelope of the beam is approximately circular, with an area around 4π mm^2. The Time Of Flight (TOF) shows a quite small bunch width, around 3 μs.

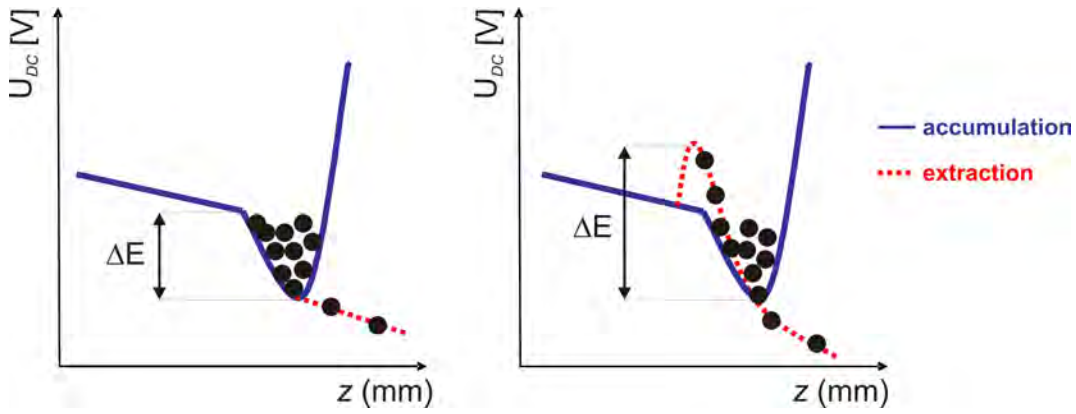

Figure 6.14: Scheme of two types of bunch extraction: normal extraction (*left side*) and "kick" extraction (*right side*).

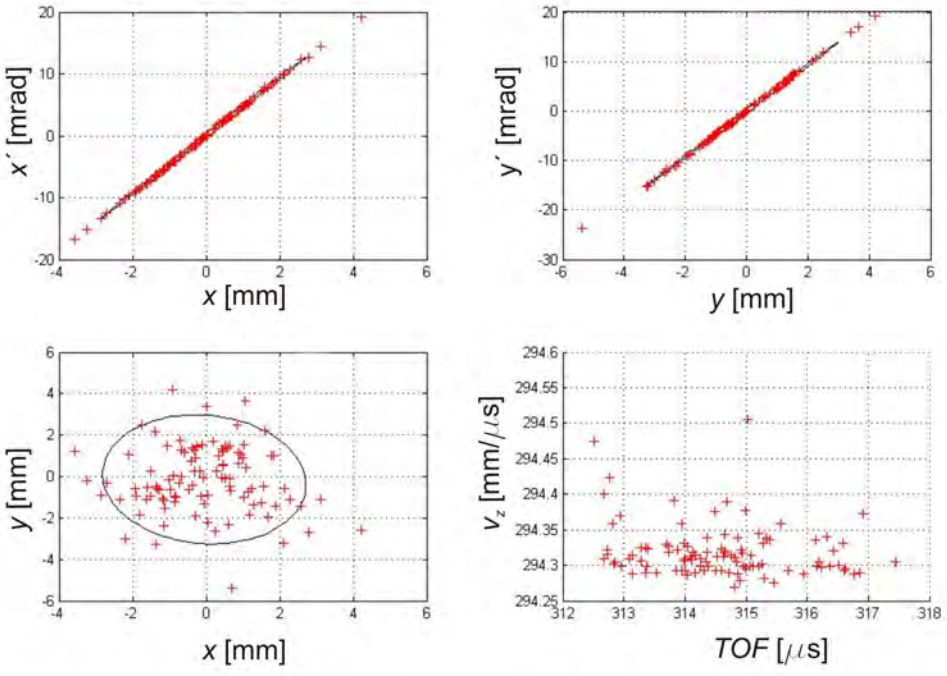

Figure 6.15: Plots for ions of Cs^+ ions accelerated after ISCOOL up to the energy of 60 keV: $x - x'$ phase space (*top left*) and $y - y'$ phase space (*top right*), transverse shape of the beam $x - y$ (*bottom left*) and time of flight plot $TOF - v_z$ for the calculation of the longitudinal emittance (*bottom right*). The conditions of the simulations are detailed in Fig. 6.11.

Electrode	Transmission mode voltage [V]	Accumulation voltage [V]	Extraction voltage [V]
Extraction plate	59992	60000	60000
1st extraction electrode	59995	59995	(*)
2nd extraction electrode	45000	45000	(*)

Table 6.4: Optimized voltages for the extraction electrodes in transmission mode and bunching mode (accumulation and extraction), based on the data from [Pet02b]. (*) Depending on the requirements of the experiments.

6.5 Space charge limit

The theory of the space charge limit was developed in Sec. 4.1.4 and in the following will be applied for the particular case of ISCOOL. Figure 6.16 shows the dependence of the maximum ion density as a function of the mass. The points have been calculated using a constant q value of 0.5. The amplitude and frequency of the RF electric field are extracted from Tab. 6.2. It is clear that within the stability region the maximum ion densities reachable n_{max} with ISCOOL are around 10^7 ion/cm^3.

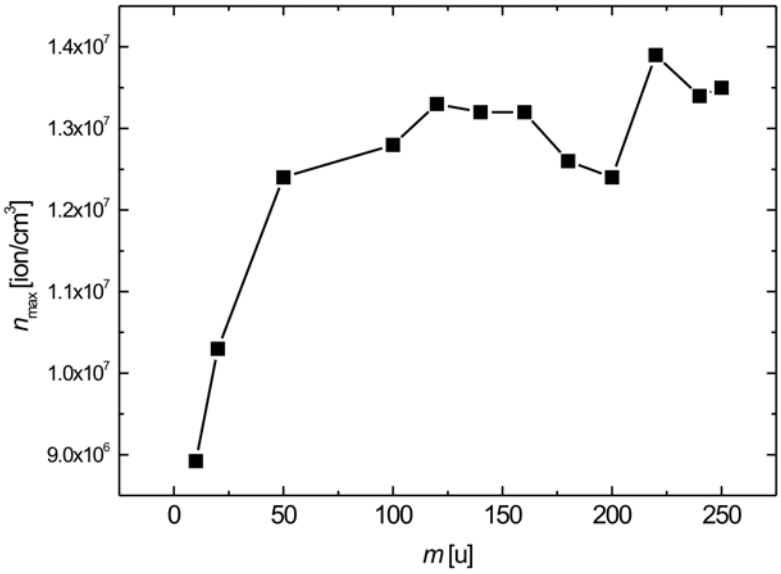

Figure 6.16: Plot of the maximum ion density inside ISCOOL in transmission mode (no bunching) as a function of the mass of the ions of the beam for a $q = 0.5$.

The maximum number of particles in transmission mode (without bunching) N_{max} can be approximated by the following expression:

$$N_{max} = \left(\pi r_b^2\right) L n_{max}. \tag{6.9}$$

L and r_b are the length and the radius, respectively, of a cylinder along the optical axis of the RFQCB cavity which approximates the space filled by the beam. Figure 6.17 shows the maximum

number of particles that can be accumulated at ISCOOL (L=800 mm and r_b=2 mm). The range is from the $0.9 \cdot 10^8$ ions for light masses ($A \approx 10$) to the $1.4 \cdot 10^8$ ions for heavy masses ($A \approx 250$).

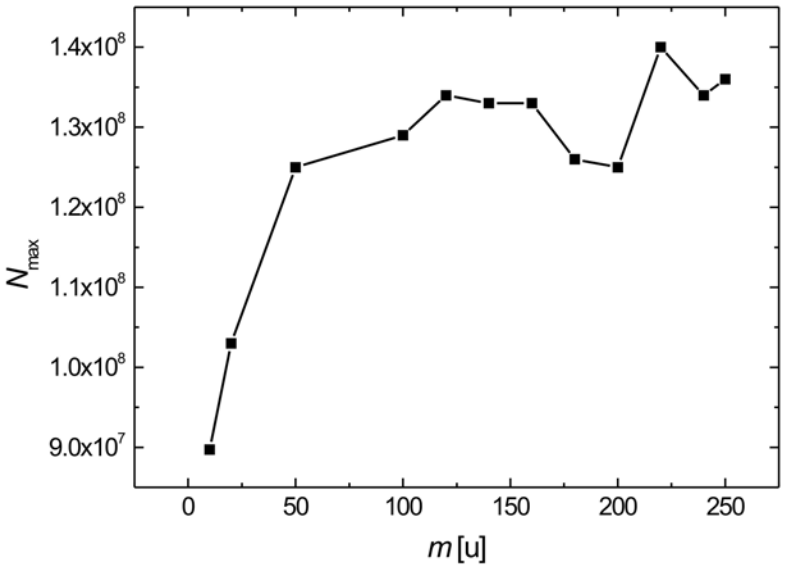

Figure 6.17: Plot of the maximum number of ions inside ISCOOL in transmission mode (no bunching) as a function of the mass of the ions of the beam for a q value of 0.5.

Chapter 7

Vacuum system of ISCOOL

The vacuum system of an RFQCB in general, and of ISCOOL in particular, has as main challenge to keep the high vacuum at the ISOLDE beam line (10^{-7} mbar) whilst adding a high gas load into the RFQCB chamber (up to 3 mbar·l/s). In short, the system consists in pumping in different stages (*differential pumping*) the buffer gas flowing directly inside the RFQCB chamber. The different sections are separated by mechanical barriers. In this case, the holes of the electrodes and the plates of the RFQCB chamber are used for this purpose. The buffer gas (normally helium) slowly flows out to the main chamber (up to 0.1 mbar) through the round hole place on each side of the RFQCB chamber. This cavity is pumped by a turbomolecular pump with a helium pumping speed around 1300 l/s. From the main chamber, the helium can only flow out via the holes of the last injection electrode or the first extraction electrode, or via the pumping side. The calculated pressure in the main chamber is around $10^{-3} - 10^{-4}$ mbar. The main goal is to reach the ISOLDE standard beam line pressure (10^{-7} mbar) inside the injection and extraction ground electrodes. For this purpose, two more turbomolecular pumps are installed, one in the injection and another in the extraction side. The helium pumping speed is 750 l/s for both pumps. In this chapter the detailed scheme of the system is presented. A model to calculate the pressure in each region is discussed and applied to the ISCOOL system. For the calculations, a code was programmed in MATLAB. The small program uses a GUI which allows the user to identify the different parameters of the cooler (holes sizes, length, pumping speeds and permeation) in order to calculate the different pressures in each section of the machine.

7.1 Scheme of the system

Figure 7.1 shows the scheme of the vacuum system for the ISCOOL project. The section is pumped by three turbomolecular pumps (TP1, TP2 and TP3) through a differential pumping system (see following sections). Due to the different pressures inside the cavities pumped by each turbopump, those turbopumps are supported by two different forepumps (F1 and F2), assuming then that the pressures in the injection and extraction side of ISCOOL are the same. Both forepumps are connected to the outlet of the recovery line of the ISOLDE vacuum system. The pumped gas is released to the ISOLDE balloons which serve to store the radioactive gases until the radiation levels are safe. In addition, another forepump (FR) is used during the pumping down to start with the operation before opening the valves since the turbopumps are in principle never stopped at ISOLDE.

The gas feeding system consists of a small stainless steel pipe (1/8 inch) which crosses one of

the axial electrodes placed in the middle-injection region of the RFQCB chamber (in the region where the higher pressure for the cooling is required). The flow of gas delivered to the RFQCB chamber is controlled by a gas valve (VHE) connected to a flow-gas controller (Pfeiffer RVC 300). The valve can be connected either directly to the gas bottle or to a gas purification system to decrease the level of impurities in the gas. On the other hand, some small flanges are conditioned to install the venting line to fill the cavities with nitrogen gas at the atmospheric pressure.

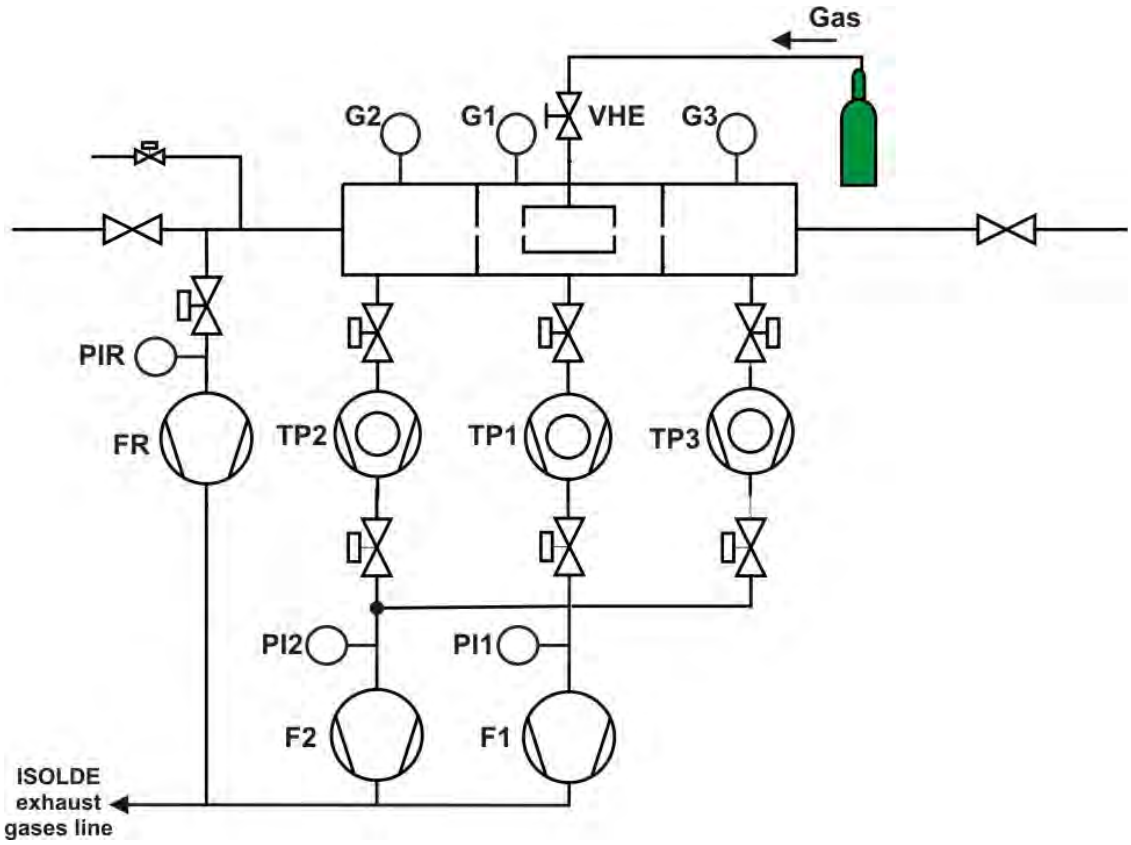

Figure 7.1: Layout of the ISCOOL vacuum system

The monitoring of the pressures of the system is done by three full range pressure gauges (G1, G2 and G3). Different range of pressures can appear in the system (mainly in the main vacuum chamber) depending on whether the gas valve is open or closed. Therefore, such full range gauges are a simpler solution than the use of Penning and Pirani gauges (double number of components). To check the pressures in the inlet of the forepumps, three Pirani gauges (PI1, PI2 and PIR) are included.

7.2 Operation procedures

To properly set up and be ready to operate a new vacuum system, it is important to define the proper procedures that have to be followed to assure a safe operation of all the components of the system. In the following, the procedures to apply for the vacuum system of ISCOOL will be detailed.

7.2.1 Pumping down

It is necessary to distinguish between the procedure for pumping down ISCOOL during the off-line tests and the procedure once it is already connected to the ISOLDE vacuum system (see Fig. 7.3 and a detail explanation in [Meu02]). This is due to the difference in the connection to the tanks of the recovery gases line when ISCOOL is connected to the ISOLDE vacuum system (see [Mul02]). The possibility that activated ions are not transmitted but pumped out by the turbopumps, makes necessary to connect the exhaust gas lines at ISOLDE to those tanks. The contaminated gas is confined in the temporary tanks until the activity decreases to an acceptable level. Then the gas in the tanks is released to the atmosphere.

Due to the placement of ISCOOL, just after the HRS, it is necessary to think about the possible radiation contamination in the exhaust gas line, even if ISCOOL is located in the experimental area (low radiation levels). Unlike the situation during the off-line tests, when the exhaust gases can be expelled to the air since the device uses a non-contaminated (stable) ion beam, the exhaust gases at ISOLDE are connected to two balloons where the gases are stored and the radioactive components decay. Once the radiation level is safe, in agreement with the CERN radiation safety rules [CER96], the gases inside the balloons can be released to the atmosphere.

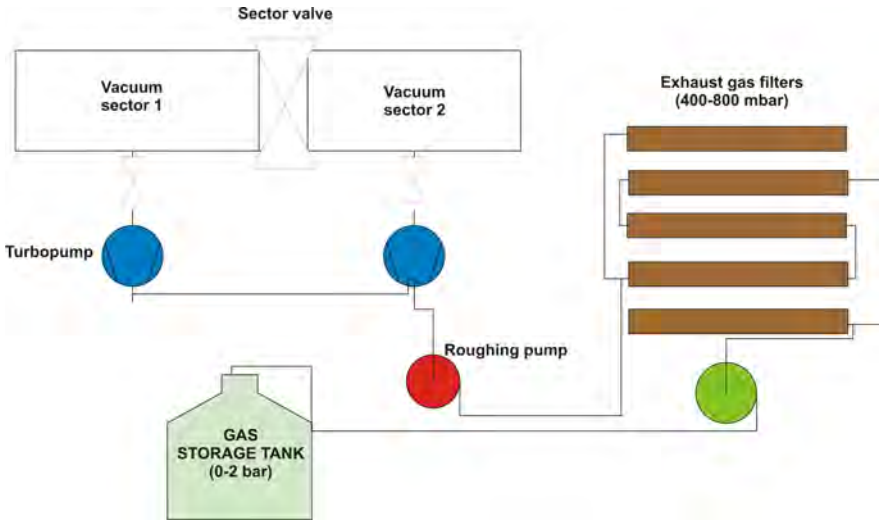

Figure 7.2: Layout of the present ISOLDE vacuum system (more information in [Meu02]).

Therefore for ISCOOL the procedure for pumping-down the beam line is identical to the procedure to pump down the other beam lines at ISOLDE. The only difference is the requirement that the valve that allows the entry of the gas into the system (VHE) must be closed during all the procedure and only can be opened once the vacuum has reached the standard ISOLDE level (10^{-7} mbar).

7.3 Theoretical approach

The complexity of the geometry of the vacuum chambers of ISCOOL makes difficult to carry out fluid simulations. For that reason, to obtain a good approximation to the real situation, a theoretical approach has been developed to calculate the pressures reached in the different sections

of the system. Figure 7.3 shows the simplified scheme used, in which the main pressures defined are:

- P_{RFQCB}: pressure inside the RFQCB chamber.
- P_1: pressure in the main chamber, directly pumped down by the turbopump 1.
- P_2: pressure in the injection part. This section is pumped by the turbopump 2.
- P_3: pressure in the extraction part. This section is pumped by the turbopump 3.
- P_{line}: pressure after the injection and extraction ground electrodes which has to correspond to the normal pressure of the rest of the beam line of the facility.

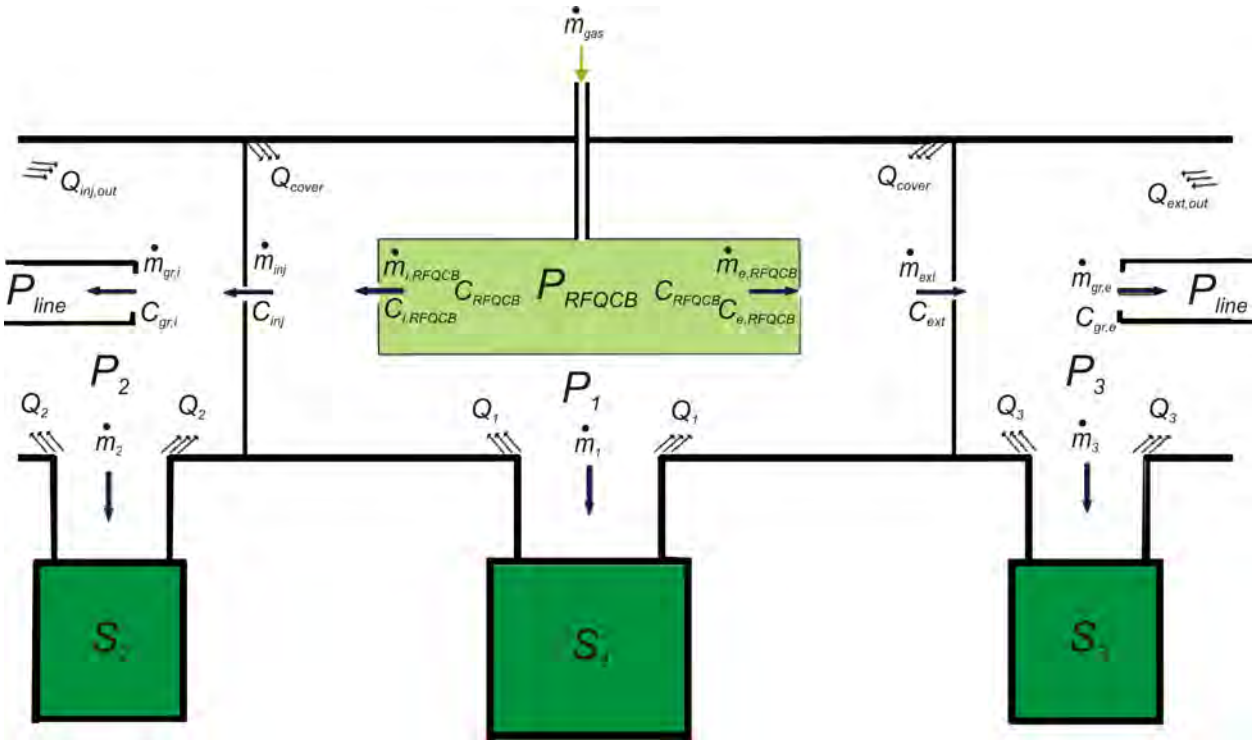

Figure 7.3: Sketch of the vacuum system showing the conductances, mass flows and pressures. For simplification, only the injection and extraction electrodes used for the differential pumping are shown.

Also the main conductances are defined as shown in Fig. 7.3:

- C_{RFQCB}: conductance of half of the RFQCB chamber.
- $C_{i,RFQCB}$: conductance of the round enter hole of the RFQCB chamber. The diameter of the hole is $d_{i,RFQCB}$.
- $C_{e,RFQCB}$: conductance of the round exit hole of the RFQCB chamber. The diameter of the hole is $d_{e,RFQCB}$.
- C_{inj}: conductance of the round hole of the last injection electrode. This hole serves to create the differential pumping between the injection side and the RFQCB chamber. The diameter of the hole is d_{inj}.

- C_{ext}: conductance of the round hole of the first extraction electrode. This hole serves to create the differential pumping between the injection side and the RFQCB chamber. The diameter of the hole is d_{ext}.
- $C_{i,g}$: conductance of the round hole of the injection ground electrode. The diameter of the hole is $d_{i,g}$.
- $C_{e,g}$: conductance of the round hole of the extraction ground electrode. The diameter of the hole is $d_{e,g}$.

The different mass flows through the machine (considered from high to low pressures) are defined by (see Fig. 7.3):

- $\dot{m}_{gas}$: mass flow of the gas entering into the RFQCB chamber.
- $\dot{m}_{i,RFQCB}$: mass flow of the gas flowing out from the RFQCB chamber to the main chamber (supposing lower pressure in this last one) through the injection side hole $d_{i,RFQCB}$.
- $\dot{m}_{e,RFQCB}$: mass flow of the gas flowing out from the RFQCB chamber to the main chamber (supposing lower pressure in this last one) through the extraction side hole $d_{e,RFQCB}$.
- $\dot{m}_{inj}$: mass flow of the gas flowing out from the main chamber to the injection sector through the last injection electrode hole d_{inj}.
- $\dot{m}_{ext}$: mass flow of the gas flowing out from the main chamber to the extraction sector through the first extraction electrode hole d_{ext} .
- $\dot{m}_1$: mass flow pumped out by turbopump 1 (main chamber).
- $\dot{m}_2$: mass flow pumped out by turbopump 2 (injection side).
- $\dot{m}_3$: mass flow pumped out by turbopump 3 (extraction side).
- $\dot{m}_{i,g}$: mass flow through the injection ground electrode.
- $\dot{m}_{e,g}$: mass flow through the extraction ground electrode.

From these definitions it is possible to obtain the expressions relating the pressure in each side. In the calculations, the pressure inside the RFQCB chamber P_{RFQCB} is supposed to be constant and fixed to a certain value for the user. The pressure in both injection and extraction ground electrodes (P_{line}) are also fixed by the pressure in the ISOLDE beam line.

The mass flow balances in the different steps of the differential pumping are expressed as:

$$\begin{cases} \dot{m}_{gas} = \dot{m}_{i,RFQCB} + \dot{m}_{e,RFQCB} \\ \dot{m}_{i,RFQCB} + \dot{m}_{e,RFQCB} = \dot{m}_1 + \dot{m}_{inj} + \dot{m}_{ext} \\ \dot{m}_{inj} = \dot{m}_2 + \dot{m}_{i,g} \\ \dot{m}_{ext} = \dot{m}_3 + \dot{m}_{e,g} \end{cases} \tag{7.1}$$

The mass flow $\dot{m}$ can be expressed as a throughput -quantity of gas flowing through the section expressed in PV units per time- if the temperature is considered constant in all the system [Laf98]. The equations are transformed into:

$$\begin{cases} \dot{Q}_{gas} = \dot{Q}_{i,RFQCB} + \dot{Q}_{e,RFQCB} \\ \dot{Q}_{i,RFQCB} + \dot{Q}_{e,RFQCB} = \dot{Q}_1 + \dot{Q}_{inj} + \dot{Q}_{ext} \\ \dot{Q}_{inj} = \dot{Q}_2 + \dot{Q}_{i,g} \\ \dot{Q}_{ext} = \dot{Q}_3 + \dot{Q}_{e,g} \end{cases} \tag{7.2}$$

Type of flow	λ	$P \cdot D$	Physics phenomenon
Viscous (rough vacuum)	$< D/100$	> 0.6 mbar·cm	Interaction molecules
Knudsen (medium vacuum)	$D/100 \div D/2$	$0.6 \div 1.3 \cdot 10^{-2}$ mbar·cm	Transition
Molecular (UHV)	$> D/2$	$< 1.3 \cdot 10^{-2}$ mbar·cm	Free molecules

Table 7.1: Type of flow as function of D, λ and $P \cdot D$, where D is the beam pipe diameter, λ the mean free path and P the pressure.

The throughput Q is related with the conductance C -factor relating the drop through a pipe of the number of molecules N passing per unit time through a cross section- and the differential pressure between both parts of the conductance analysed by the expression $Q = C\Delta P$. To simplify the calculations, hereafter the flow of gas (see the different types in Table 7.1) will be considered as molecular. This assumption produces pressures higher than in the real system [Moo98].

The conductance of a round hole in molecular flow is denoted as $C = 0.3d^2$ where d is the diameter. Hence the second equation of the array 7.2 translates into:

$$\begin{aligned} 0.3d^2_{i,RFQCB}(P_{RFQCB} - P_1) + 0.3d^2_{e,RFQCB}(P_{RFQCB} - P_1) = \\ P_1S_1 + 0.3d^2_{inj}(P_1 - P_2) + 0.3d^2_{ext}(P_1 - P_3), \end{aligned} \tag{7.3}$$

where S_1 is the pumping speed of the turbopump TP1. And simplifying:

$$\begin{aligned} d^2_{i,RFQCB}(P_{RFQCB} - P_1) + d^2_{e,RFQCB}(P_{RFQCB} - P_1) = \\ \frac{P_1S_1}{0.3} + d^2_{inj}(P_1 - P_2) + d^2_{ext}(P_1 - P_3). \end{aligned} \tag{7.4}$$

The variables in the system are P_1, P_2 and P_3, so the equation can be expressed as:

$$\begin{aligned} (\frac{S_1}{0.3} + d^2_{inj} + d^2_{ext} + d^2_{i,RFQCB} + d^2_{e,RFQCB})P_1 - d^2_{inj}P_2 - d^2_{ext}P_3 = \\ (d^2_{i,RFQCB} + d^2_{e,RFQCB})P_{RFQCB}. \end{aligned} \tag{7.5}$$

The same procedure can be applied to the third equation of the array. The expression obtained is:

$$-d^2_{inj}P_1 + (d^2_{inj} + d^2_{i,g} + \frac{S_2}{0.3})P_2 = d^2_{i,g}P_{line} \tag{7.6}$$

And the last equation of the array becomes:

$$-d^2_{ext}P_1 + (d^2_{ext} + d^2_{e,g} + \frac{S_3}{0.3})P_3 = d^2_{e,g}P_{line} \tag{7.7}$$

Finally, the equations can be grouped in a lineal equation system:

$$\mathbf{CP} = \mathbf{Q} \tag{7.8}$$

where:

$$\mathbf{C} = \begin{bmatrix} \frac{S_1}{0.3} + d^2_{inj} + d^2_{ext} + d^2_{i,RFQCB} + d^2_{e,RFQCB} & -d^2_{inj} & -d^2_{ext} \\ -d^2_{inj} & d^2_{inj} + d^2_{i,g} + \frac{S_2}{0.3} & 0 \\ -d^2_{ext} & 0 & d^2_{ext} + d^2_{e,g} + \frac{S_3}{0.3} \end{bmatrix}, \tag{7.9}$$

$$\mathbf{P} = \begin{bmatrix} P_1 \\ P_2 \\ P_3 \end{bmatrix}, \tag{7.10}$$

and

$$\mathbf{Q} = \begin{bmatrix} (d^2_{i,RFQCB} + d^2_{e,RFQCB})P_{RFQCB} \\ d^2_{i,g}P_{line} \\ d^2_{e,g}P_{line} \end{bmatrix}. \tag{7.11}$$

7.3.1 Outgassing and permeation

In every vacuum system, the sources of gas that can be considered are:

- The gas molecules of the initial atmosphere **enclosed** in the system or **injected** into the system on purpose.
- The gas which penetrates into the system as a result of **leakage**.
- The gas from the **outgassing** of the materials in the system.
- The gas (or vapours) resulting from the **vapour pressure** of the materials.
- The gas entering the system by **permeation** through the walls and windows.

In the steady-state of the system, all the sources are in equilibrium with the pumping action. In normal operation without leakages, to the gas load and the enclosed, the effects of the outgassing and the permeation should be evaluated. Eq. 7.8 is valid if outgassing and permeation effects are not taken into account.

The outgassing from the material of the chamber and the sealings (stainless steel for the vacuum chambers and in-vacuum components and the fluorocarbon rubber, FPM-VITON, for the sealing rings) will fall down if a bake-out is carried out before operation. The permeability of a seal is formulated in [Com03] and [JMP97]. The leak rate caused by a seal Q_{seal} can be expressed as:

$$Q_{seal} = q_{seal} A_{seal}, \tag{7.12}$$

where:

$$q_{seal} = \frac{K_p \Delta P}{d_{perm}}, \tag{7.13}$$

with K_p a permeation constant which depends on the material of the seal and expressed in units of [m^2/s], A the permeation area defined as $A = tL$ for an O-ring with t the thickness and L the length of the medium diameter and d_{perm} the permeation thickness. For an O-ring this is defined as half the thickness, $d_{perm} = t/2$. Grouping all the outgassing terms from the main vacuum chamber in the term $Q_{outgas-cav}$, the terms related to the injection pumping side in $Q_{outgas-inj}$ and those related to the extraction in $Q_{outgas-ext}$. Expressing the permeation as $Q_{perm}(P_{atm} - P)$ where P_{atm} is the atmospheric pressure. The matrices $\mathbf{C}$ and $\mathbf{Q}$ in Eq. 7.8 transform into:

$$\mathbf{C} = \begin{bmatrix} C_1 + Q_{perm-cav} & -d^2_{inj} & -d^2_{ext} \\ -d^2_{inj} & C_2 + Q_{perm-inj} & 0 \\ -d^2_{ext} & 0 & C_3 + Q_{perm-ext} \end{bmatrix}, \tag{7.14}$$

where C_1, C_2 and C_3 are the diagonal coefficients of the old matrix C (Eq. 7.9), and:

$$\mathbf{Q} = \begin{bmatrix} (d^2_{i,RFQCB} + d^2_{e,RFQCB})P_{RFQCB} + Q_{outgas-cav} + Q_{perm-cav}P_{atm} \\ d^2_{i,g}P_{line} + Q_{outgas-inj} + Q_{perm-inj}P_{atm} \\ d^2_{e,g}P_{line} + Q_{outgas-ext} + Q_{perm-ext}P_{atm} \end{bmatrix}. \tag{7.15}$$

Helium pressure P_{RFQCB} [mbar]	0.1
Diameter quadrupole d_0 [mm]	40
Length quadrupole L_0 [mm]	800
Diameter second injection electrode d_{inj} [mm]	4
Diameter injection plate hole $d_{i,RFQCB}$ [mm]	8
Diameter extraction plate hole d_{ext} [mm]	7
Diameter first extraction electrode $d_{e,RFQCB}$ [mm]	3
Diameter injection/extraction ground electrodes $d_{i,g}/d_{e_g}$	10

Table 7.2: List of the main mechanical and gas parameters involved and used in the vacuum calculations.

7.4 Practical calculations

7.4.1 Pressure inside the chambers

The formulae presented in the previous section were applied for the calculation of the pressure inside ISCOOL. For all the calculations presented here the following assumptions were established:

- The pressure inside the RFQCB chamber is constant and equal to 0.1 mbar which is a normal pressure for other quadrupoles of similar features.
- The outgassing and permeation is not considered for a first approach.
- The calculations are done assuming a molecular flow everywhere, which in fact is not the case in reality. However, the molecular flow implies that the gas will flow more easily through the conductances. That means that the results will always be worse in terms of pressure than in the real case.
- The buffer gas used is helium, which will be the usual operation gas of the device. Other gases, as hydrogen or argon, were not included in this study.

In Table 7.2 the main parameters involved in the vacuum calculations are summed up.

The first step was to calculate the type of flow inside the quadrupole. This can be deduced from the *mean free path* (mean distance between two atom collisions) which depends on the type of gas, the pressure and the temperature. According to the reference [O'H03], the mean free path of helium at 25 °C and 10^{-3} Torr is 147 mm. To obtain the value for the typical conditions at the RFQCB chamber, it is necessary to apply the expression:

$$\lambda_{RFQCB} = \lambda_{ref} \cdot \left(\frac{T_{RFQCB}}{T_{ref}}\right)\left(\frac{P_{ref}}{P_{RFQCB}}\right) \tag{7.16}$$

where λ_{ref} is the mean free path at certain reference conditions of pressure and temperature (P_{ref} and T_{ref}) and P_{RFQCB} and T_{RFQCB} the conditions of pressure and temperature inside the RFQCB respectively. Applying the values compiled in Tab. 7.2, the mean free path for helium inside the RFQCB chamber is around 2 mm. That means the flow is not molecular since this value is smaller than the diameter of the walls, which is supposed to be equal to the distance between opposite quadrupole rods to simplify the calculations (40 mm). Neither can it be considered really as a viscous flow (mean free path $\ll$ vacuum chamber dimensions) but a transition flow. Due to the complexity of the equations involving transition flows, it is more simple to make the calculations

Manufacturer	Model	Type	Helium pumping speed (l/s)	Flange diameter	Flange standard
Leybold	Turbovac 1100 C	Normal	750	200/250	ISO-K
Leybold	Turbovac T 1600	Normal	1150	200	ISO-F
Leybold	Turbovac T 1600	Normal	1300	250	ISO-F/CF
Leybold	MAG 1500 C/CT	Magnetic	1150	200	ISO-F
Leybold	MAG 1500 C/CT	Magnetic	1220	250	ISO-F
Leybold	MAG 2000 C/CT	Magnetic	1780	250	ISO-F
Leybold	MAG W 2000 C/CT	Magnetic	1800	250	ISO-F
Pfeiffer	TMH/U 1001 P	Normal	900	200	ISO/CF-F
Pfeiffer	TMH/U 1601 P	Normal	1100	200	ISO-K/CF-F
Pfeiffer	TMH/U 1601 P	Normal	1150	250	ISO-K/CF-F
Pfeiffer	TPH 1201 P	Normal	1300	200	ISO-K
Pfeiffer	TPH 1801 P	Normal	1650	200	ISO-K
Pfeiffer	TPH/U 2101 P/UP	Normal	1900	250	ISO-K
Pfeiffer	TMH/U 1000 MP	Magnetic	850	200	ISO-K
Pfeiffer	TMH/U 1600 MP	Magnetic	1100	200	ISO-K
Pfeiffer	TMH/U 1600 MP	Magnetic	1180	250	ISO-K

Table 7.3: Technical parameters of the turbomolecular pumps of Leybold and Pfeiffer suited for ISCOOL.

Set	Pump 1	Pump 2	Pump 3
Leybold 1	Turbovac T 1600- ISO K	Turbovac 1100 C	Turbovac 1100 C
Leybold 2	Turbovac T 1600 CF-F	Turbovac 1100 C	Turbovac 1100 C
Leybold 3	MAG 2000 C/CT	Turbovac 1100 C	Turbovac 1100 C
Pfeiffer 1	TPH/U 2101 P/UP	TMH/U 1001 P	TMH/U 1001 P
Pfeiffer 2	TPH/U 2101 P/UP	TMH/U 1601 P	TMH/U 1601 P
Pfeiffer 3	TPH 1801 P	TPH 1201 P	TPH 1201 P

Table 7.4: Different sets of three turbomolecular pumps for the project.

with the molecular flow. This underestimates the pumping capacity. Therefore, for a certain gas load, lower pressures are expected to be obtained in the real system.

To calculate the pressure inside the quadrupoles, different test sets of turbomolecular pumps were chosen for analysis. The pumps were from two suppliers that are already well known at CERN: Pfeiffer and Leybold. Both offer a limited set of turbomolecular pumps within the operating pressures and pumping speeds of the ISCOOL vacuum system. In Table 7.3 the main technical properties of the turbomolecular pumps chosen from both suppliers are described, and in Tab. 7.4 the five sets of pumps for the study: three from Leybold and 2 from Pfeiffer.

In all the sets, the pumping speed of the turbomolecular pump 1 (TP1, main chamber) is greater than for the other pumps. It is of great importance minimize as much as possible the pressure inside this chamber, that means, to obtain a very good differential pressure in the first step. There are two main reasons to minimize this pressure:

- To diminish the probability of charge exchange losses in the trap. As have been seen in the operating RFQCB's (e.g. in [Nie02]), if the pressure in the main chamber is low enough,

the impurities that could enter from outside into the chamber will not go into the RFQCB chamber, but will be pumped out.

- To decrease the pressure in the region between the extraction plate and the first extraction electrode. In this region, the beam starts the acceleration after the trapping at the final region of the RFQCB chamber. Therefore, if the pressure of the buffer gas is still too high in this region, the beam emittance could blow up due to the lack of confinement (no RF electric field applied) and the collisions with the molecules of the buffer gas that are flowing out of the RFQCB chamber.

In Figure 7.4, the pressure reached inside the main chamber (P_1) and in the injection and extraction side (P_2 and P_3) with the different sets of turbopumps (Tab. 7.4) is plotted as function of the pumping speed of the pump used in each set for pumping down the main chamber (S_1). Figure 7.5 plots those pressures as function of the pumping speeds of the turbopumps of both sides, which in all the cases have identical pumping speeds. The calculations are carried out with the parameters from Tab. 7.2.

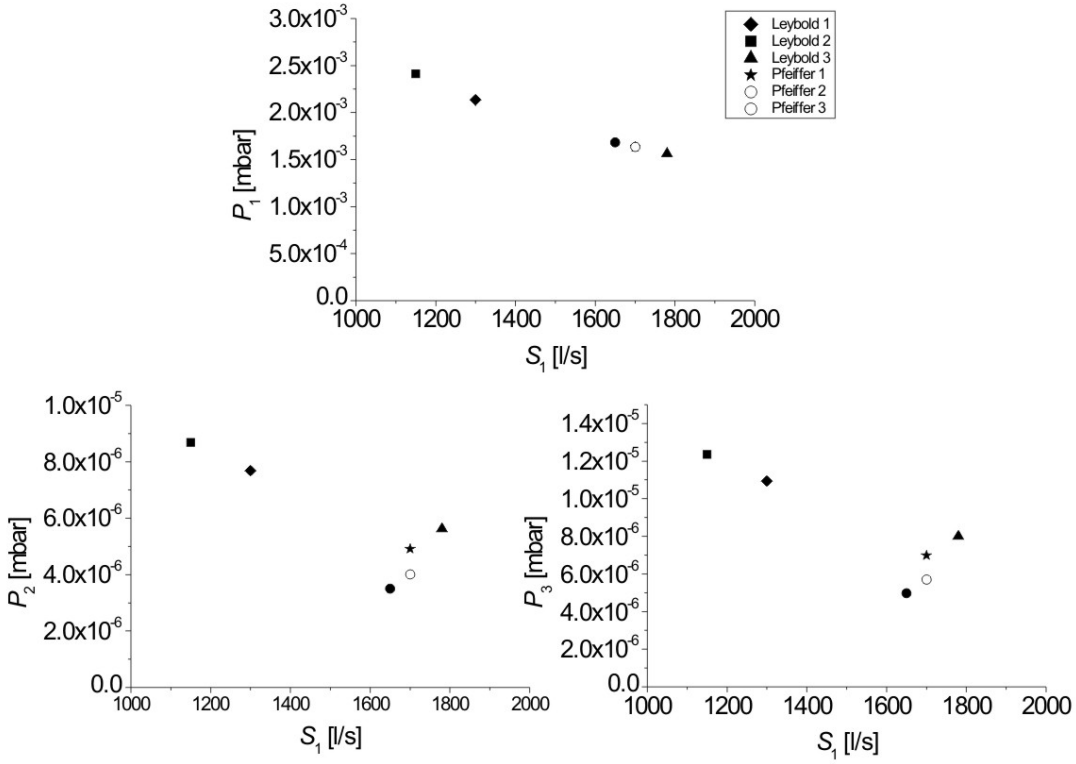

Figure 7.4: Pressure inside the main chamber P_1 and the injection and extraction side P_2 and P_3 as function of the pumping speed of the turbomolecular pump 1 S_1 for all the sets of pumps analysed in Tab. 7.4.

As already mentioned, the results obtained before were for a constant pressure inside the RFQCB chamber. Figure 7.6 plots the total gas throughput of the system versus the pressures in the main chamber P_1 and in the injection and extraction side (which are assumed to be identical, $P_2 = P_3$). The final set of turbopumps used in the set-up is used for the calculation. It is clear that,

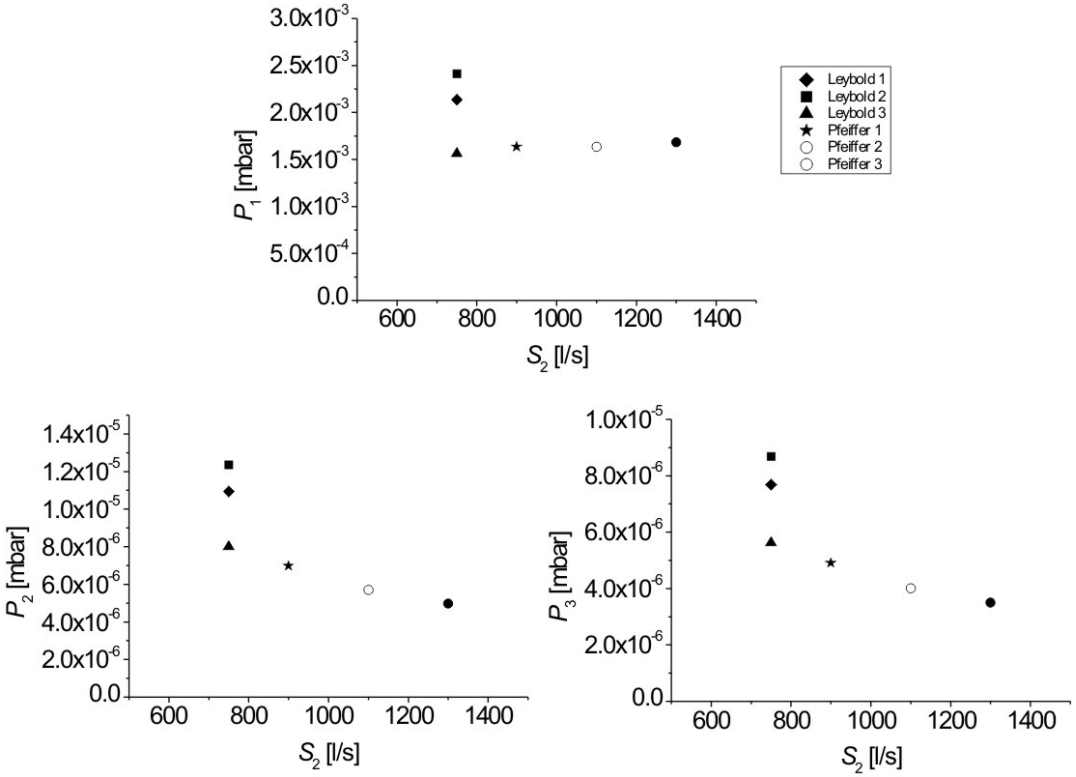

Figure 7.5: Pressure inside the main chamber P_1 and the injection and extraction side P_2 and P_3 as function of the pumping speed of the turbomolecular pump 2 and 3 ($S_2 = S_3$ always) for all the sets of pumps analysed in Tab. 7.4.

for the normal gas load, all the turbopumps will always work with the nominal pumping speed. The pumping speed of the turbopumps is constant in the high vacuum region but for medium vacuum, the pumping speed is decreasing as the pump does not have the same efficiency. For the main pump, the pumping speed will decrease for pressures lower than $6 \cdot 10^{-2}$ mbar.

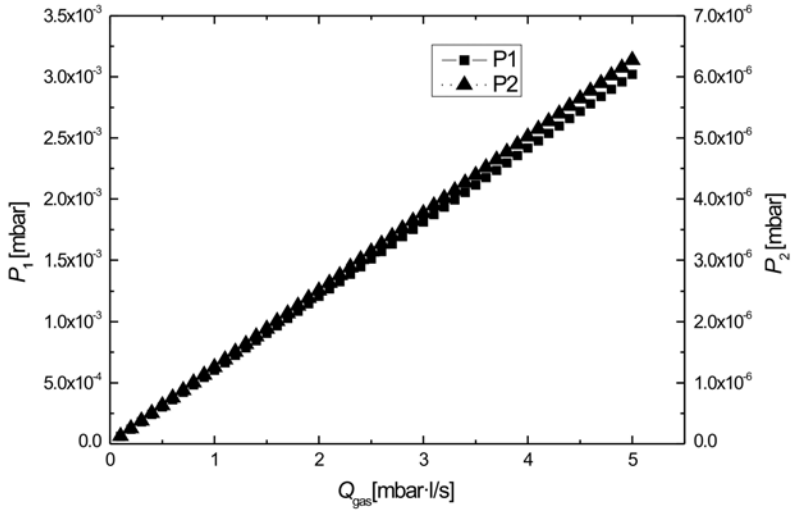

Figure 7.6: Pressure inside the main chamber P_1 and the injection/extraction side $P_2 = P_3$ as function of the gas throughput with the final set of turbopumps used and the geometrical conditions detailed in Tab. 7.2.

To determine the limits of the gas consumption it is necessary to calculate the pressure in the RFQCB chamber as a function of the diameter of the injection and extraction plates of the RFQCB chamber. For a certain input throughput, P_{RFQCB} can be easily calculated if the pressure in the main chamber P_1 is assumed much smaller ($P_{RFQCB} >> P_1$). In this system this condition is accomplished due to the large pumping speed S_1 (see Fig. 7.6). Figure 7.7 compares the pressure reached in the RFQCB chamber as function of those diameters for different fixed values of the gas throughput Q_{gas}= 1, 2, 3 and 4 mbar·l/s. The plots confirm that higher pressures can be obtained in this chamber either by increasing the total throughput of the system, or decreasing the holes of the injection and/or extraction plates. The first solution increases the pressure in the rest of the vacuum system and the second system most probably affects the beam transmission efficiency of ISCOOL. The pressure in the main chamber and in the injection and extraction side will be determined by the gas throughput and may be calculated using Fig. 7.6.

7.4.2 Forepumps

The use of the differential pumping system, with independent pressures for the three turbomolecular pumps or at least two of them as in ISCOOL (see Sec. 7.4.1), requires the use one forepump for each turbomolecular pump (TP1, TP2 and TP3). From all the three turbopumps, the choice of the size of the forepump for TP1 is the most crucial. To choose the size, it is necessary to know the pressure in the inlet of the forepump (outlet of the turbopump). Normally, the pressure could be calculated by the compression ratio (KR) of the turbopump. For TP1, the compression ratio for helium is 10^6, that means the pressure in the outlet would be $P_{vv} = 10^6 \cdot P_{HV}$, where P_{vv} is

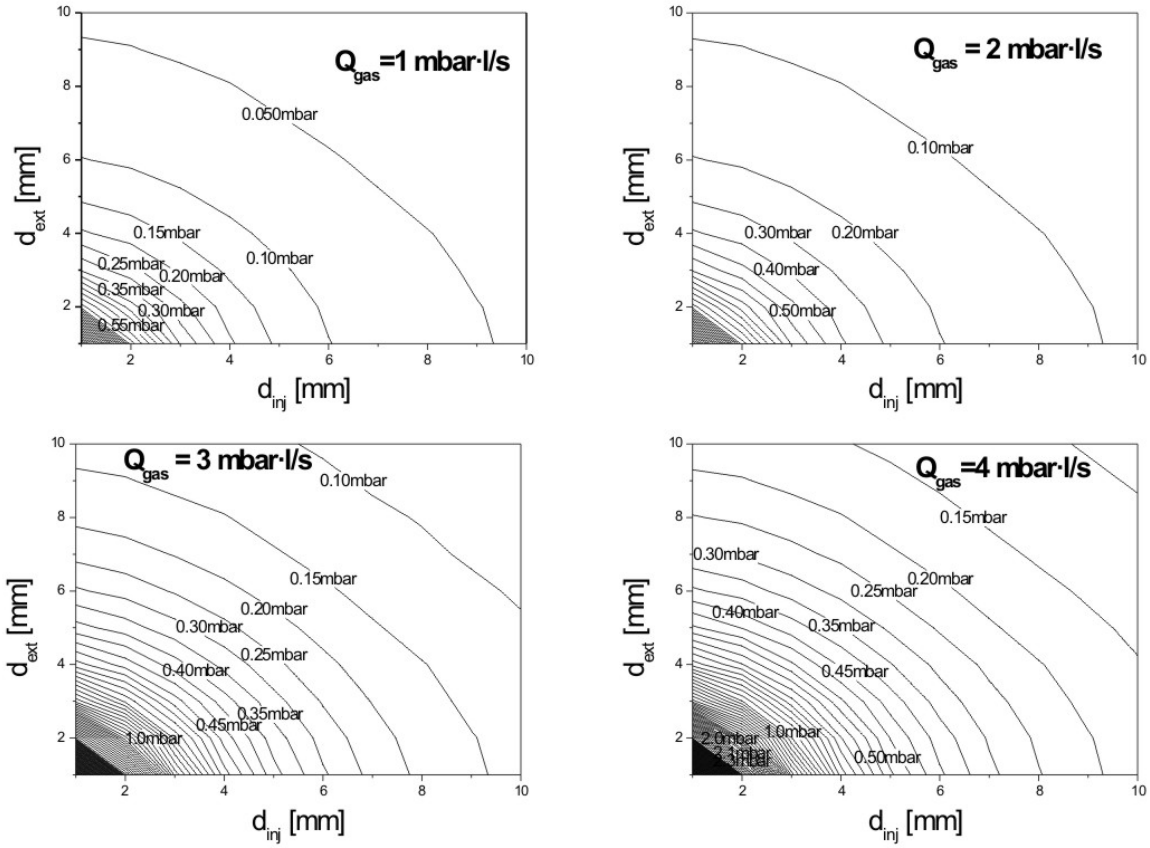

Figure 7.7: Pressure inside the RFQCB chamber P_{RFQCB} as function of the diameters of the injection and extraction plate (d_{inj} and d_{ext} respectively) for different fixed gas throughputs Q_{gas}= 1 mbar·l/s (*top left*), 2 mbar·l/s (*top right*), 3 mbar·l/s (*bottom left*) and 4 mbar·l/s (*bottom right*). For the study it is assumed $P_{RFQCB} >> P_1$.

the pressure in the outlet of the turbo and P_{HV} the pressure in the high vacuum side (inlet of the forepump). This applies if the pressure P_{HV} is low enough and there is still molecular flow and not transition or laminar flow. Otherwise, the compression ratio descends critically. Moreover, if the gas load is high (>0.1 mbar·l/s) the rotation speed of the turbo could be limited due to the friction. In this particular case, this effect does not have to be taken into account since the helium gas load is not very high. The size of the forepump will be determined by the maximum foreline pressure of the turbopump. The pressure calculated in the foreline (for a particular forepump pumping speed S_{vv}) will be:

$$P_{vv} = Q/S_{vv} \tag{7.17}$$

For TP1, the maximum foreline pressure for N_2 is 1.8 mbar. Using a forepump of 5.8 m^3/h pumping speed (1.6 l/s), the pressure P_{vv} will be around 1.2 mbar for a throughput of 2 mbar·l/s. The calculated pressure is then limit of the 50% of the maximum foreline pressure, which is the recommended pressure in these situations. Therefore the use of a bigger pump (15 m^3/h for example) would improve the situation. To stay on the safe side and to allow for probable situations where more pumping speed from the forepumps are required (for example, pumping down a long pipe for the exhaust gases), the forepump chosen for ISCOOL are: one F1 of 30 m^3/h to support TP1 and another smaller F2 of 15 m^3/h to support both TP2 and TP3 which usually will work in high vacuum conditions.

7.4.3 Pumping down time

To choose the roughing pump required for the pumping down of the new ISCOOL beam line (see Sec. 5.3), it is necessary to calculate the time taken to reach a good vacuum (before filling the RFQCB chamber with gas). The calculations were done taking into account a forepump model Adixen Pascal Series H1 (2015), with a pumping speed of 15 m^3/h. The volume of the beam line is around 0.172 m^3 (0.09 m^3 for the main vacuum chamber and 0.082 m^3 for the rest of the beam line).

The equation to work out the pressure during the pumping down is defined as:

$$\frac{P}{P_i} = e^{-(\frac{S}{V})t} \tag{7.18}$$

assuming an infinite conductance in the inlet of the turbopump. S is the constant pumping speed, V the volume to pump, t the time, P the final pressure and P_i the initial pressure in the tank. The pumping time t_{pump} required is therefore,

$$t_{pump} = -(\frac{V}{S}) \ln \frac{P}{P_i} \tag{7.19}$$

For the conditions presented, $V = 0.172$ m^3, $S = 15$ m^3/h, initially atmospheric pressure ($P_{atm} = 1$ atm) and a final pressure (before starting the turbomolecular pump) around 10^{-3} mbar, the time (applying Eq. 7.18) necessary to reach such a pressure will be 9.5 min. For this first approach calculation are not considered. For this reason, the real pumping down time will be longer.

7.5 Gas feeding and purification

As it was explained in Sec. 4.1.2, a gas has to be fed into the RFQCB chamber for the cooling process of the ion beam. As explained along the chapter, The buffer gas fills the RFQCB chamber

and it is pumped out by a differential pumping system. The main goals of the gas-handling system are therefore to:

- Maintain a constant pressure level in the RFQCB chamber.
- Minimize the level of impurities in the chamber.

The efficiency of the system drops due to the presence of impurities in the buffer gas as shown in [Nie02]. In fact, as demonstrated in [KBH$^+$01], the processes inside the gas cell can be divided as follows:

- Atom and/or ion-molecule reactions.
- Ion-impurity reactions.
- Ion-buffer gas interactions.

In the RFQCB's, the drop in efficiency is determined by the accumulation or cooling time (at ISCOOL, usually $t_{acc} < 1$ ms). The chances that the ions interact with the buffer gas and/or the impurities present increase with time spent inside the buffer gas. Figure 7.8 shows the layout of the gas-handling system.

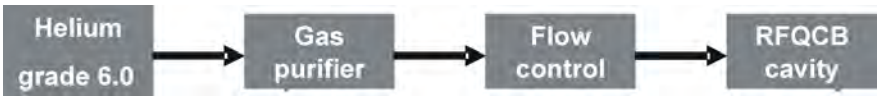

Figure 7.8: Layout of the gas-handling system

The buffer gas that will be used in a first stage is helium. The helium is provided by the suppliers in different levels of purity (see [AGA], [Car] or [Fra]). The helium type chosen for ISCOOL corresponds to the so-called grade 6.0 (99.9999% of helium). Typical impurities are H_2O (<0.5 ppm), O_2 (<20 ppb) and N_2 (<20 ppb). The impurity level in the gas can be reduced by adding a purification step (like SAES Getters PS2-GC50) that decreases the concentration of the impurities to the sub-ppb level.

The helium gas will be contained in a 50 l bottle at 200 bar. That means 10^7 mbar·l. For a calculated gas troughput of 2 mbar·l/s, the lifetime of the bottle is around 9 weeks for a continuous operation (24 hours and 7 days per week) of ISCOOL. The normal operation time of ISOLDE is 30 weeks with half of that time normally devoted to the HRS. That means it is necessary to diminish the flow or to economize the time consumption so as to minimize the change of the helium bottle during the running period.

Starting from a typical helium bottle (V=50 l and P=200 bar) and by applying the law of an ideal gas:

$$PV = nRT \tag{7.20}$$

where P is the pressure, V the volume, n the number of mols, R the universal constant of the gases ($R = 8.31$ J·mol^{-1}K^{-1} and T the temperature, one can estimate that one helium bottle (403.8 mol of helium at typical conditions) would fill once the largest tank of ISOLDE (5 m^3 at 2 bar).

The gas needs some reduction step to decrease the pressure to a level adequate for the RFQCB chamber pressure. First, the gas is flowing out from the bottle by a pressure reducer to 3-0.3 bar, connected by a Gyrolok connector to a 1/4 inch pipe. Downstream of the reducer, a gas valve (Pfeiffer EVR 116) controls the pressure or the gas flow to the RFQCB chamber. The valve accepts a pressure in the inlet up to 2.5 bar, so care has to be taken since it is in the same range than the maximum outlet pressure from the reducer. The valve can regulate pressures down to 10^{-8} mbar, and flows in the range from $5 \cdot 10^{-6}$ to $1.25 \cdot 10^{3}$ mbar·l/s. The valve is controlled by a control unit (Pfeiffer RVC 300) which is detailed in Sec. 9.2. Although the pressure inside the RFQCB chamber is only depending on the gas flow out from the valve, if it is necessary to male the control with the signal coming from a gas pressure sensor placed in the outlet of the gas valve, the value of the pressure in that region should be approximately known. The valve and the RFQCB chamber are connected by a 1/8 inch pipe. In the end of the gas inlet pipe, a ceramic feedthrough crosses the axial electrodes to electrically insulate the bottle (placed at the same voltage than the HV power supply) and the axial electrode. Inside the pipe, the gas flow cannot be assimilated any more as a molecular flow, but to an intermediate flow. The expression to calculate the conductance C in an intermediate flow is the following:

$$C = c_1 \cdot \bar{P} + c_2 \frac{1 + c_3 \bar{P}}{1 + c_4 \bar{P}}, \tag{7.21}$$

where:

$$\bar{P} = \frac{P_{sensor} + P_{RFQCB}}{2}, \tag{7.22}$$

$$c_1 = \frac{\pi}{128\eta} \cdot \frac{D^4}{L}, \tag{7.23}$$

$$c_2 = \frac{1}{6} \left(2\pi R_0 T/M\right)^{1/2} \frac{D^3}{L}, \tag{7.24}$$

$$c_3 = \left(\frac{M}{R_0 T}\right)^{1/2} \frac{D}{\eta}, \tag{7.25}$$

$$c_4 = 1.24 \left(\frac{M}{R_0 T}\right)^{1/2} \frac{D}{\eta}, \tag{7.26}$$

with P_{sensor} the pressure in the outlet of the valve, P_{RFQCB} the pressure in the RFQCB chamber, D the diameter of the pipe, L the length of the pipe, M the molecular mass in uma, T the temperature, R_0 the universal gas constant and η the viscosity of the gas at a certain temperature T.

Figure 7.9 shows the gas throughput Q_{gas} calculated as function of the pressure in the outlet of the control valve P_{sensor}. The conductance is calculated for an intermediate flow rate in a standard pipe 1/8 inch (3.125 mm of diameter). The temperature is considered constant at 293 K in the system. To calculate the average pressure, the pressure in the RFQCB chamber is fixed at 0.1 mbar. In these conditions, the viscosity of helium is 193.5 μP [Rot90]. A molecular mass of 4 u is used for helium. Four different curves according to the length of the pipe are plotted ($L = 0.5$, 1, 2 and 10 m). It is seen that the required P_{sensor} to reach a certain value of the gas throughput increases with the length of the pipe. For $L = 10$ m, the value of pressure required would be too high. For that reason, it is necessary that the gas valve is near the main chamber of the RFQCB, even if the gas bottle is then far away from the device.

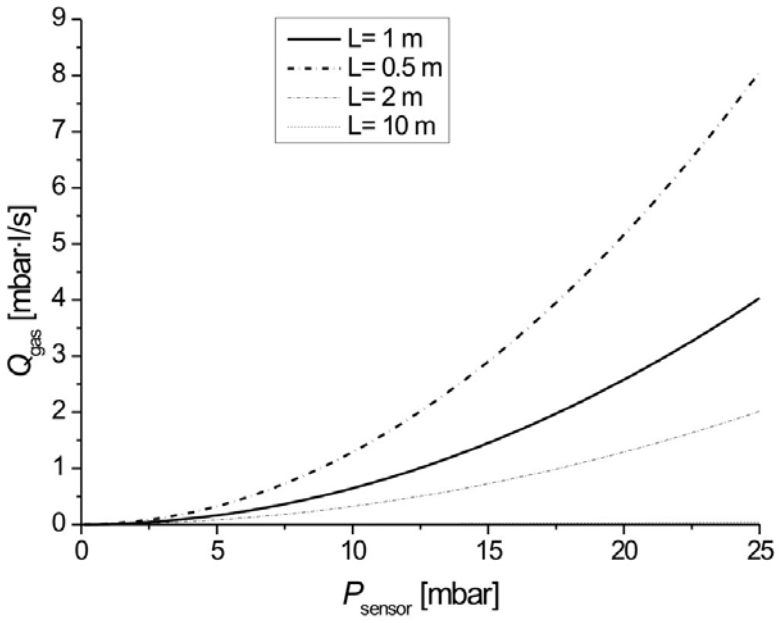

Figure 7.9: Total gas throughput of the system Q_{gas} as function of the pressure at the outlet of the valve P_{sensor}. The calculation is done for helium in a standard pipe 1/8 inch diameter, temperature of 20°C and a pressure inside the RFQCB chamber of 0.1 mbar. Lines for different pipe lengths (0.5, 1, 2 and 10 m) are plotted.

Chapter 8

Mechanical system of ISCOOL

For the ISCOOL project, the mechanical design of the RFQCB has been the most challenging and novel task. This design together with the beam line associated components followed some very specific requirements:

- Flexibility in the test phase. Implying that the inner structure of the cooler has to allow changes without major modifications (*time optimization*).
- The limited space available at ISOLDE, where the machine will be installed, forces the optimization of the dimensions of the RFQCB and all the associated components, such as the insulators, optical elements, bellows and vacuum chambers (*space optimization*).
- From time to time the cooler has to be removed from the ISOLDE beam line in order to carry out some experiments without the cooler (*move operation optimization*).

In the following chapter, the design of the mechanical system which overcomes these problems is detailed. The explanation of the important parts and how they are assembled is discussed. In addition, important topics for the operation of ISCOOL as the alignment are presented.

8.1 Design of the pieces

8.1.1 Axial electrodes

The axial electrodes are one of the most complicate parts to manufacture of the ISCOOL asembly. The four wedges shape (see Chapter 6) made necessary the fabrication with the electro-erosion technique (a charged filament which circulates at fast velocity and removes the material from the part to manufacture). Moreover, the stringent tolerances converts it in a very delicate part of the structure, to assure a correct alignment of all the assembly. Figure 8.1 illustrates the axial electrodes.

Electrodes with 4 different lengths have been manufactured for the first tests: 39 mm, 19 mm and 9 mm (see Fig. 8.1). As explained before, the reason for different lengths is that in the stopping and bunching regions of the RFQCB chamber, the electric field is very steep and has to be better controlled. Therefore, it is better to have more electrodes in those regions. In the medium region, the number of electrodes is less since it is only necessary to adjust a constant electric field around 0.1 V/cm. Table 8.1 shows the standard length for the different axial electrodes (segments). All the pieces were subject of a complete metrology verification to assure that the geometry is according to the specifications.

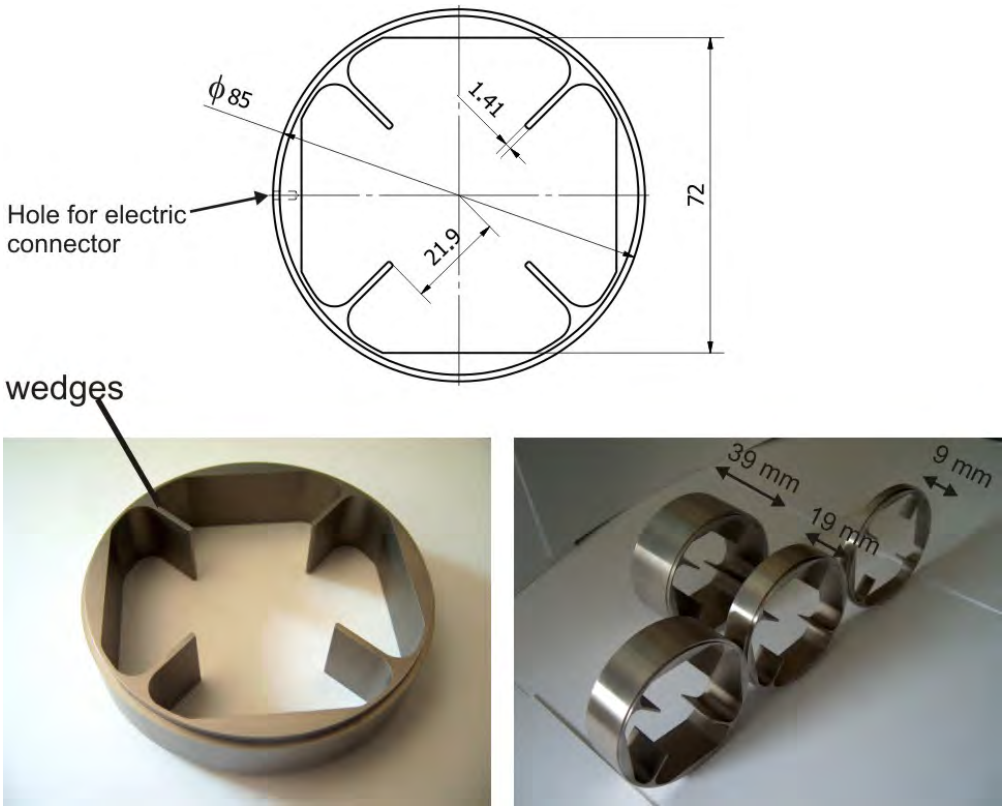

Figure 8.1: Picture of an axial electrode (*left view*) and a group of variable-depth axial electrodes (*right view*)

Segment	**1**	**2**	**3**	**4**	**5**	**6**	**7**	**8**	**9**	**10**	**11**	**12**	
Length [mm]	19	19	39	39	39	39	39	39	39[1]	39	39	39	
Segment	**13**	**14**	**15**	**16**	**17**	**18**	**19**	**20**	**21**	**22**	**23**	**24**	**25**
Length [mm]	39	39	39	39	39	39	39	19	19	9	9	9	9

Table 8.1: List of the usual distribution of segment lengths along ISCOOL. The segments can be swapped or relocated. 1) This segment contains the gas feeding and the length is corrected to give a fine adjustment of all the chamber.

The electrical breakdown in medium vacuum

The needles of the wedges and all the internal parts have been rounded to avoid electrical breakdowns inside the structure. The electric field in a point of the surface of a conductor in equilibrium is defined as:

$$E_n = \frac{\sigma}{\epsilon_0} \tag{8.1}$$

where E_n is the normal electric field to the surface (the other components of the electric field are zero), σ is the superficial density of charge (in a conductor in equilibrium the charge is spread only over the surface) and ϵ_0 is the permittivity in vacuum. In conducting surfaces, the charges accumulate in regions of more curvature (sharp edges). In these regions σ will be very big and thus the electric field in the proximities will be very intense. If this effect is not avoided it could cause a real malfunctioning of the device, limiting the voltage applied to the electrodes or even damaging the power supplies. It is difficult to determine the maximum difference of voltage that can be applied since that depends on the geometry, the gas and the pressure. Some investigations are given in [LJW53, JMM53, HR74, PHR00]. They normally present the Paschen curves (breakdown voltage vs pressure-distance) of helium either out of the region of interest for this work, or for parallel-to-parallel or point-to-parallel electrodes geometries. However, a very promising results were obtained in [Gia02]. It describes that it is feasible to reach up to 5.4 kV between two rods of an RFQCB. The diameter of the experimental device was $d = 10$ mm and the breakdown pressure for helium was 2 mbar. At a voltage of 15 kV the breakdown pressure is still high, 0.8 mbar. Even if these results are promising, it is important to avoid the presence of high fields in all the electrodes to minimize the risk of breakdown. For this reason, the critical points have been rounded, as it will be explained for each piece.

8.1.2 RF electrodes

Together with the axial electrodes, the RF electrodes (see Fig. 8.2) are the most important and delicated pieces of all the ISCOOL assembly. There are four RF electrodes that form the quadrupole which will provide the RF quadrupolar electric field to confine the beam in the transverse direction along the RFQCB chamber. The radius of these pieces is given by Eq. 2.5. At ISCOOL, $r_0 = 20$ mm, therefore the radius of the electrodes is around 23 mm. The rods are not completely cylindrical but are a section of a cylinder. This decreases the weight of the structure.

As discussed before, the corners of the section are rounded to avoid electrical breakdown between the rods and the axial electrodes. Figure 8.3 shows the strength of the electric field in the transverse plane of the RFQCB chamber if the corners of the electrodes were not rounded. It is clear how the maximum it is concentrated in the edges of the electrodes (up to 220 V/mm).

8.1.3 Insulators

Small ceramic insulators

Smaller insulators are needed in order to electrically insulate individual components of the assembly inside the vacuum chamber. The material chosen was aluminium oxide (alumina or Al_2O_3), a ceramic material with good mechanical properties (see Tab. 8.2) and with very high resistivity. In addition, ceramic materials are preferred to plastic ones inside vacuum chambers for their low outgassing and the radiation resistance. The aluminium oxide requires, however, specific tools for the machining.

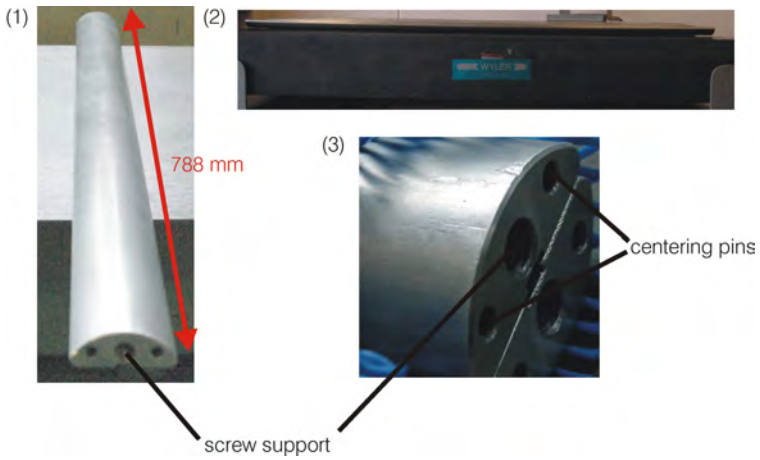

Figure 8.2: Pictures of the RF electrodes: (1) the electrode, (2) image of the electrode for a flat surface measurement, (3) detail of one of the sides with the tapped holes for the support and holes for the angular centering of the electrodes.

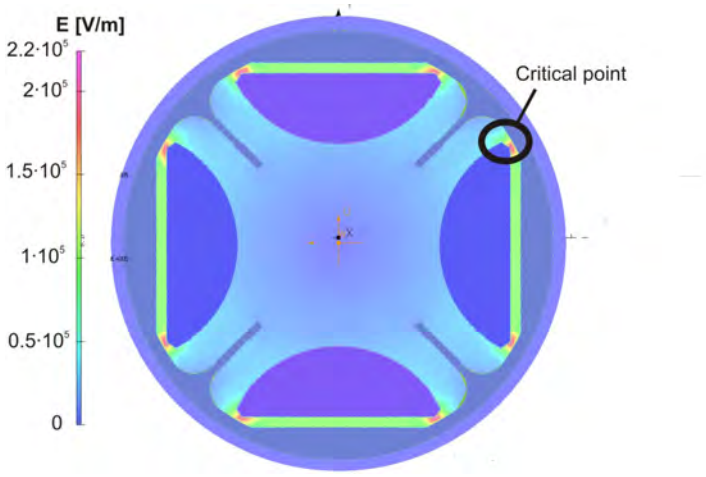

Figure 8.3: Simulation with OPERA of the strength of the electric field at the RFQCB chamber if the electrodes wedges are not rounded. The RF electrodes are at ± 200 V and the axial electrode at ground.

The most complicated pieces are those supporting the injection and the extraction electrodes and which are connected to the main vacuum chamber (see 1 in Fig. 8.4). In the injection side, the electrodes have to provide a differential potential insulation of less than 10 kV, but in the extraction side the potentials are around 20 kV. The aluminium oxide has a dielectric rigidity bigger than 10^{12} kV/mm, so only 2 mm of material is enough to carry out the electrical insulation.

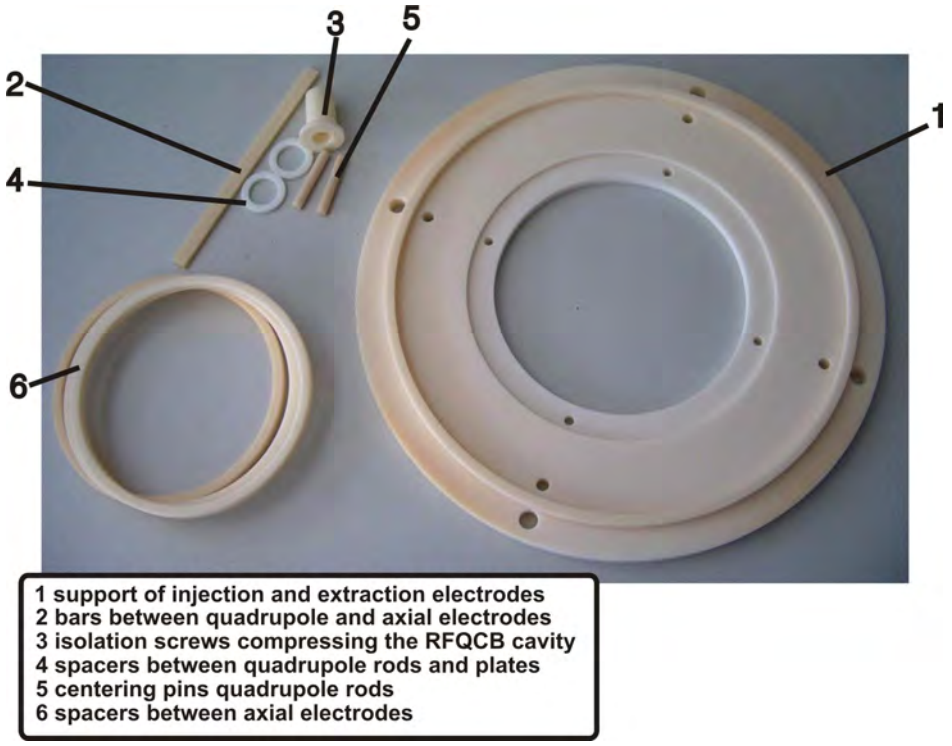

Figure 8.4: Group picture of the alumina pieces used for the assembly and electrical isolation in ISCOOL.

High voltage insulators

As the machine has to operate at a maximum 60 kV potential, it has to be electrically insulated from other components of the beam line which are grounded and from the environment surrounding the device. Various types of high voltage electrical insulators have been used at the ISCOOL assembly:

- Three large ceramic insulators of alumina with DN200 ISO-K flanges for use in vacuum on both sides of the beam line. These insulate the main pump TP1 from the main chamber (see Fig. 8.5). The external shape of the insulator is ondulated in order to maximize the path to avoid an electrical breakdown. In that way, the total length of the insulator can be reduced to 190 mm including the ISO-K flanges. The length of the ceramic is only 130 mm.

- 4 plastic (TEFLON) electrical insulators to separate the main chamber and the alignment system from the trolley (see Fig. 8.6). Similar ondulactions are also applied to these insulators, reducing the total length to only 170 mm.

Property	Unit	F99.7
Density	kg/mş	3900
Compressive strength	Pa	$3.5 \cdot 10^9$
Modulus of elasticity	Pa	$3.8 \cdot 10^{11}$
Weibull-modulus	-	> 10
Poisson-Zahl	-	0.22
Poisson number	%	0
Maximum operating temperature	°C	1950
Coefficient of expansion	10^{-6}/K	8.5
Specific heat 20 °C	J/kg·K	900
Thermal conductivity 100 °C	W/m·K	30
Specific resistance 20 °C	Ω·m	10^{14}
Colour	-	white

Table 8.2: List of the main mechanical parameters of the aluminium oxide with purity 99.7% (F99.7) involved in the design of ISCOOL [DE].

Figure 8.5: Picture of a high voltage ceramic insulator

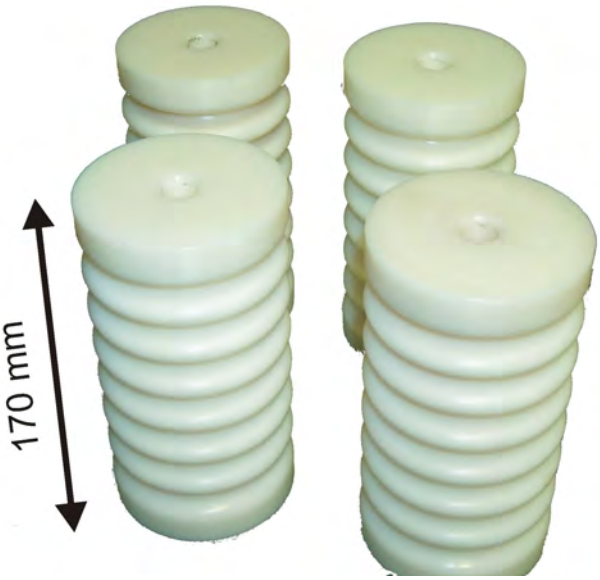

Figure 8.6: Picture of the support high voltage insulators

8.1.4 Main vacuum chamber

The RFQCB chamber of ISCOOL has to be enclosed in a high quality vacuum chamber. The main vacuum chamber is designed with a top rectangular flange which serves as support for the RFQCB structure. The flange can be lift up, giving easy access in case modifications or urgent interventions are required.

Some mechanical simulations of both the top flange and the assembly of the vacuum chamber, has been done in order to verify the deformation once the vacuum is established inside the chamber (simulated by applying uniform distributed atmospherical pressure to all the external faces). In the case of the top flange, the simulations were focused in the main deformation at the points where the pieces that support all the RFQCB structure are screwed. The results are shown in Fig. 8.7, the maximum deformation is about 90 μm for the middle point. At the points where the supports of the RFQCB structure are screwed, a deformation of only about 30 μm is found (see Fig. 8.7).

Vacuum simulations of the main vacuum chamber were also performed in order to verify whether the deformation of the body could affect the alignment of the RFQCB structure, and to test its rigidity. The simulations were carried out using a first version of the main vacuum chamber supported by four rectangular foots. It turned out that the worst areas were the side walls of the chamber (U-shape) and therefore should not affect the internal alignment of the structure. In this region, a maximum deformation of about 1 mm was calculated. The result was verified by two different software programs (ANSYS and CASTOR). Figure 8.8 illustrates the deformation of the chamber obtained with ANSYS. The maximum deformation calculated with ANSYS was a bit lower than with CASTOR but in the same range.

Even though the deformation was acceptable, it was decided to stiffen the chamber varying the design of the feet. The four rectangular feet were changed for two feet with U-shape welded to the walls of the chamber, that avoid the horizontal deformation of the main body.

A picture of the real main vacuum chamber is shown in Fig. 8.9. The vacuum test with an

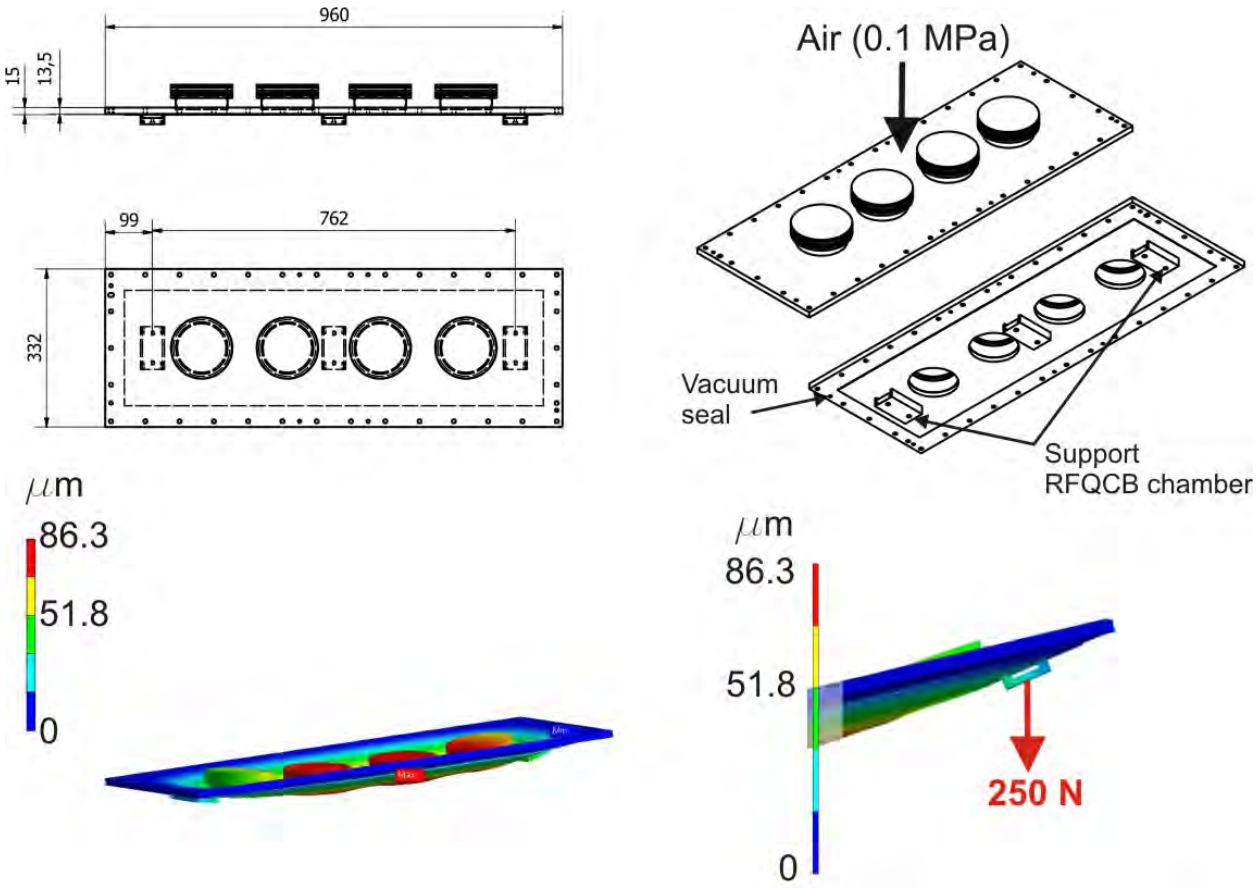

Figure 8.7: Dimensions (*top*) and simulation of the deformation (*bottom*) of the top flange of the main vacuum chamber. The total deformation caused by the air-vacuum pressure and the weight of the RFQCB chamber (bottom right) is shown.

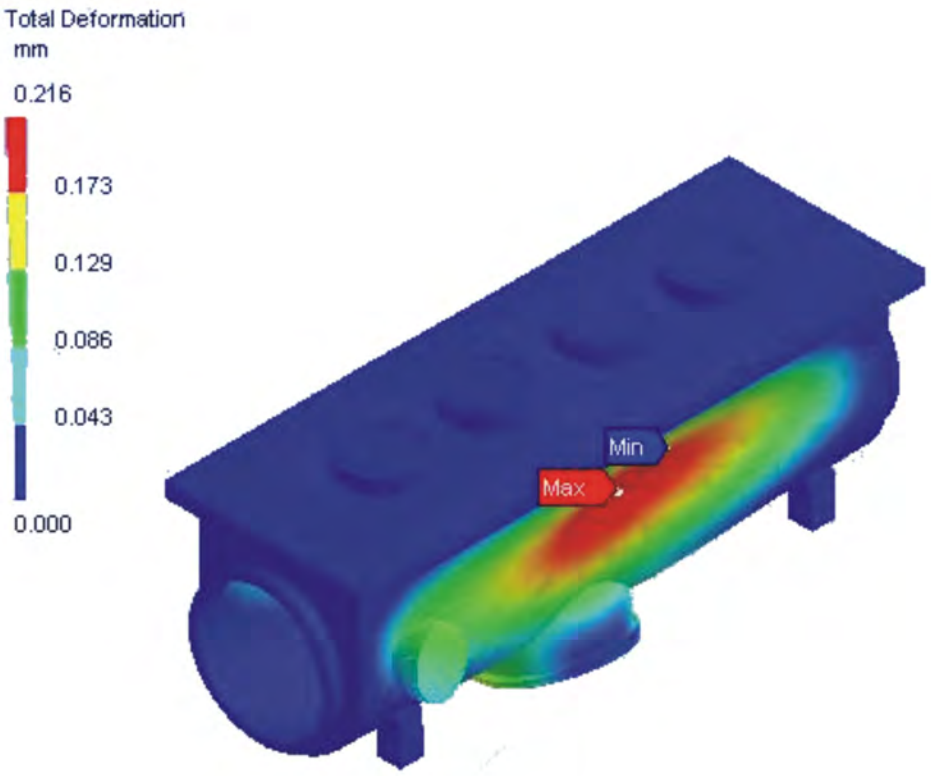

Figure 8.8: Simulation of the deformation of the vacuum chamber under atmospheric pressure using the ANSYS code.

empty chamber turned out an ultimate pressure of 10^{-9} mbar, which is very satisfactory for an ISO-K system.

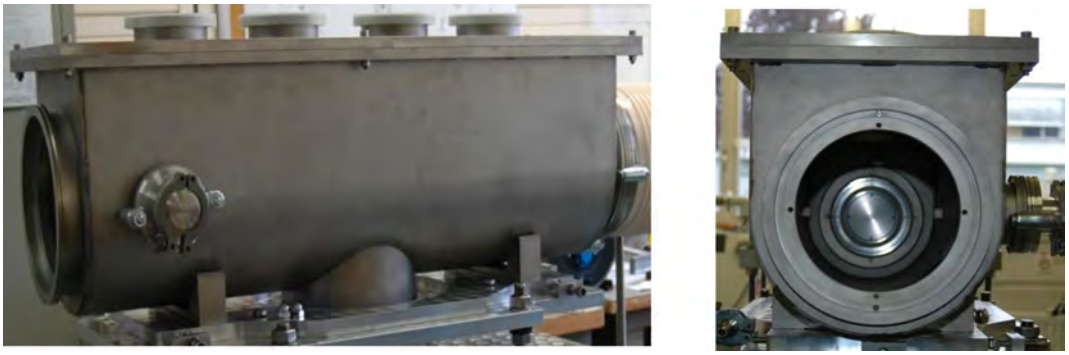

Figure 8.9: Picture of the main vacuum chamber: global view (*left*) and inner view along the axis (*right*).

8.1.5 Trolley

The support of the main vacuum chamber was designed to fulfill the following features:

- Possibility to move ISCOOL along the ISOLDE hall.
- Alignment of ISCOOL with the rest of the beam line.
- Electrical insulation of the main vacuum chamber from the ground.

The first feature, the mobility of the system, is achieved by installing the RFQCB on a movable trolley. Figure 8.10 illustrates the different parts of the trolley and the alignment system which support the RFQCB main chamber at high voltage. The alignment consists of three alignment points that will be screwed into the fixed points of the ground, assuring a proper alignment of the trailer each time.

The chassis, metallic structure supporting the beam line (left view in Fig. 8.11), was designed using square tubes 60x60 and 3 mm depth that are welded. The mechanical deformation was also tested with ANSYS. Four loads of 250 kg (P_1 in the right view of Fig. 8.11) were shared out at the four metallic sheets holding the four electric insulators. Using this environment, a maximum deformation of 20 μm was found at these sheets.

8.1.6 Ground electrodes

The ground electrodes, at the injection and the extraction, have two purposes: 1) to define the ground potential and the shape of the electric field inside the HV insulators (see Sec. 8.1.3), and 2) to protect the insulators from unwanted charge up.

The electrode structure is packed between the high voltage insulator (60 kV) and the bellow, and supported by an O-ring DN200 ISO-K. The following structure is divided into two different sections: a conical support and a sliding cylindrical electrode. Figure 8.12 shows the image of one of the ground electrodes, detailing all the parts. The sliding system is assembled with the cone by an external screw which allows the cylinder to slide and be fixed in a certain position. In that way, the distance between the ground electrode and the next electrode can be varied $\sim$100 mm.

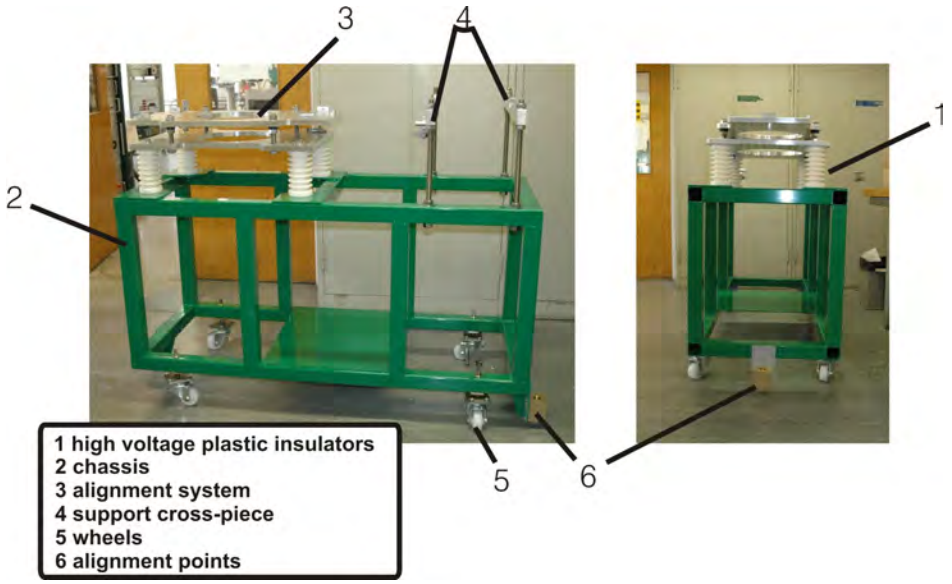

Figure 8.10: Picture of the assembly of the trailer, the alignment system and the insulators for the high voltage.

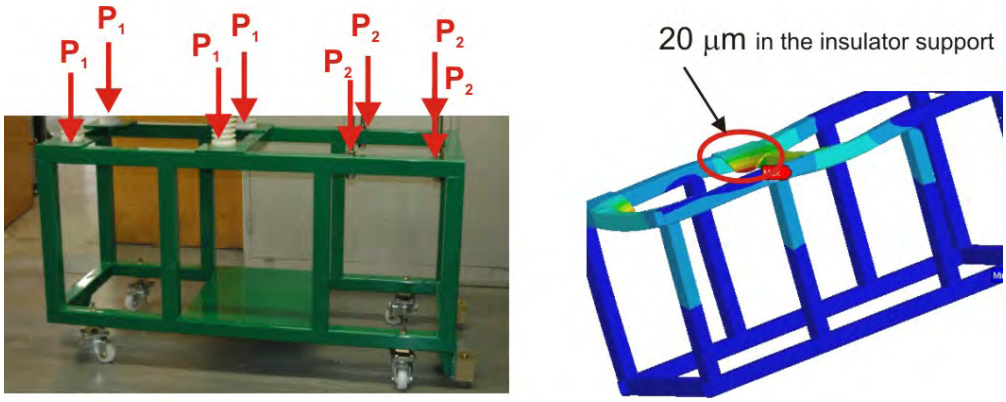

Figure 8.11: Chassis of the trolley assembly. Left view: simulation of the mechanical deformation due to weight of the beam line using the ANSYS code. Right view: picture of the part. P_1 are the load caused by the weight of the main vacuum chamber and equipment associated, and P_2 the load caused by the extraction cross-piece and equipment associated.

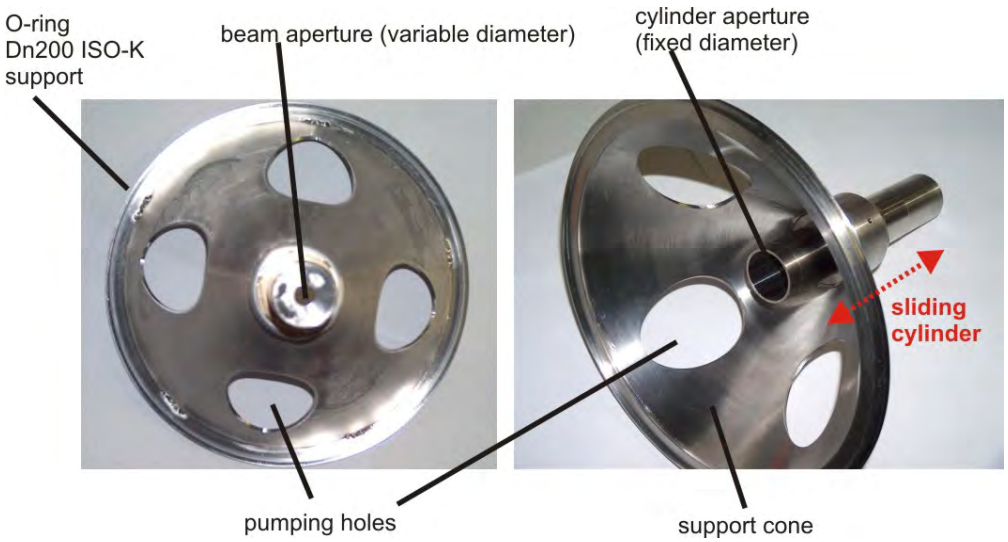

Figure 8.12: Picture of a ground electrode: top view showing the beam aperture (*left side*) and view showing the sliding system and the cone (*right side*).

The distance of the injection ground electrode with the first injection electrode, and of the extraction ground electrode with the second extraction electrode is very short in comparison with the length of the high voltage insulator (see Fig. 8.20 and 6.10 respectively). This is possible due to a higher breakdown voltage in the vacuum. Normally a rule of thumbs of 1 mm/kV is applied. Anyhow such a big differential potential (∼50 kV in the injection side) might be a problem if too short distances are demanded. Therefore, all the corners of the electrode are rounded to avoid concentration of charges that can lend to electrical breakdowns.

8.2 RFQCB chamber assembly

The RFQCB chamber assembly consists basically of a stack of variable-depth axial electrodes, separated by ceramic insulators (see Fig. 8.13). A more detailed view of the packing system is presented in Fig. 8.14. The quadrupole rods are surrounded by the axial electrodes with four-wedges which enter into the quadrupole structure. The axial electrodes are used to create the necessary axial potential. The wedges configuration reduces the required voltages (see Sec. 6.3.3). The axial electrodes are spaced and electrically insulated by ceramic insulators of 3 mm.

A first verification of the assembly concept was done during the construction phase (see Fig. 8.15). No special problems were found during the assembly, even though some of the insulators (especially the small rings spacing the bars), were found quite fragile during the compression phase. The other delicate point during the set-up was the placement of the centering pins made of ceramics which fix the angular orientation of the RF electrodes. If the misalignment among the supports is too big, the pins can break or not enter due to the small mechanical tolerances.

8.2.1 Support of the RFQCB chamber

The RFQCB chamber has to be kept together and well aligned along the optical axis of the beam line. To guarantee both conditions, some supports are used in both sides of the RFQCB chamber. A

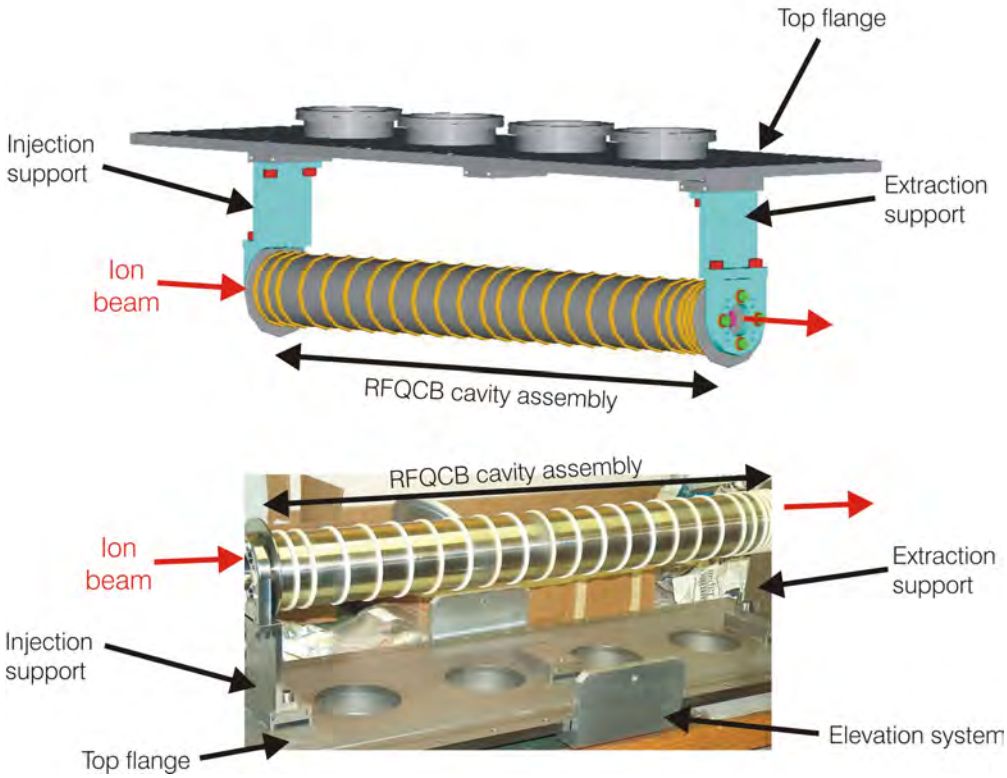

Figure 8.13: Stack of axial electrodes and insulators that encloses the quadrupole. The design with CAD tools (*top view*) and the real structure (*bottom view*) are pictured for comparison. The supports of the structure and the top cover of the main vacuum chamber are also presented.

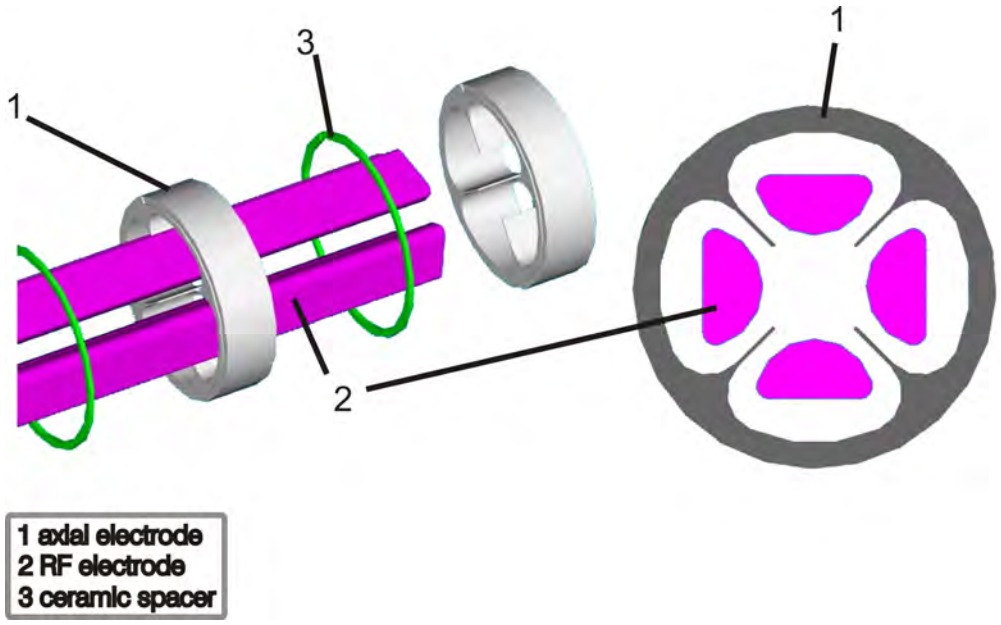

Figure 8.14: Sketch of the assembly of the RQFCB cavity (*left view*) and design of the quadrupole and the axial electrodes with the four wedges (*right view*).

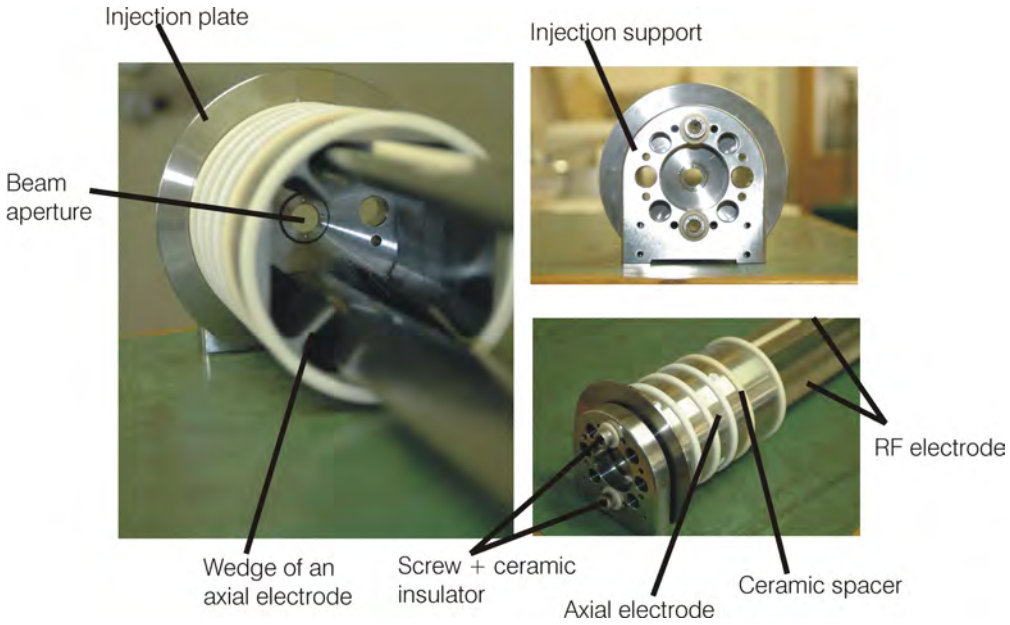

Figure 8.15: Pictures of a first assembly of the RFQCB chamber from different points of view: internal view of the cavity showing the axial electrodes separated by the ceramic spacers and supported by only two RF electrodes (*left view*); front view of the cavity, the hole where the beam is passing through is shown (*top right*); assembly of the RF electrodes with the injection plate and the injection support using screws, again only two RF electrodes bars are used (*bottom right*).

first support (2 in Fig. 8.16) gives the depth to screw the four RF electrodes and, at the same time, all the axial electrodes are compressed and separated by the ceramic spacers. This piece has four holes for the screws of the four RF electrodes, and eight holes which serves to a good alignment of the RF electrodes. A big central hole avoids an increase of the pressure in the region created together with the RFQCB chamber. This is extremely important in the extraction side, where high pressures can blow up the cooled ion beam.

Two pieces connect these supports to the top flange of the main vacuum chamber (1 in Fig. 8.16). The RFQCB chamber is therefore directly supported by the top flange. In this way it is possible to lift together the top flange and the RFQCB chamber easily using a crane or similar device. In addition, the extraction support allows a small axial displacement of all the structure to absorb the thermal dilation of the quadrupole rods if the system is baked out. This displacement is calculated to be around 2 mm for one of the quadrupoles rods (788 mm long, made of stainless steel 304 L with thermal dilation coefficient 17.2 μm/m·K) for a bake-out temperature of 150°C. In the case of the alumina the thermal dilation coefficient is smaller (8.5 μm/m·K), so the external part of the RFQCB chamber (axial electrodes and ceramic insulators) is expanding a bit less, around 1.8 mm.

Elevation system

A special elevation system for handling the assembly has been constructed and is used for the insertion/extraction of the RFQCB chamber assembly into the main vacuum chamber. The system permits the rotation of the RFQCB chamber assembly together with the top flange and it is stable either with the RFQCB chamber up or with the RFQCB chamber down thanks that the axis of

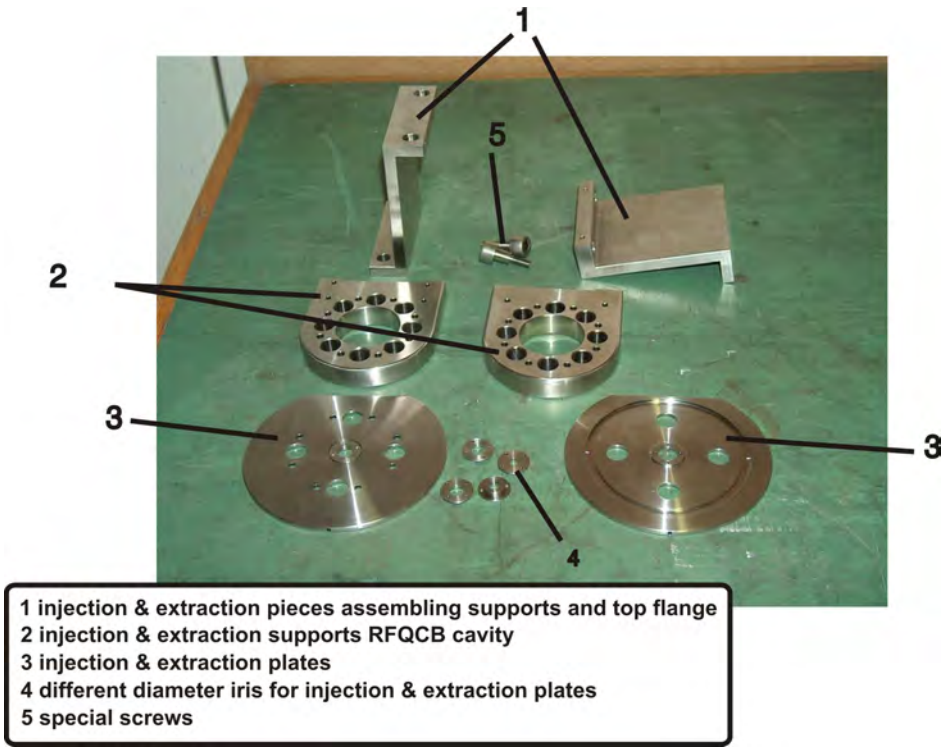

Figure 8.16: Picture of different parts related to the support and assembly of the RFQCB chamber with the top flange of the main vacuum chamber.

rotation was calculated to pass by the center of gravity of the system. The calculation was done with Autocad Mechanical Desktop using the right density for the materials: $3.98 \cdot 10^{-3}$ kg/m^3 for Al_2O_3 (electric insulator pieces) and $7.84 \cdot 10^{-3}$ kg/m^3 for stainless steel (rest of pieces). The center of the assembly of the RFQCB chamber+top cover is placed $\sim$ 60 mm down from the external rectangular surface of the top cover. As a matter of interest, the mass of the system is ~ 62 kg.

8.3 The electrodes inside the main vacuum chamber

The electrodes that are supported from the main vacuum chamber can be divided in three different groups from the mechanical and optics point of view. Figure 8.17 details the electrodes forming the structure of ISCOOL. Only the ground electrodes (injection and extraction) are not presented. The first group is made of the injection electrodes that decelerate and inject the beam into the RFQCB chamber (see Fig. 8.20), the second part corresponds to the electrodes part of the RFQCB chamber (see Fig. 8.17) and the last part is about the extraction electrodes to accelerate the beam to the initial longitudinal energy (see Fig. 8.22).

The injection and extraction electrodes are supported by the main vacuum chamber through an ceramic insulator whose main function is to electrically insulate both electrodes from each other and the vacuum chamber.

In the injection side (see Fig. 8.19), both electrodes are to simulate flat surfaces with cylindrical holes in the center for the passage of the ion beam. To accomplish the required distance coming from the beam optics simulation, and the constraints derived from the supports of the RFQCB

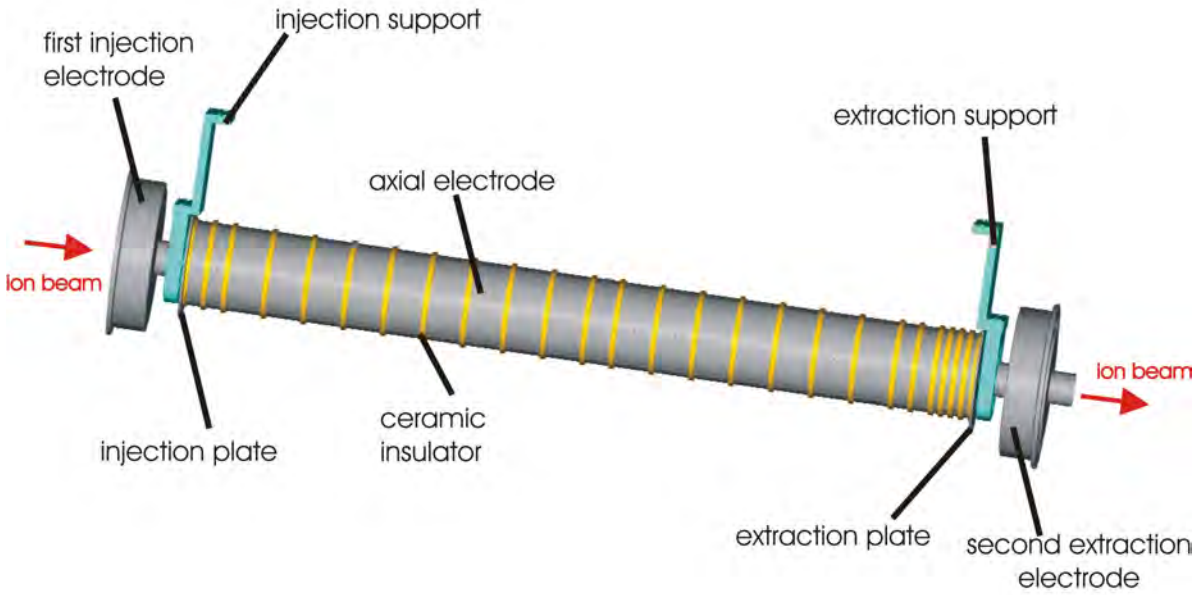

Figure 8.17: Representation of the electrodes attached to the main vacuum chamber.

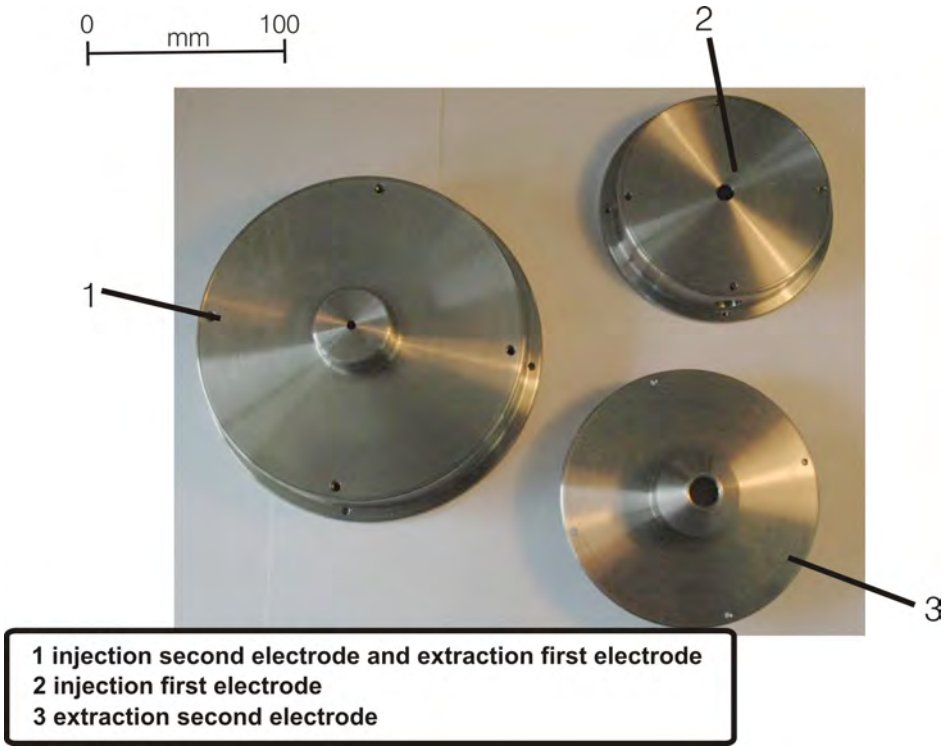

Figure 8.18: Picture of the injection and extraction electrodes.

chamber, the second injection electrode cannot be a complete flat surface but it is manufactured with a central region which enters into the structure of the RFQCB chamber support to approach it to the injection plate without disturbing the optics (see part 2 in Fig. 8.18). Simulations with SIMION has shown that the electric fields in the central region (interesting for the ion beam) are not perturbed by this modification in the shape of the electrode. The first injection electrode has a more typical shape with a flat surface (see part 1 in Fig. 8.18). The electrodes are manufactured in two separate parts which are assembled with screws. This is done to make it easier to modify the diameter of the holes or shape of the electrodes. In addition, the distance between the injection electrodes, or the distance to the injection plate, can be modified by adding some washers to the screws. The assembly is shown for the injection side in Figs. 8.19 and 8.20.

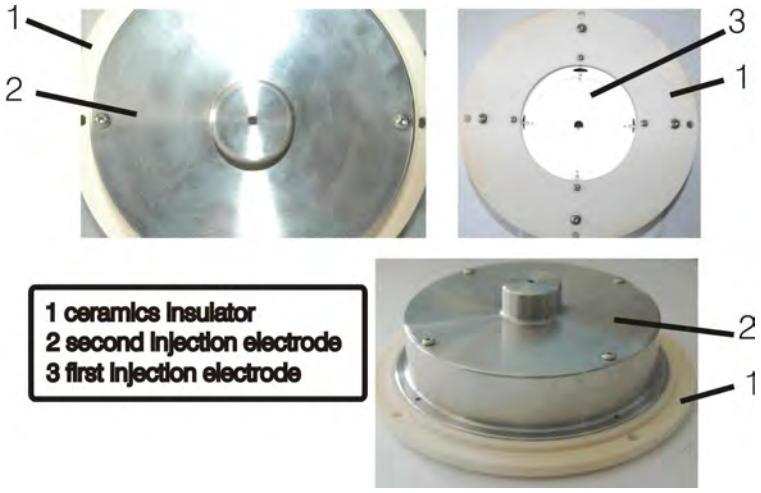

Figure 8.19: Picture of the injection optics electrodes assembled with the ceramics insulator.

In the extraction side (see Fig. 8.21) the problem is very similar to that discussed above for the injection side. The first extraction electrode looks mostly identical to the second injection electrode, with only difference in diameter of the center hole due to optical reasons. The second extraction electrode is totally different of the first injection electrode and it is manufactured in one part. The central region is formed up by a combined piece with a cone shape in a first section and a cylindrical shape thereafter (see 3 in Fig. 8.18). The assembly is shown in Figs. 8.21 and 8.22.

The study of the quality of the extraction electric field with the real mechanical electrodes shape is shown in Fig. 8.23. If it is compared with Fig. 6.11, it appears that the potential are not modified along the axis of the quadrupole. The conclusion is, thus, that the mechanical shapes of the electrodes do not affect the extraction of the ions. The same results may be extrapolated to the injection part, since the electrodes configuration is similar and even more simple from the mechanical point of view.

Finally, Figure 8.24 shows the schematic assembly of the electrodes inside the main vacuum chamber. The main parts (injection, RFQCB chamber and extraction) are indicated. With this configuration, and with manufacturing tolerances down to 20 μm for some of the supports, the electrodes of the main chamber (injection electrodes, injection and extraction plates of the RFQCB chamber and extraction electrodes) have a maximum misalignment of 200 μm.

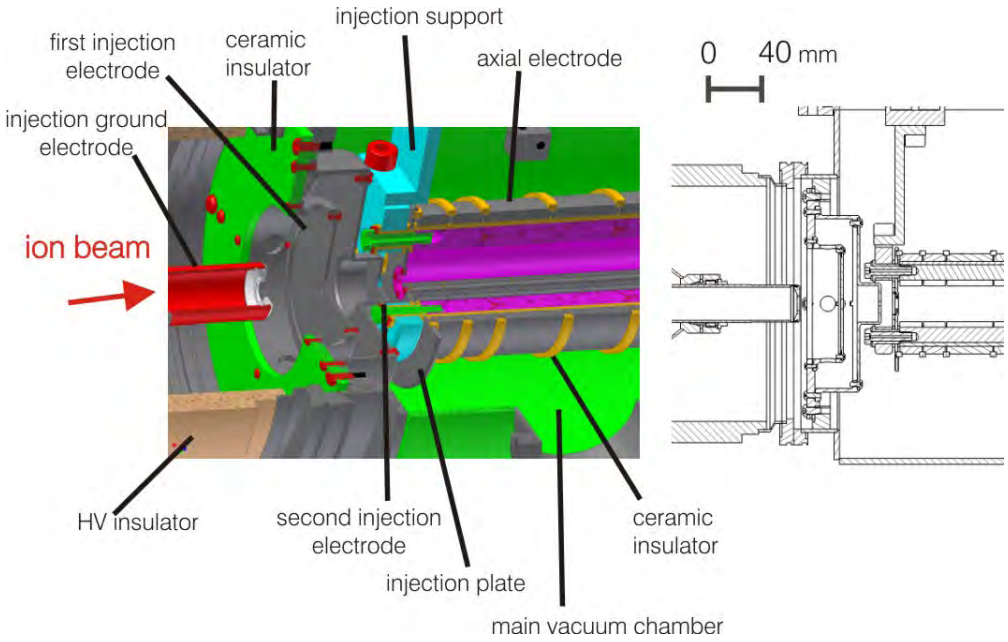

Figure 8.20: Representation of the injection part of ISCOOL. The injection ground electrode, which is not attached to the main vacuum chamber, is also represented here. The high voltage insulator is also shown.

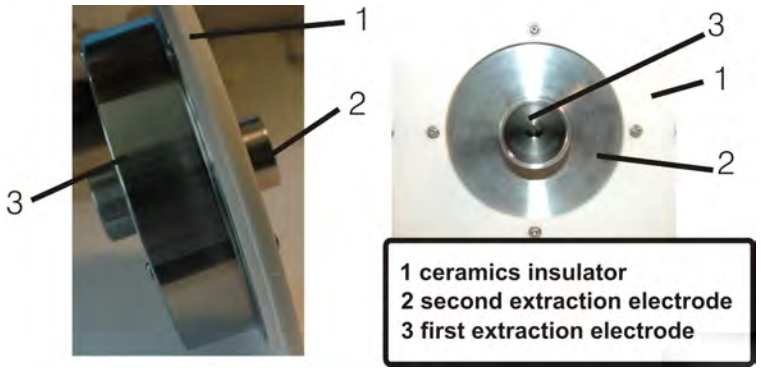

Figure 8.21: Picture of the extraction optics electrodes assembled with the ceramics insulator.

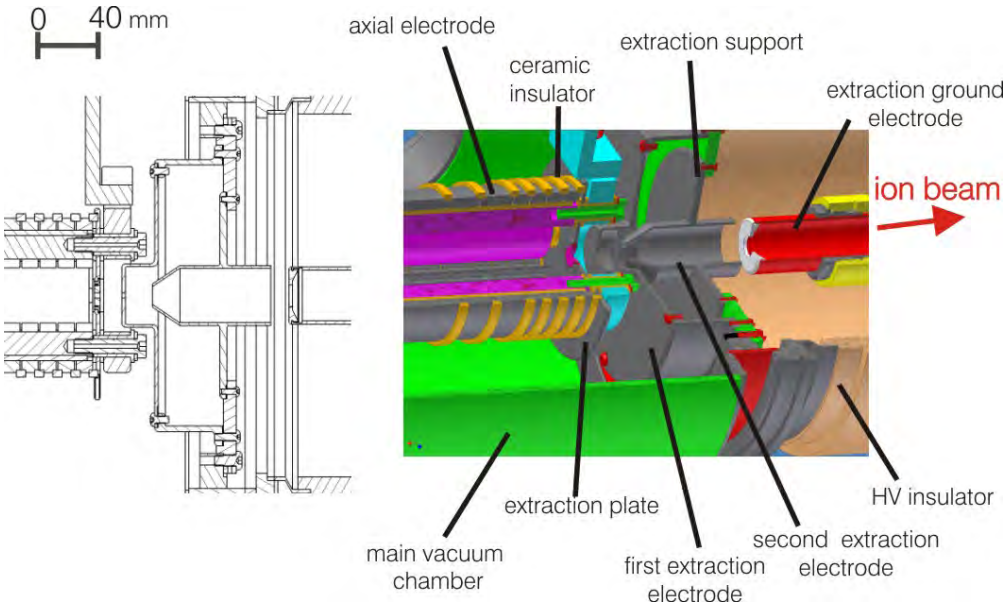

Figure 8.22: Representation of the extraction part of ISCOOL. The extraction ground electrode, which is not attached to the main vacuum chamber, is also represented here together with the high voltage insulator.

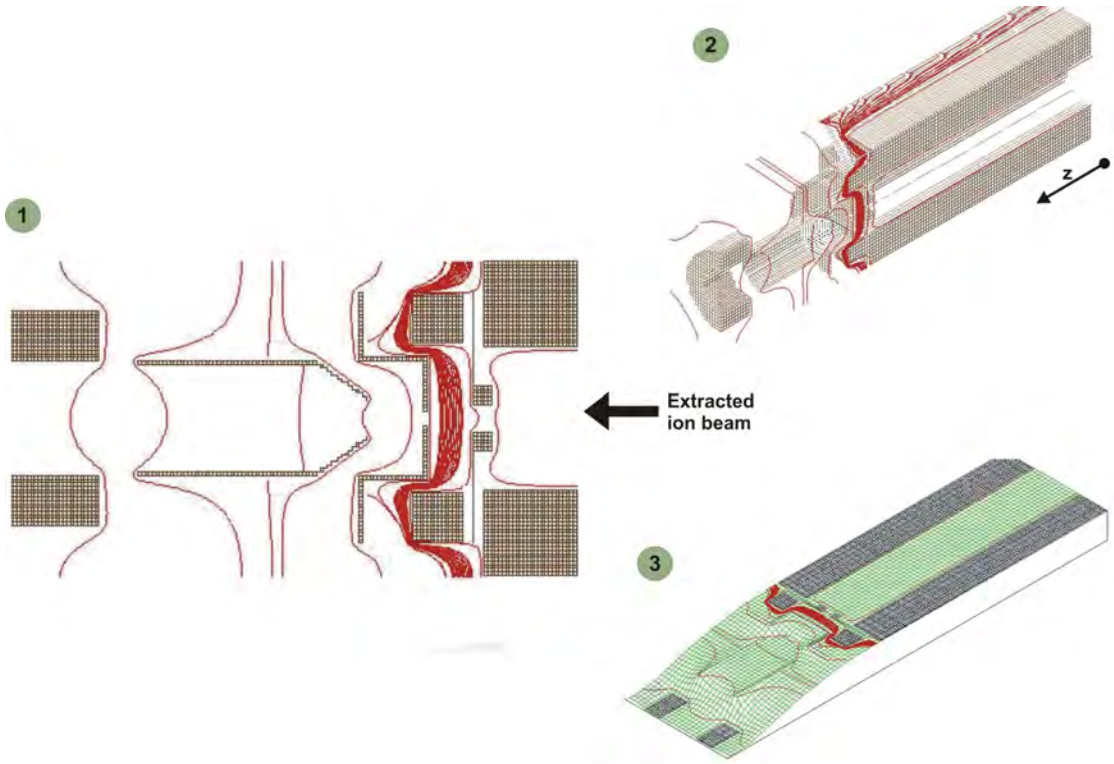

Figure 8.23: Simulation of the extraction optics of ISCOOL with the real geometry: 1) Longitudinal cut, 2) 3D half cut, 3) 3D representation of the electric potential in the moment of the extraction. The equipotentials lines are shown and may be compared with those ones of the ideal geometry in Fig. 6.11.

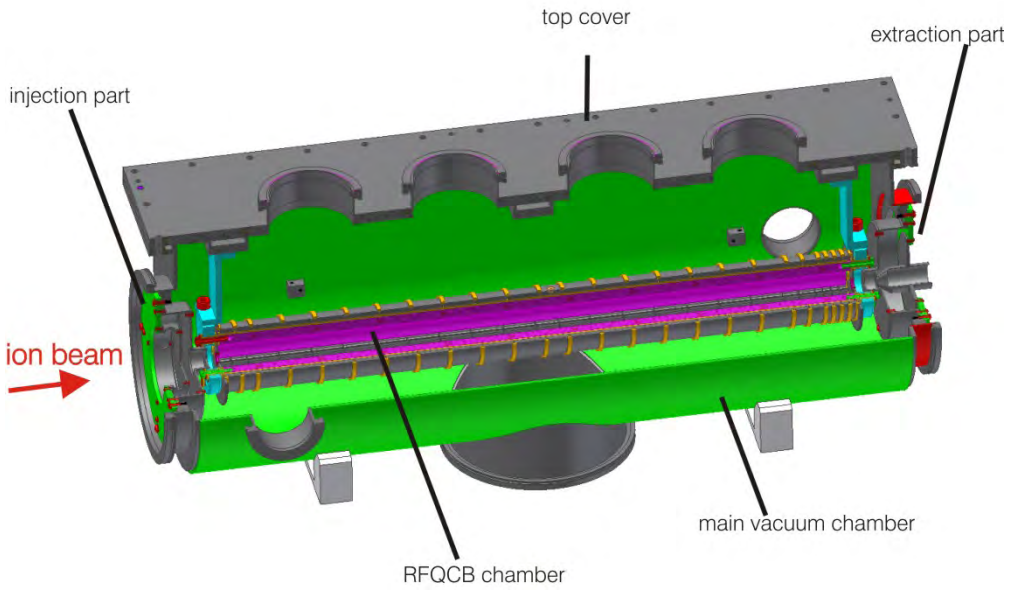

Figure 8.24: Three quarters section of the main vacuum chamber with the injection electrodes, the RFQCB chamber and the extraction electrodes assembled.

8.4 Alignment system

At present, the alignment at ISOLDE is done without using reference points or girders along the beam lines. Therefore, the alignment of new elements added to the ISOLDE beam line or the replacement of existing elements has to be carefully thought out, since a direct optical alignment has to be done. For the new ISCOOL beam line, a reference point to align the present beam line is placed on the floor inside the HRS area (point E in Fig. 8.25). This region is a restricted area with high radiation levels during the operation period, so the alignment of ISCOOL with the beam line can only be done during the shutdown period.

The final alignment of the vacuum chamber with the beam line will be done using a system of metallic plates which allow the technicians to adjust the system in the three coordinates: vertical, horizontal and longitudinal. The first alignment has to be done using the reference alignment point of the existing beam line, which is placed in the separator section (see Fig. 8.25).

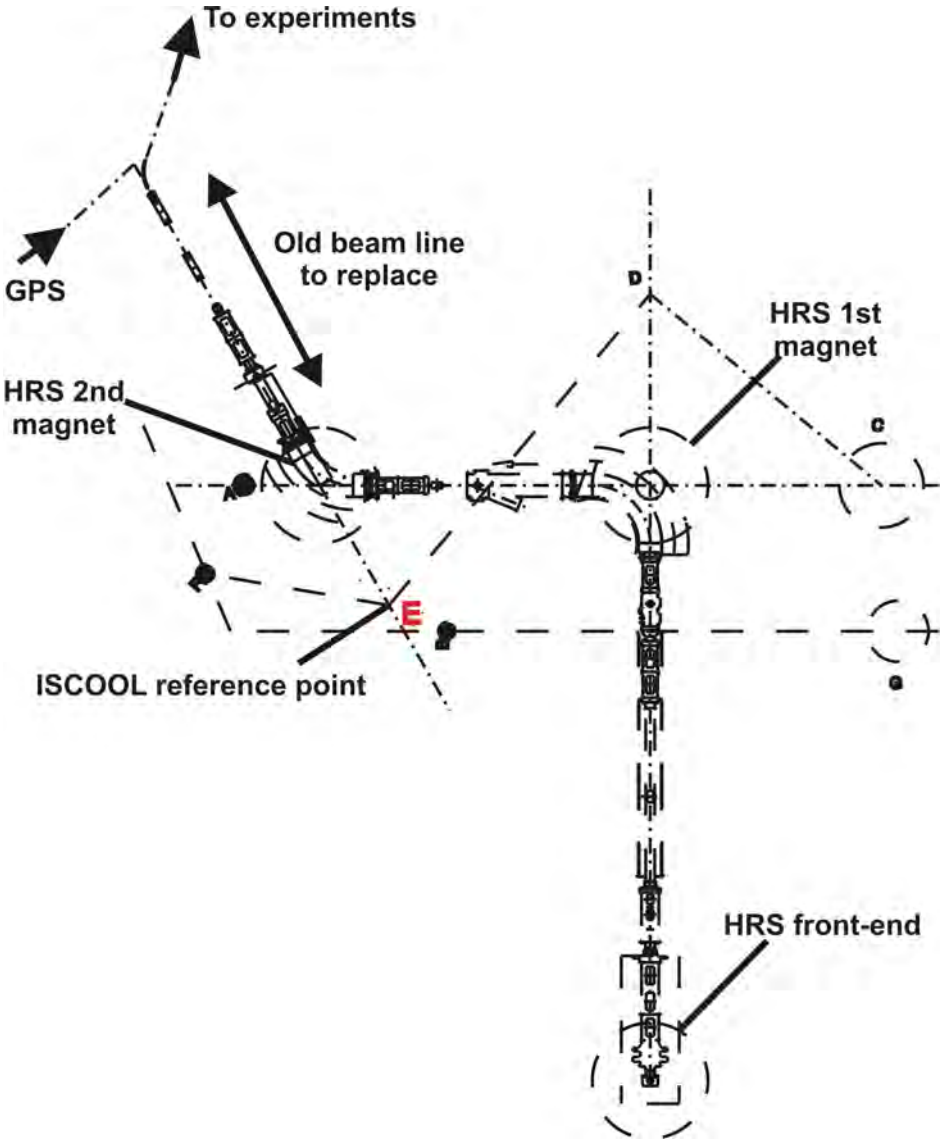

Figure 8.25: Layout of the alignment geometry of the reference point -E- for the HRS-merging switchyard section [Cho].

Chapter 9

Electronics and control system of ISCOOL

9.1 The electronics system

The RFQCB's are operating in medium Radio Frequency frequency range, which extends from 300 kHz to 3 MHz. This differs from the RFQ accelerating cavities where this range is up to some hundred of Gigahertz (ultra high and super high frequency). Although that seems to simplify the task of the RF engineers, the specifications of this device make the RF supply design quite challenging. To tune the operation parameters of the RFQCB, it is necessary to have the freedom to independently play with the amplitude and the frequency of the RF in a wide range. However, the system has been in this case simplified thanks to decoupling the electrostatic axial field from the RF. However, these power supplies have to assure good accuracy and stability for an efficient beam trapping. The fast-switch of the potential well in the last section of the RFQCB chamber is another task that is discussed along this chapter. The supplies for all the electrodes are placed on a high voltage platform to minimize the amplitude of the voltages. The primary power of the power supplies (380 V at 60 kV) is delivered by an insulation transformer.

In addition, some other aspects are important for the design of all the electronics devices of ISCOOL, like the hardware compatibility with the ISOLDE control system and existing devices and the cost of all the system. In the next sections a further discussion about the design of the requirements for all the components of the electronics system is given and the final options chosen are explained.

9.1.1 Global layout

Figure 9.1 shows the scheme of the electronics components for the new ISCOOL beam line. The RF supply, the power supplies for the axial electrodes (AX1 to 25), the injection and extracion plates (INJP and EXTP) and the high voltage power supplies for the injection (INJ1 and INJ2) and extraction electrodes (EXT2) work on a 60 kV high voltage platform. An insulation transformer provides 380 V at 60 kV. The scheme also represents the fast switches between the power supplies for the latest axial electrodes. Some HV power supplies on ground are required for the electrodes of the injection and extraction quadrupole triplets. In addition, the safety switches that protect the system in case there is overpressure inside the vacuum chambers, or the high voltage is open whilst the HV is turned on.

All the control units and devices related to the RF amplification are placed on the HV platform, due to the RF voltage amplitude applied to the quadrupole is biased to the HV. The oscillator head is located over the ISCOOL top flange, close to the RF vacuum feedthroughs. The reason is that

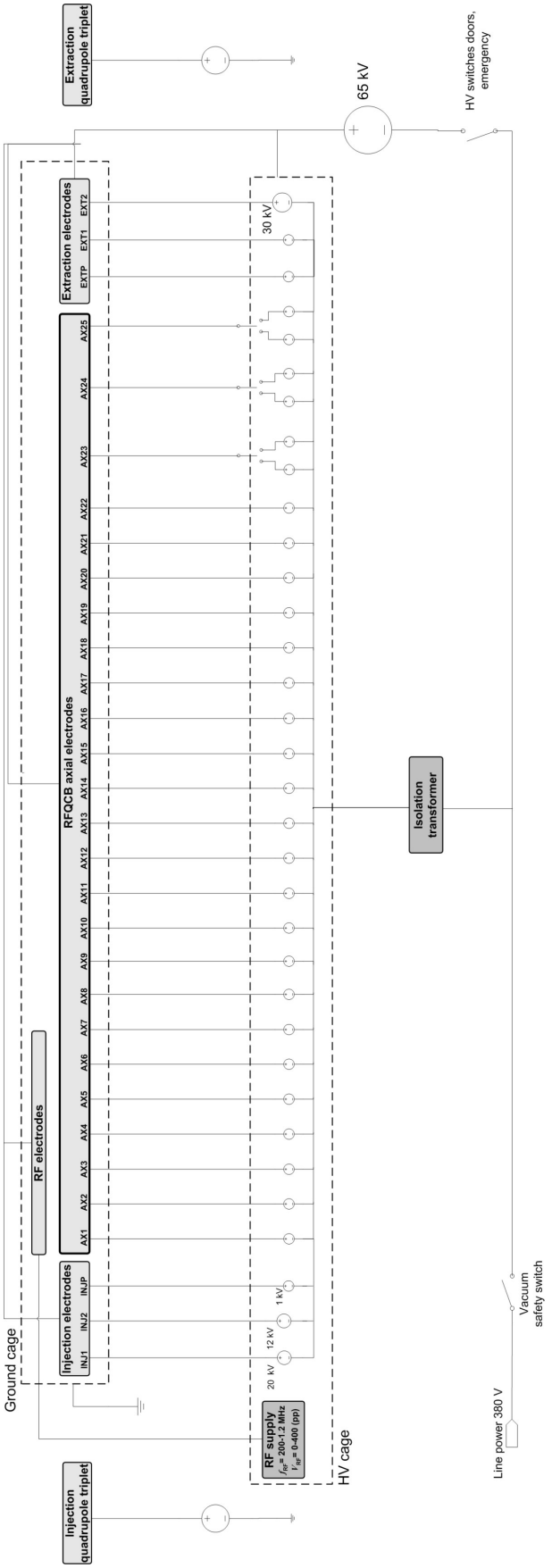

Figure 9.1: Scheme of the electronics system for the new ISCOOL beam line.

the longer the distance between the RFQCB chamber and the oscillator, the greater the capacitance of the system due to the additional capacitance of the cables. The feedthroughs used for the RF are made of copper capable to handle voltages up to 12 kV and temperatures from -269 °C up to 450 °C. One feedthrough is placed for each of the 180° shifted RF signals (RF+, RF-). Each one has a measured capacitance of 20 pF against the ground and of 10 pF against the electrodes.

9.1.2 Radio frequency amplifier

The RF electric quadrupole field necessary for the operation of ISCOOL cannot be supplied by typical commercial wave function generators due to the high voltage amplitude, which is out of the range of the standard devices. The procedure necessary to design such a device is:

- Define the frequency voltage and amplitude voltage range according to the stability constraint q defined in Eq. 4.11.
- Simulate and calculate the capacitance of the RFQCB chamber.

Different options are presented for the RF amplification. One solution is the use of a commercial function generator and a **broadband amplifier** together with a transformer. This solution has been used in other devices [Her01, Rod03]. The drawback of this solution is the cost. The complete system (function generator, broadband amplifier and transformer) is expensive due to the demanding technical specifications. Another proposed solution was the use of a **self-tuned oscillator** in frequency and amplitude. With two input signals using DC power supplies (magnet current and voltage amplitude), it is possible to get an output signal according with the specifications.

Simulations of capacitance of the RF field

Some simulations were performed to check the capacitance that the RF device would have to handle. After some attempts with different electric field simulation programs, the simulations were done using the Opera code. The model was imported from a CAD software (Mechanical Desktop in this case). Therefore the simulations are carried out with the designed pieces, although with surface simplifications to minimize the amount of required computer hardware.

The capacitance was calculated making an analysis of an electrostatic field applied to the RF electrodes. The axial electrodes are simplified by a continuous vacuum chamber connected to ground. The capacitance can be calculated using the expression:

$$W = \frac{CU^2}{2}, \tag{9.1}$$

where W is the stored energy of the electric field, C the capacitance and U the voltage between the two electrodes of the capacitor. In the case of the quadrupole with the vacuum chamber (axial electrodes), the system is a bit more complex as shown in Fig. 9.2. In this figure, C_1 represents the capacitance between the two pair of opposite quadrupole rods, and C_2 the capacitance of the rods with the chamber, U_1 the voltage applied to one pair of opposite rods, U_2 the voltage to the left pair and U_3 the voltage applied to the axial electrode. Symmetry of the system around the longitudinal axis is assumed. The expression for the stored electrostatic energy reads:

$$W = \frac{1}{2}\left[4C_1(U_1 - U_2)^2 + 2C_2(U_1 - U_3)^2 + 2C_2(U_2 - U_3)^2\right]. \tag{9.2}$$

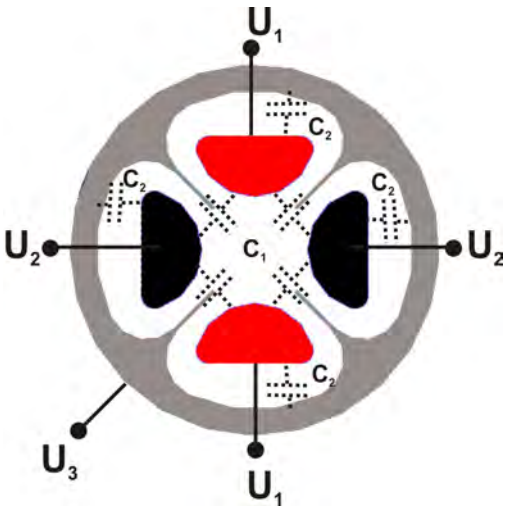

Figure 9.2: Scheme of the capacitances layout at ISCOOL. For these tests, one pair of opposite rods of the quadrupole is at potential U_1 and another pair at U_2. Two capacitances should be considered: 1) C_1 between the pair of rods, and 2) C_2 between the rods and the axial electrodes (U_3 for these simulations).

Simulation	U_1 [V]	U_2 [V]	U_3 [V]	W [J]
a	200	-200	0	1.83990E-05
b	100	300	0	2.21614E-05
c	100	-100	0	4.59976E-06
d	200	-200	-	7.80096E-06

Table 9.1: Values used for the electrostatic simulations with Opera of the capacitances of the RFQCB chamber for several simulations (a, b, c and d). The meaning of the energy W and the voltages U_1, U_2 and U_3 is explained in the text.

To find C_1 and C_2 it is necessary to solve the following linear system:

$$\begin{bmatrix} W_a \\ Wb \end{bmatrix} = \begin{bmatrix} (U_{1a}-U_{2a})^2 & \left((U_{1a}-U_{3a})^2+(U_{2a}-U_{3a})^2\right)/2 \\ (U_{1b}-U_{2b})^2 & \left((U_{1b}-U_{3b})^2+(U_{2b}-U_{3b})^2\right)/2 \end{bmatrix} \begin{bmatrix} C_1 \\ C_2 \end{bmatrix}, \tag{9.3}$$

where the subindexes a and b represents two different simulations, a and b, with the conditions and results detailed in Tab. 9.1. Solving the system, values of $C_1 = 2.3$ pF and $C_2 = 220.7$ pF are obtained.

The solutions are verified by running a simulation with new conditions (simulation c). The result of the simulation (see Tab. 9.1) agrees with the result obtained by evaluating Eq. 9.2. As example, Fig. 9.3 plots the simulation of the vectors of the electric field when the voltage of $\pm$200 V is applied and the equipotential lines of the electric field for the same simulation.

The total load capacitance of the system C_{ISCOOL} is evaluated with the expression:

$$C_{ISCOOL} = 4C_1 + C_2, \tag{9.4}$$

which yields $C_{ISCOOL} = 229.9$ pF. This value can be compared with the obtained in other simulation (d). In this case, the axial electrodes surrounding the quadrupole rods are removed. Therefore only U_1, U_2 and C_1 are present. Using a simple relation $W_d = C_1(U_1 - U_2)^2/2$, the capacitance between adjacent corresponds in this case to 24.3 pF. Therefore, the load capacitance is 97.5 pF.

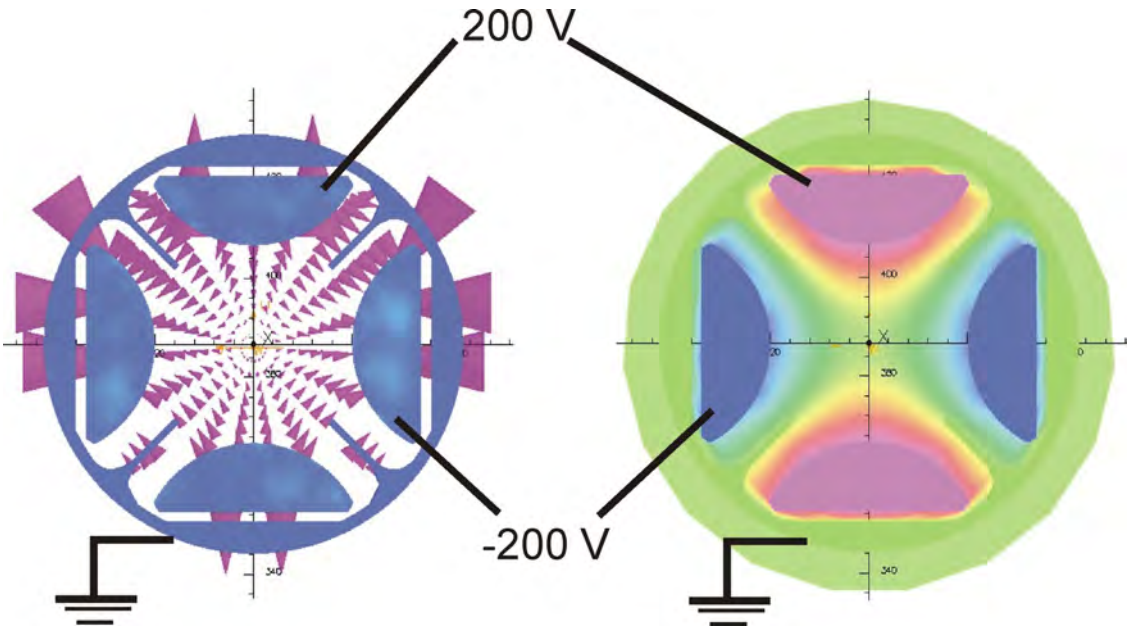

Figure 9.3: Simulations of the quadrupole field in the RFQCB chamber for a difference potential between adjacent rods of 400 V (conditions simulation a): vectors of the electric field (*left view*) and potential lines (*right view*).

The capacitance between adjacent rods C_1 is increased due to the removal of the wedges of the axial electrodes, which were shieldin most of the field lines. However, the loss of the capacitance between quadrupole rods and axial electrodes decreases the load capacitance of the system C_{ISCOOL}. In the real system, some other capacitances, which were not simulated for simplification, will increase the load seen by the RF supply:

- Between the end of the quadrupole rods and the injection and extraction plates.
- Between the screws supporting the quadrupole rods and the closest electrodes.
- The length of the different cables.
- The RF feedthroughs (20 pF each one)

Choice of the RF supply

As mentioned before, two devices were proposed as the RF supply for ISCOOL: 1) the commercial broadband amplifier and 2) the oscillator head developed by K. Rudolph from LMU and which has been used in other ion guides and ion traps (see [JGA97, DBD$^+$01]). To decide which one would be the best solution for ISCOOL operation, some measurements were performed to test the capabilities of both systems in the real ISCOOL asembly. Both devices were connected to the RFQCB assembly (see Sec. 8.2) in atmosphere conditions. The capacitance of the system was measured. The result corresponds to the capacitance of a pair of opposite rods of the quadrupole since they are connected together to provide shifted 180° to both pair of rods. The measured value against the ground was 295 pF. This value differs from the calculated value (see Eq. 9.4). The measured capacitance is then as expected, a bit higher than the simulated, due to the reasons explained above. The differences between the real device and the simulated geometry, are

probably the capacitance of the cables. In the following the results of the tests are detailed and discussed.

Broadband amplifier
A broadband amplifier Amplifier Research AR75A250M4 (75 W) was used for the tests. The input signal for the amplifier was provided by a Stanford Research Function generator. Between the amplifier and the two pair of rods a small transformer was placed providing two signals shifted 180°.

First the AR amplifier was tested with full gain and using less than 300 mVpp in the function generator. The frequency was fixed in the function generator and the amplitude was changed from 0 to 300 mVpp. For amplitudes more than 0.2 mVpp, the signal in the rods (measure by an oscilloscope with a probe 1:10) was either not stable (at 200 mVpp) or not sinusoidal (at 300 mVpp). The level of noise was too high and the value of the output frequency was random.

Later the gain of the amplifier was set to half gain. Better output signals were obtained in this case although with higher input amplitudes from the frequency generator (up to 90 mVpp). Figure 9.4 shows the results obtained. $V_{RF-in}(pp)$ is the peak to peak amplitude voltage set in the function generator and $V_{RF-out}(pp)$ is the peak to peak amplitude voltage on one of the pair of rods. It is clear that the requirements (see Tab. 6.2) are achieved with this configuration. The problem appears if ISCOOL is operated with higher frequencies. For frequencies higher than 0.8 MHz, the amplifier saturates for high amplitudes. To achieve higher amplitudes also for frequencies higher than 0.8 MHz, a more powerful broadband amplifier would be required.

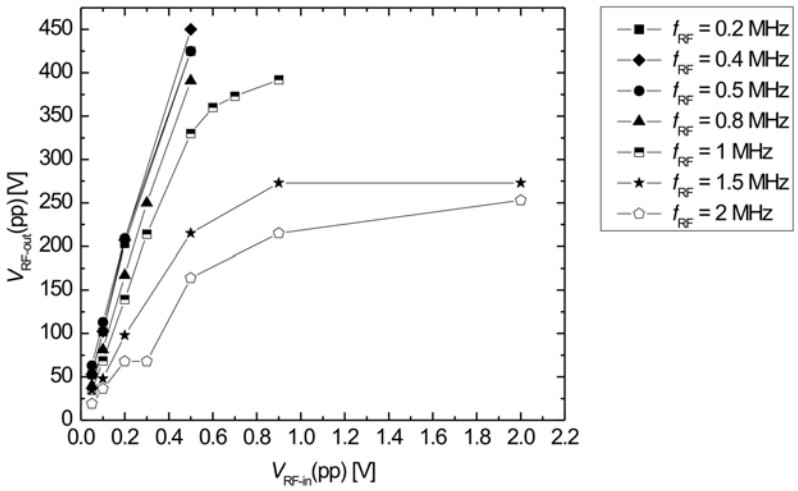

Figure 9.4: Plot of the output voltage from the broadband amplifier of 75 W as function of the input voltage for different frequencies set in the function generator.

If a 150 W broadband amplifier were used for the amplification (and all the other parameters constants) the relation of the voltages achieved (in first approach) will be the following:

$$U_2 \approx U_1 \sqrt{\frac{P_2}{P_1}} \tag{9.5}$$

and the new scaled plot would look similar to Fig. 9.5. The results would improve (around 100 V gain for 2 MHz signal at 500 mVpp in the function generator). However, a more powerful amplifier would be suitable for better results at 1 or 2 MHz.

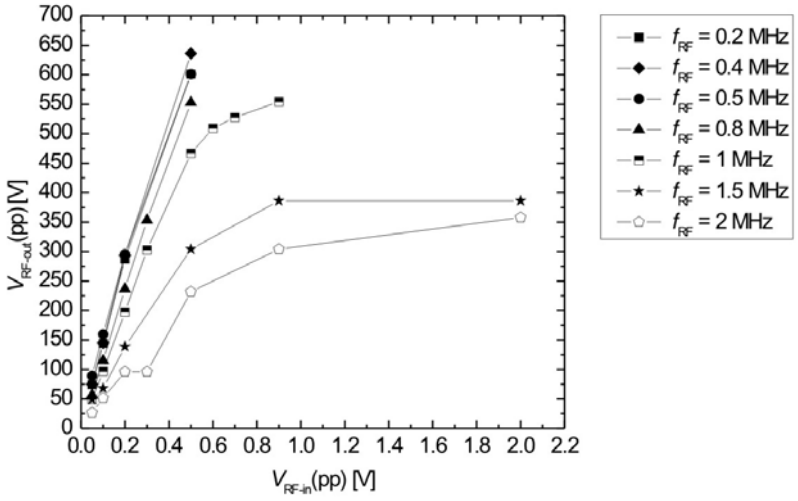

Figure 9.5: Plot of the scaled output voltage for 150 W of the broadband amplifier of 75 W as function of the input voltage for different frequencies set in the function generator.

Oscillator

The other device tested was a system developed by Klaus Rudolph from Munich university [Rud]. The system is based on a push-pull LC oscillator which is driven by two power MOSFET's, as shown in Fig. 9.6. The oscillation is produced by a positive capacitive feedback. The capacity C of the resonant circuit is given by:

$$C = C_{ISCOOL} + C_{out} + C_{coil}, \tag{9.6}$$

where C_{ISCOOL} is the load capacity (the RFQCB chamber), C_{out} the MOSFET capacities and C_{coil} the coil capacities. The inductance L is represented by a ferrite core with the appropriate number of windings to give the lowest oscillator frequency. The resonant frequency of the circuit f_{res} is expressed then by:

$$f_{res} = \frac{1}{2\pi}\sqrt{\frac{1}{LC}} \tag{9.7}$$

The higher resonant frequencies are achieved by superposing the RF magnetic field in the coil to a DC magnetic field. The latest lowers the effective permeability of the ferrite material. This transductor principle has already been used in the synchrotrons. In this way, the frequency variation is possible only by changing the DC current which generates the magnetic field, without any mechanical movement. The system is able to operate at any working point of the frequency-amplitude space with the following limitations: (200 kHz-1.2 MHz) and a limit in amplitude of 400 V. For a single coil, the highest frequency is limited to around six times the lowest frequency. However, the

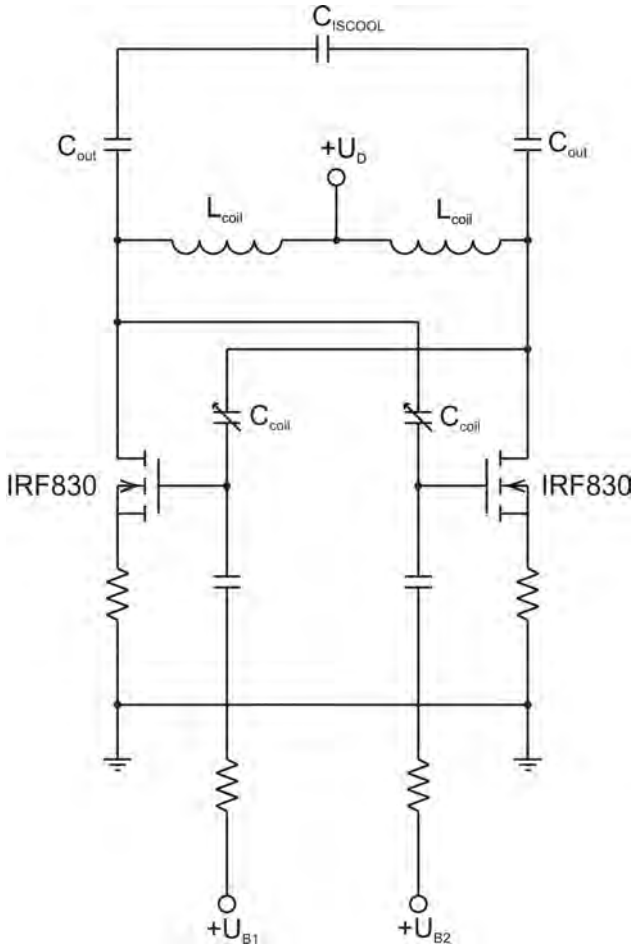

Figure 9.6: Electronics scheme of the push-pull LC oscillator [Rud].

range of frequencies could be extended by adding a second coil (1-5 MHz). An automatic switch could be integrated in the circuit to select the proper coil.

In the testing system, the frequency is set by changing the magnet current with a 0-15 V power supply and the voltage by adjusting a high voltage power supply (0-300 V). Figure 9.7 shows the result of a test of the dependance of the frequency of the output voltage. For a set input current ($I_{in} = 0.1$ A) for a frequency 0.3 MHz, the input voltage (which in principle set the output voltage) is scanned. The input voltage amplitude is changed but the bias voltage was not tuned. It is clear than the frequency is relatively constant with the voltage, but for higher amplitudes the frequencies decreases (without feedback). The maximum frequency error (between the input and output frequencies) is around 10%. In the operative version the frequency is tuned by an automatic loop of the bias voltage with high precision. The requirements of frequency and amplitude were accomplished by the system, although the verification in real conditions would be the best way to test the stability and reliability of the system.

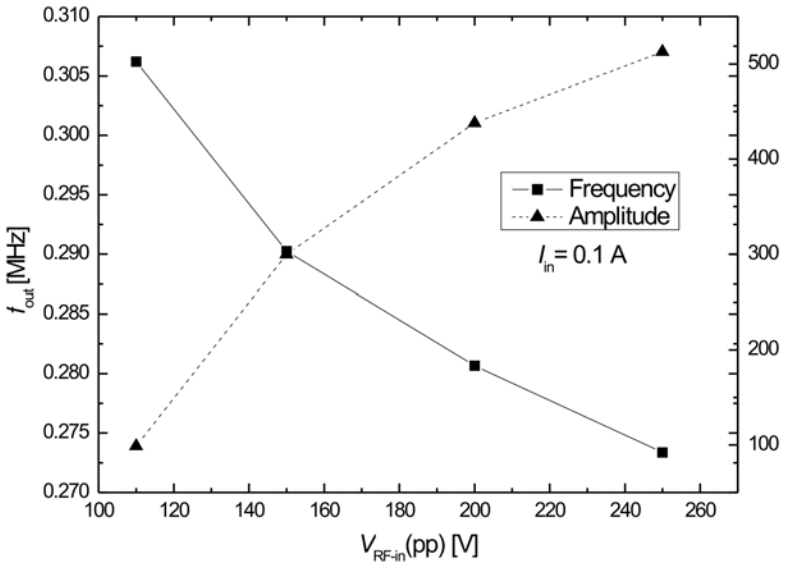

Figure 9.7: Plot of the output frequency and voltage amplitude as function of the input voltage amplitude for a set input magnet current.

Conclusions

Although higher frequencies could be achieved with the broadband amplifier, the oscillator is better adapted to the requirements of the system in terms of frequency and amplitude. The amplifier would be a good option in case experimental tests with ion beam shows that higher frequencies or amplitudes require the efficiency of the system to be increased. But, for performance and price, the oscillator is the first choice for the off-line tests.

A subsequent test at the maximum expected voltage of the quadrupole rods showed no electrical breakdowns. Only some problems with the orientation of the axial electrodes appeared but those were easily solved.

9.1.3 Power supplies for the axial electrodes

These power supplies provide the DC voltage to the axial electrodes which create the axial field used to guide the ions through the longitudinal axis of the trap (see Chapter 2). Each electrode has a different power supply. That means around 27 power supplies (25 axial electrodes and the injection and extraction plate, but depending on the electrodes configuration) are needed. In the design study two different solutions were considered:

- The use of 16-channel 1 kV units.
- The modification of existing ISOLDE standard supplies (DC24-3500).
- Use of a voltage divider for the electrodes in the center region of the RFQCB chamber.

Despite the higher cost, the compatibility argument with ISOLDE weighed heavily to choose the ISOLDE standard supplies. The power supplies are similar to the existing standard ISOLDE power supplies but modified to work around lower voltages, 0.5 kV (1 in Fig. 9.8). The voltage divider was left out to maximize the flexibility to optimize the axial field without major modifications.

To bring the DC voltages into the vacuum chamber, two commercial 19-multipin feedthroughs were used. This solution greatly diminishes the space required which fits with the limited space available in the four small top flanges. In a first step, a chassis (code C30014) converts the 25 individual channels in a multiwire cable, leaving some connections free for possible future needs.

Figure 9.8: Pictures of the different DC power supplies for the ISCOOL system: 1) 0.5 kV DC power supplies, 2) 12.5 kV and 20 kV power supplies and 3) HV power supply up to 65 kV.

9.1.4 High voltage power supply

ISCOOL needs to work on a high voltage platform (see Sec. 6). The maximum operating energy is 60 keV, thus the HV power supply has to provide at least 60 kV. For compatibility with the ISOLDE control system, the power supply FUG HCN 140-65000 was selected (see Fig. 9.8). This power supply has been successfully used at the ISOLDE off-line mass separator. For laser spectroscopy experiments some more requirements are demanded:

- A long term (24 hours, time required for a measurement plus calibration) DC voltage stability of less than 1 eV.
- Voltage ripple of less than 1 eV.

The HV power supply has an 8-hour stability of $< 10^{-4}$ and a voltage ripple $< 5 \cdot 10{-}5$. That means a ripple of less than 3 V (peak-to-peak) for 60 kV and 6 V of stability. The specifications of the selected power supply are in the limit of these requests, but a big capacitance or a software stabilization can be implemented in order to fulfil the requirements of the spectroscopy experiments.

9.1.5 Isolation transformer

The isolation transformer provides the operating voltage -380 V- to the power supplies placed on the high voltage platform. It is a quite delicate device since the experience shows that a lot of electrical breakdowns or leakages currents can be produced if it is not well installed or designed. The same isolation transformer used in the off-line mass separator will be used for the ISCOOL project. It consists of a powerful and massive transformer that minimizes the risks explained above.

9.1.6 Electronic feedthroughs for the vacuum

Special feedthroughs designed for vacuum devices are required for voltage connections. Figure 9.9 shows the connectors used in the project. The connectors are specially suitable for vacuum purposes and they are welded by an electron beam process to the flange. The connectors are placed in some of the four ISO-K DN100 flanges on the top flange of the main chamber (see Sec. 8.1.4). One of the flanges contains the two 19-pin connectors for the signal to the axial electrodes, together with two SHV 20 kV connectors for the injection electrodes. The two connectors for the RF power are located alone in another flange.

9.1.7 Fast switches

To release the ions accumulated in the potential well in the last section of the RFQCB chamber, it is necessary to change the applied voltages quickly on some of the last electrodes. The optimization of these voltages adapts the timing and optical properties of the released ion bunches according to experimental needs. A fast modification of the voltages is obtained by connecting the necessary electrodes to two DC power supplies (see Sec. 9.1.3) with fast switches. The fast switches selected are the Behlke GHTS-30. These switches has a very quick and stable time response which fits the application very well. They are mounted in an independent box with two plugs for the two power supplies and one for the timing signal (TTL) and one for the 5 VDC.

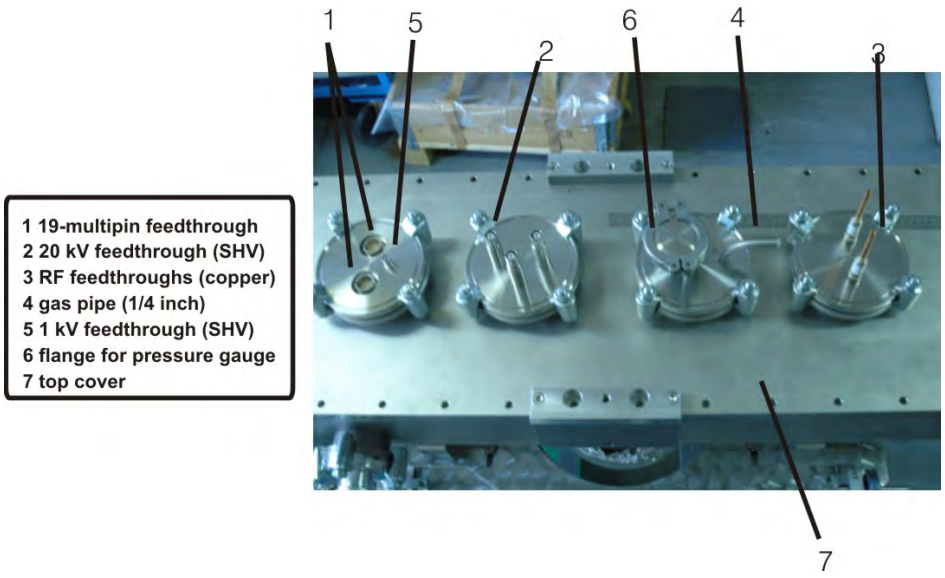

Figure 9.9: Picture of the different type of vacuum feedthroughs used for the voltage electrodes. The components are assembled in the flanges of the top cover. The flange for gas feeding and measurement is also shown.

Another possible option is the use of fast amplifiers which can switch between two power supplies delivering small potential values. The advantage of this option is its greater versatility in signal waveform delivered to the electrode, e.g. ramping the voltage instead of square timings. The drawback is the switching time which is longer than in the option of the fast switches.

9.2 The control system

The main goal in designing an user-oriented control system is to make it as easy-to-use as possible. That means that the user does not need to be very experienced to use the machine. Although ISCOOL will be placed in the ISOLDE experimental hall, where the beam transmission is responsibility of the experimentalists, it might wise to leave the beam optimization of ISCOOL to the engineers in charge of ISOLDE operation, considering it as a part of HRS optimization. However, ISOLDE has already a complex control system and it would not be desirable to increase the level of complexity of the system after the implementation of the RFQCB and the beam line associated. Moreover, some experiments directly connected and taking profit of the cooling and bunching capabilities of ISCOOL, could be very interested to control by themselves the operating parameters.

The purpose of the design of the ISOLDE control system is to balance the requirements of a full and robust implementation in the ISOLDE control system, and the requirements of operation and tuning by the experimentalists. The combination of industrial systems (Programmable Logic Controllers) and friendly user applications is the solution outlined in this chapter. More information can be found in [PG05].

9.2.1 Scheme of the design

The control system for ISCOOL (and the components included in the beam line) can be divided in different subsystems depending on the type of element which is to be controlled. Anyhow in the final scheme there is an interdependence between the different elements which makes the control a complex design. The subsystems can be itemized according to the type of elements to control as:

- **Vacuum**. Turbopumps, forepumps, pressure gauges, valves and gas feeding systems are included. The vacuum control must include automatized processes for the start of pumping down the line, control of the gas pressure inside the trap, safety switches and venting of the system.

- **DC > 1 kV**. Four devices to be controlled can be considered as high voltage devices: the high voltage power supply itself, two power supplies at the injection side and one at the extraction side. In the case of the last two items, the power supplies are placed on the high voltage platform.

- **DC < 1 kV**. In a first step there are 28 power supplies to be controlled (25 axial electrodes, injection and extraction plates and first extraction electrode). Only the voltage amplitude has to be controlled since these are steady-state power supplies. For the pulsing, the voltage is switched between two power supplies using the fast-switches. The width of the pulse is around 100 μs.

- **Diagnostics**. Two existing diagnostic boxes, one before and one after ISCOOL, will be used for beam intensity and beam profile measurements. The total efficiency of the line can be worked out through the Faraday cup measurements in these boxes. With the scanner before the merging switchyard there will be the possibility to optimize the optics of the extraction quadrupole triplet placed downstream of ISCOOL.

- **Radio Frequency**. The RF field is created by an oscillator governed by a control unit. The control unit has three inputs: an ON/OFF signal (0-3 V) to switch on/off the RF, a signal to assign the RF frequency (0-10 V), and other signal for the RF voltage amplitude (0-10 V). It has also four outputs, all of them analogs: the real RF frequency and amplitude values, the DC value and the magnet current value.

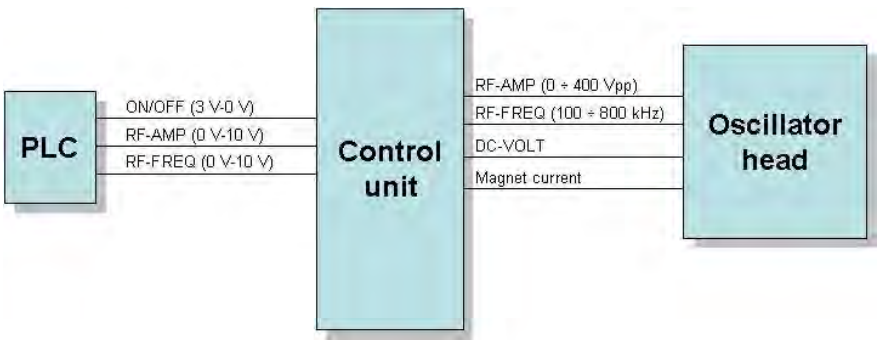

Figure 9.10: Control scheme for the oscillator solution for RF amplification.

- **Timing**. The accumulation and bunching of the beam into ISCOOL has to be linked to the frequency of aperture of the HRS beam gate and therefore to the frequency of the proton pulse from the PSB. Therefore the general timing signal of the CERN accelerators will be used as input.

A simplified scheme of the control system is presented in Fig. 9.11.

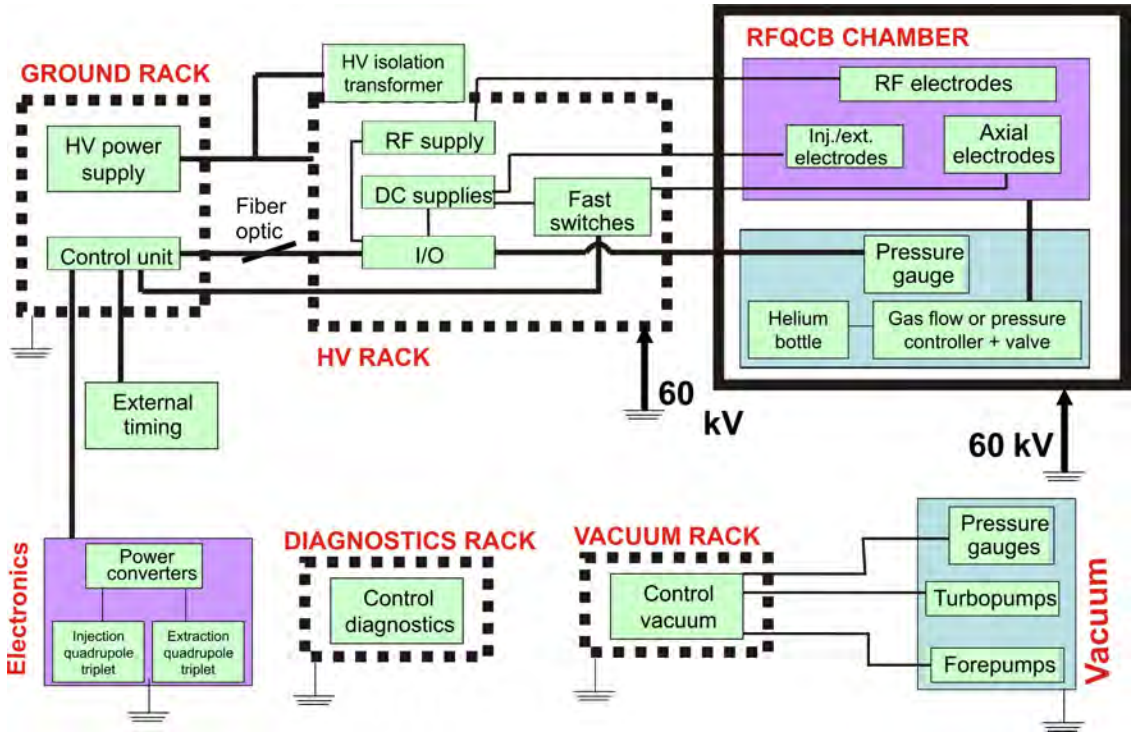

Figure 9.11: Scheme of the control system.

The system has to foresee the case when ISCOOL is removed from the beam line and only the quadrupole triplets are remaining from the point of view of the control. In that case, just the voltage amplitudes of both quadrupoles must be controlled, as for any other standard quadrupole triplet of the ISOLDE transfer beam lines. As the diagnostic devices also remain in the beam line, they can still help in the optimization of the device. Hereafter, the output parameters are considered as the signals sent to the devices by the control system (input by the users) and the input parameters the signals received by the control system from the devices (output of the devices).

Output parameters

The control system should vary the amplitude of the RF voltage, the frequency of the RF voltage (both set through the RF amplifier, see Sec. 9.1.2), voltages applied to the axial electrodes, the high voltage, the gas flow inside the chamber and the timing of the pulsing electrodes. Therefore the output parameters can be divided in:

- Voltage to apply, current limitation and on/off signal regarding the HV power supply and the small DC power supplies.
- TTL signal for the fast switches.

- Voltage to apply to the valve or gas pressure to control the gas unit.
- Voltage and frequency of the RF amplifier.

The previous signals will be either processed by a PLC or by another type of communication device. During the off-line tests, the working sets are developed in LABVIEW.

The best strategy for an efficient and fast tuning of ISCOOL is to collect in a database optimized settings for different isotopes and masses. This would be the starting point as is already done in other beam lines at ISOLDE. Hence the process requires to test all the beams at ISOLDE. Even though not great changes in the RFQCB are expected for comparable masses, bigger changes are expected for the configuration between heavy and light ions in order to keep constant the Mathieu parameter q (see Chapter 2).

Input parameters

The control system should monitor all the voltages and pressures supplied to ISCOOL, to allow at least a manual tuning. The safety vacuum switches are automatic and not dependent on the monitoring of the vacuum pressure signals.

9.2.2 Hardware layout

The control system is governed by a Programmable Logic Controller (PLC) system based on the Siemens Simatic S7 solution which is standard at CERN. Such a PLC allows the control of a lot signal inputs and outputs and moreover it is possible to program internally these signals and linked the system with a PC.

The CPU (model 315-2 DP) is placed on ground and is linked to an Ethernet coupler, which allows the system be controlled by an Ethernet connection, and to an Siemens OBT, which transform the Profibus signal in an standard optical fiber optic cable with simplex connections (Siemens standard). The fiber optic is used to link the CPU (at ground) to the input/outputs which are on the HV platform. 4 modules with 8 analog inputs (AI), and 4 modules with 8 analog outputs control the power converters for the electrodes of ISCOOL. In addition, other modules control the signals of the RF supply, the gas flow or to monitor the vacuum gauges. The modules for the control of the HV are placed on the electronic rack on ground.

9.2.3 Control for off-line tests

Before the final installation in ISOLDE, ISCOOL has been tested in an off-line test bench (see Chapter 5). The tests require the control of the main devices of ISCOOL which cannot be operated manually. For this purpose, a control system based in a LABVIEW platform has been designed. In Figure 9.12, a simplified scheme of the design is presented.

The use of a PLC is justified because it is a more robust system than the PC itself in front of adverse environments (electrical sparks, data transfer errors,...). In addition the PLC (with CPU SIEMENS ST-300) will be afterwards perfectly integrated in the standard ISOLDE control system.

A graphical interface in LABVIEW has been designed under supervision of this work [TP05] to control directly the input and output voltages of the power supplies. The connection between LABVIEW and the PLC is directly made through Ethernet. The PLC can be directly programmed by LABVIEW thanks to the support from the PLC department at CERN which has developed

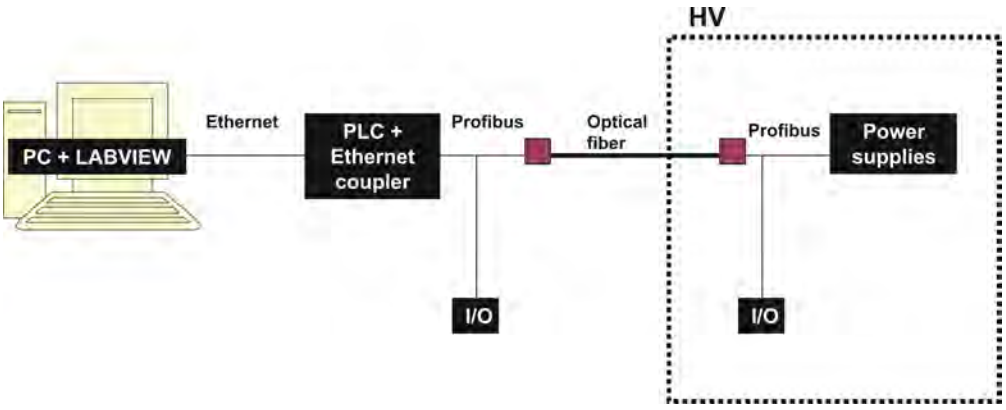

Figure 9.12: Scheme of the control system for the off-line system. Only the DC power supplies on HV will be in principle controlled.

some LABVIEW libraries which control directly the PLC without using an OPC server. The main interface, which appears once the program is launched, is shown in Fig. 9.13.

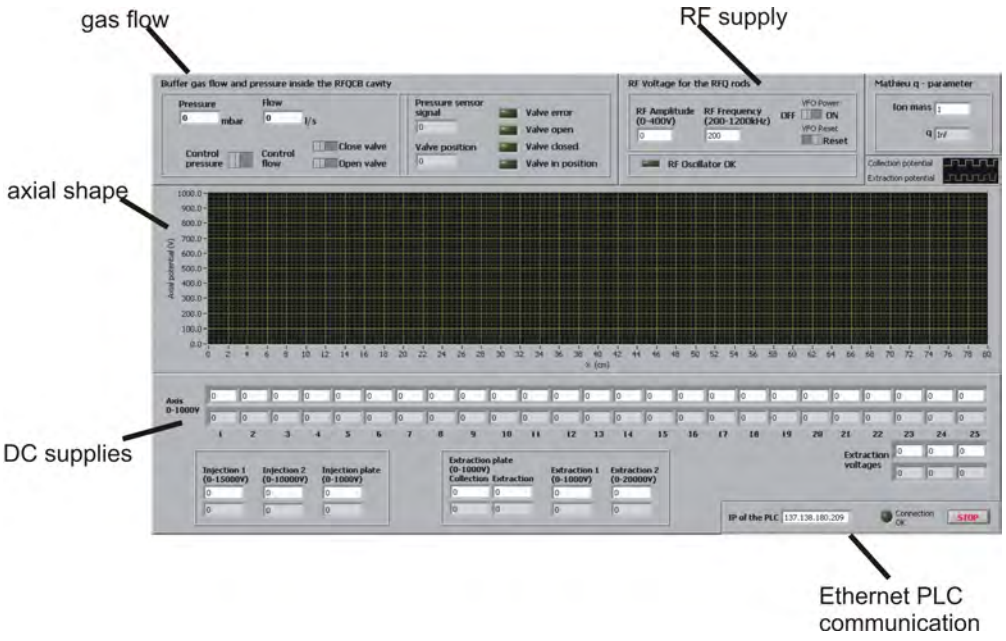

Figure 9.13: Main interface of the LABVIEW test bench control system (courtesy of T. Tallinen). The controls for the DC supplies, the RF supply and the gas flow are indicated.

The design concept of this control system allows easy upgrades and implementation of novel devices, e.g. the control of the movement of the Faraday cups upstream and downstream of ISCOOL. Two digital outputs of the grounded modules are used for this purpose. All the other signals (analog and digital) are controlled by the modules placed on the high voltage platform.

Timing

To bunch the ions inside ISCOOL, it is necessary to fast-switch the voltage of the last axial electrodes. In the test bench, one push-pull fast-switch from BEHLKE will be used to check its proper

application to this purpose. This kind of switch uses as input two voltages and a TTL signal for the timing control. To create the TTL signals, which will be pulses of a determined period (equal to the cooling/accumulation time of ISCOOL), a simple function generator will be used in the test bench.

Another possibility is the use of a PLC ST-300 function module, the FM 352-5 fast-boolean processor. The module allows the programming of 12 inputs and 8 outputs with a maximum cycling scan of 1 μs. The features fit the requirements of the ISCOOL timing: the input could be used by the trigger of the HRS. Anyhow two main problems come out for the implementation of this module:

- The I/O signals are HTL (24 V) and not TTL, so a conversion device should be implemented.
- There is no know-how at CERN about the capabilities of this module. A most concrete study by the control group should be carried out.

Control of the gas line

As mentioned in Sec. 7.5, the gas entering in the RFQCB chamber is regulated by a gas valve which is controlled by a gas control unit (Pfeiffer RVC 300). Such a control unit offers different possibilities for the control: by Profibus, by RS-232 or directly connecting to the I/O units of the PLC. At ISCOOL, as the gas bottle and the valve are working on the high voltage platform, the control unit is also placed on the HV electronics rack (see Chapter 9.1). The use of the I/O of the PLC is the easiest way to link the valve with the control system. The unit can be switched to work in *Flow mode* or in *Pressure mode*. In *Flow mode*, the user sets a certain level of flow which is calibrated by the manufacture as a certain aperture of the valve. The valve is then working in open mode, without feed-back. Another possibility is to work on the *Pressure mode*. For this kind of operation, it is necessary to place a pressure gauge downstream of the valve. The user then sets the value that would desire in the region of this sensor, and the pressure gauge acts as a feedback for the stabilization of the pressure.

At ISCOOL, in principle it would be more efficient to work in flow mode, since the pressure that would be desired to stabilized is the one in the RFQCB chamber. Unfortunately, with the present technology is not possible to measure directly this pressure, so as the pressure in this chamber is given by the gas flow and the diameters of the holes in the injection and extraction plate, the Flow mode seems to suit the best to the RFQCB purposes. However, a monitoring of the other pressures of the system is mandatory to avoid overpressures in the system that can propagate and contaminate all ISOLDE.

Chapter 10

Assembly of ISCOOL and future upgrades

10.1 Assembly of ISCOOL

Previous chapters have established the design parameters of the new ISCOOL and the new beam line. After the end of the mechanical design, the fabrication process started. All the mechanical pieces were manufactured during this thesis work in collaboration with the workshops from some institutes. In addition, all the pieces which are required for the different systems were ordered or designed in parallel with the mechanical fabrication. ISCOOL was asemblied at the ISOLDE workshop without any major problems detected. Figure 10.1 shows a picture of the final assemly of the RFQCB chamber just before placing it into the main vacuum chamber.

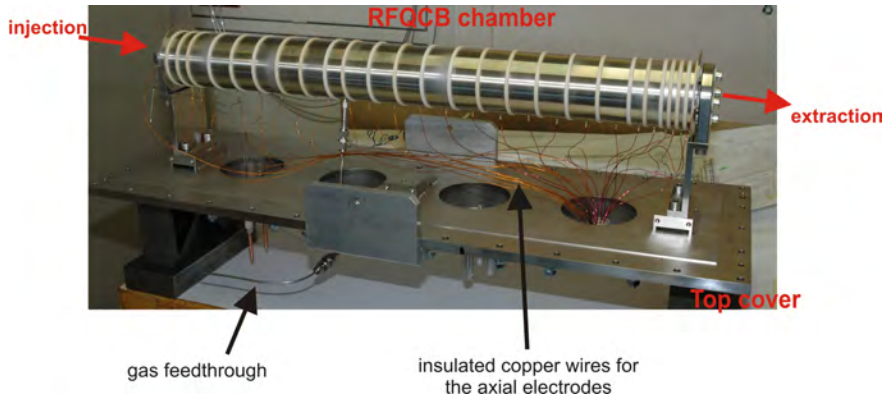

Figure 10.1: Picture of the RFQCB assembly+top cover with the electronics wires before the installation inside the main vacuum chamber.

The distribution of the axial electrodes in the RFQCB chamber was done following the parameters given in Tab. 8.1. The gas feedthrough was placed in one of the electrodes between the middle and the injection (axial electrode number 9, see figure). The length of this electrode was also adjusted to obtain a correct compression of all the structure.

10.2 Off-line test bench

Before the first tests with RIB's and the final installation on-line at ISOLDE, it is of course necessary to check that the system is running as expected and tuned according to all operational

parameters. For this purpose a test bench has been constructed in the ISOLDE off-line laboratory (see Fig. 10.2).

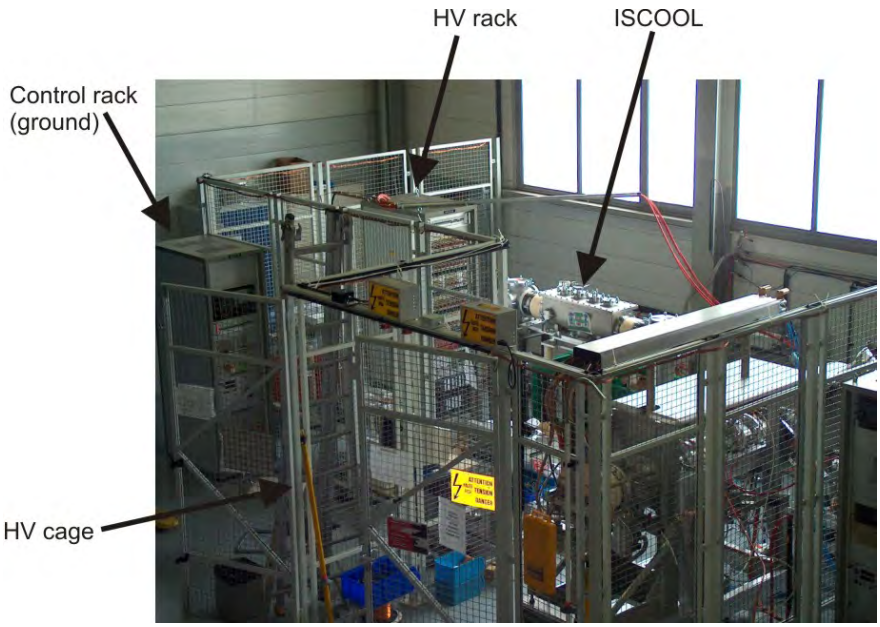

Figure 10.2: Picture of the setup to test ISCOOL at the ISOLDE off-line laboratory.

The first requirement was to construct a cage around the experimental place since ISCOOL will work at 60 kV. The region enclosed by the cage is used to develop the tests of ISCOOL and the tests of the new front-end for the ISOLDE targets. For the tests of ISCOOL are necessary other devices which will not be used later on the on-line beam line: an ion source to provide stable ions and diagnostic devices to check the performance of ISCOOL. In the following the beam line will be detailed.

10.2.1 General scheme of the test bench

The test bench beam line does not have strong requirements from the optical correction element downstream of ISCOOL. In first tests, the combination of a surface ion source, the injection quadrupole triplet and ISCOOL, will serve for a first check-out of all the components and first transmission yields. Figure 10.3 shows a threedimensional view of the layout of the off-line test bench beam line in building 275. The emittance meter placed in the figure is the same as the one used for the tests in REXTRAP (see Chapter 11 and Sec. 3.5.4).

Figure 10.4 shows the real assembly of ISCOOL at the test bench. The assembly described in the past section were moved to the test bench and carefully aligned. The turbopumps were mounted and connected to the forepumps. The vacuum valves were not installed to simplify the operation in the first tests. The conceptual design proposed in the last chapters has then been proved. The electronics and control have been tested and commissioned, the mecanical parts assembled successfully and the vacuum and gas feeding components installed.

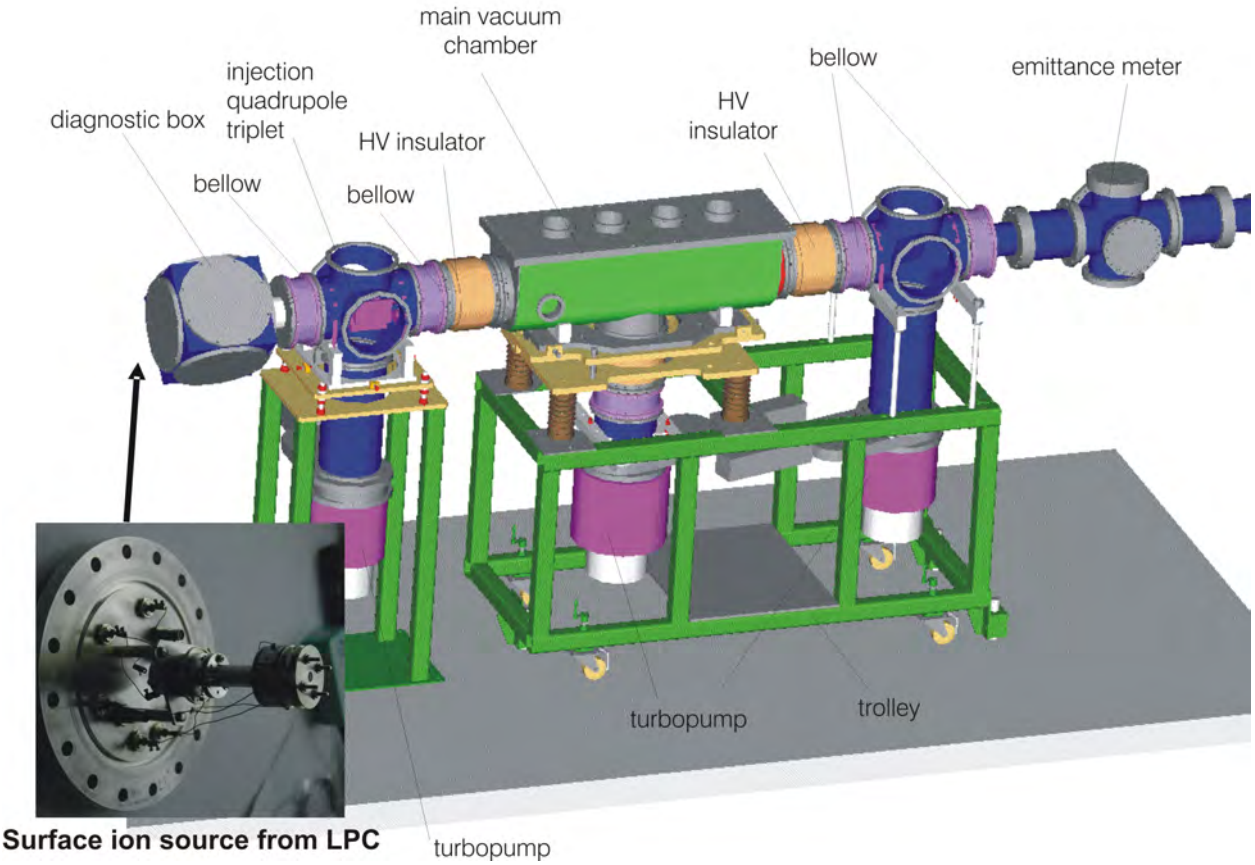

Figure 10.3: 3D design of the test bench beam line. The main components are identified. The ion source before the diagnostic box is zoomed.

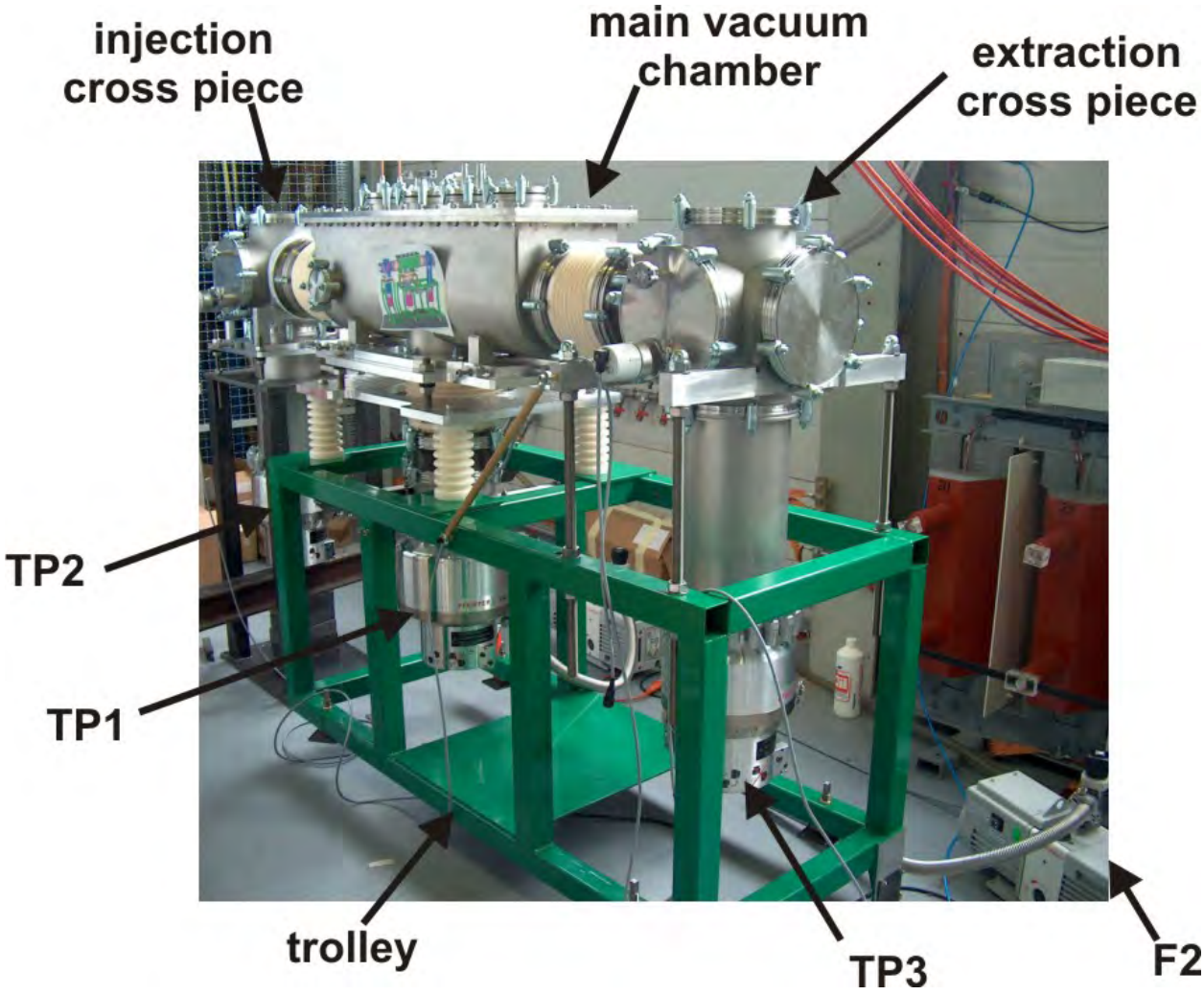

Figure 10.4: Picture of the real set-up of the components at the test bench after assembly of the in-vacuum parts. The vacuum system is mounted and the electronic and gas feedthroughs ready for operation.

10.2.2 The ion source

The off-line tests of any beam preparation device require a stable beam delivered by an ion source. The best results would be obtained if the properties of the beam released by the ion source are well-known, and can be compared with those of the beam extracted by ISCOOL. Originally, the first tests were planned to be performed with the stable ion source used by the MISTRAL experiment. Even some measurements were carried out to check the quality of the beam released by this ion source (transverse emittance and intensity), see [Pod04a]. Unfortunately, the combination of unexpected delays of the ISCOOL project, and the approval of a new run of the MISTRAL experiment, obliged the planning to be changed. Finally, a surface ion source from the LPC-Caen (see Fig. 10.3), already used for the tests of the LPC RFQ buncher, was installed.

10.2.3 Diagnostic devices

The diagnostic devices in the test bench must provide the following values:

- The intensity of the beam before and after the cooler to calculate the efficiency
- The energy spread of the bunches.
- The position of the beam before the cooler to achieve a proper injection.
- The Time Of Flight (TOF) of the bunches after the cooler.
- The quality of the beam optics before and after the cooler, particularly the transverse emittance.

Hence the following equipment is installed in the beam line:

- A combination of standard Faraday cup (FC) and scanner from ISOLDE before the cooler and an FC after the cooler (see Chapter 3). They allow the efficiency of the cooler to be measured. They are also used for the optimization of the injection and extraction optics. It can also give an indirect measurement of the energy spread (see Sec. 3.5.5).
- A MultiChannel Plate (MCP) for measurement of the TOF of the ISCOOL extracted beam. It will control the quality of the bunches delivered to the beam and the contamination of the ISCOOL beam.
- An emittance meter after the cooler. To measure the cooling performance of ISCOOL. An emittance meter before ISCOOL would be desirable, but nowadays the existing emittance meters are permanent destructive devices. At least some measurements of the emittance of the ion source should be carried out in another beam line.

The control of the FCs is integrated in the ISCOOL test bench control system (see Sec. 9.2.3) and therefore the FCs are remotely controllable by a computer. The emittance meter has its own software, and it is then also completely controllable by computer.

10.3 Future plans and machine improvements

The design of ISCOOL can be upgraded and optimized with the tests of new schemes in the mechanical design. Fortunately, the flexibility of the design of ISCOOL allows an easily implementation of further developments in the machine without redesigning all the device.

Cryogenic implementation

According to the most recent results on RFQCB's, the logical step forward to improve the efficiency of the device is to decrease the temperature of the gas, mainly in the bunching area. Therefore a cryogenic system would be necessary, as the one already tested at the LEBIT RFQ buncher (see [SBL+03]). A cryogenic vessel containing liquid nitrogen or helium could be implemented in the area surrounding the last section of the cooler, together with a thermic isolation and a cryogenic line with an inlet to keep the level of liquid. The implementation of such a system would increase the performance, but also increase the level of complexity of the system.

Laser purification

In order to purify the trapped beam, one could think of using the interaction of a laser (see [Nie03]). One would then need to modify the beam merging switchyard downstream of the cooler. The idea would be to get a straight section from the merging switchyard, that will allow the laser to interact with the confined ions of ISCOOL.

Low bunching section pressure

A high pressure inside the RFQCB chamber is needed to have a better cooling of the beam with the ion-gas collisions. Once the beam is cooled, there is no further reason to maintain the pressure and in fact a high pressure is a problem during the acceleration process, because that blows-up the beam increasing the beam emittance again. The best solution will be to keep the first section of the RFQCB chamber (500-700 mm) with the gas pressure required, and using a lower pressure for the trapping-accumulation-bunching section (last 100 mm) of ISCOOL. To reach this goal two main solutions, that will require further developments, are proposed:

- **Miniquadrupole with small aperture**. Placing a small quadrupole with RF focusing scaled to that of the big quadrupole between the cooling and the bunching section, would reduce the pressure at the bunching section. It would improve the extraction and acceleration of the beam, and would decrease the molecular formation that diminishes the efficiency of the system. Some simulations were done out of the scope of this work [Pet02a].

- **New conductances**. A much easier technical solution would be to add new flow conductances that would expel the gas before the hole of the extraction plate. The new conductances could be obtained by adding new holes either to the ceramic spacers or to the axial electrodes. For manufacturing reasons, the holes in the ceramic spacers are a better option. The holes could consist in simple slits at the ceramic rings, with a certain thickness e, as shown in Fig. 10.5. The sum of the area of all the slits should be equal to the area of the extraction plate, to obtain approximately the same effect in terms of gas throughput than without the holes. Therefore for a hole of the extraction plate of 3 mm diameter, the total area of the slits should correspond to 7.1 mm^2. The total area created by N slits A_{slits} can be approximated by:

  $$A_{slits} = N(d/2)e\alpha, \tag{10.1}$$

  where e_{int} is the axial space between axial electrodes that create the conductance, d the inner diameter of the ceramic spacers and α is the angle of the hole in radians. For 5 ceramic spacers with $e_{int} = 1$ mm in the last part of ISCOOL, the angle necessary to obtain 7.1 mm^2 is around $\alpha = 2°$ (for $d = 82$ mm). That corresponds approximately to a gap width $a \approx 3$ mm for each spacer.

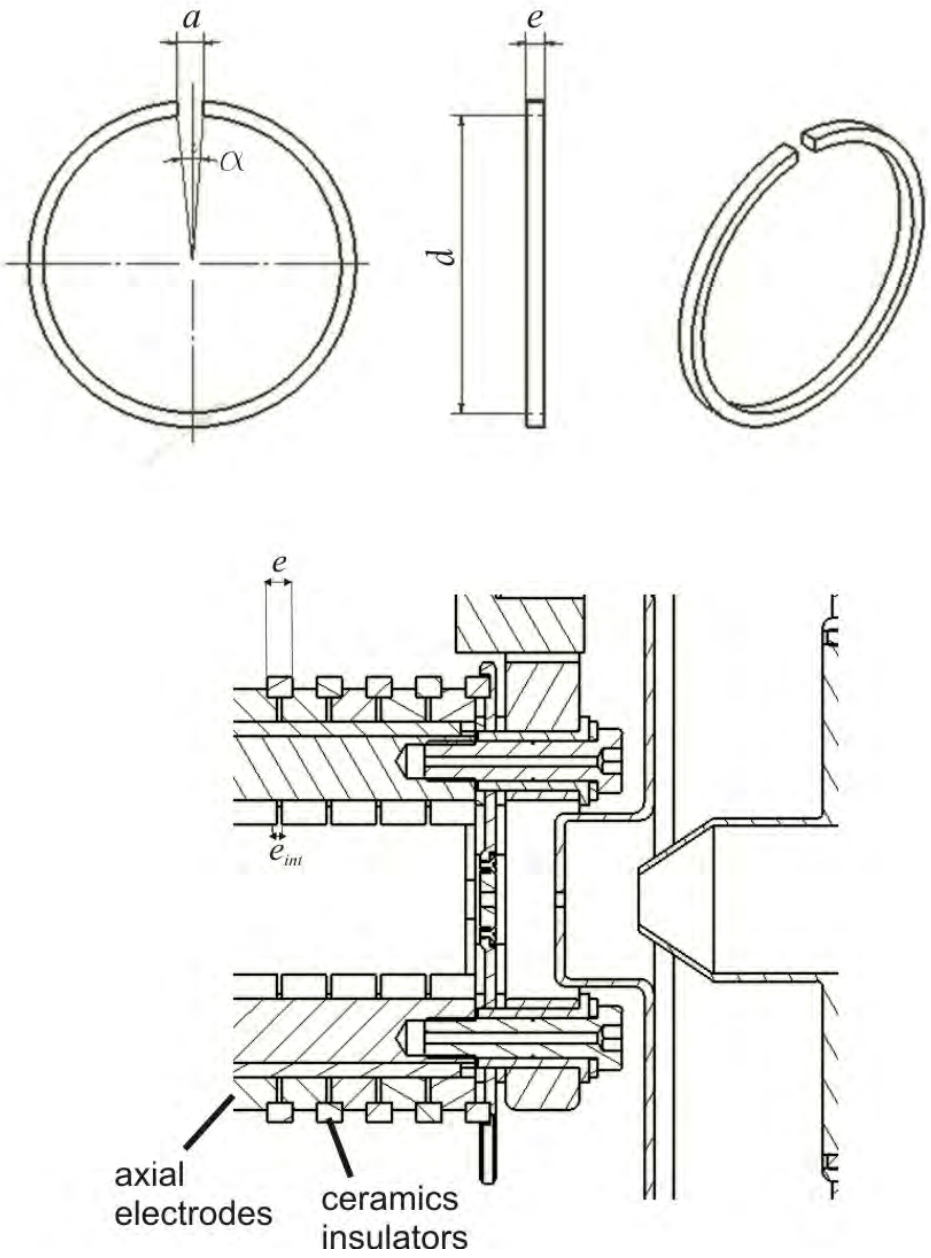

Figure 10.5: Scheme of the insulators proposed to create a differential pumping inside the RFQCB chamber. The important dimensions of the piece (*top*) and the assembly (*bottom*) are shown.

Chapter 11

Comparison of cooling methods for Penning traps

As discussed in previous chapters (see Chapter 1 and 3), new developments in ISOL facilities depend partly on the progress in manipulation of RIB to obtain more intense and optically improved ion beams. It has turned out that these goals are partially contradictory since higher intensities tend to decrease the ion optical properties. Thus increased beam intensities are a major challenge for the present cooling devices and among the novel requirements specified in design studies of new RIB, as in the EURISOL DS for example.

To investigate the effect of high intensity beams ($> 10^8$ ions injected into a Penning trap), some measurements have been carried out with REXTRAP at the REX-ISOLDE experiment (see Sec. 1.3.2). The goal of the measurements was to check the performance of the Penning trap at high intensities with the current technical operation conditions, and to test new methods proposed to enhance the performance of the trap, i.e. to maintain the beam quality at high current levels.

In this chapter the results from the experiments comparing the new *rotating wall cooling* technique (see Sec. 4.2.1) with the well established *sideband cooling* technique are presented and discussed.

11.1 Layout of the experiment

The measurements were carried out in the low-energy part of REX-ISOLDE (see Sec. 1.3.2), and most of the time using only REXTRAP (and not REXEBIS and the transfer beam line (BTS) from REXTRAP to REXEBIS and the mass separator, see Sec. 1.3.2). The scheme of the low-energy part of REX-ISOLDE was already shown in Fig. 1.10.

11.1.1 REXTRAP layout

Figure 11.3 shows the layout of the Penning trap REXTRAP. All the system is enclosed inside a high voltage cage and over a high voltage platform. REXTRAP operates at a maximum high voltage of 60 kV, which agrees with the maximum energy of the ISOLDE beam 60 keV. Table 11.1 shows the normal operation parameters of REXTRAP.

Like ISCOOL, the optics system of REXTRAP is divided in the deceleration part (60 keV to injection), the trap itself and the re-acceleration. In REXTRAP the beam is confined in the middle of the trap, as shown in Fig. 11.2. A potential well is created in this part. The center

Buffer gas	Neon (or Argon)
Gas pressure	$< 10^{-3} mbar$
Magnetic flux density strength B	3 T
Confinement t_{acc}	< 20 ms
Trap capacity	< 10^8 ions
Trap length	900 mm
Longitudinal emittance (60 keV)	5 μs·eV

Table 11.1: Main operation parameters of the Penning REXTRAP at REX-ISOLDE.

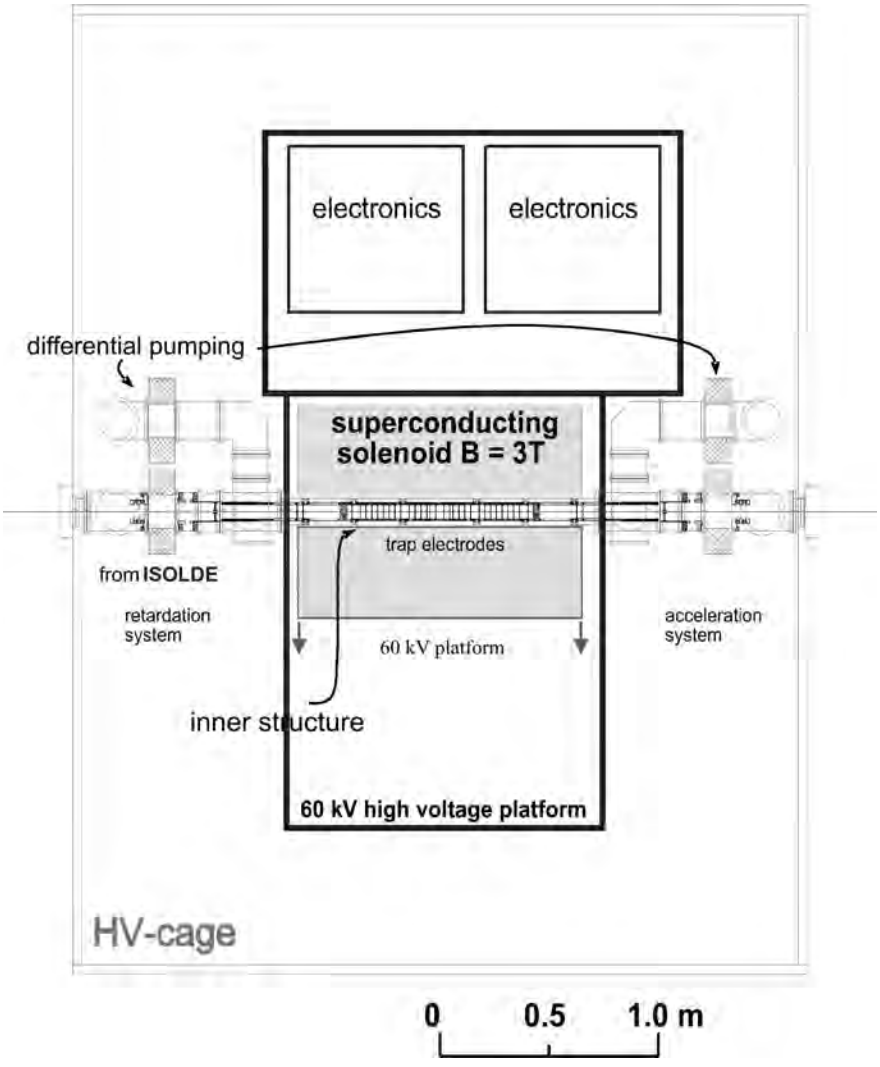

Figure 11.1: Scheme of REXTRAP and the high voltage cage.

electrodes are eight-folded to apply the additional RF voltages for the different types of cooling. The pressure at REXTRAP is lower than at ISCOOL ($\sim 10^{-4}$ mbar). The differential pumping to ISOLDE is not so critical, as shown in the bottom plot of Fig. 11.2. The trap is usually filled with neon -sometimes with argon- for the buffer gas cooling of the beam. Typical frequencies are: $f_+ \approx 1$ MHz, $f_z \approx 44$ kHz and $f_- \approx 1$ kHz.

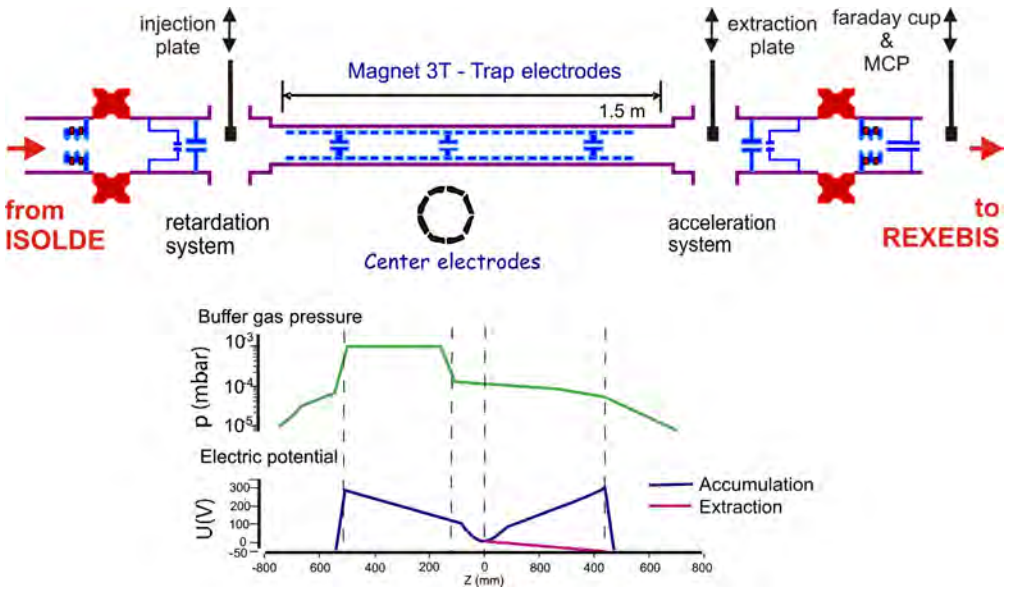

Figure 11.2: Structure of the REXTRAP electrodes and diagnostics devices. The axial potential and the pressure along the trap are also plotted.

11.1.2 Beam line for the emittance measurements

For the measurements of the optical quality of the beam extracted from REXTRAP, only the trap itself and a straight beam line after the trap were involved (see Fig. 11.3). As illustrated before, from REXTRAP the beam can be bent to the BTS and delivered to REXEBIS (see Sec. 1.3.2), bent to the WITCH experiment [BAB+03] or continue straight to the measurement beam line section.

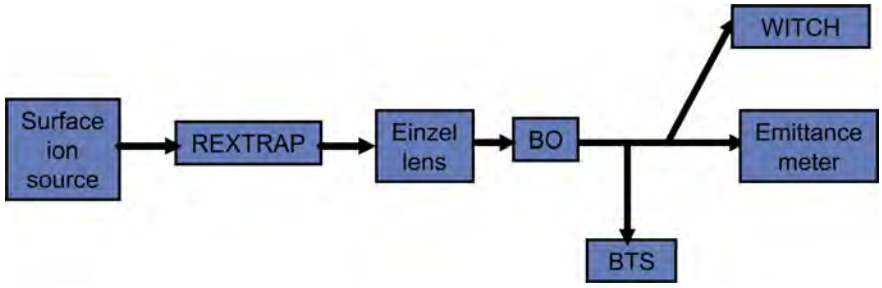

Figure 11.3: Sketch of the beam line used to test the cooling methods.

To control the transport of the beam after the extraction from REXTRAP, several optical elements and different pumping orifices are placed along the beam line (see Fig. 11.4). The transport of the beam properly to the emittance scanner requires an optimization of the einzel lens just after

Cooling method	Energy [keV]	t_{cool} [ms]	U_c(pp) [V]
no cooling	30	20	-
sideband	30	20	18
rot. wall quadrupolar	30	20	30
rot. wall dipolar	30	20	30

Table 11.2: Fixed parameters during the analysis of the cooling frequency, the TOF measurements and the injection into EBIS. The energy denotes the injection and extraction energy of the beam, t_{cool} is cooling time or cycling time of the trap and U_c(pp) is the peak-to-peak amplitude voltage of the RF field added for cooling purposes.

the trap which controls the focus of the beam. The benders deliver the beam to the different beam lines. Some diagnostic devices are placed along the line to measure the properties of the beam. In addition, a diaphragm has been added in the beam line by the WITCH experiment for a better control of the beam.

The emittance meter used for these measurements is based on the double-slit concept (see for further information [Rei02, Huc02] and Sec. 3.5.4). An electron multiplier was installed after the emittance scanner to amplify the signal received as the intensity extracted from REXTRAP was low.

11.1.3 Beam line for the global efficiency

Further measurements were made using the complete low-energy preparation stage, i.e. REXTRAP, the BTS, REXEBIS and the mass separator, to measure the global performance of the beam delivered by REXTRAP. The results of the measurement are presented in Sec. 11.2.7.

11.2 Results of the measurements

Systematic measurements, focused basically on the efficiency and the optical properties of the beam, were carried out during several periods in the past years. The present section details and discusses the technical properties of the trap obtained.

11.2.1 Cooling frequency at REXTRAP

To verify a correct operation of the cooling method applied, a frequency scan of the transverse electrical RF field (see Sec. 4.2) was carried out for each measurement with different beam intensity. A presence of a resonance proved the method and from the resonance curve the optimum frequency was determined. Figure 11.5 shows the optimum frequencies for each cooling method as function of the number of ions injected. The plot confirms the dependance of the frequency of the cooling methods with the number of ions accumulated inside the trap. It was obtained under conditions summarized in Tab. 11.2. These are the same conditions as those used to obtain the data presented in Sec. 11.2.7. For all three cooling methods, the resonance frequency increases with the number of accumulated ions.

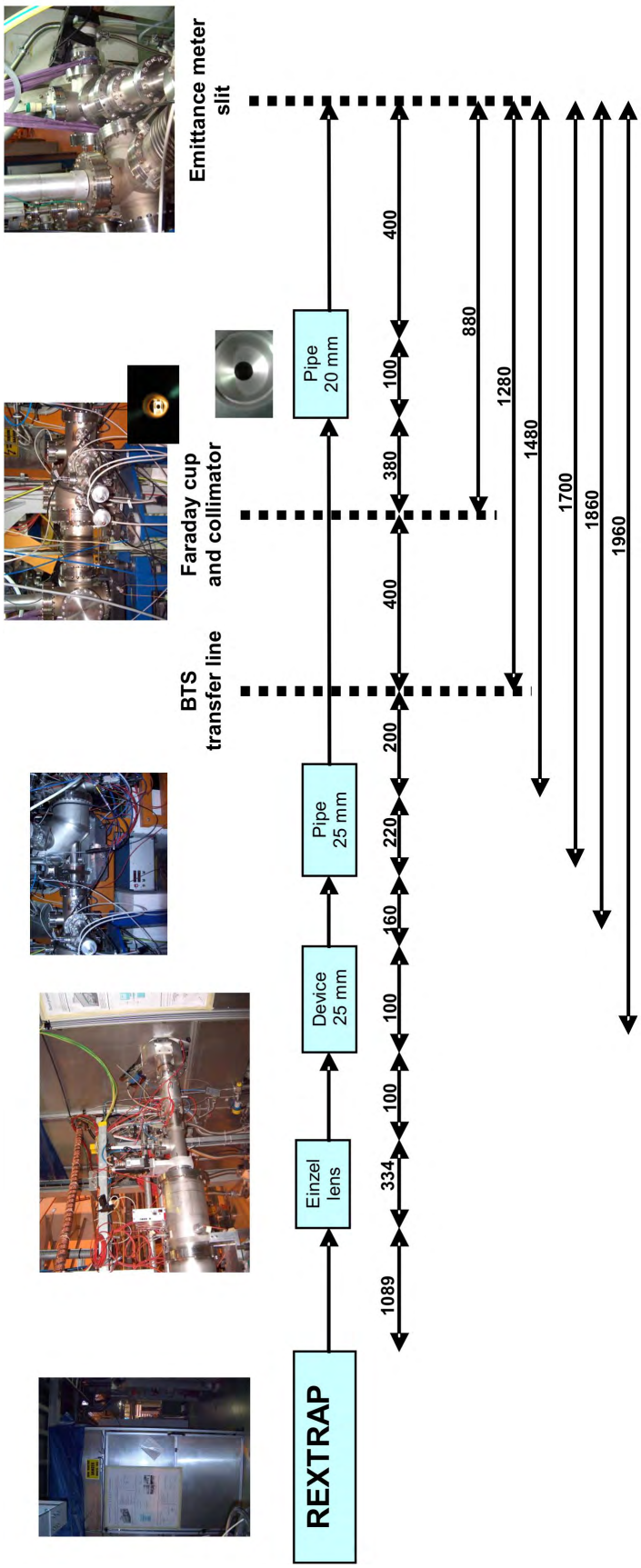

Figure 11.4: Layout of the beam line from REXTRAP to the emittance meter.

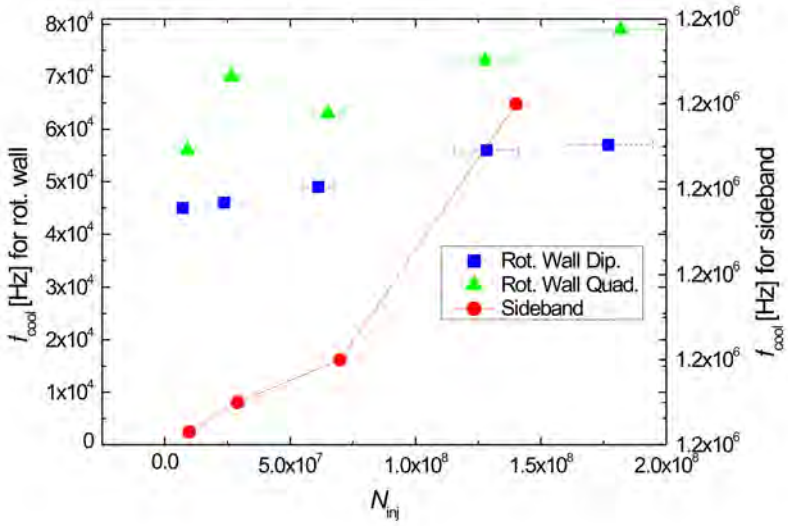

Figure 11.5: Resonance frequency f_{cool} for different cooling methods as a function of the number of ions injected into REXTRAP.

11.2.2 Time structure of the REXTRAP pulse

The Time-Of-Flight (TOF) signal recorded for the beam extracted from REXTRAP shows differences depending on both the method used for the cooling and the number of ions injected. Figure 11.6 compares the TOF spectra for the different cooling methods at the lowest and highest intensities measured. Figures B.1, B.2, B.3 and B.4 (see Appendix B) present the complete evolution of the TOF with the number of ions injected into the trap for the no-cooling, the sideband method, the rotating wall quadrupolar and the rotating wall dipolar method. The parameters used during the measurements are those listed in Tab. 11.2.

In all the TOF spectra, independently of the cooling method, two peaks appear. The right one correspond to potassium singly-charged ions ($A = 39$), which is the element released by the ion source. The other peak is due to the presence of neon buffer gas ions ($A = 20$) from the trap, although other contaminants cannot be discarded. The width of the potassium peak increases, for the four techniques, with the number of ions injected.

The presence of contaminants in the extracted beam means that it is necessary to remove the undesirable beam from the data to obtain a correct analysis of the measurements, particularly for the trap efficiency figure. The percentage of contaminants in the beam was calculated from the ratio of the integrals of the contaminant peak and the whole signal. Figure 11.7 plots the percentage of potassium in the beam for the four techniques as function of the injected ions in the trap. However it must be said that for extracted beams larger than 1 nA, whatever the cooling method, the peaks of potassium and buffer gas are overlapping and therefore the calculation provides a percentage of potassium in the beam which is a bit approximative and optimistic.

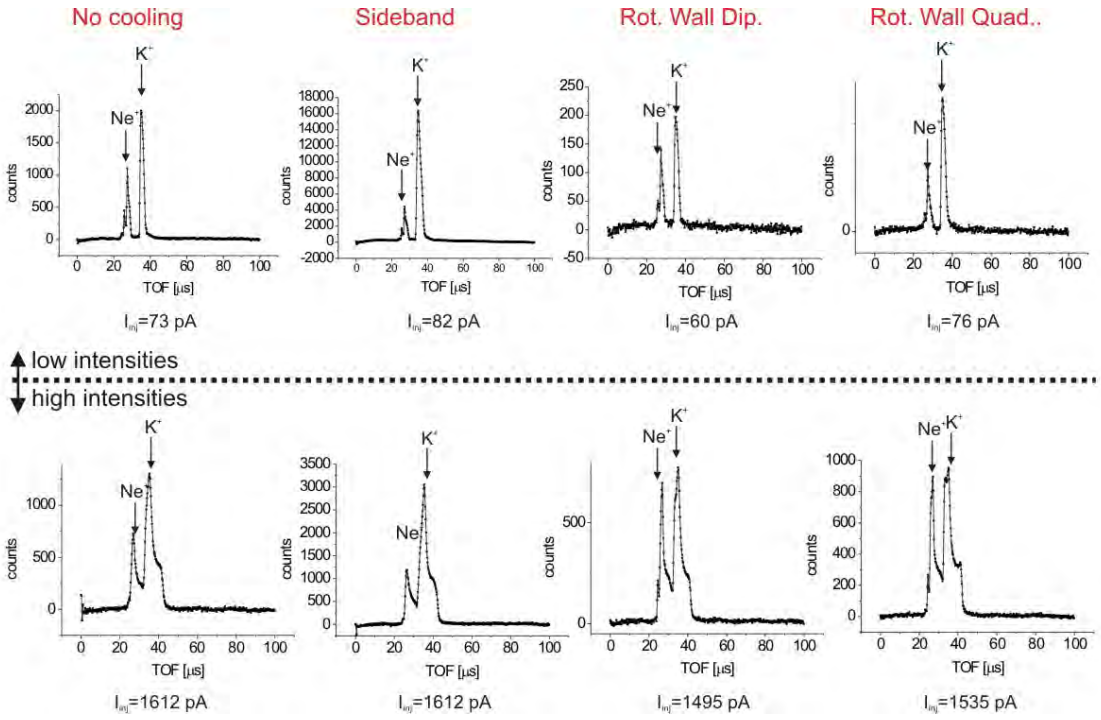

Figure 11.6: Plot of TOF spectra of the extracted beam from REXTRAP for the different cooling methods at low and high injected intensities.

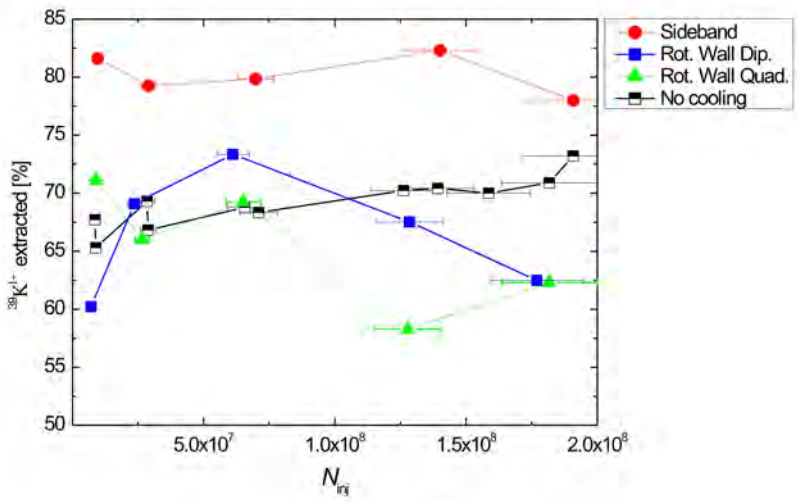

Figure 11.7: Percentage of potassium in the beam extracted from REXTRAP at 30 keV for different cooling methods as a function of the number of ions injected into the trap.

11.2.3 Efficiency of REXTRAP

At REXTRAP, the efficiency of the apparatus (η_{trap}) is defined as the ratio of the extracted ions (N_{ext}) over the injected ions (N_{inj}) per cycle:

$$\eta_{trap} = \frac{N_{ext}}{N_{inj}} \tag{11.1}$$

Experimentally, the efficiency is calculated from the current measured on a plate at the injection (I_{inj}) and at a Faraday cup (see Sec. 3.5.1) at the extraction (I_{ext}). Both of them measure the average current per cycle, for the injected ISOLDE beam in the first case and the extracted bunched beam in the latter. Hence, it is more straight forward to write the efficiency as:

$$\eta_{trap} = \frac{I_{ext}}{I_{inj}} \tag{11.2}$$

In the following, the efficiency plots from several measurement periods with different experimental conditions are presented. All the plots include the efficiencies for the three cooling methods and also the efficiencies without the presence of any RF cooling (no cooling). In this way it is possible to better compare and have a reference level for the performance of the cooling methods.

At 60 keV

In Figure 11.8, the efficiencies measured for all the cooling methods at 60 keV are plotted as function of the number of ions injected per cycle into the trap. The detailed conditions for these measurements are presented in Tab. 11.3.

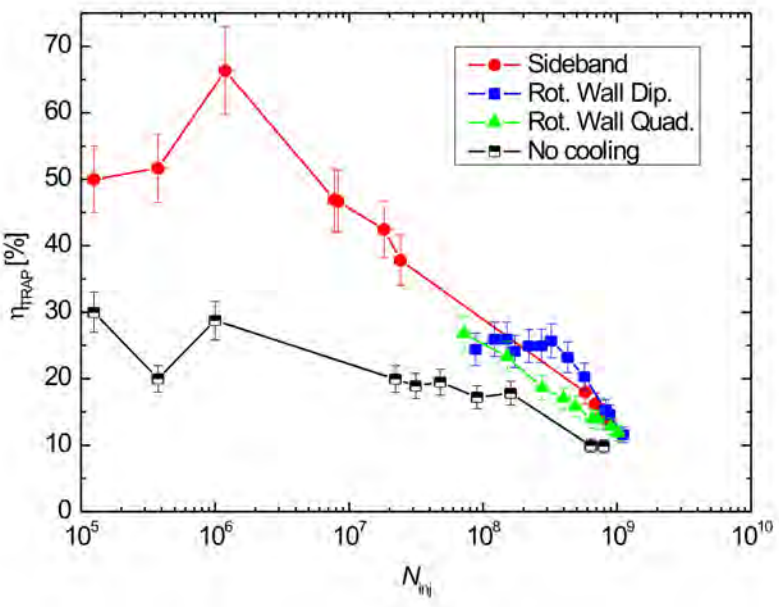

Figure 11.8: Efficiency for different cooling methods at REXTRAP depending on the number of ions injected for measurements at 60 kV.

Cooling method	Energy [keV]	$t_{cool}[ms]$	U_c(pp) [V]
no cooling	60	20	-
sideband	60	20	18
rot. wall quad.	60	20	30
rot. wall dip.	60	20	30

Table 11.3: Fixed parameters during the efficiency and transverse emittance measurements at 60 keV at REXTRAP. See explanation of each parameter in Tab. 11.2.

The graph shows clearly that the efficiency decreases with the number of ions injected. Sideband cooling appears as the best efficiency method globally in the region below 10^8 ions. In this region, sideband cooling achieves to improve the efficiency around 50% more than without no cooling. For more than 10^8 ions all methods give similar performance in terms of efficiency.

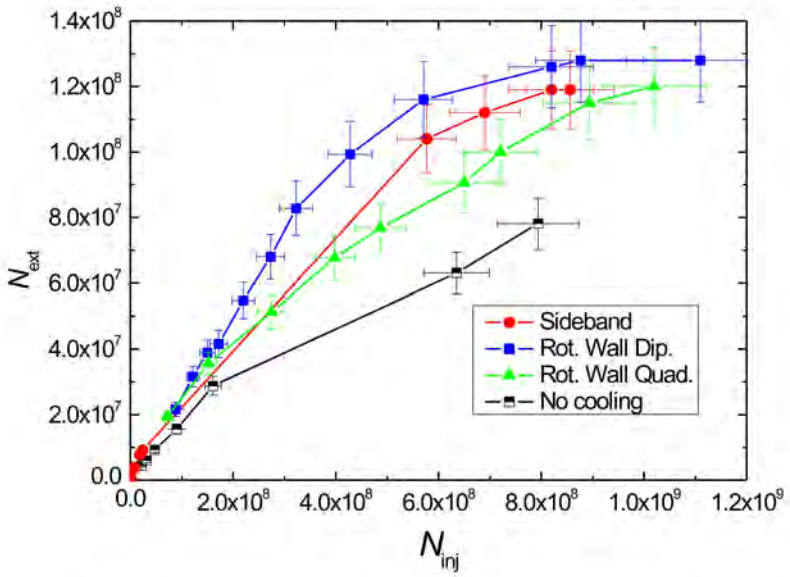

Figure 11.9: Plot of the number of ions leaving from the REXTRAP as a function of the number injected at a beam energy of 60 keV.

When the number of ions injected is larger than 10^8, the improvement of the efficiency (compared with no cooling) is not so spectacular. It seems that some kind of a saturation effect exists in this region. The effect can also be well observed plotting the number of ions entering versus the number of ions leaving the trap (Fig. 11.9). The dipolar rotating wall cooling is the technique that provides the best efficiency at high currents. At the region from 10^8 to $5 \cdot 10^8$ ions, dipolar rotating wall cooling obtains an efficiency around 25% of the efficiency but then decreases down to an efficiency of around 12% at 10^9 ions. It is important to point out that no analysis of the TOF signal of the extracted beam was carried out for these measurements. As a consequence results obtained can be partially distorted.

At 30 keV

Further measurements were carried out at 30 keV. Figure 11.10 plots the efficiencies calculated for all the cooling methods at 30 keV as function of the number of ions injected per cycle into the trap. The detailed conditions for the new measurements are presented in Tab. 11.4.

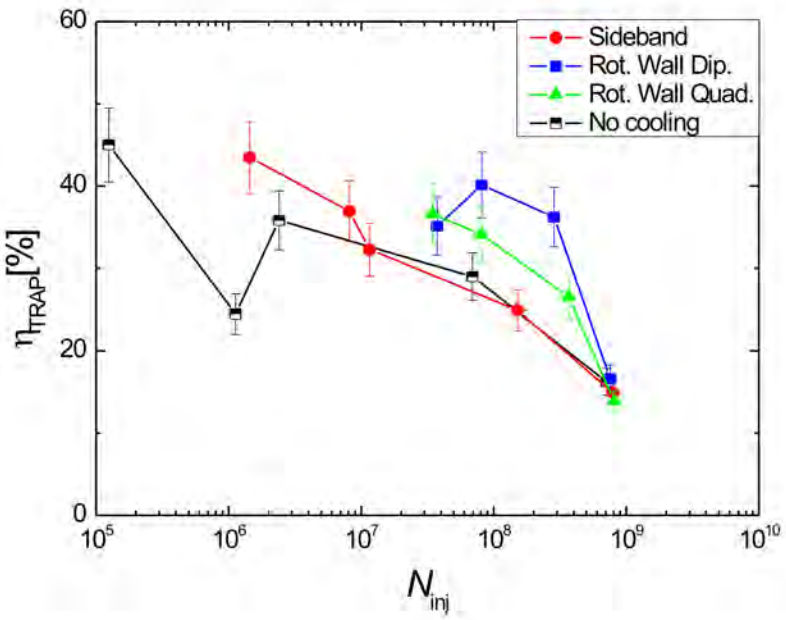

Figure 11.10: Efficiency of different cooling methods at REXTRAP depending on the number of ions injected for 30 keV beam energy.

It is clear that for these measurements the sideband cooling was not well optimized, but the slopes obtained for the rotating wall cooling and the no cooling are quite similar to the ones at 60 keV. Some conclusions can be obtained with this figure:

- The dipolar rotating wall cooling is still a better method than the quadrupolar one.
- Both rotating wall cooling methods are displaying the best performance in the range between 10^8 to 10^9 ions injected.
- The saturation of all methods at 10^9 ions injected is still present and no method is capable of surpassing this limitation.

It should be pointed out that the ion composition of the TOF signals was not analyzed for the 30 keV case, and this can affect the result.

As function of the cooling/cycling time

Figure 11.11 presents the result of a measurement of the efficiency of the trap for different cycling/accumulation times (t_{acc}) with no transverse RF cooling applied. The settings are similar to those in Tab. 11.3 but the cooling/accumulation time parameter is variable. Clearly the efficiency

Cooling method	Energy [keV]	$t_{cool}[ms]$	U_c(pp) [V]
no cooling	30	20	-
sideband	30	20	18
rot. wall quad.	30	20	30
rot. wall dip.	30	20	30

Table 11.4: Fixed parameters for the efficiency and transverse emittance measurements at 30 keV. See explanation of each parameter in Tab. 11.2.

without cooling decreases linearly for high accumulation times. The loss of efficiency is mainly due to the increase of the radius of the magnetron motion of the ions inside the trap. The ions are lost in the walls of the trap or have just a too high transverse energy to go through the extraction plate of the trap. Summarizing, the global effect is a linear decay of the efficiency which is function of the time of the ions in the trap (cooling or cycling time).

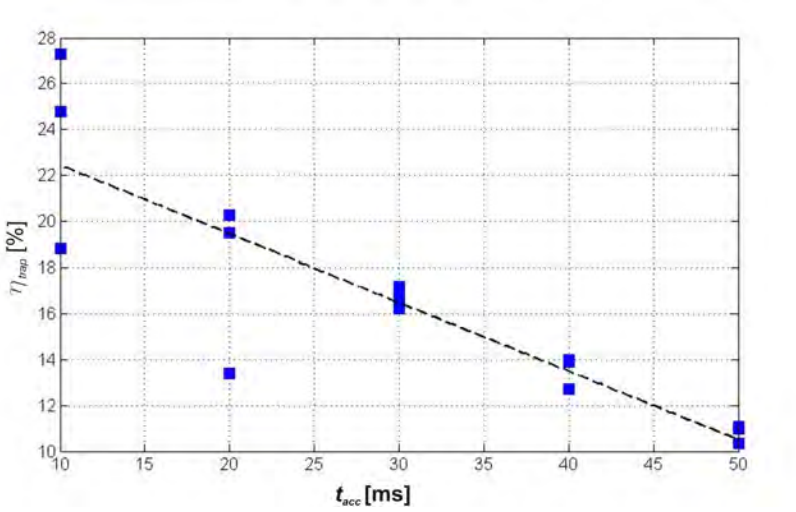

Figure 11.11: Efficiency of REXTRAP without cooling at 60 keV operation energy as a function of the cooling time.

As function of the cooling time and the voltage amplitude

The trap efficiency η_{trap} can also be studied as a function of the cooling time t_{cool} of the trap and the voltage amplitude of the RF electrical field supplied for the cooling U_c, for the same number of ions injected and with the same resonance frequency for the ion cooling. The goal of this kind of measurements is to search for the best point to be placed to get the best trap efficiency in a wide range among the plane $t_{cool} - U_c$.

Some measurements were made with the different ion cooling techniques to measure their efficiencies. For all these measurements, the injected ion current into REXTRAP was stabilized to a fixed value. The number of ions injected is chosen to be, for each technique, inside the range where the technique has proven mostly efficient (see Sec. 11.2.3). That means, the number of ions injected for the rotating wall were higher than for the sideband cooling.

Figure 11.12 shows the contour plot of the trap efficiency for the sideband cooling technique with a stable current of 66.5±2.5 pA at a total ion beam energy of 60 keV. The range of the voltage amplitude U_c is determined by the maximum amplitude that can be supplied, which corresponds to 18 V (peak-to-peak) for the sideband cooling. The figure demostrates that the best efficiency was achieved for the maximum amplitude U_c and a cooling time $t_{cool} = 20$ ms.

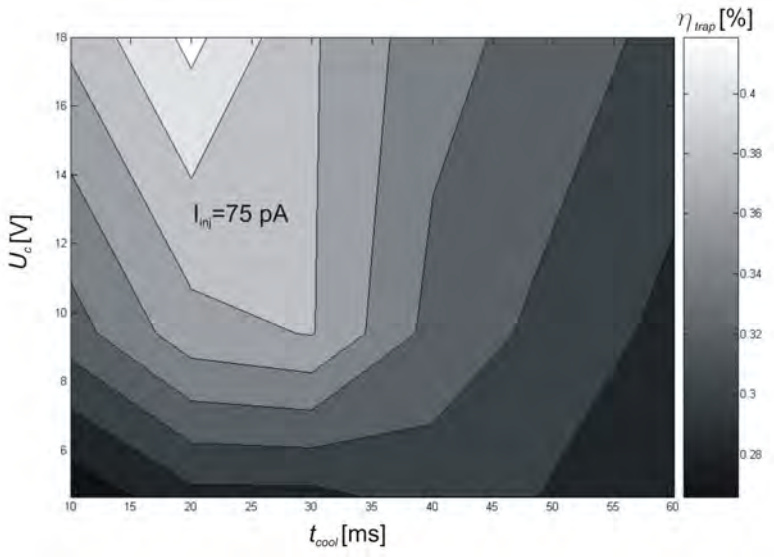

Figure 11.12: Contour plot showing the efficiency of the sideband cooling method at REXTRAP as a function of the cooling time t_{cool} and the amplitude of the RF electrical field U_c.

A similar study was done for the dipolar rotating wall cooling, as shown in Fig. 11.13. In this case, the best efficiency was obtained with a cooling time of 20 ms and a RF electrical field amplitude around 15 V. Surprisingly, the maximum efficiency does not occur at the maximum amplitude achievable (30 V). The RF electrical field dependance seems to be stronger. A stable operation for dipolar rotating wall cooling would correspond to a voltage amplitude of the RF electrical field around 15 V and a cooling time between 20 ms and 40 ms.

Further investigations could be carried out with different number of ions injected into the trap. The goal of those measurements would be to verify whether the optimized operation parameters in the plane t_{cool}-U_c are related with the injected ions. Moreover the efficiency dependence on the beam energy should be checked. That would give a complete map for an efficient operation of REXTRAP.

11.2.4 Transverse emittance of extracted beam from REXTRAP

Due to the limited acceptance of the REXEBIS [Wen01], it is of importance to minimize the transverse emittance of the extracted cooled beam from REXTRAP. Hence a set of transverse emittance measurements (see Sec. 2.2.1) were performed with different beam energies to compare the different cooling techniques. The results are discussed below. The data of the phase space of the REXTRAP released beam for each measurement was acquired by an emittance meter (see the layout in Sec. 11.1). All emittances are calculated using ELENA, a self-written code developed in MATLAB that allows the data from the emittance meter to be loaded and generates the phase space plots (for further information about the program see Appendix A).

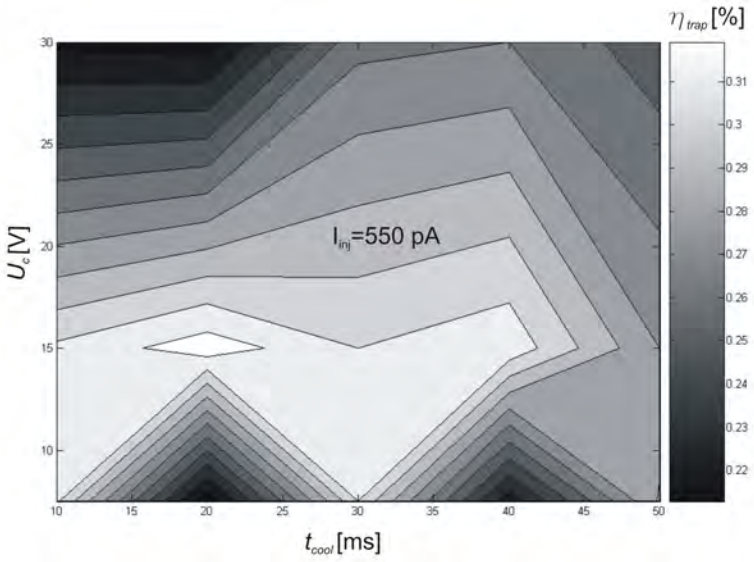

Figure 11.13: Contour plot showing the efficiency of dipolar rotating wall cooling at REXTRAP as a function of the cooling time and the amplitude of the RF field.

At 60 keV

Figure 11.14 compares the phase spaces obtained for different cooling methods at low and high intensities. The plot of all the measurements is presented in Appendix A.

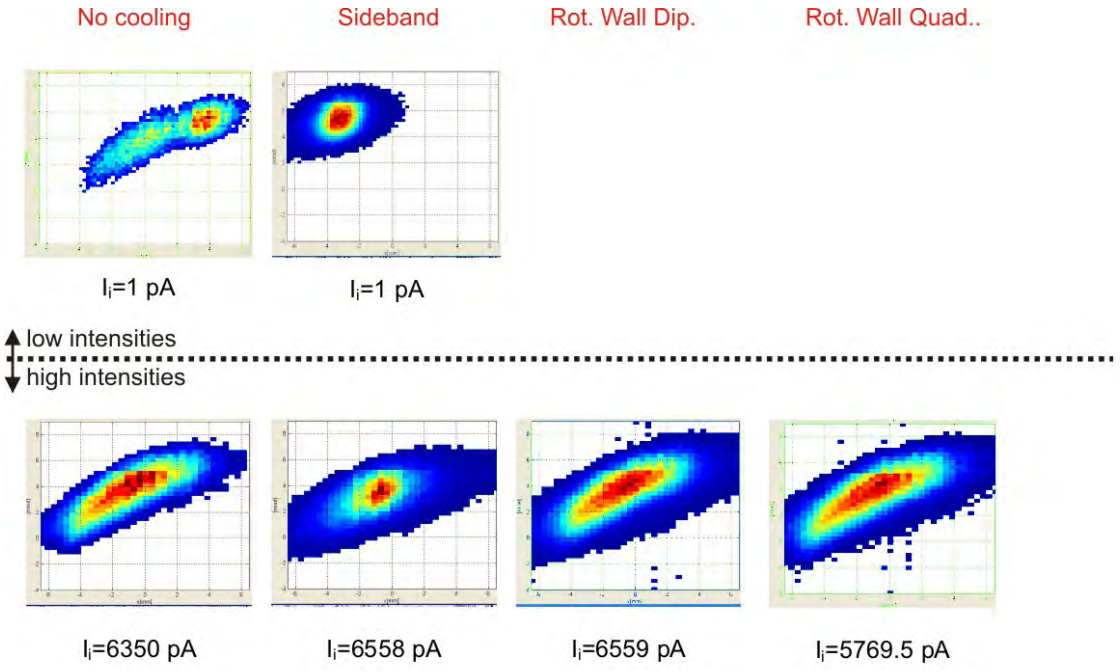

Figure 11.14: Comparative phase space recordings of the extracted beam from REXTRAP at 60 keV for the different cooling methods at low and high injected intensities. Rotating wall cannot be applied for low intensities.

Figure 11.15 shows the value of the 90% geometrical transverse emittance of the beam at 60 keV ($\epsilon^{90\%}_{60keV}$) as a function of the injected ions. For a low number of ions, the sideband cooling gives the lowest emittance values and the rotating wall cooling method cannot be used since no resonance could be found. In this region the emittance using sideband cooling is improved up to a 50% compared to no cooling. For more than $2 \cdot 10^8$ ions, the emittance given by the sideband cooling increases. From $4 \cdot 10^8$ to 10^9 ions, all three methods give very similar emittance values, and comparable to the value obtained without cooling.

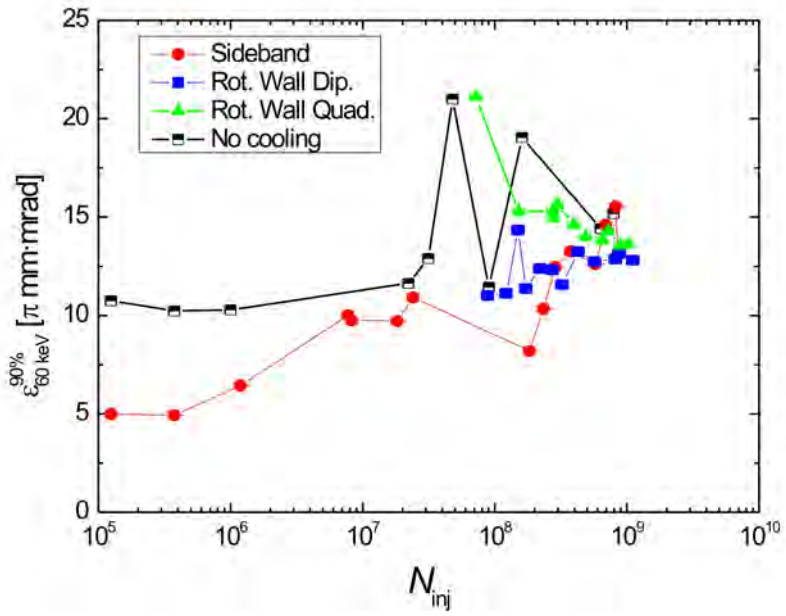

Figure 11.15: 90% geometrical transverse emittance at 60 keV from different cooling methods as a function of the number of ions injected.

To summarize, sideband cooling is the best technique for weak beams. At high number of ions the cooling improvement made by the techniques can not be seen clearly, and the emittance obtained with all cooling methods are similar to the emittances without applying any cooling.

In Section 2.2 it was shown that another way to consider the emittance is to calculate it statistically. Here the statistical emittance is calculated using the 2σ standard deviation of the data in x and x', the so-called Lapostolle emittance [Lap70]. As was shown before, this emittance corresponds to approximately 90% of the geometrical transverse emittance if the data has a gaussian distribution. Figure 11.16 plots the values of the Lapostolle emittance for cooling methods versus the number of injected ions. The plot is similar to Fig. 11.15 but here the oscillations in the values are much bigger, which means that value are not so confident and that geometrical emittance calculations applies better for this data.

A cut was found after an accurate analysis of the measured phase spaces with the tracker capability of ELENA (see Appendix A). The cut was located around 1700 mm before the measurement point, which coincides with a differential pumping pipe of 25 mm diameter before the BTS line (see Fig. 11.4). This cut affected the acceptance of the emittance meter.

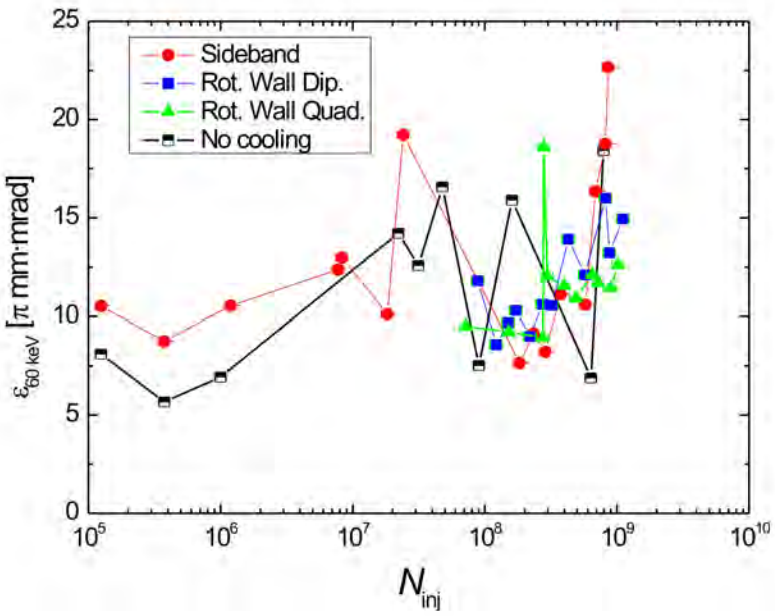

Figure 11.16: Lapostolle emittance at 60keV using different cooling methods at REXTRAP. The emittance is plotted versus the number of ions injected.

For these measurements no TOF analysis was carried out, so for high intensity beams with no cooling and rotating wall cooling method, the phase space is probably contaminated and is bigger than if it only includes the potassium ion beam.

At 30 keV

Due to the transmission problems occurring during the measurements at 60 keV, new measurements were carried out to improve the performance. For that reason all the optics elements of the beam were carefully optimised. Most of the attention was devoted to centering the diaphragm installed by WITCH, which was thought to be the source of the problems in the last measurements. In addition a lower beam energy was fixed to verify if a bigger beam could be handled. The result was that the emittance was still cut. Unlike it happened in the measurements at 60 keV, in this case the cut is observed a bit closer to REXTRAP, in the kicker (see Fig. 11.4 and Fig. 11.17), which means the focal point was changed. That confirmed the real emittance out from REXTRAP is difficult to be measured with the existing configuration of the beam line.

Disregarding the cut, Figure 11.18 compares the phase spaces obtained for different cooling methods at low and high intensities. The plot of all the measurements is presented in Appendix A.

Fig. 11.19 shows the 90% geometrical emittance at 30 keV as function of the number of ions injected. To more clearly present the effectiveness of the cooling, the current density distribution over the phase space can be plotted in three dimensions and in a same scale for the different methods. This is done in Tables B.9 and B.10 as function of the beam intensity and cooling method.

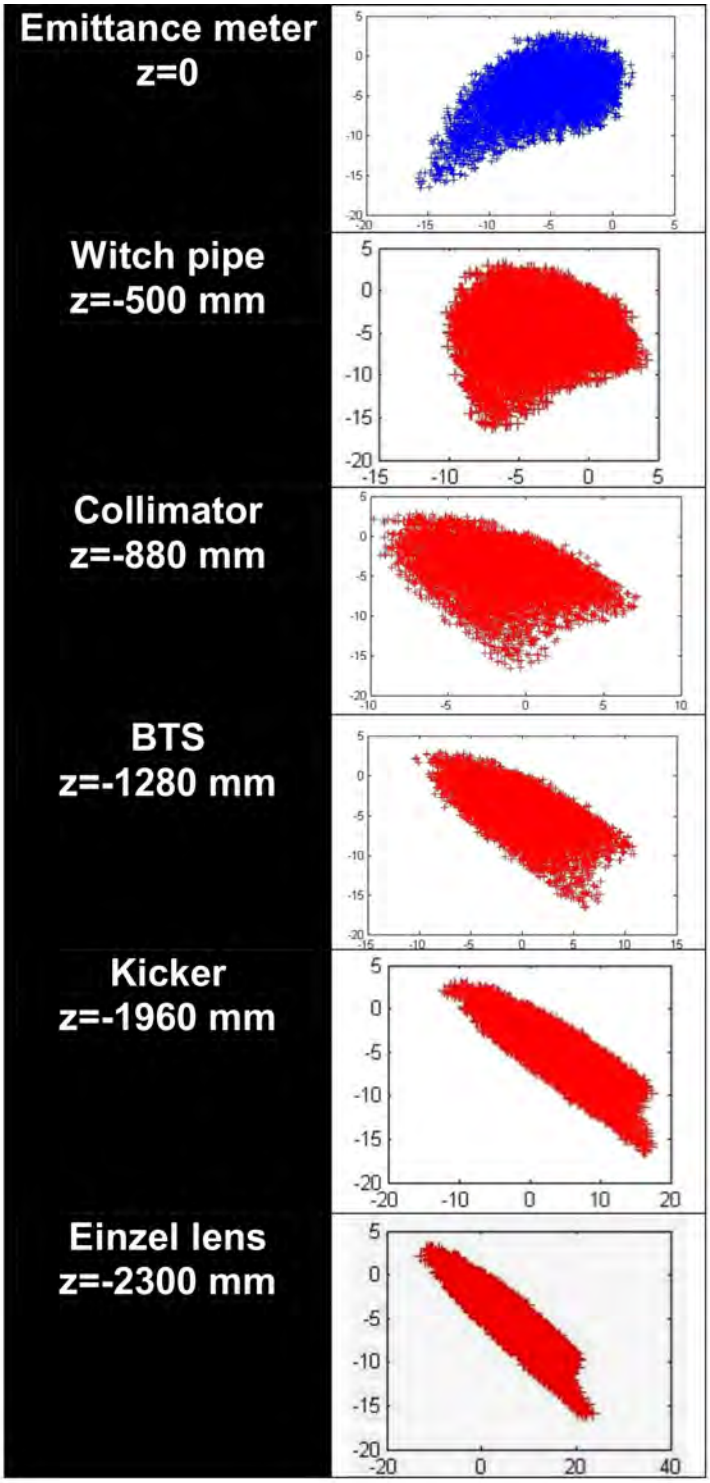

Figure 11.17: Phase space plots for a non-cooled beam at 30 keV and 5.7 nA traced backwards with ELENA.

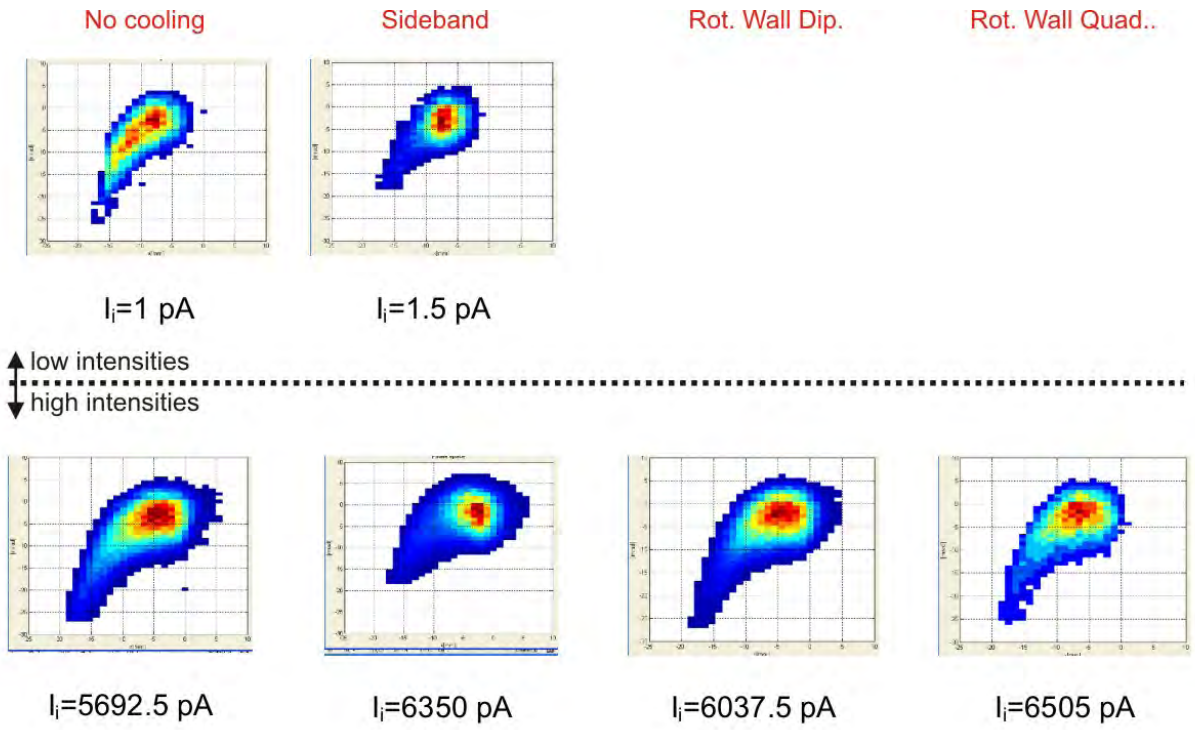

Figure 11.18: Comparative phase space recordings of the extracted beam from REXTRAP at 30 keV for the different cooling methods at low and high injected intensities. Rotating wall cannot be applied for low intensities.

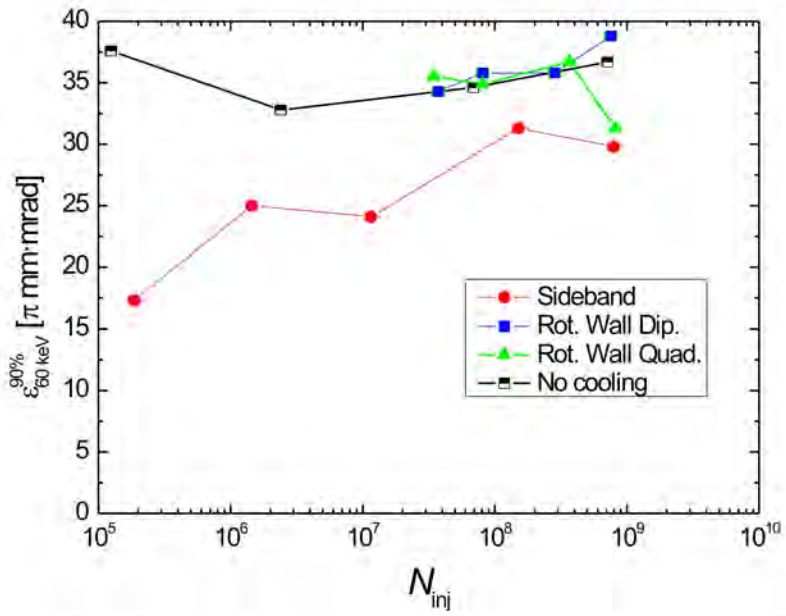

Figure 11.19: 90% geometrical emittance at 30 keV for different cooling methods depending on the number of ions injected.

11.2.5 Brilliance of the extracted beam from REXTRAP

For a more complete study of the optical quality of the extracted beam, the brilliance can be calculated. It would give more information about the size of the beam, normalized for the number of ions present in the beam in that moment (see Sec. 2.3). The problems to apply this quantity to the REXTRAP measurements are:

- The transverse emittance is supposed to be equal in both phase spaces.
- There is an error in the value of the transverse emittance due to the cut in the phase space.
- The extraction intensity was measured with a large error of 10%. Transverse phase spaces measured with a larger error have not been taken into account.

In the following discussions all these items are taken into account.

At 60 keV

Figure 11.20 shows the brilliance as function of the number of ions injected for the measurements at 60 keV. The plot confirms what was seen in the efficiency plots. The beam released by the sideband cooling method has the best optical properties for the whole range of ions injected. According to this plot, the dipolar rotating wall cooling obtains better results compared with the non-cooling. However, the quadrupolar wall cooling decreases the quality of the beam (most probably due to a strong beam contamination).

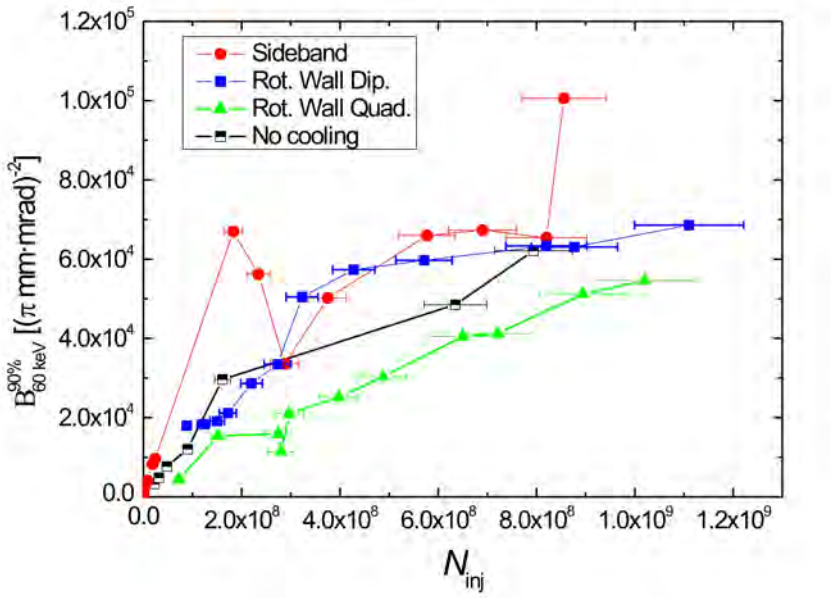

Figure 11.20: Comparison of the beam extracted brilliance from REXTRAP at 60 keV for different cooling methods as function of the number of ions injected and using 90% geometrical transverse emittance (assuming are symmetrical in both phase spaces).

At 30 keV

Figure 11.21 shows the brilliance as function of the number of ions injected for the measurements at 30 keV. Again the sideband cooling comes out as the most suitable method. The dipolar rotating wall cooling seems to tend to get better results in the range from 10^8 to $4{\cdot}10^8$ ions injected, although there is a lack of measurements in that region to confirm the veracity of the effectiveness of the dipolar in that region. In addition, the saturation effect around 10^9 ions injected is not clearly visible this time.

11.2.6 Cooling efficiency of REXTRAP

So far an independent analysis of the most important parameters for a good beam transmision and injection into EBIS has been done through the efficiency of the Penning trap, and the emittance and the brilliance of the extracted beam.

In order to make a better choice of the type of cooling, another very useful parameter to analyze is the cooling efficiency as presented in Sec. 2.4 and defined in Eq. 2.40. This expression can also be expressed as:

$$\eta_B = \epsilon_{inj,x}\epsilon_{inj,y}\frac{\eta_{trap}}{\epsilon_{ext,x}\epsilon_{ext,y}} \tag{11.3}$$

In the particular case of REXTRAP, the emittance of the ion source ($\epsilon_{inj,x}, \epsilon_{inj,y}$) is unknown so only the expression:

$$\eta_{Bred} = \frac{\eta_{trap}}{\epsilon_{ext,x}\epsilon_{ext,y}} \tag{11.4}$$

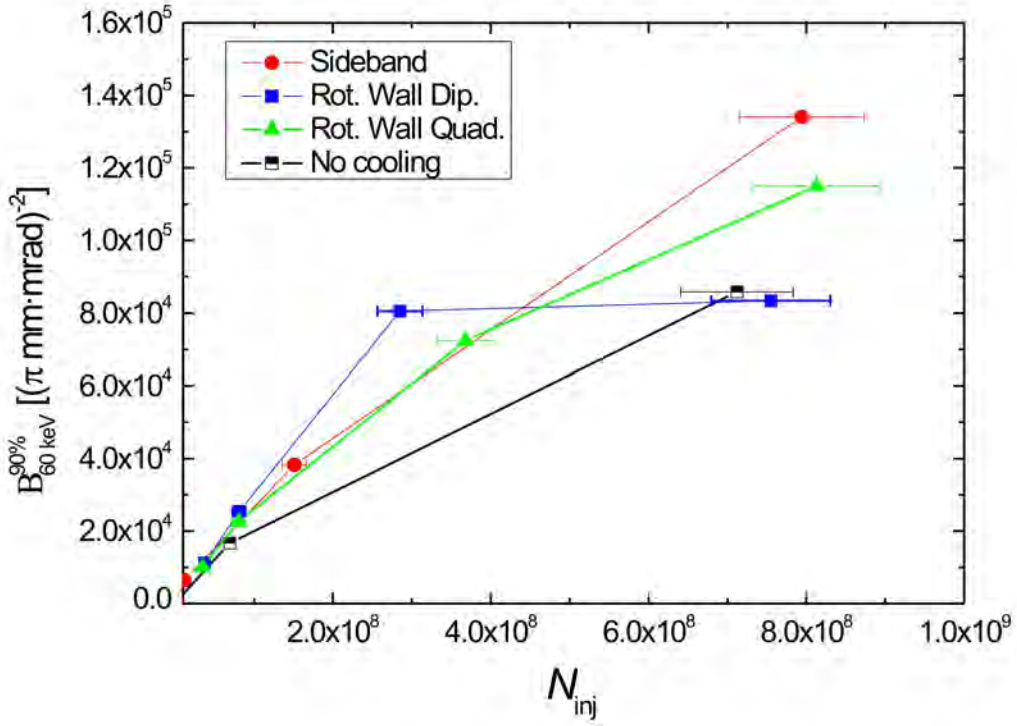

Figure 11.21: Comparison of the brilliance of the beam extracted at 30 keV for different cooling methods as function of the number of ions injected and using 90% geometrical transverse emittance (assuming are symmetrical in both phase spaces).

can be plotted, as function of the efficiency of the trap η_{trap} and the emittance in both transverse planes, supposed to be equal $\epsilon_x = \epsilon_y$ both for the injected and for the extracted beam.

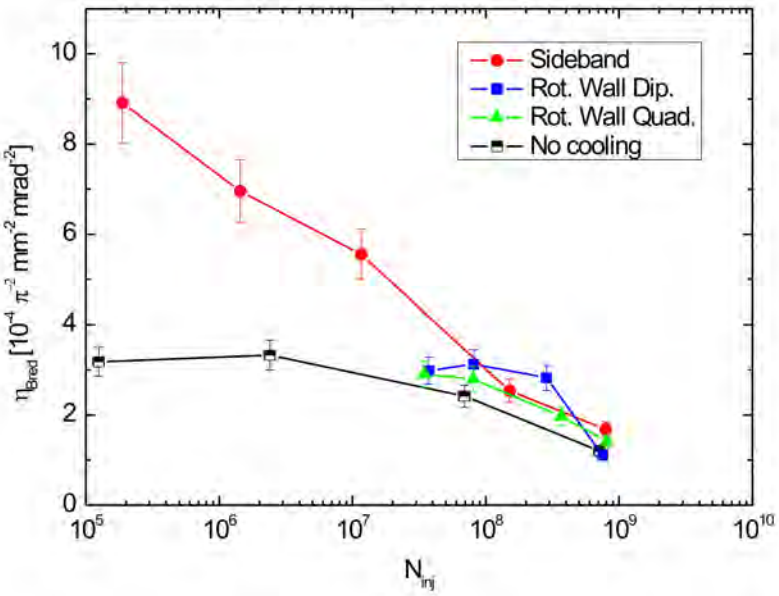

Figure 11.22: Reduced cooling efficiency in REXTRAP η_{Bred} at 30 keV calculated as ratio of the efficency and the 90% geometrical transverse emittance.

Figure 11.22 shows the tendencies of the cooling efficiency for the different types of cooling analyzed. It can be observed that the sideband cooling technique is the best option for less than 10^8 ions injected into the trap. In all the range where rotating wall manages to operate, the dipolar rotating wall cooling seems to obtain better results (although no contamination analysis was carried out). From around 10^9 ions, the trap seems to be filled and there is no cooling method which can improve the brilliance.

11.2.7 Beam injection into REXEBIS

The best way to verify the quality of the ion beam, obtained with the different cooling methods, is to inject it into and charge bred inside the REXEBIS (see Sec. 3.4.2) and thereafter measure the extracted current after the mass separator. That means, unlike the ion beam out from REXTRAP, the beam does not have any undesirable elements, e.g. rest gas. Hence the efficiency depends only on the optics quality of the ion beam. Better cooled beams in REXTRAP would mean better global efficiencies.

First of all, the ion beam was optimized at an energy of 30 keV for injection into REXEBIS from REXTRAP using sideband cooling , which is the normal cooling method. The mass separator was tuned for $^{39}K^{10+}$. Once a good efficiency was obtained with the normal method some systematic measurements were done by varying only the number of ions injected (changing the beam gate of the injected beam) and the resonance frequency for the sideband cooling (scanned for each measurement). All the other parameters at REXTRAP, REXEBIS and the mass separator

Cycle frequency f [Hz]	Electron beam current I_e [mA]
50	235.9

Table 11.5: Fixed parameters at REXEBIS during the injection measurements from REXTRAP.

were kept constant. At the same time, measurements with no cooling at all in the trap were done to observe the real performance of the other cooling methods.

After the measurement with sideband cooling, the trap was prepared for the use of the rotating wall dipolar method. The same parameters than before were kept for the ion source, the trap (except the resonance frequency), the EBIS and the mass separator. Finally, the same was done with the rotating wall quadrupolar cooling method. The main trap parameters used in the measurements are summarized in Tab. 11.2. Table 11.5 gives the parameters for the EBIS and the mass separators.

Efficiency

The total efficiency of the beam η_{total} is measured as:

$$\eta_{total} = \frac{N_{ext-ms}}{N_{inj-REXTRAP}} \tag{11.5}$$

where $N_{inj-REXTRAP}$ is the number of ions injected into REXTRAP and N_{ext-ms} is the number of ions extracted from the mass separator. $N_{inj-REXTRAP}$ is calculated from the intensity of the ion beam measured at the injection plate of REXTRAP:

$$N_{inj-REXTRAP} = \frac{I_{ip}}{f} = I_{ip} t_{cool} \tag{11.6}$$

where I_{ip} is the mean intensity measured at the injection plate and f is the cycling frequency. Correspondingly,

$$N_{ext-ms} = \frac{I_{RFQ}}{C f_{EBIS}} \tag{11.7}$$

where I_{RFQ} is the mean intensity measured at the faraday cup just after the mass separator, f_{EBIS} the breeding cycle frequency and C is the charge of the ions measured which is $C = Qe$ where Q is the charge state (10 for the potassium ions measured in the injection tests) and e is the elemental charge. The f_{EBIS} is synchronized to the trap frequency and therefore: $f_{EBIS} = 1/t_{cool}$. Therefore, finally the total efficiency η_{total} can be calculated as:

$$\eta_{total} = \frac{I_{RFQ}/Q}{I_{ip} t_{cool}} \tag{11.8}$$

Figure 11.23 compares the global efficiency (η_{total}) for different cooling methods as function of the number of ions injected into the trap. As mentioned before, all the measurements were done with the same optics parameters and at a beam energy of 30 keV. The graph clearly outlines the good behavior of the sideband cooling for less than 10^8 injected ions. Both rotating wall cooling methods (dipolar and quadrupolar) have a similar response but there is no improvement in relation with the trap working without applied cooling.

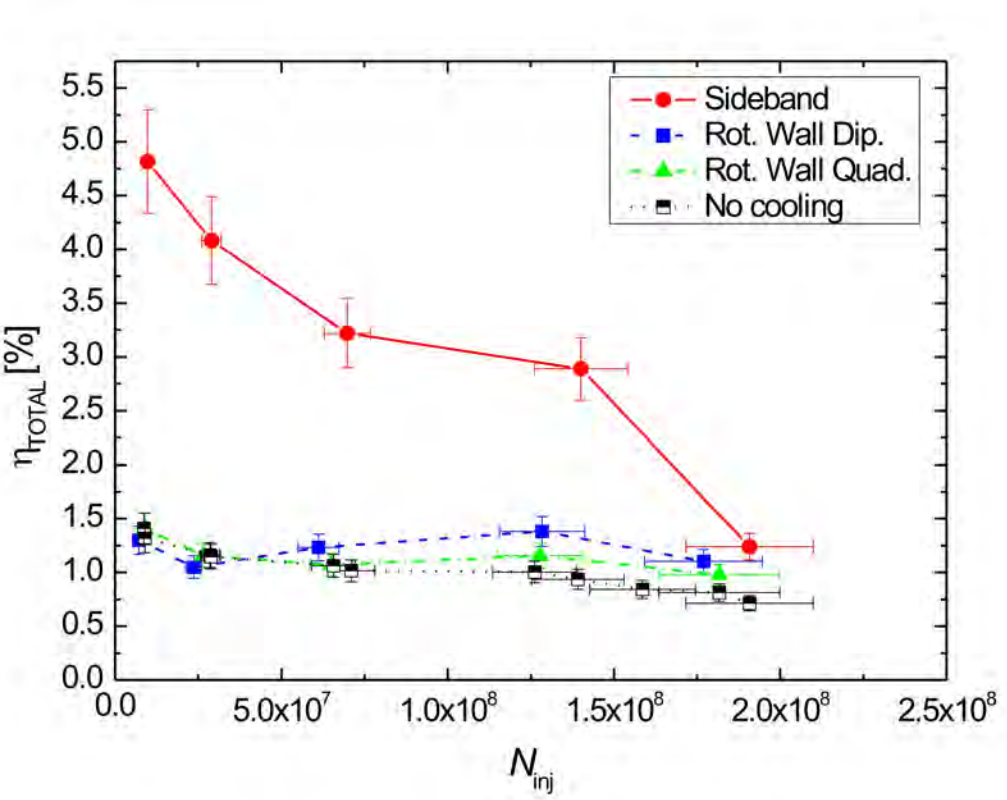

Figure 11.23: Comparison of the global efficiency η_{total} at 30 keV beam energy for different cooling methods as function of the injected ions into REXTRAP.

11.3 Conclusions

When summarizing the results obtained from the different cooling methods at REXTRAP, it is clear that the sideband cooling technique is the best performing method for preparing the beam for injection into the REXEBIS. For less than 10^8 ions injected into the trap, it is also the best method in terms of both efficiency and transverse emittance out the trap. In fact, in that region, the rotating wall cooling methods do not work (lack of cooling frequency resonance). The emittance obtained with sideband cooling fulfills the requirements of acceptance of REXEBIS (10 πmm·mrad at 60 keV) for less than 10^8 ions.

In the region between 10^8 and 10^9 ions the conclusion is not clear-cut. For all the cooling methods, the improvement in neither efficiency nor emittance is not so evident with respect to no cooling. Anyhow when both figures are taken into account (brilliance and cooling efficiency), the dipolar rotating wall cooling seems to be advantageous for this region. However, the difficulties to obtain guaranteed figures for the emittance and the contamination existing in the delivered beam with the rotating wall methods, make the sideband still the best method. For bigger number of ions the traps is saturated and the decrease in brilliance is constant for all the methods. Hence no cooling method is satisfactory in this region, although sideband cooling still achieves to improve a bit the beam optics, but in minor proportion than for less than 10^8 ions injected into the trap.

In the future, further tests with different voltage amplitudes of the rotating wall electrical field applied should be carried out in order to check if the method could be improved by increasing of the Lorentz force compressing of the ion cloud. In addition, the rotating wall seems to increase the extraction of rest gas and other contaminants, therefore not only increasing the extraction efficiency of the required element. A theoretical study of the reasons should be carried out. Only after the completion of these studies the rotating wall cooling can fully be discarded as a high intensity technique. In addition, attempts to use high voltage amplitudes in the sideband cooling could be investigated.

The present study has established the current limits for the manipulation of more intense RIB's and has given the guidelines for the continuation of the studies with the rotating wall technique.

Conclusions

In the frame of this work some important achievements in the field of the beam preparation have been done. As the most important one, the complete design and assembly of a new RFQCB for ISOLDE, ISCOOL, ready for off-line commissioning and later on-line installation after the HRS. This new device is a step forward general purpose RFQCBs, not only devoted to a single experiment, but capable to adapt the beam extraction to the characteristics of experiments. That represents a real milestone for the integration in the future second generation facilities as HIE-ISOLDE, which are the step before the construction of the EURISOL facility. Besides the general purpose ability, ISCOOL will be in combination with the new magnet design for the HRS, a test bench for the research in higher resolution mass separators. More pure, efficient and intense beams are expected from this design.

In addition ISCOOL has some features that makes it an unique machine among the other RFQCBs. In the optics and mechanical design, a design of the injection and extraction part which comes from the experience taken from the first generation devices, and a new layout of the axial electrodes which allows better control of the extraction. This work has also afforded a new model for the design of the vacuum system. Further developments of the model (intermediate flow, turbomolecular and roughing pumps, ,time dependent pumping speeds of the turbopums) can be integrated). The integration into the ISOLDE vacuum system has been studied. The control and electronics represents an important point to give the device the reliability necessary for operation as an on-line device. The control is done by a PLC (for first time implemented in these kind of devices), and the RF supply has been ordered specially to meet the frequency and amplitude requirements. In the same framework, the other electronics components are standard CERN devices, reliable and with easy maintenance. The other components of ISCOOL (e.g. gas feeding line) have been chosen by the experience acquired in the past RFQCB in operation in other facilities. The dissertation presents, in general, an engineering point of view to facilitate the design of future similar devices, with a detailed explanation of all the process and stages followed. Moreover, the assembly of ISCOOL and the set-up of the test bench has been presented. The systems designed in the framework of this thesis work without problems and the system is ready for commissioning.

This dissertation has also studied the rotating wall cooling as the method for cooling more intense beams in a Penning trap, when the space charge effects are not negligible. The analysis has concluded that, in the present conditions, the rotating wall cooling does not improve the beam extracted and sideband cooling is still the best method applicable. The constraint in REXTRAP on the amplitude of the voltage for the cooling implies that further investigations should be done with higher amplitudes. Moreover the beam extracted with sideband cooling is more pure than the beam extracted using the rotating wall technique. That implies that further studies of the effect of the rotating wall field over the rest gas, and the influence of the buffer gas pressure on the efficiency of the method should be done. The emittance measurements did not give not a clear answer, due

to the presence of too many optics elements in the measurement line that make difficult the data acquisition. However, the efficiency measured after injection of the REXTRAP beam into the REXEBIS and later mass separation agrees with these results. In addition, during this dissertation a complete software for the analysis of the emittance measurements was developed. The same software might be used for other experiments to analyze future data.

The emittance measurements at REXTRAP have shown up that for more than 10^8 ions injected into REXTRAP, the emittance out is higher than the acceptance of REXEBIS. The use of ISCOOL as injector of REX-EBIS could improve the global efficiency of REXEBIS, in particular, and of all REX-ISOLDE in general. Once ISCOOL will be working on-line, complete tests of the benefits of the injection of the cooled and bunched beam from ISCOOL have to be carried out.

Appendix A

ELENA: new software for emittance analysis

During the analysis phase of the emittance measurements done at REXTRAP (see Chapter 11), the development of a new software to provide an easy and straight forward analysis of the data taken with the emittance meter was done. These results were compared with those obtained using other analysis programs. The software proposed is ELENA (Engineering tooL for Emittance aNAlysis), a stand-alone program developed in MATLAB 7.0.1®with its GUIDE toolbox.

A.1 Main features

The software provides the analysis of data taken with an emittance meter. The aim is to automatize and make as easy as possible the analysis work, trying to obtain a reliable value for the emittance. The following features are added to assure its functionality:

- Data acquisition from several types of emittance meters. Data files from the LMU emittance meter [Wil02] and from the NTG emittance meter.
- Emittance plots in several formats: image, contour, filled contour or 3D.
- Geometrical emittance calculation using three different algorithms: percentage of the maximum current level, percentage of intensity.
- rms emittance calculation.
- Plot of the results from the fit of geometrical and rms emittance.
- Automatic/manual offset.
- Emittance plot as a function of the number of intensity levels taken into account for the calculation.
- Gaussian distribution test of the data.
- Track back and forward the beam space through drift beam lines.

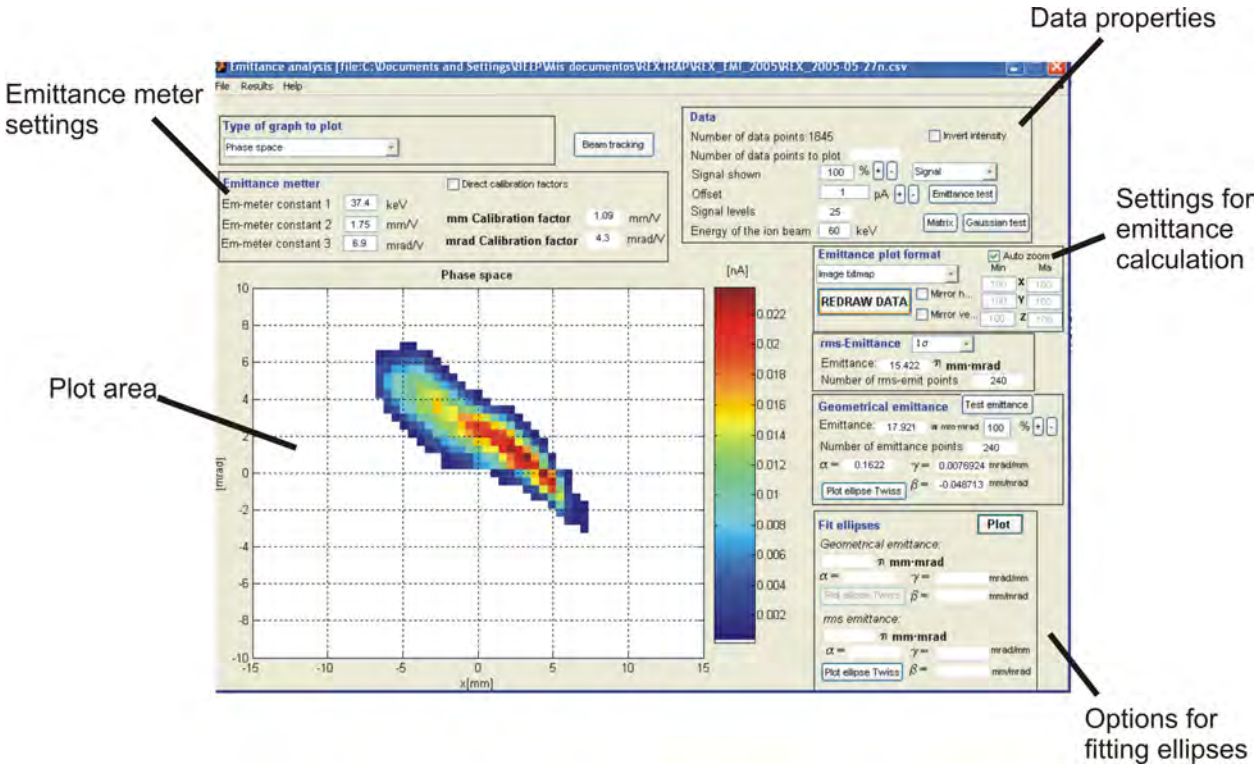

Figure A.1: Picture of the main graphical user interface of the program.

A.2 Strategies of software calculations

A.2.1 Background signal level

In most of the measurements carried out with an emittance meter, the data obtained would contain noise coming from the electronics. The noise will be random and with an intensity much less than the data of the beam. For that reason, in most of the cases the electronics noise fits the level of sensitivity of the instrument. Low intensity beams will need either to amplify the signal using an electron multiplier (if possible), or to increase the data taking time. However, even if the noise is small, it is necessary to be able to remove it from the data for a better visualization and calculation analysis. ELENA handles this problem in two different ways.

Automatic

As soon as a data file is open, ELENA analyzes the data and then plots the phase space in the *Plot area*. Automatically, ELENA eliminates those points which give a negative current value (or positive in the beam has been captured with negative current). If necessary, the data can be recovered using the manual offset later on (see next section).

Manual

A manual offset can be applied to the data. This value is chosen by the user and it is then substract to all the data. In that way, the values that are negative after this operation are not represented in the phase space and are eliminated of the matrix for the calculations. Unfortunately, in this version

of the program if it is not possible yet to remove noise of the phase space selecting the points to be removed, marking them dragging the cursor in the *Plot area*.

A.2.2 Non-normalized emittance

One of the main capabilities of the program is the calculation of the non-normalized emittance of the phase space analyzed. The geometrical and statistical emittances (see Chapter 2)can be supported and calculated by the program.

Geometrical

ELENA calculates the area enclosed by the percentage of beam selected by the user. For the calculation of the percentage, two different approaches are used:

- Current percentage. The calculation is done as:

$$I_{min} = (\%_{user}/100) \cdot I_{max} \tag{A.1}$$

  where I_{max} is the maximum current of a point captured in the beam, $\%_{user}$ the percentage chosen by the user and I_{min} the minimum current of a point in the new data, all data with a current minor than I_{min} is removed from the beam.

- Signal levels percentage. The data is transformed in percentage of the total current of the beam. That means that each level (points of the data with the same intensity) have the same percentage value. The total beam current is calculated adding up all the current from all the points. The levels enclosing an area with a value of percentage of area enclosed minor or equal to that chosen by the user are shown in the figure and involved on the calculations.

The signal levels percentage should give a better approximation to the geometrical emittance. Anyway, for a good calculation it is also necessary to interpolate the data since the signal levels rarely contains the percentage required by the user.

A.2.3 rms-Emittance

Calculating the statistical deviation of the data, it is possible with ELENA to show the rms-emittance for a certain value of σ. In addition, the ellipse which can be fit with the value calculated and the Twiss parameters, can be plot in the *Plot area* together with the real data for comparison.

A.2.4 Tracking of the transverse phase space

The software has the capability to track the portrait of the phase space back or forward through drift beam lines (without beam optics elements). This tool is very useful to observe how the phase space evolves through the beam. It can be used to see if the beam obtained with the emittance meter fits the size of the elements that it has passed, analyzing the possibility of cuts in the measurements.

The algorithm shown in Fig. A.2 has been used to track the phase space obtained with the emittance meter . The algorithm is based in assigning a number of points to each square (that depends on the resolution of the emittance meter) proportional to the intensity captured by the emittance meter. In that way, the discrete matrix captured for the emittance meter is converted in a scattered plot. Once the phase space is converted into a scattered plot form, with two vectors, one for the transverse space coordinate (normally in mm) and one for the transverse angle spread coordinate (normally in mrad), the beam is tracked to the new point desired by the user according to [Wol87]:

$$\mathbf{x}_2 = \mathbf{x}_1 + \Delta z \cdot (\mathbf{x'}_1/1000) \tag{A.2}$$

$$\mathbf{x'}_2 = \mathbf{x'}_1 \tag{A.3}$$

where $\mathbf{x}_1$ and $\mathbf{x}_2$ represent the vectors of the transverse space coordinate in the initial and final position respectively, $\mathbf{x'}_1$ and $\mathbf{x'}_2$ the vectors the transverse angle spread at the initial and final position in mrad, and δz the longitudinal distance between the initial and the final position. δz is positive in case tracking the beam forward and negative if the track is done backwards.

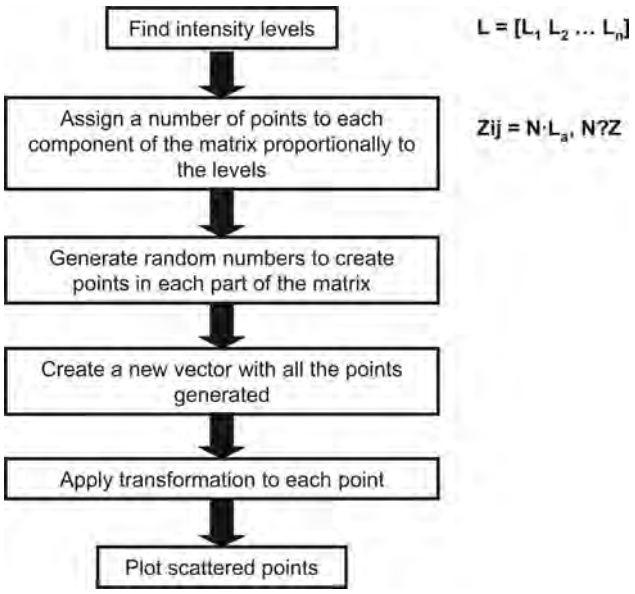

Figure A.2: Scheme of the algorithm to track the beam.

Appendix B

Phase spaces of the beam extracted from REXTRAP

This Appendix contains tables and figures to give further and deeper information about the measurements carried out at REXTRAP and which have been explained and discussed in Chapter 11.

B.1 Summary tables of the TOF measurements

Figures B.1, B.2, B.3 and B.4 present the plots of the Time Of Flight signal for no cooling, sideband, dipolar and quadrupolar rotating wall cooling, respectively, per different injection currents into REXTRAP. The discussion is found in Sec. 11.2.2.

B.2 Summary phase spaces

Here a complete series of tables representing different views of the phase spaces, ordered by the cooling method and as function of the number of ions injected, are presented.

B.2.1 Measurements at 60 keV

Complete graphical documentation of the phase space measurements discussed in Sec. 11.2.4 is given in the next sections.

Two-dimensional views

Tables B.1, B.2,B.3 and B.4 represent the contour phase space plots at 60 keV for different cooling methods as function of the number of ions injected.

Phase spaces back-traced in the BTS pipe

Tables B.5, B.6 and B.7 show the measured phase spaces (at different scales) back.traced 1700 mm, to a point which corresponds to the BTS beam pipe (supposed to be the region where the beam is cut). The comparison of the back-traced transverse phase spaces allows the percentage of the beam which is cut to be checked as a function of the injected intensity .

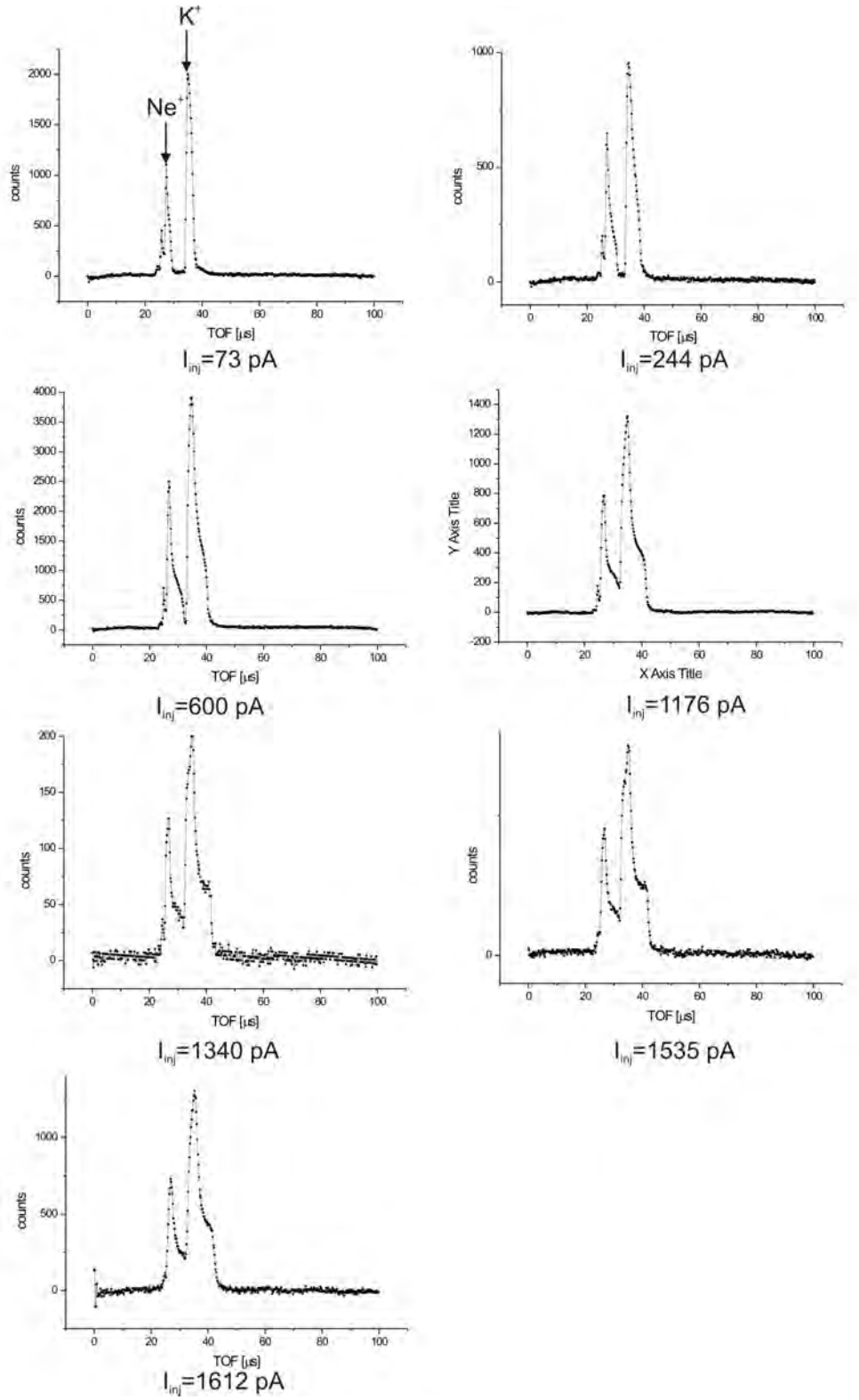

Figure B.1: Time structure of the pulse extracted from REXTRAP at 30 keV for different injected ion beam currents and without applying any cooling method to the Penning trap (f_{cycle}=50 Hz).

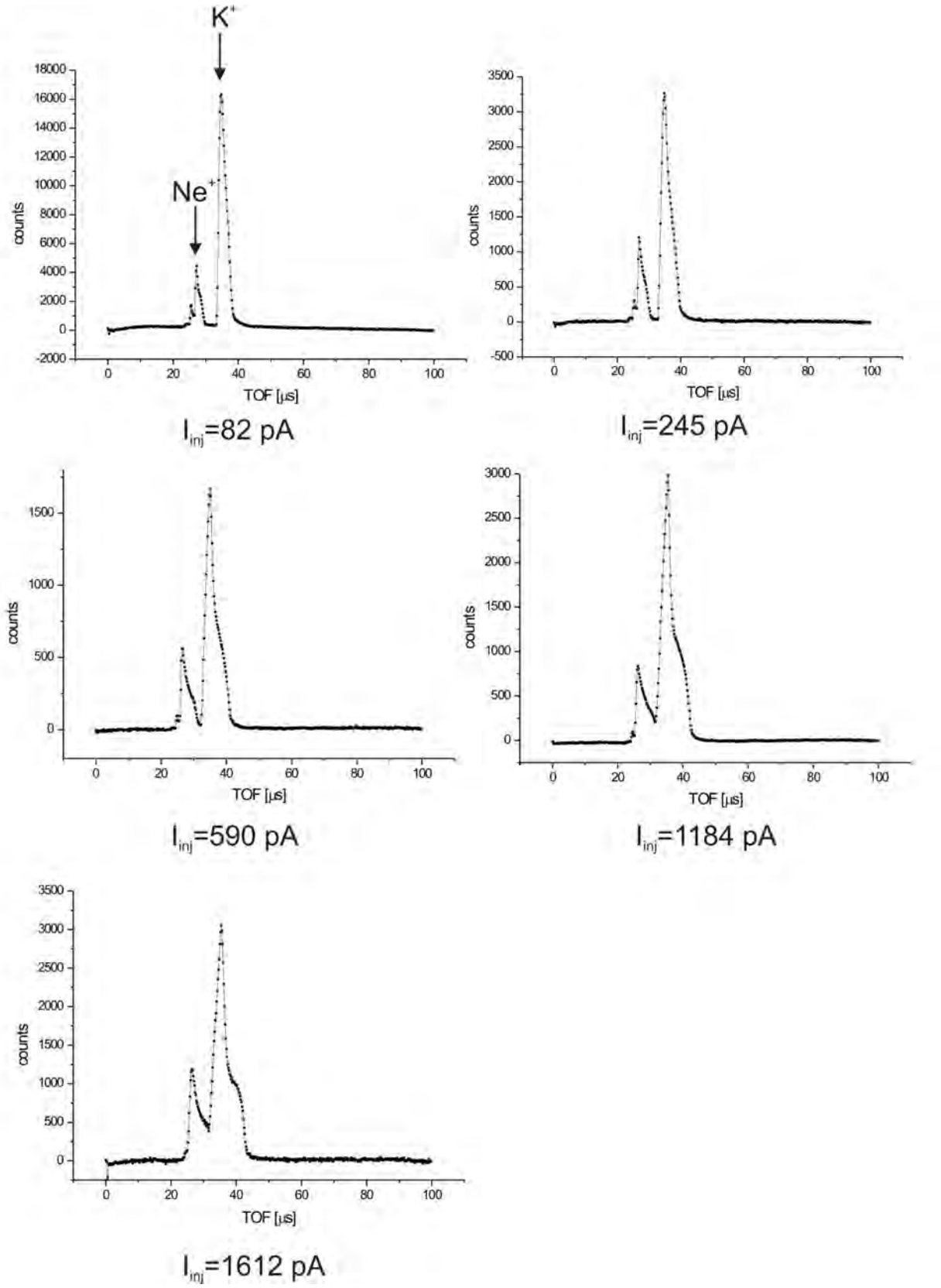

Figure B.2: Time structure of the pulse extracted from REXTRAP at 30 keV for different injected ion beam currents with the sideband cooling method applied (V_{pp}=18 V, f_{cycle}=50 Hz).

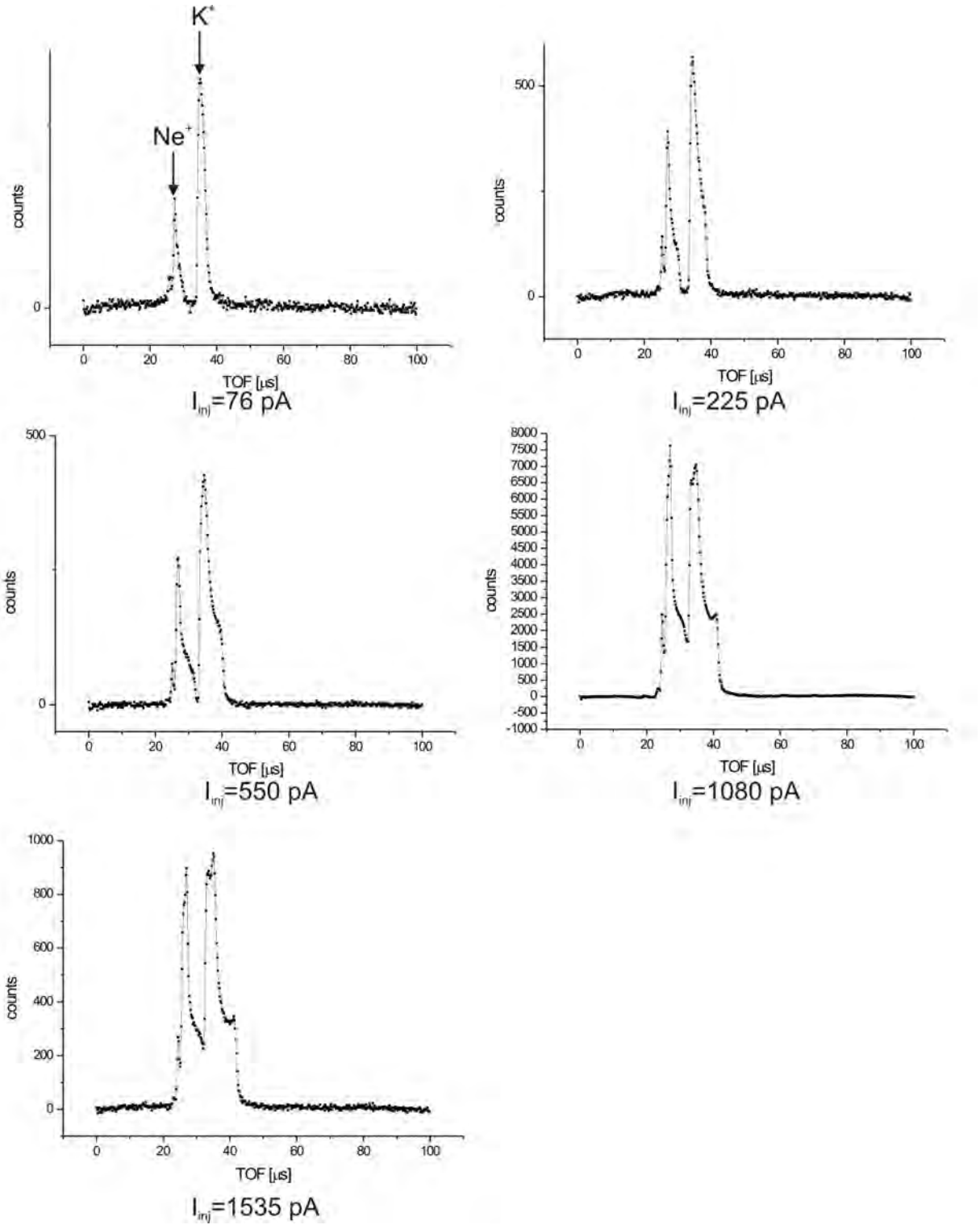

Figure B.3: Time structure of the pulse extracted from REXTRAP at 30 keV for different injected ion beam currents with the rotating wall quadrupolar cooling method applied (V_{pp}=30 V, f_{cycle}=50 Hz).

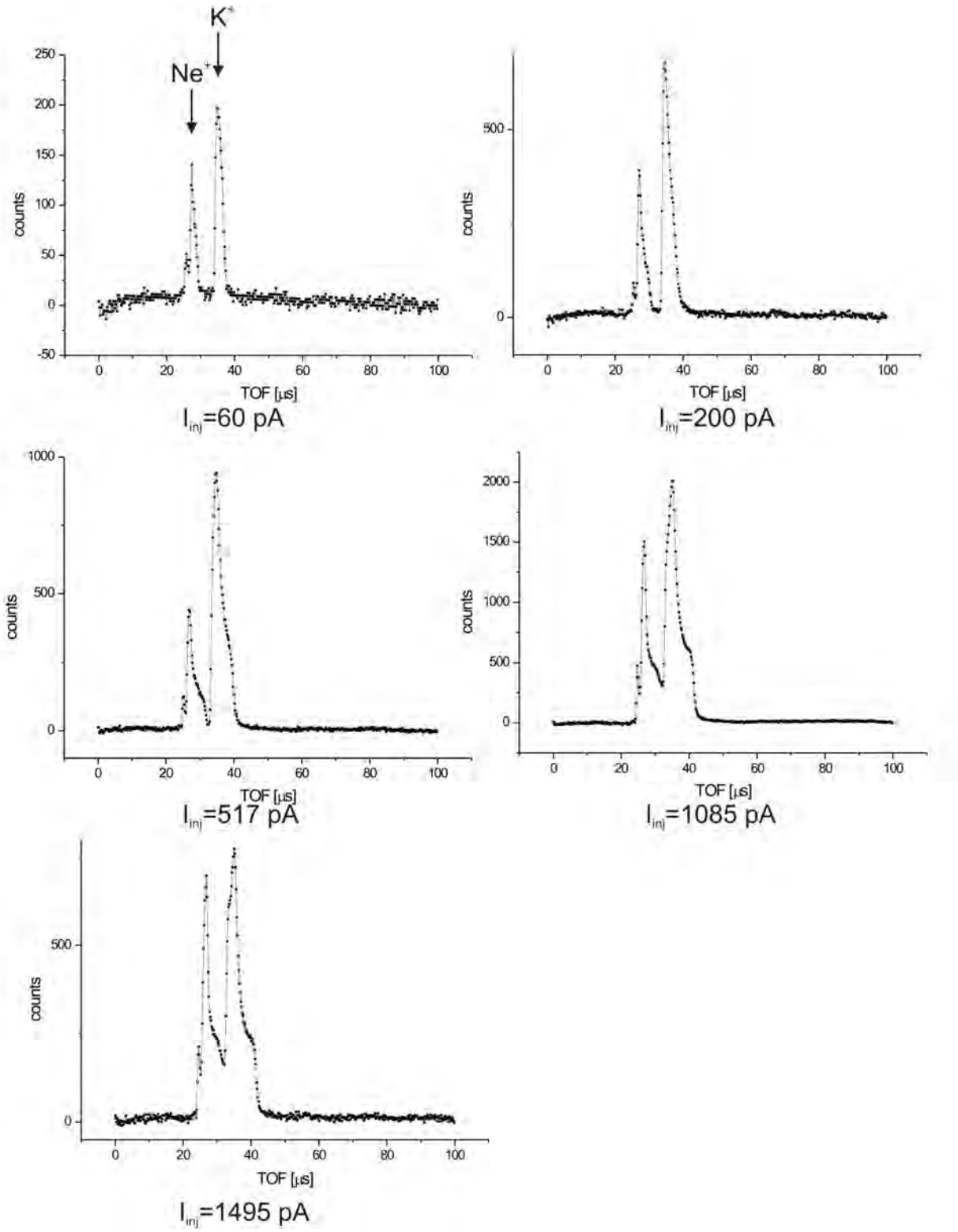

Figure B.4: Time structure of the pulse extracted from REXTRAP at 30 keV for different injected ion beam currents with the rotating wall dipolar cooling method applied (V_{pp}=30 V, f_{cycle}=50 Hz).

No cooling	Sideband	Dipolar Rot. Wall	Quadrupolar Rot. Wall
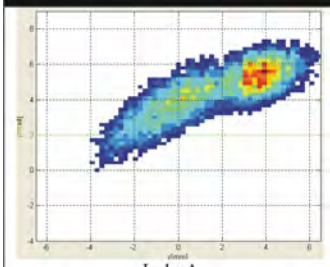 I_i=1 pA	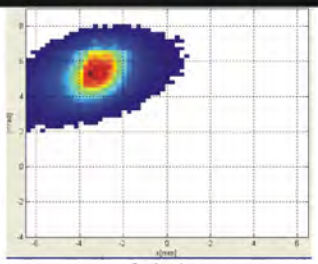 I_i=1 pA		
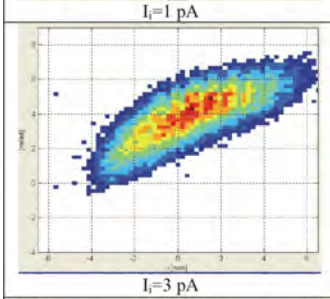 I_i=3 pA	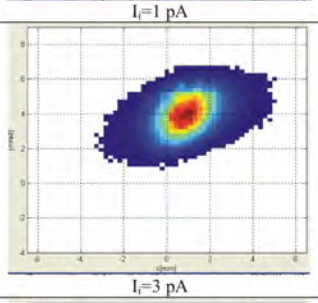 I_i=3 pA		
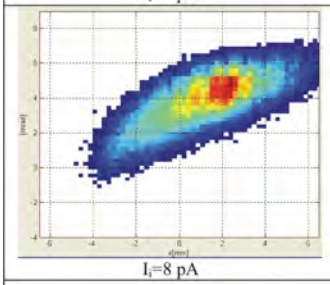 I_i=8 pA	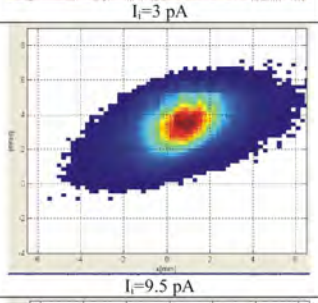 I_i=9.5 pA		
	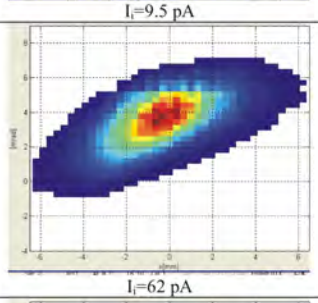 I_i=62 pA		
	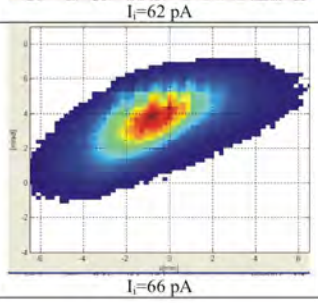 I_i=66 pA		

Table B.1: The measured phase spaces at 60 keV for the different cooling methods as function of the beam intensity out of the trap (same scale for all graphs).

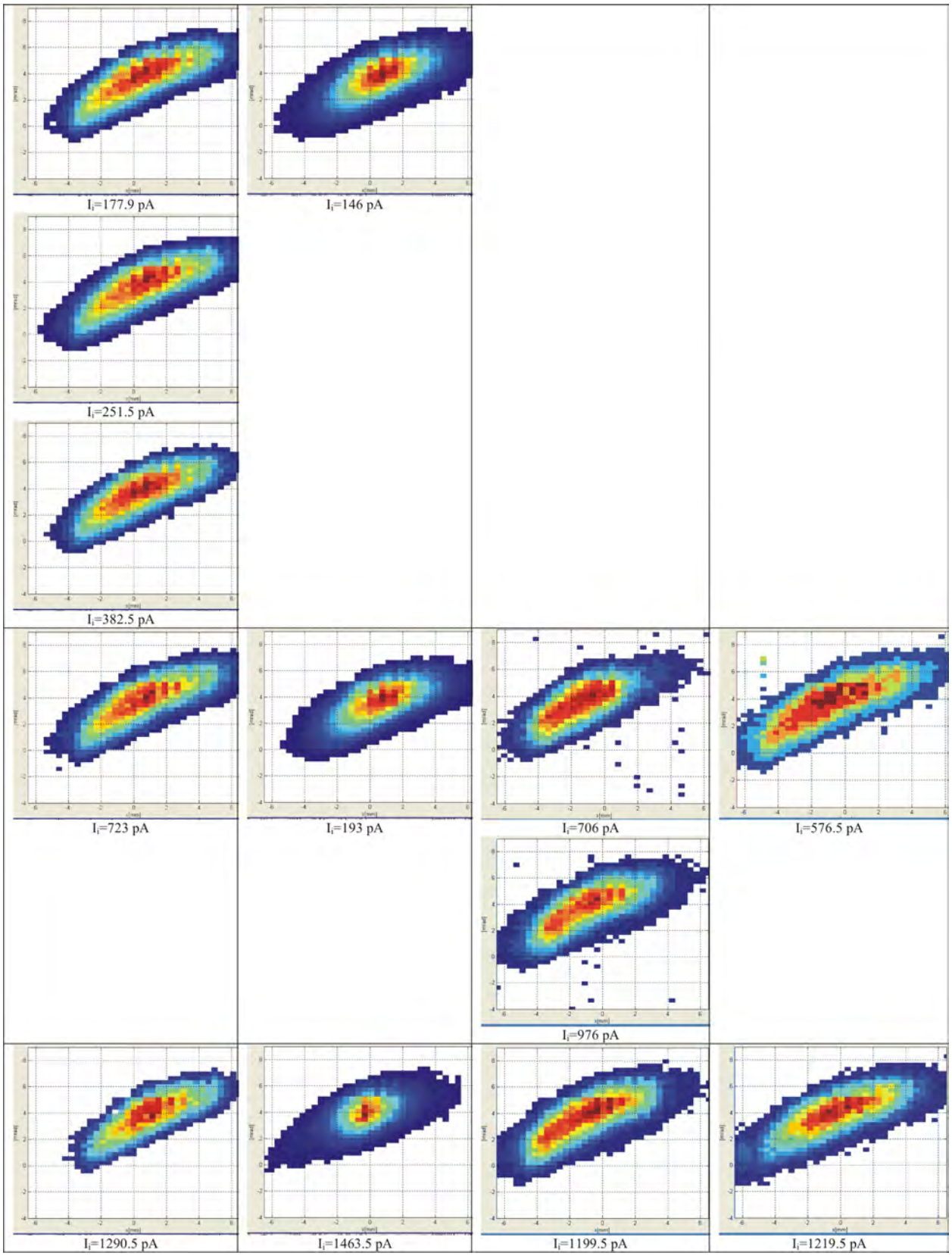

Table B.2: (cont.) The measured phase spaces at 60 keV for the different cooling methods as function of the beam intensity out of the trap (same scale for all graphs).

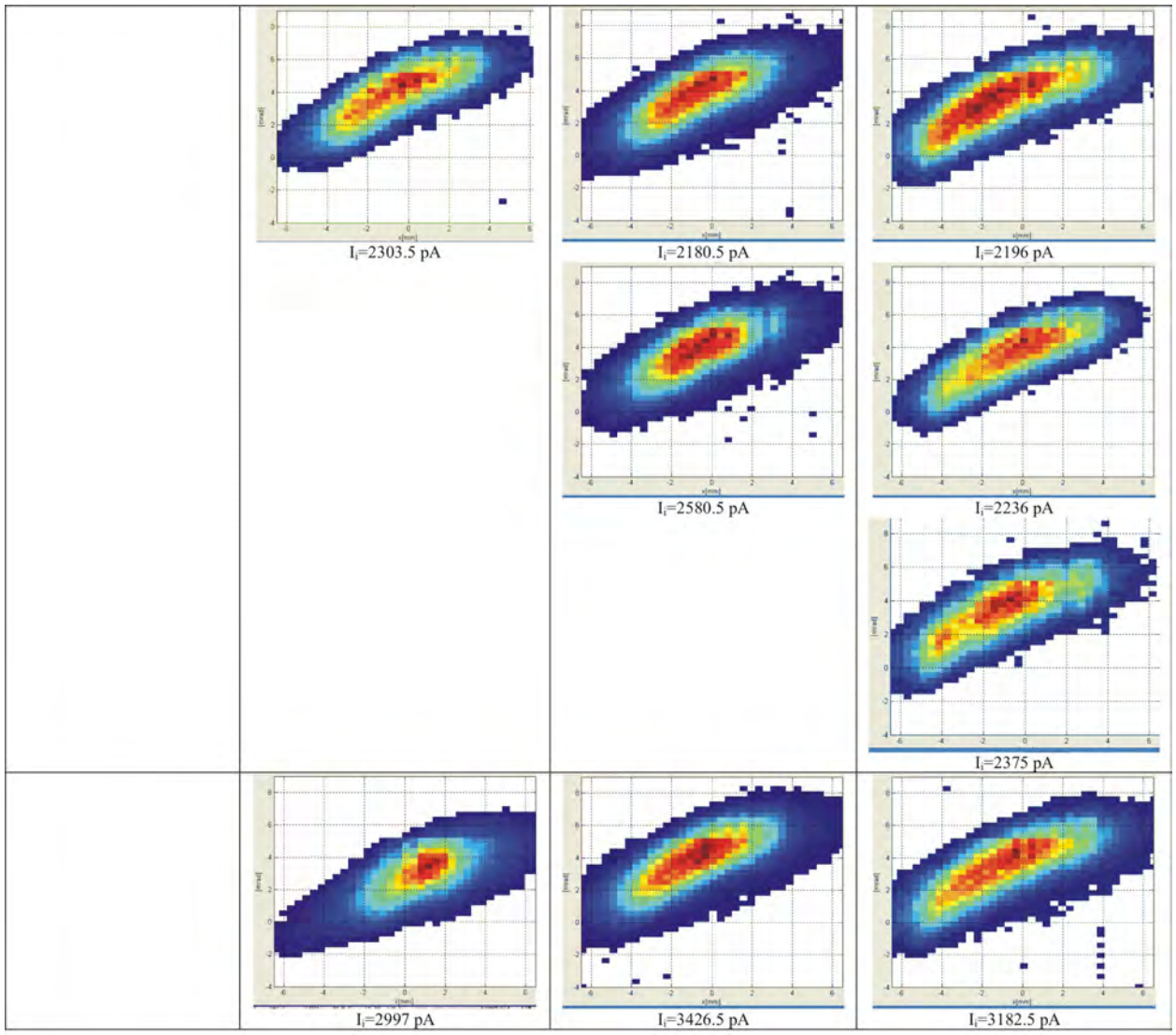

Table B.3: (cont.) The measured phase spaces at 60 keV for the different cooling methods as function of the beam intensity out of the trap (same scale for all graphs).

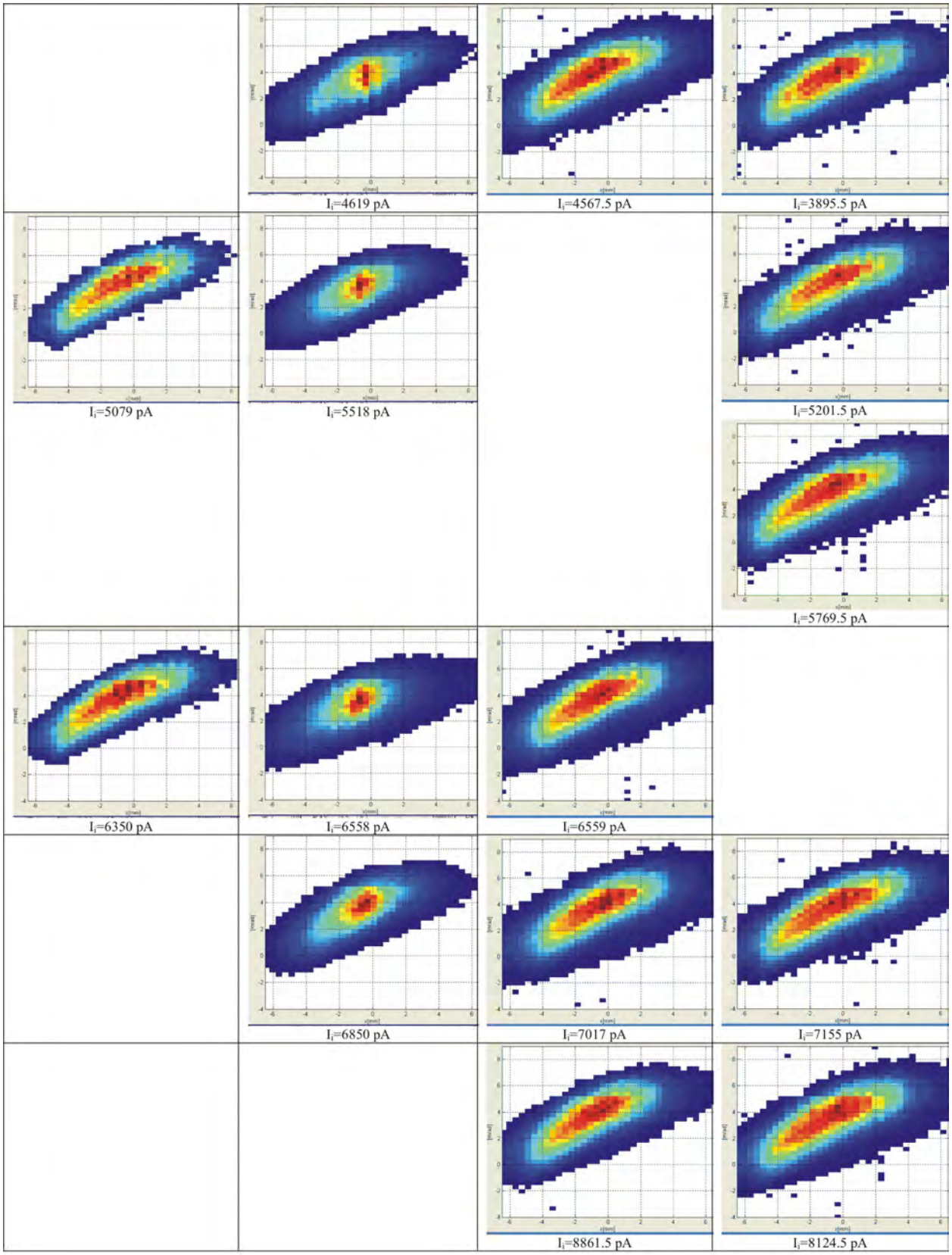

Table B.4: (cont.) The measured phase spaces at 60 keV for the different cooling methods as function of the beam intensity out of the trap (same scale for all graphs).

No cooling	Sideband	Dipolar Rot. Wall	Quadrupolar Rot. Wall
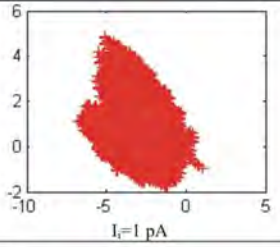 I_i=1 pA	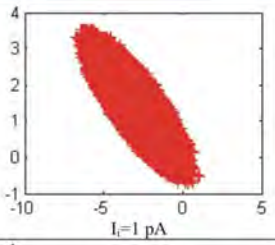 I_i=1 pA		
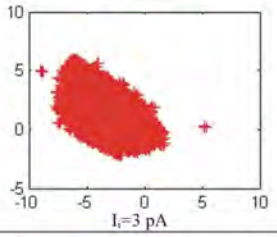 I_i=3 pA	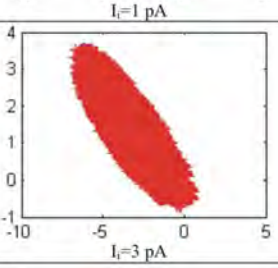 I_i=3 pA		
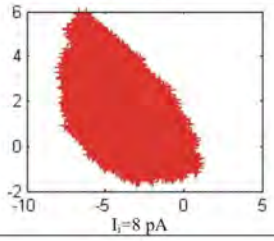 I_i=8 pA	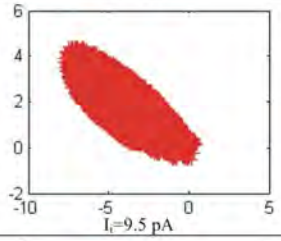 I_i=9.5 pA		
	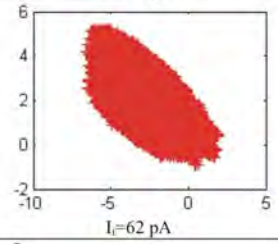 I_i=62 pA		
	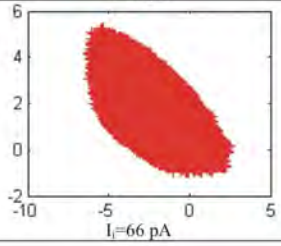 I_i=66 pA		

Table B.5: Back-traced 1700 mm (BTS line) phase spaces for the measurements at 60 keV for the different cooling methods as function of extracted beam from the trap (N.B. different scales).

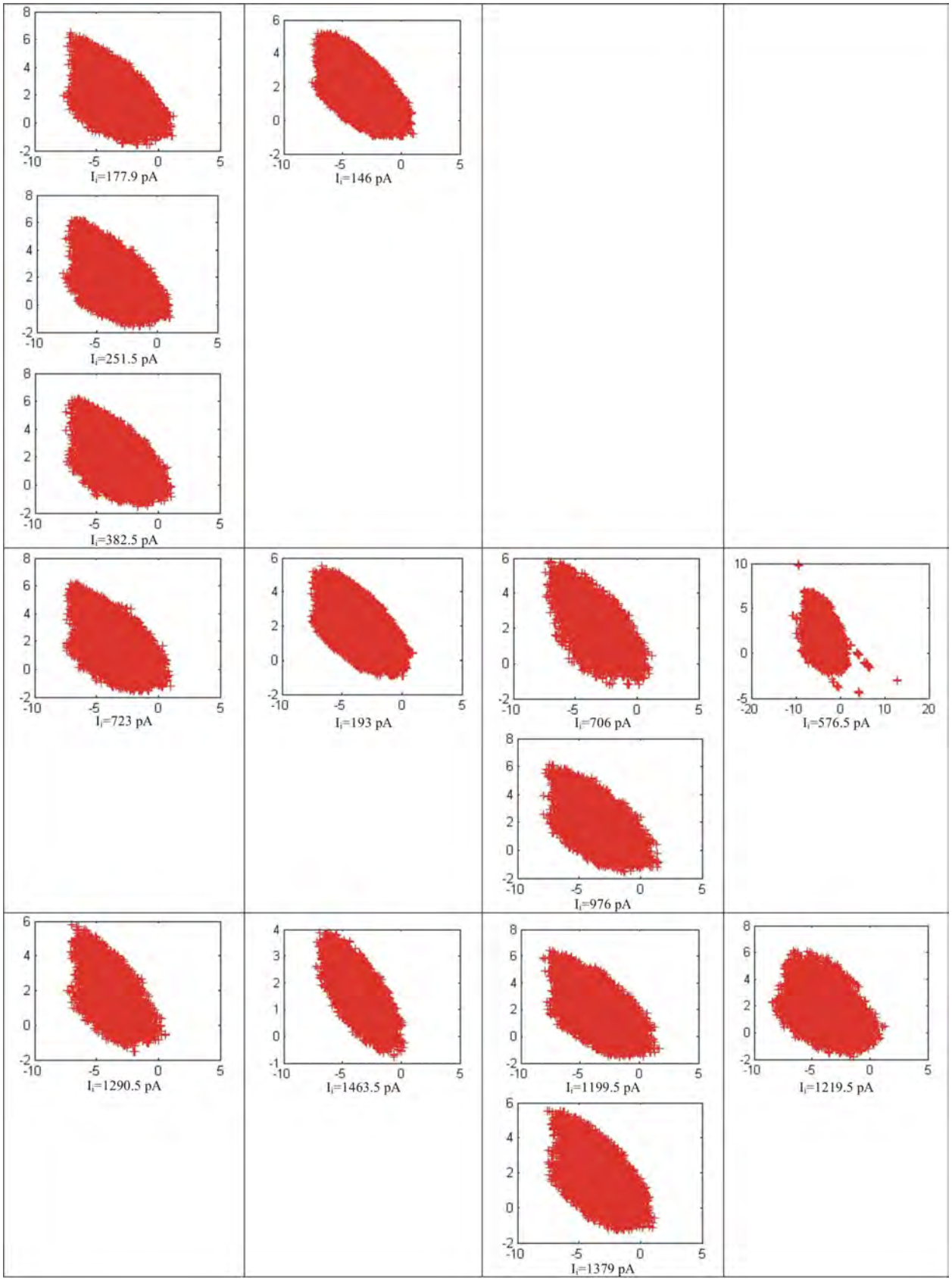

Table B.6: (cont.) Back-traced 1700 mm (BTS line) phase spaces for the measurements at 60 keV for the different cooling methods as function of extracted beam from the trap (N.B. different scales).

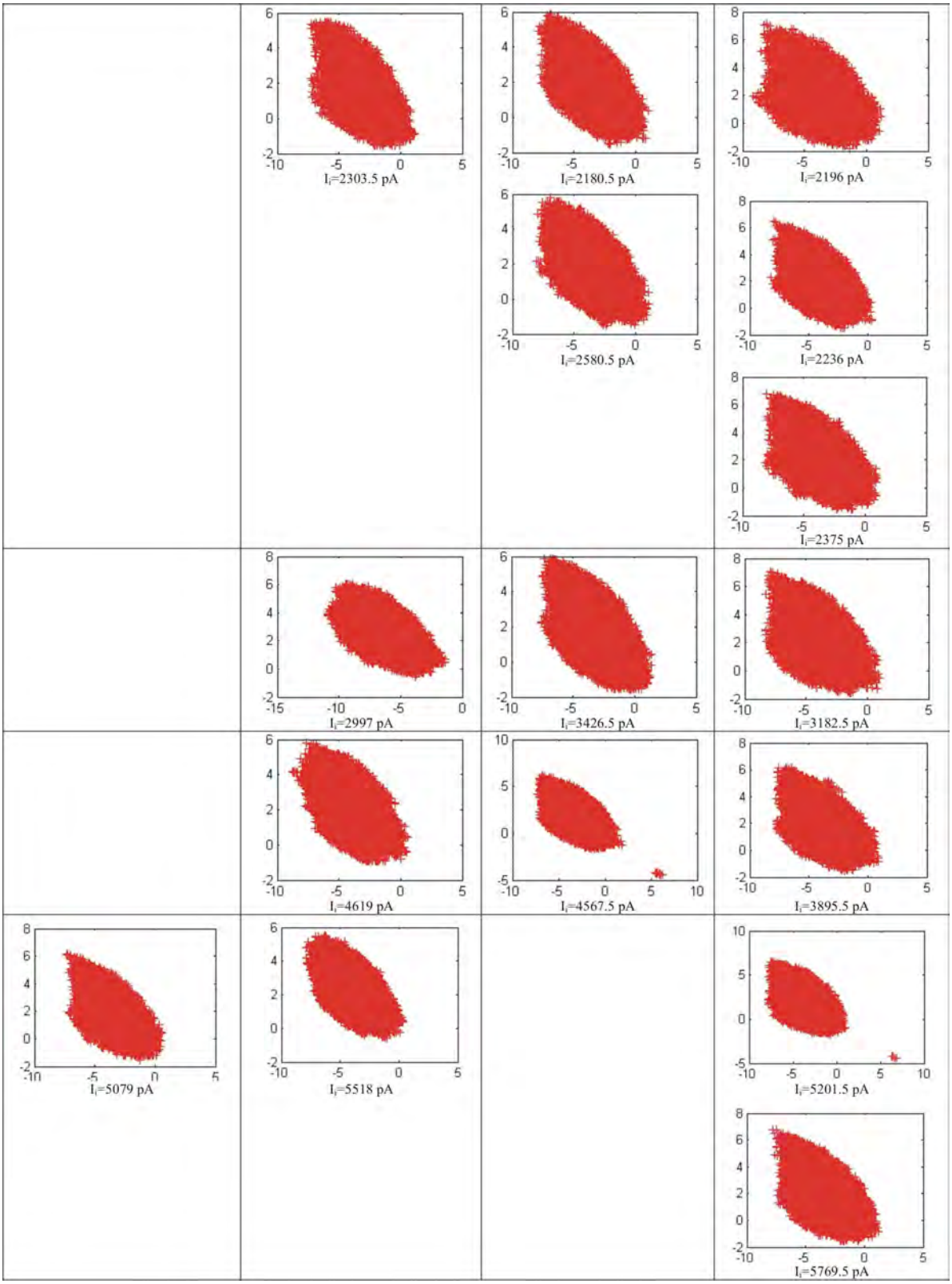

Table B.7: (cont.) Back-traced 1700 mm (BTS line) phase spaces for the measurements at 60 keV for the different cooling methods as function of extracted beam from the trap (N.B. different scales).

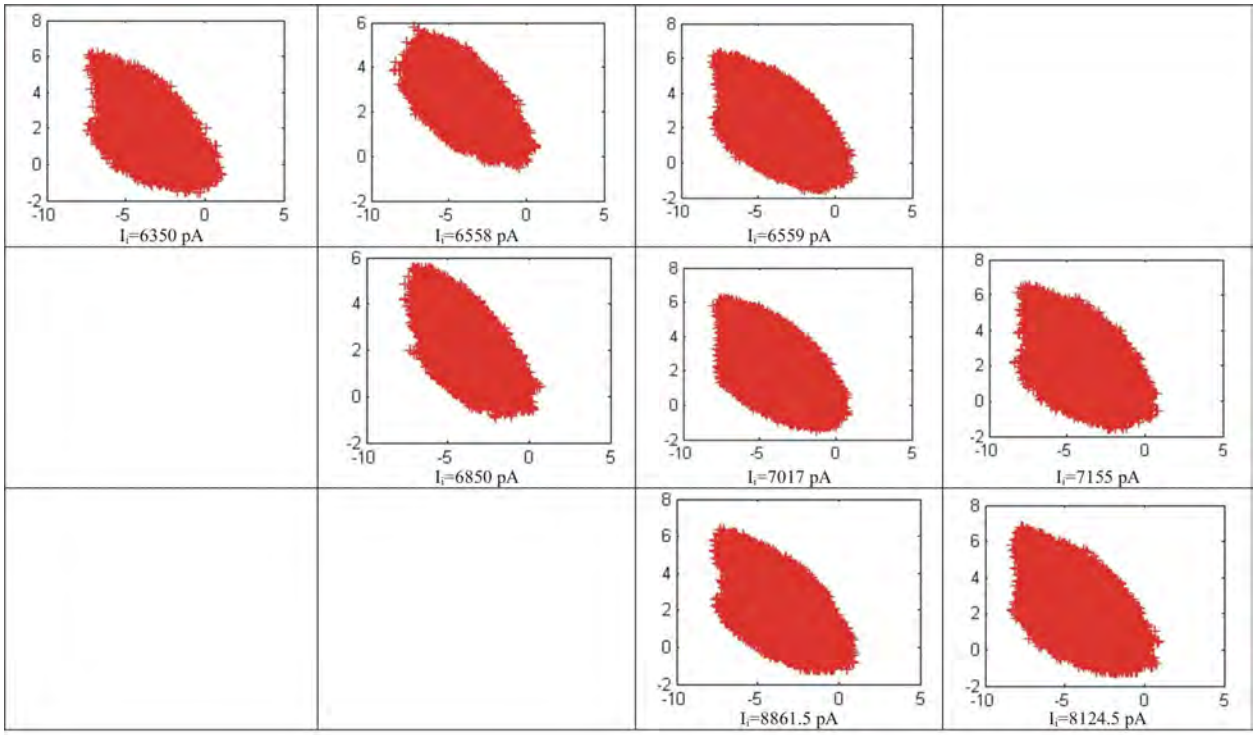

Table B.8: (cont.) Back-traced 1700 mm (BTS line) phase spaces for the measurements at 60 keV for the different cooling methods as function of extracted beam from the trap (N.B. different scales).

B.2.2 Measurements at 30 keV

A complete graphical documentation of the phase space measurements discussed in Sec. 11.2.4 is given in the next sections.

Two-dimensional views

Table B.9 represents the contour phase space plots at 60 keV for different cooling methods as function of the number of ions injected.

Three-dimensional views

Table B.10 shows intensity modulated phase-space recordings. This allows for a visual comparison of the cooling methods.

Phase spaces back-traced to the kicker

Table B.11 shows the measured phase spaces (at different scales) back-tracked 1960 mm, to a point which corresponds to the position of the kicker (supposed to be the region where the beam is cut). The comparison as function of the injected intensity allows the percentage of phase space to be checked (or beam if both are supposed symmetrical).

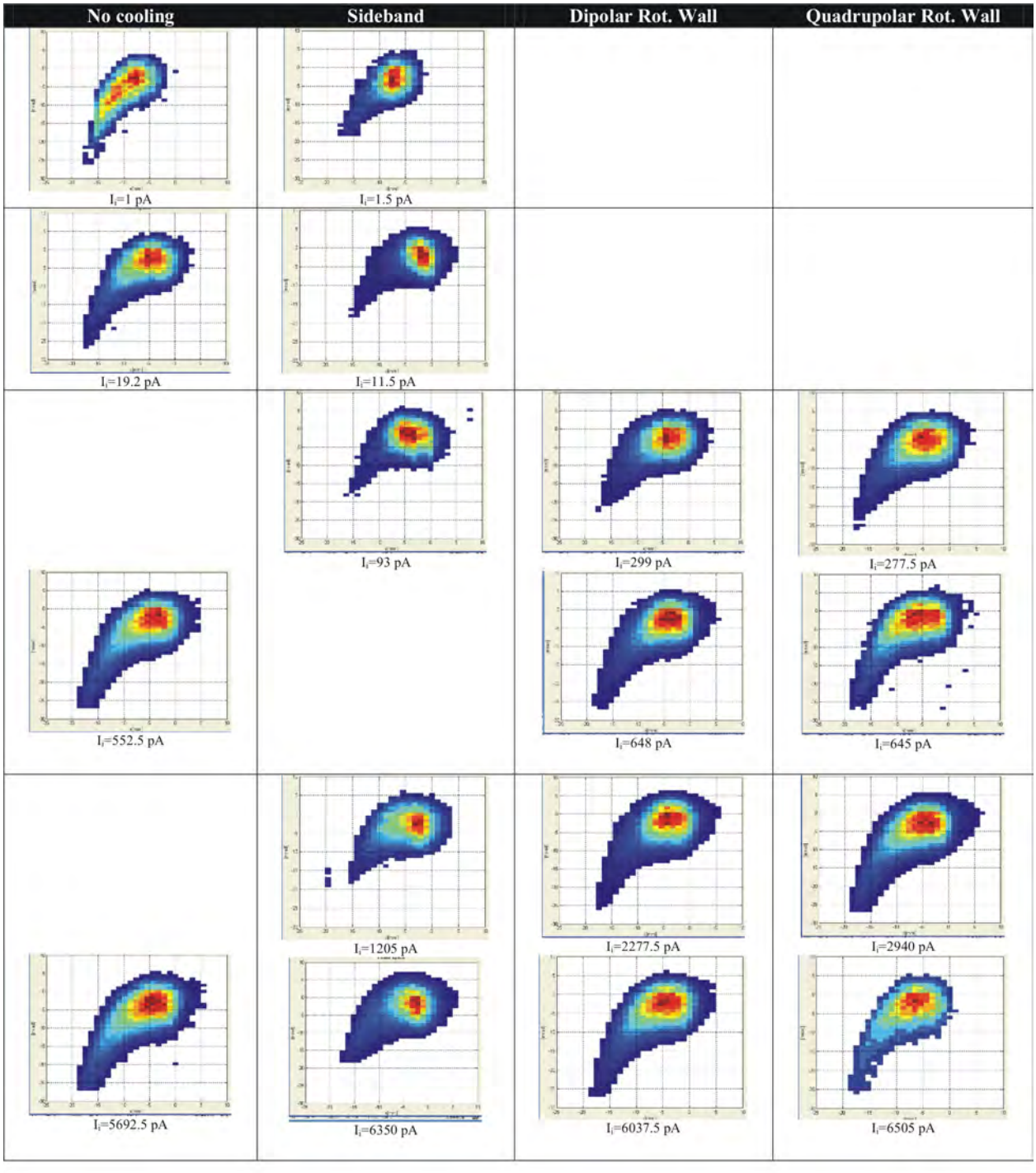

Table B.9: Phase space recordings at 30 keV for the different cooling methods in function of the beam intensity out of the trap (same scale for all graphs).

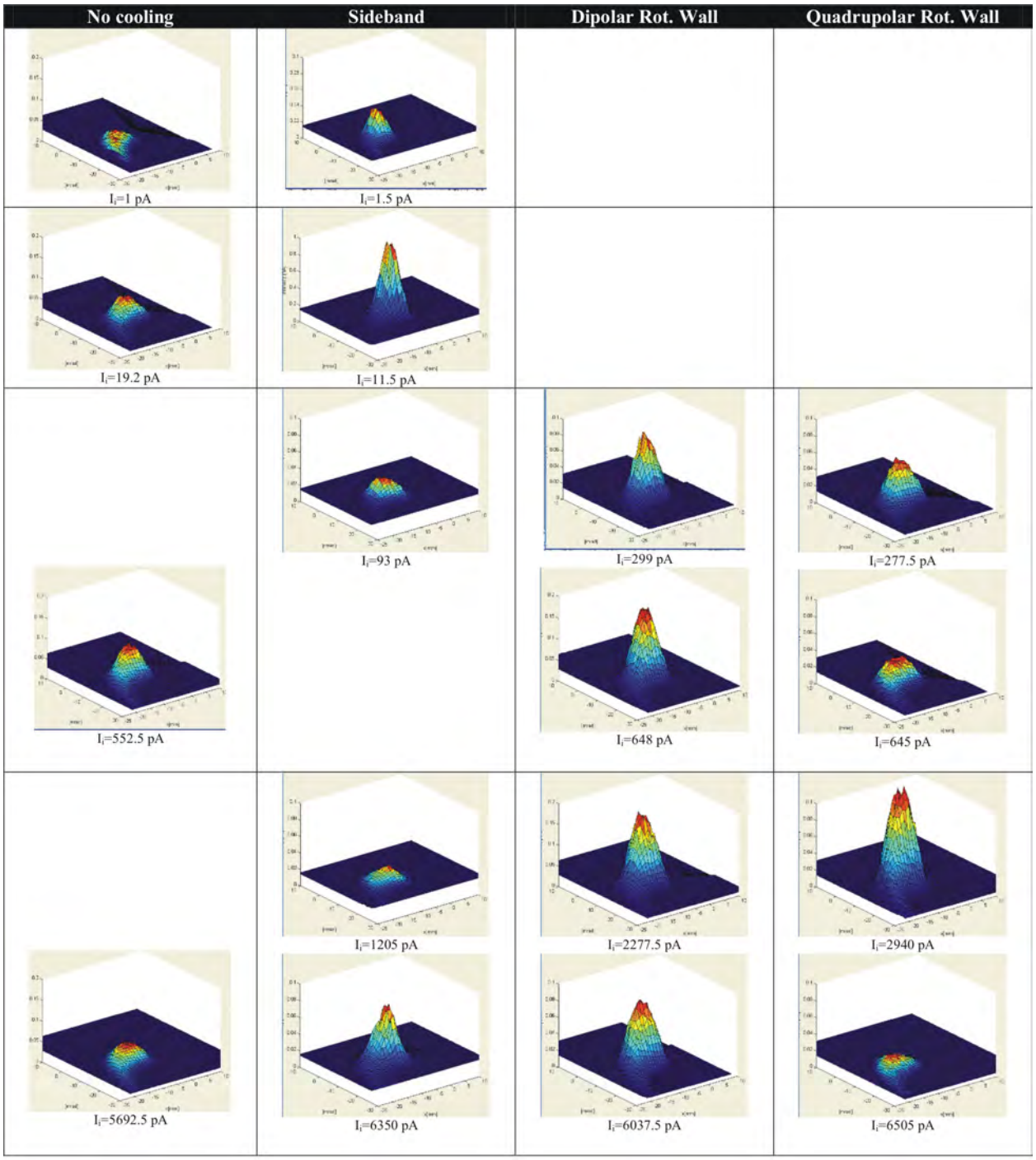

Table B.10: Phase space recordings at 30 keV for the different cooling methods as function of the beam intensity out of the trap (same scale for all graphs).

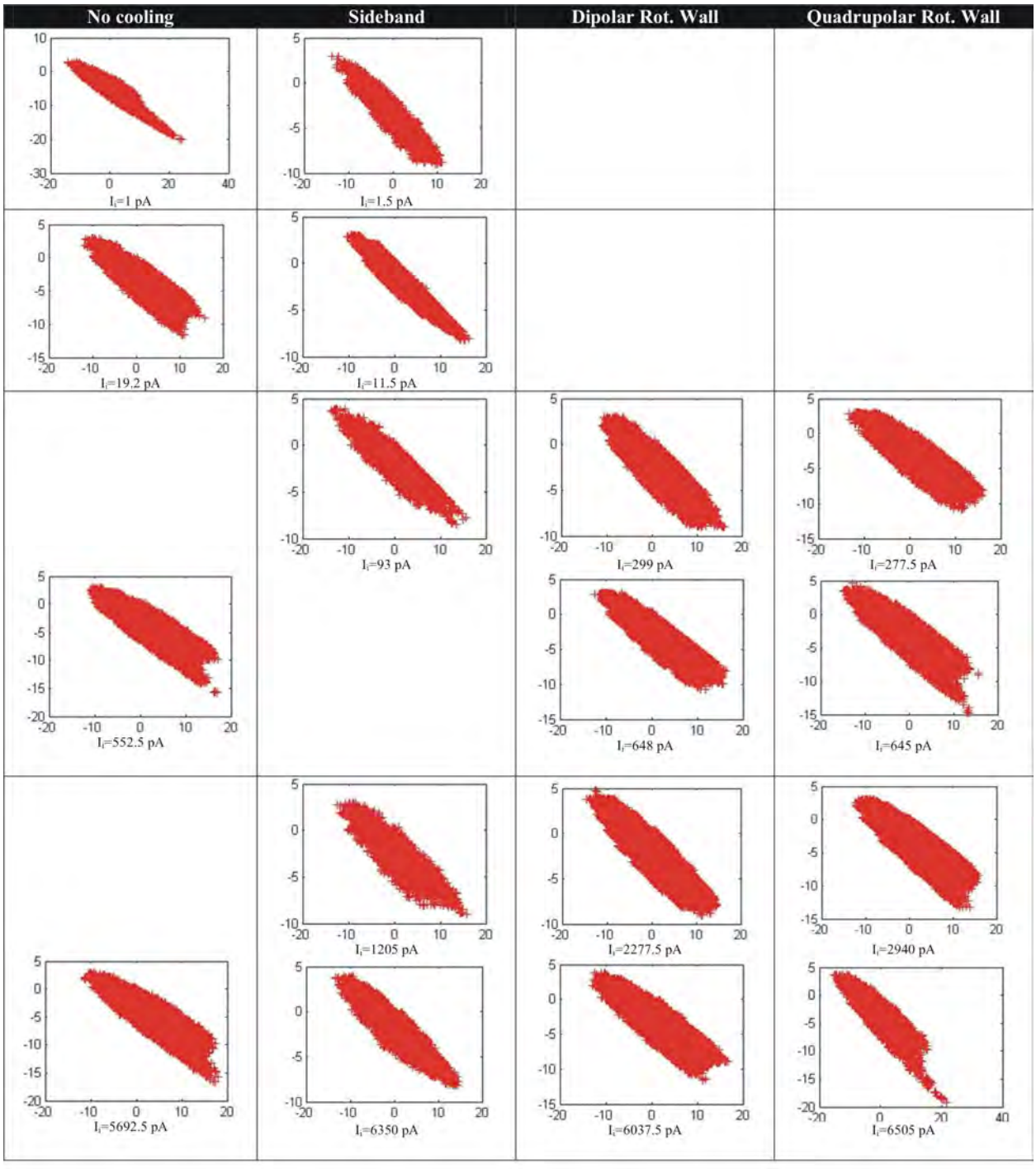

Table B.11: Phase-space plots back-traced 1960 mm (kicker) for the different cooling methods and beam intensities out of the trap.

Bibliography

[ACSW05] F. Ames, J. Cederkall, T. Sieber, and F. Wenander. The REX-ISOLDE facility. design and commissioning report. Technical Report CERN-2005-009, CERN, 2005.

[AGA] AGA. AGA chemical and pharmaceutical gases and equipment, special gases.

[AHD98] F. Anderegg, E. M. Hollmann, and C. F. Driscoll. Rotating field confinement of pure electron plasmas using trivelpiece-gould modes. *Phys. Rev. Lett.*, 81:4875–4878, 1998.

[Ars64] F. M. Arscott. *Periodic differential equations*. Pergamon Press, 1964.

[ASH83] P. W. Allison, J. 0. Sherman, and D. Holtkamp. An emittance scanner for intense low-energy ion beams. *IEEE Trans. Nucl. Sci.*, NS-30(4):2204, August 1983.

[Äystö01] J. Äystö. Development and applications of the IGISOL technique. *Nucl. Phys. A*, 693:477, 2001.

[ÄystöJ03] J. Äystö and A. Jokinen. Ion beam coolers in nuclear physics. *J. Phys. B*, 36:573–584, 2003.

[BAB+03] M. Beck, F. Ames, D. Beck, G. Bollen, B. Delauré, J. Deutsch, V. V. Golovko, V. Yu.Kozlov, I.S. Kraev, A. Lindroth, T. Phalet, W. Quint, K. Reisinger, P. Schuurmans, N. Severijns, and B. Vereecke. Witch: A recoil spectrometer for SS-decay. *Nucl. Phys. A*, 721:C1103–C1106, 2003.

[Bac00] C. Bachelet. Tests et développements d'un emittance-mètre pour la mise en évidence d'un refroidessement de faisceaux pour l'expérience MISTRAL. Master's thesis, Université Paris XI, 2000.

[Bac04] C. Bachelet. *Mesure de masse de noyaux à halo et refroidissement de faisceaux avec l'expérience MISTRAL*. PhD thesis, L'Université Paris XI, Orsay, 2004.

[BDD+04] G. Ban, G. Darius, D. Durand, X. Fléchard, M. Herbane, M. Labalme, E. Liénard, F. Mauger, O. Naviliat-Cuncic, C. Guénaut, C. Bachelet, P. Delahaye, A. Kellerbauer, L. Maunory, and J. Y. Pacquet. Transport and cooling of singly-charged noble gas ion beams. *Nucl. Instrum. Methods A*, 518(3):712–720, 2004.

[Bil01] J. Billowes. Laser spectroscopy of radioisotopes and isomers. *Nucl. Phys. A*, 682:206c–213c, 2001.

[BSD+04] G. Bollen, S. Schwarz, D. Davies, P. Lofy, D. Morrissey, R. Ringle, P. Schury, T. Sun, and L. Weissman. Beam cooling at the low-energy-beam and ion-trap facility at NSCL/MSU. *Nucl. Instrum. Methods A*, 532:203Ű209, 2004.

[But05] P. Butler. private communication, 2005.

[Cam55] Robert Campbell. *Théorie générale de l'équation de Mathieu et de quelques autres équations différentielles de la mécanique*. Paris: Masson, 1955.

[Car] Carbagas. http://www.carbagas.ch.

[Car72] J. O. Carrico. *Dynamical Mass Spectrometry*, 3:1, 1972.

[CCE+02] R. Catherall, J. Cederkall, K. Elder, V.N. Fedosseev, H. Fynbo, U. Georg, T. J. Giles, E. Hagebo, A. Joinet, O. C. Jonsson, U. Koester, C. Lau, J. Lettry, T. Nilsson, H. L. Ravn, M. Santana-Leitner, L. Weissman, and the ISOLDE collaboration. Measurement of the production cross-sections of neutron-rich kr and xe isotopes. In J. Äystö, P. Dendooven, A. Jokinen, and M. Leino, editors, *Exotic Nuclei and Masses 2001*, pages 382–383. Springer-Verlag, 2002.

[CER96] CERN. *Protection agains ionizing radiation: Radiation safety manual*, 1996. EDMS 335729.

[Cho] C. Chollet. private communication.

[Com03] Professional Enginnering Computations. Outgassing and permeation, 2003.

[Dah00] D. A. Dahl. Simion for the personal computer in reflection. *Int. J. Mass Spectrom.*, 200:3, 2000.

[Daw95] P.H. Dawson. *Quadrupole mass spectrometry and its applications*. Amer. Vac. Soc. Classics, 1995.

[DB00] M. Drewsen and A. Brøner. Harmonic linear paul trap: Stability diagram and effective potentials. *Phys. Rev. A*, 62:045401, 2000.

[DBD+01] P. Delahaye, G. Ban, D. Durand, A.M. Vinodkumar, C. Le Brun, E. Lienard, F. Mauger, O. Naviliat, J. Szerypo, and B. Tamain. Weak interaction studies using a paul trap. *Hyp. Int.*, 132:475–480, 2001.

[DE] FRIATEC DE. http://www.friatec.de.

[Deh67] H. G. Dehmelt. Radiofrequency spectroscopy of stored ions I: Storage. *Adv. At. Mol. Phys.*, 3:53, 1967.

[Den97] P. Dendooven. The development and status of the IGISOL technique. *Nucl. Instrum. Methods B*, 126:182, 1997.

[EAM88] E. W. McDaniel E. A. Mason. *Transport of ions in gases*. John Wiley and Sons, New York, 1988.

[Ero02] T. Eronen. Simulation of injections optics for an RFQ cooler and buncher. Technical report, CERN, 2002.

[FHKB+01] J. Dilling F. Herfurth, A. Kellerbauer, G. Bollen, S. Henry, H.-J. Kluge, E. Lamour, D. Lunney, R. B. Moore, C. Scheidenberger, S. Schwarz, G. Sikler, and J. Szerypo. A linear radiofrequency ion trap for accumulation, bunching, and emittance improvement of radioactive ion beams. *Nucl. Instrum. Methods A*, 469:254–275, 2001.

[FIN04] FINUPHY. *Handbook on Interdisciplinary Use of European Nuclear Physics Facilities*. GANIL, Caen, France, 2004.

[Fon01] C. W. Van Fong. *Phase space dynamics in a linear RFQ trap for Time-of-flight mass spectrometry*. PhD thesis, McGill University, 2001.

[For03] P. Forck. *Lecture notes on Beam Instrumentation and Diagnostics*. Joint University Accelerator School, 2003.

[Fra] Messer Group France. http://webshop.messergroup.com/control/main.

[Fri] T. Fritioff. private communication.

[GCF+03] T. Giles, R. Catherall, V. Fedosseev, U. Georg, E. Kugler, J. Lettry, and M. Lindroos. The high resolution spectrometer at ISOLDE. *Nucl. Instrum. Methods B*, 204:497–501, 2003.

[Gel00] R. Geller. *Rev. Sci. Instrum.*, 71(2):612–616, 2000.

[Gho95] P.K. Ghosh. *Ion traps*. Clarence Press, Oxford, 1995.

[Gia02] O. Gianfrancesco. Design principles of high field RFQ device for ion cooling and confinement. Master's thesis, McGill University, 2002.

[GWW+03] H. Geissel, H. Weick, M. Winkler, G. Münzenberg, V. Chichkine, M. Yavor, T. Aumann, K. H. Behr, M. Böhmer, A. Brünle, K. Burkarda, J. Benlliure, D. Cortina-Gil, L. Chulkov, A. Dael, J.-E. Ducret, H. Emling, B. Franczak, J. Friese, B. Gastineau, J. Gerl, R. Gernhäuser, M. Hellström, B. Jonson, J. Kojouharova, R. Kulessa, B. Kindler, N. Kurz, B. Lommel, W. Mittig, G. Moritz, C. Mühle, J. A. Nolen, G. Nyman, P. Roussell-Chomaz, C. Scheidenberger, K. H. Schmidt, G. Schrieder, B. M. Sherrill, H. Simon, K. Sümmerer, N. A. Tahir, V. Vysotsky, H. Wollnik, and A. F. Zellern. The super-FRS project at GSI. *Nucl. Instrum. Methods B*, 204:71–85, May 2003.

[HAD00] E. M. Hollmann, F. Anderegg, and C. F. Driscoll. Confinement and manipulation of nonneutral plasmas using rotating wall electric fields. *Phys. Plasmas*, 7(7):2776–2789, 2000.

[HAH+97] X.-P. Huang, F. Anderegg, E. M. Hollmann, C. F. Driscoll, , and T. M. O'Neil. Steady-state confinement of non-neutral plasmas by rotating electric fields. *Phys. Rev. Lett.*, 78:875–878, 1997.

[HDc94] D. Habs, P. Van Duppen, and REX-ISOLDE collaboration. Radioactive beam experiment at ISOLDE: Coulomb excitation and neutron transfer reactions of exotic nuclei. *CERN-ISC94-25*, 1994.

[Hen04] W. F. Henning. FAIR - an international accelerator facility for research with ions and antiprotons. In J. Chrin et al., editor, *EPAC 2004, Lucerne, Switzerland*, page 50. EPS-AG/CERN, 2004.

[Her01] F. Herfurth. *A new ion beam cooler and buncher for ISOLTRAP and mass measurements of radioactive argon isotopes*. PhD thesis, Rupertus Carola University of Heidelberg, 2001.

[HGR95] G. Münzenbergh H. Geissel and K. Riisager. Secondary exotic nuclear beams. *Annu. Rev. Nucl. Sci.*, 45:163, 1995.

[Hie04] A. Hieke. 3d electro-pneumatic monte carlo simulations of ion trajectories and temperatures during rf quadrupole injection in the presence of gas flow fields. In *52nd ASMS Conference on Mass Spectrometry and Allied Topics*, Nashville, TN, May 2004.

[Hie05] A. Hieke. Ion sources for biomolecules with controlled superposition of electric and pneumatic fields. In *2005 Nanotechnology Conference and Trade Show*, Anaheim, CA, May 2005.

[HJH+04] S. Heinz, J. Äystö, D. Habs, S. Hegewisch, J. Huikari, A. Nieminen, S. Rinta-Antila, M. Schumann, and J. Szerypo. A radio frequency ring electrode cooler for low-energy ion beams. *Nucl. Instrum. Methods A*, 533:239–247, 2004.

[HKS+00] D. Habs, O. Kester, T. Sieber, H. Bongers, S. Emhofer, P. Reiter, P.G. Thirolf, G. Bollen, J. Aystö, O. Forstner, H. Ravn, T. Nilsson, M. Oinonen, H. Simon, J. Cederkall, F. Ames, P. Schmidt, G. Huber, L. Liljeby, O. Skeppstedt, K.G. Rensfelt, F. Wenander, B. Jonson, G. Nyman, R. von Hahn, H. Podlech, R. Repnow, C. Gund, D. Schwalm, A. Schempp, K.-U. Kühnel, C. Welsch, U. Ratzinger, G. Walter, A. Huck, K. Kruglov, M. Huyse, P. Van den Bergh, P. Van Duppen, L. Weissman, A.C. Shotter, A.N. Ostrowski, T. Davinson, P.J. Woods, J. Cub, A. Richter, and G. Schrieder. The REX-ISOLDE project. *Hyp. Int.*, 129:43–66, 2000.

[HR74] R. Hackam and G. R. Govinda Raju. Electrical breakdown of a point-plane gap in high vacuum and with variation of pressure in the range $10^7 10^2$ torr of air, nitrogen, helium, sulphur hexafluoride, and argon. *J. Appl. Phys.*, 45(11):4784–4794, November 1974.

[Huc02] G. Huchet. Mesures d'émittance d'un faisceau d'ions intense séparé en masse. Master's thesis, Centre de Spectrométrie Nucléaire et de Spectrométrie de Masse, 2002.

[IBBW95] W. M. Itano, J. C. Bergquist, J. J. Bollinger, and D. J. Wineland. Cooling methods in ion traps. *Physica Scripta*, T59:106–120, 1995.

[Jeo03] S. C. Jeong. *Nucl. Instrum. Methods B*, 204:420–427, 2003.

[JGA97] R. M. Jones, D. Gerlich, and S. L. Anderson. Simple radio-frequency power source for ion guides and ion traps. *Rev. Sci. Instrum.*, 68:3357–3362, 1997.

[JLMP03] A. Jokinen, M. Lindroos, E. Molin, and M. Petersson. RFQ-cooler for low-energy radioactive ions at ISOLDE. volume 204, pages 86–89, 2003.

[JMM53] J. D. Craggs J. M. Meek. *Electrical breakdown of gases*. Clarence Press, Oxford, 1953.

[JMP97] M. L. Johnson, D. M. Manos, and T. Provost. Gas permeation and leakage through reusable seals. *J. Vac. Sci. Technolog. A*, 15:763, 1997.

[KBH+01] Yu. Kudryavtsev, B. Bruyneel, M. Huyse, J. Gentens, P. Van den Bergh, P. Van Duppen, and L. Vermeeren. A gas cell for thermalizing, storing and transporting radioactive ions and atoms. part i: Off-line studies with a laser ion source. *Nucl. Instrum. Methods B*, 179:412–435, 2001.

[KBK+95] M. König, G. Bollen, H.-J. Kluge, T. Otto, and J. Szerypo. Quadrupole excitation of stored ion motion at the true cyclotron frequency. *Int. J. Mass Spectr. Ion Proc.*, 142:95–116, 1995.

[Kim97] T. Kim. *Buffer gas ion cooling of ions in a RFQ ion guide*. PhD thesis, McGill University, 1997.

[Kos02] U. Koster. Intense radioactive-ion beams produced with the isol method. *Eur. Phys. J. A*, 15:255–263, September 2002.

[KSE+03] O. Kester, T. Sieber, S. Emhofer, F. Ames, K. Reisinger, P. Reiter, P. G. Thirolf, R. Lutter, D. Habs, B. Wolf, G. Huber, P. Schmidt, A. N. Ostrowski, R. Von Hahn, R. Repnow, J. Fitting, M. Lauer, H. Scheit, D. Schwalm, H. Podlech, A. Schempp, U. Ratzinger, O. Forstner, F. Wenander, J. Cederkäll, T. Nilsson, M. Lindroos, H. O. U. Fynbo, S. Franchoo, U. C. Bergmann, M. Oinonen, J. Äystö, P. V. Den Bergh, P. V. Duppen, M. Huyse,

N. Warr, D. Weisshaar, J. Eberth, B. Jonson, G. Nyman, M. Pantea, H. Simon, G. Shrieder, A. Richter, O. Tengblad, T. Davinson, P. J. Woods, G. Bollen, L. Weissman, L. Liljeby, and K. G. Rensfelt. Accelerated radioactive beams from REX-ISOLDE. *Nucl. Instrum. Methods B*, 204:20–30, 2003.

[Kug00] E. Kugler. The ISOLDE facility. *Hyp. Int.*, 129:23–42, 2000.

[Laf98] J. M. Lafferty. *Foundations of Vacuum Science Technology*. Wiley-Intervenience, New York, 1998.

[Lap70] P. M. Lapostolle. Quelques proprietes des effets de la charge d'espace dans des faisceaux continus. *CERN-ISR/DI*, 70(36), 1970.

[Law83] J. D. Lawson. *Space charge optics 2*. Academic Press, Inc., USA, 1983.

[LBM92] M.D.N. Lunney, F. Buchinger, and R.B. Moore. The temperature of buffer-gas cooled ions in a paul trap. *J. Mod. Opt.*, 39:349, 1992.

[LCF+98] J. Lettry, R. Catherall, G. J. Focker, O. C. Jonsson, E. Kugler, H. Ravn, C. Tamburella, ISOLDE Collaboration, V. Fedoseyev, V. I. Mishin, G. Huber, V. Sebastian, M. Koizumi, and U. Koster. Recent developments of the ISOLDE laser ion source. volume 69, pages 761–763. AIP, 1998.

[Lin04] M. Lindroos. Review of isol method. In CERN, editor, *Proceedings of EPAC 2004*, pages 45–49, Lucerne, Switzerland, 2004. CERN-AB-2004-086.

[LJW53] F. Llewellyn Jones and G. C. Williams. The electrical breakdown of gases in non-uniform fields at low pressure. *Proc. Phys. Soc. B*, 66:345–361, 1953.

[LKL+00] Alexander Loboda, Andrew Krutchinsky, Olga Loboda, James McNabb, Victor Spicer, Werner Ens, and Kenneth Standing. Novel linac ii electrode geometry for creating an axial field in a multipole ion guide. *Eur. J. Mass Spectrom.*, 6:531–536, 2000.

[LTB75] G. Lawson, J. F. J. Todd, and R. F. Bonner. Theoretical and experimental studies with the quadrupole ion storage trap ('QUISTOR'). *Dynamical Mass Spectrometry*, 4:39, 1975.

[Lun04] D. Lunney. A mistral spectrometer accoutrement for the study of exotic nucleids. 2004.

[LWY71] G. E. Lee-Whitting and L. Yamazaki. Semi-nalytical calculations for circular quadrupoles. *Nucl. Instrum. Methods*, 94:319, 1971.

[MA91] A. C. Mueller and R. Anne. Production of and studies with secondary radioactive ion beams at LISE. *Nucl. Instrum. Methods B*, 56/57:559, 1991.

[MBB+01] M. Maier, C. Boudreau, F. Buchinger, J.A. Clark, J.E. Crawford, J. Dilling, H. Fukutani, S. Gulick, J.K.P. Lee, R.B. Moore, G. Savard, J. Schwartz, and K.S. Sharma. Stopping, trapping and cooling of radioactive fission fragments in an ion catcher device. *Hyp. Int.*, 132:517–521, 2001.

[McL47] N. W. McLachlan. *Theory and applications of Mathieu functions*. Clarendon, Oxford, 1947.

[McL51] Norman W McLachlan. *Theory and application of Mathieu functions*. Oxford: Clarendon Press, 1951.

[MD68] F. G. Major and H. G. Dehmelt. Exchange-collision technique for the rf spectroscopy of stored ions. *Phys. Rev.*, 170:91, 1968.

[Meu02] S. Meunier. The ISOLDE vacuum system. In CERN, editor, *Workshop on Radiation Protection Issues Related to Radioactive Ion-Beam Facilities (SAFERIB)*, pages 140–148, Geneva, Switzerland, 30 October- 1 November 2002. CERN-2003-004.

[MFH+79] G. Münzenberg, W. Faust, S. Hofmann, P. Armbruster, K. Güttner, and H. Ewald. The velocity filter ship, a separator of unslowed heavy ion fusion products. *Nucl. instrum. methods*, 161(1):65–82, 1979.

[MFK+93] V.I. Mishin, V.N. Fedoseyev, H.-J. Kluge, V.S. Letokhov, H.L. Ravn, F. Scheerer, Y. Shirakabe, S. Sundell, 0. Tengblad, and ISOLDE Collaboration. Chemically selective laser ion-source for the CERN-ISOLDE on-line mass separator facility. *Nucl. Instrum. Methods B*, 73:550, 1993.

[MH89] R. E. March and R. J. Hughes. *Quadrupole storage mass spectrometry*. John Wiley and sons, 1989.

[Moo88] R. B. Moore. Ion beam RFQ confinement and cooling. 1988.

[Moo98] R. B. Moore. Buffer gas cooling of ion beams. 1998.

[Mue00] A. C. Mueller. An overview of radioactive beam facilities. In J.L. Laclare, Gif sur Yvette, W. Mitaroff, Ch. Petit-Jean-Genaz, J. Poole, and M. Regler, editors, *Proceedings EPAC 2000*, pages 73–77, 2000.

[Mul02] A. Muller. Contamination of the ISOLDE vacuum system. In CERN, editor, *Workshop on Radiation Protection Issues Related to Radioactive Ion-Beam Facilities (SAFERIB)*, pages 149–158, Geneva, Switzerland, 30 October- 1 November 2002. CERN-2003-004.

[NCB+02] A. Nieminen, P. Campbell, J. Billowes, D. H. Forest, J. A. R. Griffith, J. Huikari, A. Jokinen, I. D. Moore, R. Moore, G. Tungate, and J. Äystö. On-line ion cooling and bunching for collinear laser spectroscopy. *Phys. Rev. Lett.*, 88:094801, 2002.

[Nie02] A. Nieminen. *Manipulation of low-energy radioactive ion beams with an RFQ cooler; application to collinear laser spectroscopy*. PhD thesis, University of Jyväskylä, 2002.

[Nie03] A. Nieminen. The new ion beam cooler at jyväskylä. *Nucl. Phys. News*, 13(1), 2003.

[NL05] T. Nilsson and M. Lindroos. The HIE-ISOLDE report. CERN-AB-2005-DRAFT, 2005.

[O'H03] J. F. O'Hanlon. *A users's guide to Vacuum Technology*. Wiley-Intervenience, New York, 2003.

[Pen36] F. M. Penning. Introduction of an axil magnetic field in the discharge (glimmentladung) between two coaxial cylinders. *Physica*, 3:873, 1936.

[Pet02a] M. Petersson. private communication, 2002.

[Pet02b] M. Petersson. A Monte Carlo method for the simulation of buffer gas cooling inside a radio frequency quadrupole. Master's thesis, Linköping University, IFM, 2002.

[PG05] I. Podadera and T. Giles. Overview of the control system for the ISCOOL project. *CERN-AB-NOTE-2005-024*, 2005.

[PHR00] G. Bánó P. Hartmann, Z. Donkó and K. Rózsa. Effect of different elementary processes on the breakdown in low-pressure helium gas. *Plasma Sources Sci. Technol.*, 9:183–190, 2000.

[Pod04a] I. Podadera. Design of a second generation RFQ ion cooler and buncher (RFQCB) for ISOLDE. *Nucl. Phys. A*, 746C:647–650, 2004.

[Pod04b] I. Podadera. RFQ cooler and buncher (and beam line associated). Technical report, CERN-AB-NOTE-2004-062, 2004.

[PR55] W. Paul and M. Raether. *Z. Phys.*, 140:262, 1955.

[PS53] W. Paul and H. Steinwedel. *Z. Naturforsch.*, 8 A:448, 1953.

[RA89] H. V. Ravn and B. W. Allardyce. On-line mass separators. *Treatise on Heavy-Ion Sci.*, 1989.

[Rav92] H. Ravn. Status and future developments for on-line mass separators. *Nucl. Instrum. Methods B*, 70:107, 1992.

[RBM88] S. Gulick R. B. Moore. The transfer of continuous beams and storage ring beams into electromagnetic traps. *Physica Scripta*, T22:28, 1988.

[RCG00] C. M. Surko R. C. Greaves. Inward transport and compression of a positron plasma by a rotating electric field. *Phys. Rev. Lett.*, 85:1883–1886, 2000.

[Rei02] K. Reisinger. Emittance measurements on the sideband cooling technique and introduction of the rotating wall cooling technique at REXTRAP. Master's thesis, Technische Universität München, 2002.

[RMD+05] D. Rodríguez, A. Méry, G. Darius, M. Herbane, G. Ban, P. Delahaye, D. Durand, X. Fléchard, M. Labalme, E. Liénard, and O. Naviliat-Cuncic. The LPCTrap for the measurement of the $\beta - \gamma$ correlation in ^{6}he. *Eur. Phys. J. A direct*, 25:705–707, 2005.

[Rod03] D. Rodríguez. *An RFQ for accumulation and cooling of heavy radionuclides at SHIPTRAP and high precision mass measurements on unstable Kr isotopes at ISOLTRAP*. PhD thesis, Universidad de Valencia, 2003.

[Rot90] A. Roth. *Vacuum technology*. Elsevier sciences, 1990.

[RS94] J. Rossbach and P. Schmuser. *Fifth general accelerator physics course*, volume 24, chapter Basic course on accelerator physics, pages 17–88. CERN, January 1994.

[Rud] K. Rudolph. private communication.

[SBB+91] G. Savard, St. Becker, G. Bollen, H. J. Kluge, R. B. Moore, Th. Otto, L. Schweikhard, H. Stolzenberg, and U. Wiess. A new cooling technique for heavy ions in a penning trap. *Phys. Lett. A*, 158:247–252, 1991.

[SBL+03] S. Schwarz, G. Bollen, D. Lawton, A. Neudert, R. Ringle, P. Schury, and T. Sun. A second-generation ion beam buncher and cooler. *Nucl. Instrum. Methods B*, 204:474, 2003.

[Sor00] P. Sortais. *Rev. Sci. Instrum.*, 71(2):617–622, 2000.

[SVGDW+79] T. Symons, Y. P. Viyogi, P. Doll G. D. Westfall, D. E. Greiner, H. Faraggi, P. J. Lindstrom, and D. K. Scott. *Phys. Rev. Lett.*, 42:40, 1979.

[The03] The EURISOL collaboration. *The EURISOL report*. GANIL, 2003.

[TP05] T. Tallinen and I. Podadera. The ISCOOL test bench control system. Technical report, CERN, Geneva, Switzerland, 2005. CERN-AB-Note-2005-.

[vD00] P. van Duppen. *Hyp. Int.*, Proc. APAC 1999, 2000.

[VDCJ+98] P. Van Duppen, J. G. Correia, A. Jokinen, J. Lettry, M. Lindroos, E. Kugler, H. Raimbault-Hartmann, H. L. Ravn, O. Tengblad, B. Jonson, P. G. Hansen, L. Liljeby, K. G. Rensfelt, R. Wyss, M. Grieser, D. Habs, T. Härtlein, R. Von Hahn, C. M. Kleffner, P. Reiter, D. Thirolf, P. G. Schwalm, H. Deitinghoff, A. Schempp, H. Backe, G. Bollen, G. Huber, K. L. Kratz, H. J. Kluge, U. Ratzinger, K. P. Lieb, M. Schumacher, G. Schrieder, P. A. Butler, P. Nolan, D. Warner, B. Gelletly, P. Baumann, P. Dessagne, A. Huck, A. Knipper, C. Miehé, G. Walter, G. Marguier, Cl. Serre, B. Visentin, J. L. Faure, E. D. Donets, E. Beebe, M. Huyse, D. Forkel-Wirth, G. Sletten, and B. Herskind. The REX-ISOLDE project. *Nucl. Instrum. Methods B*, 139:128–135, 1998.

[Wen01] F. J. C. Wenander. *Charge breeding and production of multiply charged ions in EBIS and ECRIS*. PhD thesis, Chalmers University of Technology, 2001.

[Wen04] F. Wenander. Charge breeding techniques. *CERN-AB-2004-035*, 2004.

[Wil02] A. Wilfart. Untersuchungen zur optimierung von ionenstrahlkühlern. Master's thesis, Ludwig-Maximilians-Universität München, 2002.

[Wil05] R. Wilfinger. *Proton Induced Thermal Stress-Wave Measurements for ISOLDE and CNGS*. PhD thesis, Vienna University of Technology, Atominstitut of the Austrian Universities, and CERN, European Organization for Nuclear Research, ISBN 92-9083-266-5, 2005.

[WLL03] F. Wenander, J. Lettry, and M. Lindroos. Transverse emittance investigation of ISOLDE target-ion sources. *Nucl. Instrum. Methods B*, 204:261–266, 2003.

[Wol87] H. Wollnik. *Optics of charged particles*. Academic Press, San Diego, 1987.

[WSL59] R. W. Wuerker, H. Shelton, and R. V. Langmuir. Electrodynamic containment of charged particles. *J. Appl. Phys.*, 30:342, 1959.

List of Figures

List of Tables

Acknowledgements

Without the help of your family, your friends, your colleagues and your coordinators, there would be no chance to write a thesis just by your own. A doctoral thesis, above all if it is located in a foreign country, is a long period in which one constantly need the support, both personal and scientific, from the people one has around. For that reason, I cannot finish without dedicating at least several lines to that people, trying not to forget anyone....

First of all, I would like to acknowledge the guidance and support from Dr. Ari Jokinen, coordinator of the ISCOOL project in the beginning and main source of a lot of ideas which this thesis contain. I want to recognize the help from Prof. Francisco Calviño. I would never forget the day he proposed me to apply for the CERN doctoral programme. Thanks for guiding me and helping me from the distance along these years. I would also want to acknowledge Dr. Mats Lindroos, who has been my CERN supervisor and thesis director and has followed and supported the project from the beginning. I would like to thank them for having had the though task of correcting and proofreading my thesis.

It is impossible to develop such a big project without the help of many people that in major or minor way have collaborated or to whom I have bothered. I am to mention specially the ISOLDE mechanical group: Jacques, Stefano and Nicolas. I have really learned a lot from you. Thanks for your patience.

The last part of the thesis was possible thanks to the REX-ISOLDE team: Fredrik, Pierre and Romain. Thanks Fredrik for his support from the beginning of my stay here in the REX measurements and in the ISCOOL project. À Romain pour faire amusantes les longues periodes de measures d'emittance et pour son preciouse aide. Et à Pierre pour son aide constante, bonne chance avec ISCOOL!

I cannot forget all the ISOLDE team, my work family during this period. Specially The "crazy" austrians, Roman and Martin. But also Ermanno, Daniel, Luis, Manoli, Bernard, Richard, Magda, Chabouh, Genevieve and Jacques. Thanks to make work life at CERN much more funny and easier.

I would like to acknowledge the precious help of the different CERN groups for the design of all the ISCOOL systems: Julien, Nicolas, Thomas and Erwin with the electronics, David and Sophie with the vacuum, Frank with the controls, Tomas and Tim with the optics or Alexander with the safety protection. Thank you all.

Many european institutions have been supporting the development and construction of ISCOOL. I am very much obliged to the Nuclear Department of the University of Manchester (Jonathan and Ernesto) and the CSNSM (Dave, Jean-François, Cyril and Celine). The support in the manufacturing of the first pieces from LMU (Oliver) and the Johannes Gutenberg-Universitat (Klaus) and the RF electronics (Klaus). The help and the experience from the University of Jyväskylä, Arto, Tommi, Joonas and Tuomas.

I cannot finish without recognising and giving my sincere acknowledgements to Daniel and

Olof for their invaluable help proof-reading this manuscript, giving very interesting and clever suggestions and comments.

My doctoral period implied to discover a new city, new friends, a new life. I will never forget the help from Alex, Toni, Juan, Bobo, Esther, Mirko, Luis, Riiicharl, Arturo, Cristina, Oscar, Montse, Stef, Raquel, Eduardo, Marco, Pedro, Alberto, Federico, Dave, Sonia, Alberto, Andrés, Silvia, Eli, Jero, Maria and all the others. Your friendship is my main conclusion.

Una nueva vida en la que he echado tanto de menos a los de antes, y que por suerte han seguido estando ahí, apoyándome desde la distancia. A mis viejos amigos de Reus: Ferran, Serra, Bartolo, Penadés, Xesca, Machado, Marta, Francesc, Carles, David, Marta, Xus, Cerve, Max, Dolors, Noe. Com no, als project leaders de la universitat, a en Mateu i en Sanchesss, gràcies per les vostres inoblidables visites!

Pero si algo me ha faltado durante todo este tiempo y a quien debo las gracias, es a toda mi familia, a mis padres, la niña, mis abuelos, mis tías y tíos, mis primas y primo, y todos los demás. Gracias a su esfuerzo, a su apoyo y a su amor he podido llegar libremente hasta aquí.

Y para el mayor descubrimento de esta tesis y mi mayor amiga y soporte durante los difíciles últimos tiempos. Sería ella quien merecería una cátedra... solo por soportarme. Gracias Marikiya.